IJL, Issue 2, Vol. 23, 2024
https://doi.org/10.31900/ijl.v23i2.449

Research Article

Diagnosis of Polycystic Ovary Syndrome using Free Testosterone levels via Surface Enhanced Raman Spectroscopy Induced by Gold Nanostar

Ruaa E. Imran*, Rawaa A. Faris

Institute of Laser for Postgraduate Studies, University of Baghdad, Baghdad, Iraq
** Email address of the Corresponding Author: ruaa.eesa2101m@ilps.uobaghdad.edu.iq*

Article history: Received 18 Jan. 2024; Revised 1 Apr. 2024; Accepted 7 Apr. 2024; Published online 15 Dec. 2024

Abstract

Background: Polycystic ovary syndrome (PCOS) manifests as anovulation, oligomenorrhea, and hyperandrogenism in women of reproductive age, affecting around 5-10% of this population. There is a pressing want for a rapid, inexpensive, and uncomplicated approach to qualitatively and quantitatively detect free testosterone in patients with Polycystic Ovary Syndrome (PCOS).
Materials and methods: This study utilized surface-enhanced Raman spectroscopy (SERS) coupled with gold nano star (GNS) to amplify the optical signal to detect serum-free testosterone in PCOS patients. The study comprised 56 PCOS women age range (17-45years) who were sent from different governorates to the Baghdad Medical City.
Results: Highly resolved and high-quality surface-enhanced Raman scattering (SERS) spectra were obtained for free testosterone adsorbed on a substrate. These spectra exhibited characteristic bands of free testosterone and allowed for the detection of low levels (1.7 nM/mL), with an enhancement factor (EF) of 59 *105.
Conclusions: Based on the current knowledge this paper represents the pioneering effort to ascertain the concentration of free testosterone with the SERS technique. It is possible to efficiently early detection of PCOS by measuring the very low concentration of serum-free testosterone in a low-cost technique.

Keywords: SERS, GNS, EF, PCOS, Free Testosterone.

1. Introduction

Polycystic ovary syndrome (PCOS) is the most common endocrine disease in women, supplying them with several viable mixtures of symptoms and signs and a number of phenotypes. Women diagnosed with polycystic ovary syndrome (PCOS) face a heightened susceptibility to insulin resistance and hyperandrogenism, both of which can significantly impact their overall well-being around middle age and lead to enduring difficulties such as Irregular Menstrual Cycles, Infertility, Weight Management Issues, Excessive Hair Growth (Hirsutism, Acne and Skin Problems, Mood Disorders and Increased Risk of cancer

daises [1]. Testosterone & Free testosterone are the primary sex hormones and anabolic steroids found in males [2]. In both sexes, testosterone is an androstanoid with 17 beta-hydroxy and 3-oxo groups. It plays an essential role in health and well-being, affecting mood, behavior, and preventing osteoporosis [3]. Excessive androgen production is considered the primary factor driving the development of PCOS symptoms. Hyperandrogenism results from the overproduction of androgens by both the ovaries and the adrenals, leading to clinical manifestations such as hirsutism, acne, androgenic alopecia, and elevated testosterone levels [4]. Hyperandrogenism is a defining feature of PCOS in women, and it occurs due to the disruption of normal ovarian or adrenal function, resulting in excessive androgen production.

Androgen excess in PCOS initially impacts folliculogenesis, impairing it. During the early, gonadotropin-independent stage, increased androgen levels stimulate the formation of primordial follicles and raise the number of small antral follicles [5]. Numerous studies have indicated that elevated androgen levels pose a persistent risk factor in the onset of PCOS. Elevated testosterone levels are associated with obesity, particularly abdominal fat, insulin resistance, and an increased risk of glucose intolerance [6]. The latest clinical guidelines in endocrinology recommend utilizing elevated levels of total and free testosterone for the purpose of diagnosing PCOS [7]. Testosterone predominantly binds to sex hormone-binding globulin (SHBG) and albumin, with a little proportion (1-2%) circulating as unbound free testosterone (free T) not associated to proteins. Only the percentage of testosterone that is not bound to proteins can enter the cell and have an effect on androgen activity [8]. Free testosterone is suggested as the best responsive indicator for identifying androgen excess in medical practices [9].

In current years, bio-photonic and electrochemical detection techniques have been utilized in early clinical analysis. Specificity for any given biomarker is often realized using antibodies. The exact binding of an antibody to its target antigen in a multipart combination such as serum and plasma affords the revealing and quantification of diseases at levels as low as pictograms (pg) [10]. Sample concentration is the main issue criticized in bio-sensing. While ordinary sensors can handle concentrations of about little mM, nano-bio-sensors have the possibility to detect concentrations of about Femto Molar (fM) or even Ato Molar (aM). This ability to detect such fractional amounts of biomolecules stands as an advantage in detection diseases in the early stage of development so that specialists can interact and provide help to patients [11]. Bio-sensing has become increasingly popular due to the exceptional optical properties of NPs. Noble metal nanoparticles (NPs) have been utilized to establish a variety of highly sensitive bio-sensing techniques for nucleic acids, proteins, antibodies, enzymes, and other biological molecules. These techniques explore different physicochemical properties of NPs, including Localized surface Plasmon's Resonance (LSPR), fluorescence enhancement/quenching, SERS, electrochemical activity, and more [12]. Many research groups have reported success in detecting biomarkers or analytes using SERS systems; their ultimate goal is to advance POC technology.

Targeting cancers, diagnosing malaria, and recognizing bacterial meningitis are just some of the various uses for SERS techniques [13]. Gold nanostars (GNS) are a type of nanomaterial with many branches and sharp edges that behave as SERS "hotspots". These nanostars have been found to provide better SERS enhancement factors (EF) compared to nanospheres, making them the preferred choice for colloidal SERS substrates. SERS is an extension of standard Raman spectroscopy that uses an extremely weak optical effect to amplify Raman intensities by a factor of 104-106 in order to improve signal throughput and sensitivity. Because of its sensitivity and specificity, SERS technology has received a lot of attention and has been widely used in chemistry and biochemistry during the last few decades [14]. Different structures have been recognized for improving and evaluating SERS signals, as the metal's shape affects the organization of nanomaterials in the local electric field, and therefore, the distribution of SERS performance. GNS with different divisions and cutting edges function as SERS hotspots across diverse shapes, leading to higher SERS enhancement factors (EF) in comparison to nanorods and nanoparticles [15].

This study employed the SERS approach for the detection of Free Testosterone in the serum samples of Iraqi patients with PCOs. Subsequently, gold nanostructured SERS biosensors were utilized to evaluate their efficiency. To the best of our understanding, there has been no prior global research that has using the SERS approach to examine these predictive markers for PCOs.

2. Experimentally Procedures

The study comprised of 56 PCOS women and 27 control healthy women age range (17-45 years) who were sent from different governorates to Baghdad Medical City.
The levels of free testosterone in the serum were examined following the withdrawal of 5 ml of venous blood.

2.1 Chemicals and Instruments

A free testosterone kit was purchased from DRG Instrument GmbH /Germany) in different concentrations (0, 0.2,1,4,20and 100pg/ml). Nanoparticles, Spain, who supplied gold nano star (GNS) 0.2 mmol/L of 0.040 mg/mL of 40 nm of GNS form of polyvinyl pyrolidone.

2.2 Free testosterone Level measurement by Uv-Vis spectroscopy

The UV-Vis. analyses of samples (solutions) are carried out using UV- Vis. Shimadzu Spectrophotometer (UV-1800) to obtain the sample spectra.

2.3 Free testosterone Level measurement by SERS

In order to measure the SERS spectra 10µml of free testosterone with different concentration (0, 0.2,1,4,20and 100pg/ml) were mixed with one drop of 40nm colloidal gold nano star and mixed well at room temperature. In quartz cuvette, the mixture was exposed to 532nm for 10sec.

2.4 Statistical analysis

Frequency, percentage, mean, and standard deviation were utilized to depict the information in whole statistical analyses using SPSS version 25.0 software. When comparing more than two variables, an ANOVA is utilized to assess how the mean level of the numerical data differs. The correlation between numerical data was assessed using the Pearson correlation regression coefficient (r). A significant threshold of $p < 0.05$ was selected.

3. Results

3.1 Free testosterone Level measurement by Uv-Vis spectroscopy

In order to study the optical properties of free testosterone uv-vis spectrum as shown in Figure 1. The wide absorption spectrum was detected at regions from 200nm to 300nm. The absorption peaks increased with increasing in free testosterone concentrations.

3.2 Free testosterone Level measurement by SERS

From the Raman spectra, it may be inferred that only a subset of the Raman bands is now identified, specifically at 263, 662, 1469, 2154, 2672, 3288, and 4298 cm-1. Figure 2 demonstrates the presence of typical Raman bands for free testosterone in the range of approximately 662 to 1469 cm−1. These bands can be attributed to vibrations in the hydrocarbon, carbonyl, and carboxylic functional groups [13].

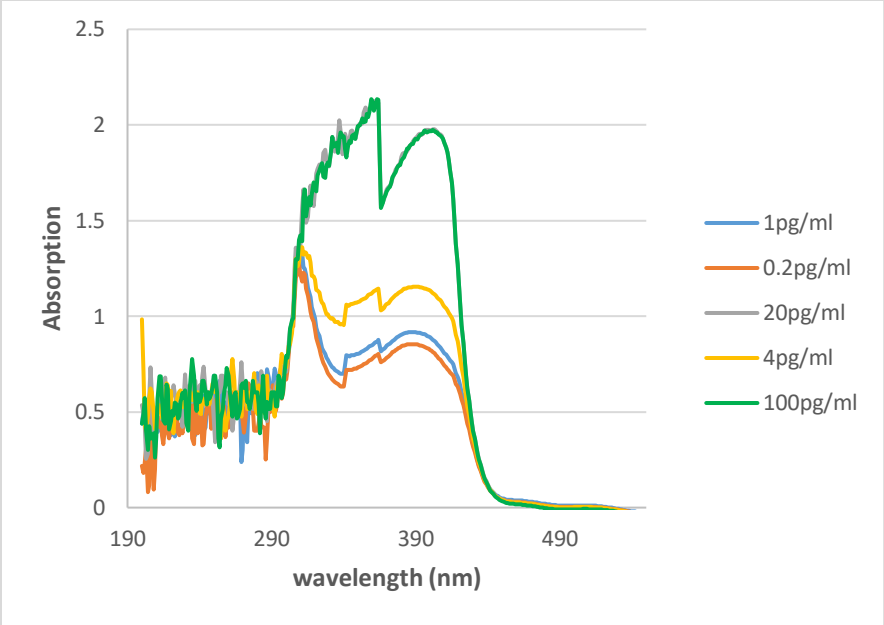

Fig. 1: Uv-Vis Spectrum of different concentrations of free Testosterone (0.2,1,4,20and 100pg/ml).

The SERS of free Testosterone 40 nm and GNS determined was found to have the most effective enhancement effect compared to other SERS substrates tested in this study. Therefore, GNS was selected as the preferred substrate for detecting trace amounts of free testosterone in blood. Highly resolved and high-quality surface-enhanced Raman scattering (SERS) spectra were obtained for free testosterone adsorbed on a substrate. These spectra exhibited characteristic bands of free testosterone and allowed for the detection of low levels (1.7 nM/mL). The SERS spectra were superior to the typical Raman spectrum of free testosterone. The relative strength variations observed in the characteristic bands were attributed to the interaction between free testosterone molecules and the active metal surface [16]. Therefore, it can be deduced that the limit of detection (LOD) for free testosterone is the same as the LOD for its most intense Raman peak, which is situated at a Raman shift of 1630 cm^{-1}. To estimate the concentration of free testosterone, we can utilize a univariate analysis that examines the strength of the free testosterone peak at 1640 cm^{-1}. This peak is associated with the stretching of the (C-C) and (C-N) rings. The Raman peak at 1640 cm^{-1}, which was excited at a wavelength of 532 nm, exhibited the maximum intensity among the Raman peaks associated with free testosterone. In comparison to other Raman peaks observed in samples that have been diluted of free testosterone, this particular peak was more easily quantifiable. Consequently, using this peak as our primary indicator resulted in a significantly reduced limit of detection for free testosterone. SERS largely arises from the electromagnetic enhancements of plasmonic nanostructures and, to a lesser extent, from chemical enhancement. The cutting tips on GNS possess structural properties that generate a highly confined electromagnetic field, making them 'hot spots' for SERS.

Prior research has indicated that GNS exhibited a notably greater enhancement in SERS in both colloids, when compared to gold nanorods or gold nanospheres, following their adsorption on a paper substrate [12]. The concentration of free testosterone was determined by utilizing the EF to assess the associated enhancement in performance for the paper substrate. This was accomplished at the aforementioned ideal conditions, as given by the subsequent mathematical expression[12]:

$$EF = (I_{SERS}/C_{SERS}) / (I_{RS}/C_{RS}) \quad (1)$$

Where:

I_{Raman} is the Raman signal intensities of free testosterone only.

I_{SERS} is the Raman signal intensity of free testosterone after adding GNSs.

C_{SERS}: sample concentration
C_{RS}: standard concentration

SERS and Raman measurements quantify the concentration of free testosterone compounds, while I_{SERS} and I_{RS} represent the intensity levels of free testosterone at 1640 cm^{-1} in SERS and classic Raman spectra. Similarly, C_{SERS} and C_{RS}. With the use of GNS, a mean EF of 59 * 105 was reached for the free testosterone under these optimum conditions.
Significantly, the degree of the SERS reaction was highest for the gold nanostars (GNS), as shown in Figure 2. The core principle of SERS is based on amplifying the spatial extent of metallic nano-materials to harness the excitation of SPR. However, aggregation was inadequately regulated, leading to heightened unpredictability and intricacy within the already complex system. To improve the topical electromagnetic field linked to the SPR, a viable strategy is to amplify topical nanomaterial curves.
It has been proved that when two spherical nanomaterials are properly clustered or clumped together, the SPR band is separated into different pieces, including longitudinal and transverse components. With the exception of two modes (quadrupole and dipole) in nanoparticles, there was no differentiation between them.

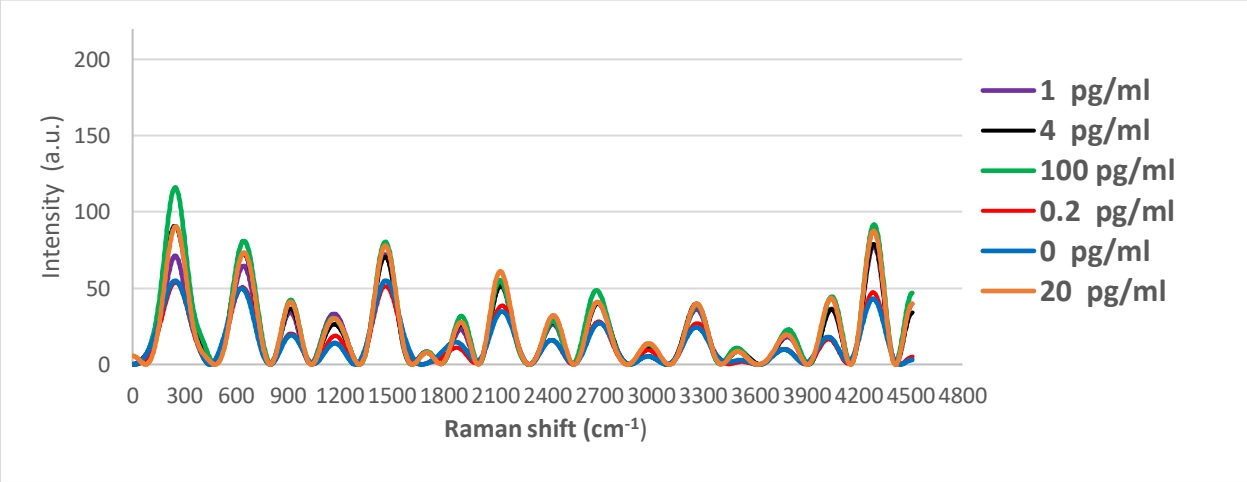

Fig. 2: Raman Spectrum of different concentrations of free Testosterone (0, 0.2,1,4,20and 100pg/ml) without GNS.

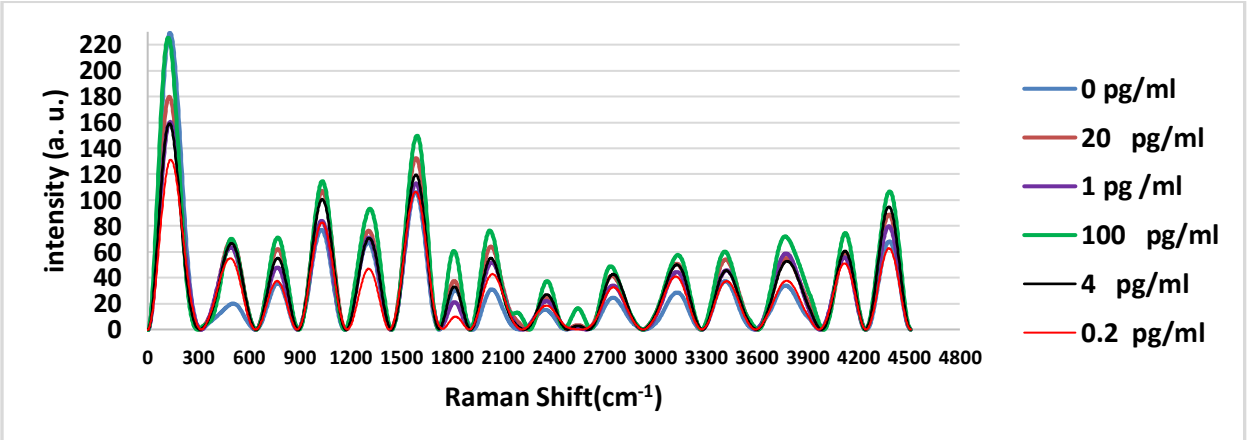

Fig. 3: Raman Spectrum of different concentrations of free Testosterone(0, 0.2,1,4,20and 100pg/ml) with GNS.

During the investigation of nano-triangles, researchers have observed four distinct surface resonances as a result of their anisotropic shape: out-of-plane dipole and quadrupole, as well as in-plane dipole/quadrupole. Nano stars possess a greater number of sharp edges and exhibit unique properties as highly complex an isotopically shaped nanoparticle. These nanoparticles exhibit many modes of vibration, each occurring at slightly different frequencies within gold materials. The Raman enhancement ratio was investigated as shown in figure 4.

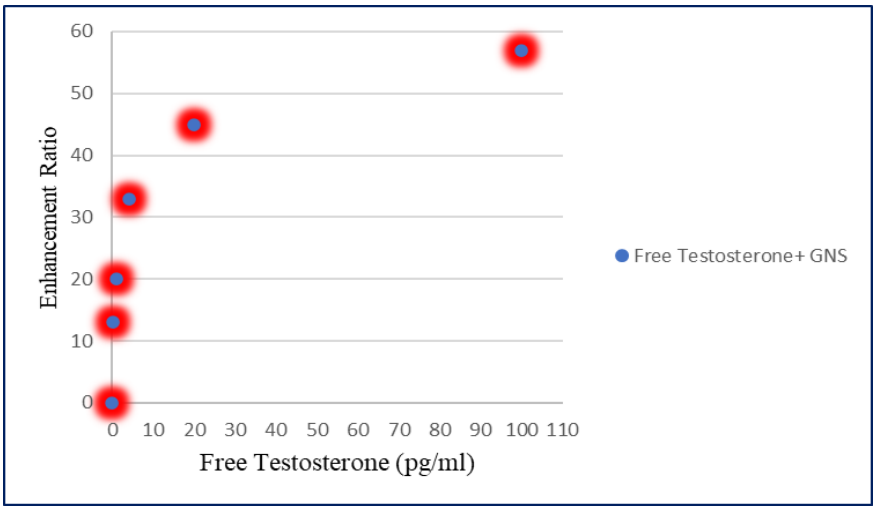

Fig. 4: Raman enhancement ratio of free testosterone with GNS (40 nm).

It has been proved that when two spherical nanomaterials are properly clustered or clumped together, the SPR band is separated into different pieces, including longitudinal and transverse components. With the exception of two modes (quadrupole and dipole) in nanoparticles, there was no differentiation between them. Nano stars possess a greater number of sharp edges and exhibit unique properties as highly complex isotopically shaped nanoparticles. These nanoparticles exhibit many modes of vibration, each occurring at slightly different frequencies within gold materials.

In order to assess the diagnostic efficacy of three different approaches (Elisa, Raman, SERS with GNSs) in detecting free testosterone at an early stage. These methods exhibit a much higher Area under the curve (AUC) compared to Raman pure. Among these methods, the one utilizing SER) with GNSs demonstrates the highest performance, with AUC values of 0.74, 0.79, and 0.88, respectively. AUC values closer to 1 indicate the screening measure reliably distinguishes among samples with patients and healthy women.

The comparison study was conducted to address the limitations of specificity and sensitivity associated with individual hormone visualization. Therefore, we employed gold nanostructures to improve the performance of surface-enhanced Raman spectroscopy (SERS). The concentration of free testosterone in PCOS patients was markedly decreased compared to the healthy control submit oneself ($P = 0.022$), As shown in Table 1.

4. Conclusions

In conclusion, the Free Testosterone SERS tags have been effectively synthesized and demonstrate that the amalgamation of GNSs can function as a sensor for free testosterone concentrations. This method was very simple and straight forward methods without any complications in procedures. The whole procedures done in five minutes only. The arrangement of the GNS produces organize an array (regular surface structure) that influences the SERS of the sample, resulting in increased EF which can be used to detect very low concentrations of free testosterone in a low-cost technique.

Table 1: Mean distribution of Free testosterone in sera of studied groups.

Assay	Age groups / Year	PCOS			Controls		
		N	Mean	Std. Deviation	N	Mean	Std. Deviation
Free Testosterone by traditional Method (Elisa)	15 - 25	20	25.7033	15.58490	11	58.0705	46.49889
	26 - 35	26	38.3068	25.01109	10	46.2768	20.65601
	36 - 45	10	30.5996	9.03356	6	48.9217	50.61042
	P- value	P = 0.108 NS			P = 0.783 NS		
Free Testosterone by SERS	15 - 25	20	1.11075	.662984	11	.54700	.325418
	26 - 35	26	.80550	.571512	10	.52070	.187116
	36 - 45	10	.50240	.210335	6	.53083	.209523
	P- value	P = 0.022 S			27	P = 0.973 NS	

5. Institutional Review Board (IRB) license

This study has received approval from the Ethical Committee of the Ministry of Health (MOH) of Iraq as cross-sectional research. Each participant granted their informed consent.
Approval from the Scientific Research Ethics Committee was received (No. 31) in 10/1/2024.

References

[1] R. J. Al-Ghanny, M. M. B. Al-Moosawi, and B. A. Abd, "Effects of vitamin D deficiency in polycystic ovarian syndrome," Iraqi J. Sci, pp. 33–42, 2022.
[2] "Retrieved Understanding the risks of performance-enhancing drugs," Mayo Clinic, 2019.
[3] N. Bassil, S. Alkaade, and J. E. Morley, "The benefits and risks of testosterone replacement therapy: a review, " Ther," Ther. Clin. Risk Manag, vol. 5, no. 3, pp. 427–448, 2009.
[4] K. R. Reddy et al., "CYP11A1 microsatellite (tttta)n polymorphism in PCOS women from South India," J. Assist. Reprod. Genet., vol. 31, no. 7, pp. 857–863, 2014.
[5] V. Nisenblat and R. J. Norman, "Androgens and polycystic ovary syndrome, " Curr," Curr. Opin. Endocrinol. Diabetes Obes, vol. 16, no. 3, pp. 224–231, 2009.
[6] Q. A. Ibraheem, L. H. A. Al Obaidy, G. A. Nasir, and M. T. Al Obaidi, "Fat mass and obesity association gene polymorphism in PCOS Iraqi women," Baghdad Sci. J., vol. 17, no. 3(Suppl.), p. 1103, 2020.
[7] R. S. Legro et al., "Diagnosis and treatment of polycystic ovary syndrome: an Endocrine Society clinical practice guideline," J. Clin. Endocrinol. Metab., vol. 98, no. 12, pp. 4565–4592, 2013.
[8] G. L. Hammond, "Access of reproductive steroids to target tissues," Obstet. Gynecol. Clin. North Am., vol. 29, no. 3, pp. 411–423, 2002.
[9] N. F. Goodman, R. H. Cobin, W. Futterweit, J. S. Glueck, and R. S. Legro, "American College of Endocrinology, and Androgen Excess and PCOS Society disease state clinical review: guide to the best practices in the evaluation and treatment of polycystic ovary syndrome - part1," Endocrine Practice, vol. 21, no. 11, pp. 1291–1300, 2015.
[10] R. A. Faris, Z. F. Mahdi, and A. M. T. Al-Layla, "Preliminary study of the insulin growth factor binding protein-3 (IGFBP3) level in Iraqi women with breast cancer," in AIP Conference Proceedings, 2021.
[11] R. A. Faris, Z. F. Mahdi, M. M. K. Al-Tu'ma, and F. J. Al-Tu'ma, "Surface enhanced Raman spectroscopy based sensitive and specific detection of vitamin D3, glycated hemoglobin, and serum lipid profile of breast cancer patients," in AIP Conference Proceedings, 2023.
[12] A. M. T. Allayla, R. A. Faris, and Z. F. Mahdi, "Construction of insulin-like growth factor nanocomposite biosensor by Raman spectroscopy," Vib. Spectrosc., vol. 114, no. 103252, p. 103252, 2021.
[13] A. M. Ondieki, Z. Birech, K. A. Kaduki, P. W. Mwangi, M. Juma, and B. M. Chege, "Label-free assaying of testosterone and growth hormones in blood using surface-enhanced Raman spectroscopy," Vib. Spectrosc., vol. 129, no. 103605, p. 103605, 2023.
[14] A. M. Alwan, M. S. Mohammed, and R. M. Shehab, "The performance of plasmonic gold and silver nanoparticle-based SERS sensors," Iraqi J. Sci., pp. 1320–1327, 2020.

[15] F. G. Hamzah and H. R. Mahmood, “Signature of plasmonic nanostructures synthesised by electrical exploding wire technique on surface-Enhanced Raman Scattering,” Iraqi J. Sci., pp. 167–179, 2021.
[16] F. J. Moaen and H. R. Humud, “Raman scattering enhancement by silver nanostructures prepared by electrical exploding wire technique,” Iraqi J. Sci., pp. 2017–2024, 2022.

تشخيص متلازمة المبيض المتعدد الكيسات باستخدام مستويات هرمون التستوستيرون الحرة عبر تحليل رامان الطيفي المحسن للسطح بواسطة الذهب النانومتري ذو الشكل النجمي

رؤى عيسى عمران* , رواء احمد فارس

معهد الليزر للدراسات العليا، جامعة بغداد، بغداد، العراق

البريد الالكتروني للباحث*: ruaa.essa2101m@ilps.uobaghdad.edu.iq

الخلاصة

الخلفية: تظهر متلازمة المبيض المتعدد الكيسات (PCOS) على شكل انقطاع الإباضة، وندرة الطمث، وفرط الأندروجين لدى النساء في سن الإنجاب، مما يؤثر على حوالي 5-10٪ من هذه الفئة من السكان .هناك حاجة ملحة لاتباع نهج سريع وغير مكلف وغير معقد للكشف نوعيًا وكميًا عن هرمون التستوستيرون الحر لدى المرضى الذين يعانون من متلازمة المبيض المتعدد الكيسات.(PCOS)

المواد والطرق: استخدمت هذه الدراسة مطيافية رامان المحسّنة على السطح (SERS) مقترنة بنجمة النانو الذهبية (GNS) لتضخيم الإشارة الضوئية للكشف عن هرمون التستوستيرون الخالي من المصل لدى مرضى متلازمة تكيس المبايض .شملت الدراسة 56 امرأة مصابة بمتلازمة تكيس المبايض من الفئة العمرية (17-45 سنة) تم إرسالهن من محافظات مختلفة إلى مدينة الطب في بغداد.

النتائج: تم الحصول على أطياف تشتت رامان (SERS) عالية الدقة وعالية الجودة من أجل هرمون التستوستيرون الحر الممتز على الركيزة .أظهرت هذه الأطياف نطاقات مميزة من هرمون التستوستيرون الحر وسمحت باكتشاف المستويات المنخفضة (1.7 نانومتر/مل)، مع عامل تعزيز (EF) قدره 59 * 105.

الاستنتاجات: استنادا إلى المعرفة الحالية تمثل هذه الورقة الجهد الرائد للتأكد من تركيز هرمون التستوستيرون الحر باستخدام تقنية SERS. من الممكن الكشف المبكر عن متلازمة تكيس المبايض بكفاءة عن طريق قياس التركيز المنخفض للغاية لهرمون التستوستيرون الخالي من المصل باستخدام تقنية منخفضة التكلفة.

الكلمات المفتاحية : مطيافية رامان السطحية المحسنة, الذهب النانومتري ذو الشكل النجمي, عامل التعزيز, متلازمة المبيض المتعدد الكيسات, هرمون التستوستيرون الحر.

IJL, Issue 2, Vol. 23, 2024
https://doi.org/10.31900/ijl.v23i2.470

Research Article

A Computational Fluid dynamic (CFD) Modeling and FE Simulation of (NiBSi) Coating via Selective Laser Melting Process

Walaa Isam Rasool *, Ziad Aeyad Taha

Institute of Laser for Postgraduate Studies, University of Baghdad, Baghdad, Iraq
** Email address of the Corresponding Author:walaa.isam1101a@ilps.uobaghdad.edu.iq*

Article history: Received 29 Mar. 2024; Revised 27 Apr. 2024; Accepted 5 May 2024; Published online 15 Dec. 2024

Abstract: Powder bed methods, including selective laser melting (SLM), provide significant versatility in both design and manufacturing processes. However, the existing limitation of this method lies in its ability to produce single-material parts. For intricate multi-material requirements such as coating processes, optimal solutions involve a customized integration of diverse materials required to control the melting and solidification process within the different metals' interfaces. In this study, a computational fluid dynamic (CFD) model is created to analyze the two-metal SLM process, two types of metal used in this study NiBSi as a coat material on the surface of the stainless steel 316L. The model relies on classical physics laws to derive the governing equations, which are subsequently solved using the ANSYS FLUENT software. A User-Defined Function (UDF) written in C-language is utilized to define the heat source, and then it is executed over the cell face center in each time step. The melting of NiBSi powder on a stainless steel substrate was studied, and liquid mass fraction, laser power, and scanning speed were considered as the parameters of the investigation. The model undergoes a validation process using online-published data to confirm its accuracy and reliability before exploring four power values and four scanning speeds as parameters. The model predictions revealed a perfect interface region between the two metals and a clear correlation between the laser power and the size of the fully melted zone.

Keywords: CFD modeling, selective laser melting, two-metal SLM, coating.

1. Introduction

Additive manufacturing (AM) simplifies the production of complex components with customized geometric features, potentially heralding a new era in industrial evolution. Powder bed fusion (PBF) is considered as a principal and commonly used approach in metal AM processes [1-5]. Generally, it is categorized as electron powder bed fusion, selective laser sintering, direct metal laser sintering, and selective laser melting (SLM) [6-9]. Notably, among these, SLM represents a significant advancement in

AM technology, given its capability to produce components with a refined microstructure and exceptional mechanical properties [10-13]. During the SLM process, the temperature distribution undergoes rapid changes due to the energy beam's fast movement. Localized high energy input can result in a substantial temperature gradient, causing elevated residual stresses, and reduced wear resistance and hardness in the final products [14]. SLM parameters, including scanning speed, scanning strategy, spot size, and laser power exert considerable influence on the quality of the produced parts. Effectively optimizing these parameters is a crucial technique for attaining the targeted microstructure, densification, and mechanical properties of the produced parts [15, 16]. For instant various deficiencies, such as balling effects, or significant residual stresses can be managed by appropriately optimizing the scanning strategy in the AM process [17, 18]. Stainless steel is a frequently employed feed metal powder in the SLM process. This preference is attributed to various factors, including ease of use, safety, and relatively low cost. Specifically, 316L stainless steel finds extensive use in the aerospace industry due to its corrosion resistance and commendable specific strength [19]. However, Stainless steel components manufactured using SLM technology often exhibit low hardness and suboptimal surface quality. Hence, there is a genuine need for post-processing methods to improve protection and surface quality, as noted by Wang, Shen [20]. For example, the creation of a super-hydrophobic layer on the SLM substrate can significantly enhance corrosion resistance, self-cleaning properties, and resistance to snow accumulation. Techniques such as plasma etching, anodic oxidation, and phase separation are employed to develop the hydrophobic layer. However, it is acknowledged that these methods can be costly and involve harsh conditions, limiting their application. Alternatively, the SLM coating technique has recently emerged as having significant potential in selective deposition, allowing for the modulation of produced parts as needed [20]. In this regard, Konovalov, and Osintsev [21] investigated the feasibility of modifying the surface of the Ti-based alloy Ti-6.5Al-1Mo-1V-2Zr through the deposition of a SLM coating using Ni-based super alloy Ni-16Co-11Cr powder. The coating thickness varies between 70 and 130 μm, and the coating is composed of several phases, the main ones including titanium TiCo0.5Ni0.5, Ti0.25Al0.75, TiNi, TiCrAl. The nano hardness of the coating reaches a maximum of 10.5 GPa at a distance of 50 μm from the surface, which is twice as high as that of the Ti-based substrate. Another study by Shojaei and Trabia [22] examined the impact of applying a Ti/SiC Metal Matrix Nanocomposite coating (MMNC) to a Ti–6Al–4V substrate. The coating, deposited using the SLM technique, was tested alongside uncoated Ti–6Al–4V samples. Hypervelocity impact experiments, conducted with projectile velocities ranging from 3.7 to 5.4 km/s, revealed that the Ti/SiC MMNC coating improved impact resistance by reducing both impact diameter and crater depth. In a related study, Freitas, de Oliveira [23] applied boron-modified stainless steel coating to the surface of low carbon steel (AISI 1020) using SLM. The produced coatings, with thicknesses ranging from 200 to 600 μm, were metallurgically bonded to the substrate. This coating process exhibited wear resistance, displaying a specific wear rate of approximately $4.5\times10{-}5$ $mm^3{\cdot}N^{-1}{\cdot}m^{-1}$, significantly outperforming the substrate with a specific wear rate of about $1.8\times10{-}3$ $mm^3{\cdot}N^{-1}{\cdot}m^{-1}$. Cheng, Xu [24] used jet electrochemical machining to eliminate surface defects on SLM-formed parts prior to the application of a nickel coating, aimed at extending the operational service life. The electrochemical machining effectively eliminated nearly all surface defects from the SLM process, creating a consistent microporous structure that seamlessly integrated with the nickel coating. The resulting coating exhibited optimal corrosion resistance and binding strength. In a 3.5 wt% NaCl solution, the corrosion potential reached 20.196 V, with a maximum binding force of 35 N. Younsi, Boher [25] adopted the SLM to apply cobalt-based alloy coatings onto a C35 steel substrate.

The study explored the correlations among interlayer times, crystalline structures, iron dilution, and micro-hardness for varying numbers of layers. The findings showed that decreasing the interlayer time elevated the temperature within the melting bed and facilitated material transfer from the substrate. Also, the coating thickness comprised a Co-Cr-Fe mixture, delineated into two regions: a transition zone near the interface and a stabilized zone closer to the substrate. Notably, the actual coating thickness consistently increased when the interlayer time was reduced. Given that the SLM process comprises multiple parameters, time-consuming, and high costs, there is a demand for effective and precise numerical models to simulate the process [26]. Different numerical techniques have been presented recently to model the

process. In this context, Liu, and Fang proposed a mesoscale computational fluid dynamics (CFD) model to predict porosity in the SLM process [27]. The model takes into account the heat accumulation from previous tracks and the impact of scanning strategies for SS 316L and Ti-6Al-4V, respectively. Yu and Zhao developed an advanced three-dimensional computational model for precise simulations of the multiphysics multiphase processes associated with SLM. The model integrates a semi-coupled resolved CFD, multi-phase, and Discrete Element Method (DEM)[28] . A study by Xu, and Jiang [29] created a sophisticated 3D particle-scale CFD model for the selective parallel dual laser melting (SPDLM) process. The model enables the simulation of the dynamic behavior of molten pools of a Nickel-based superalloy. The study particularly focused on investigating phenomena such as necking, wetting, and pores near the overlapping region. The predicted results demonstrated that the SPDLM process enhances the re-melting rate and improves the wettability of the overlapping region. More recently, Anand and Chang [30] formulated a model to predict the properties of the melt pool on the first layer of the SLM process. A numerical simulation was conducted to acquire the transient temperature and velocity distribution throughout the process. Then, the obtained results were integrated with the proposed model. The model's efficacy was validated with experimental results and melt pool characteristics reported in previous publications. The model exhibited a Root Mean Square Error (RMSE) between 0.49 and 0.53. The review of existing literature indicates that numerous investigations have delved into improving the performance of the SLM process through diverse experimental and modeling techniques. However, a significant gap has been identified in the topic modeling of the SLM process, more particularly modeling coating using SLM.

In this study, an attempt has been made to construct a 3D model utilizing the CFD techniques to optimize the parameters of the NiBSi powder SLM coating process on an SS 316L substrate produced using another SLM process.

2. SLM coating background

Components manufactured by SLM technology are usually identified to exhibit insufficient hardness and subpar surface quality. Among the different technologies that have been tested to develop the quality of the produced parts' surface is the SLM. It has gained significant interest because of its versatility, adaptability, and numerous parameters that can be optimized. Laser energy, spot diameters, scanning speed, and hatch distance are some of these parameters. Conducting experimental optimization for such a broad range of parameters could be a time-consuming and costly operation. A well-established and verified numerical model can efficiently accomplish the task in a cost-effective and time-efficient manner, with a negligible margin of error.

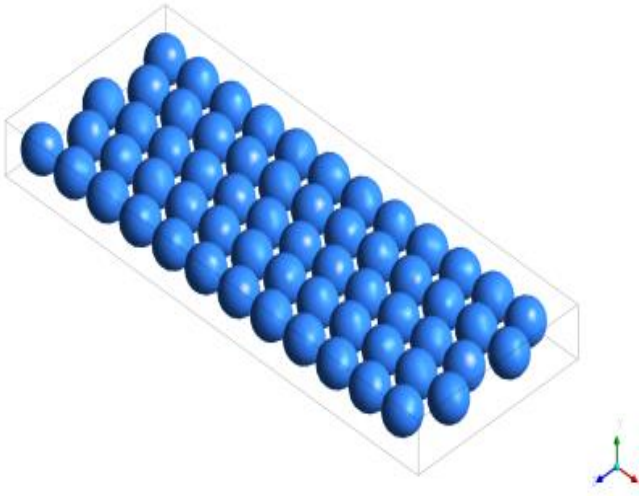

Fig.1: Geometry of the model showing the configuration and arrangement of the Ni powder particles.

The primary discretization technique employed in the CFD code is the finite volume method (FVM). In this approach, the governing equations for fluid dynamics are formulated using the conservation laws. It is noteworthy to mention that the CFD code allows for solving the fluid case either in a steady or unsteady manner using an iterative method. Initially, an approximate estimate is assumed, and then these values are iteratively adjusted until convergence is achieved. The term "convergence" in this context signifies that there will be no additional alteration in the variables during the subsequent iteration. ANSYS WORKPENCH R19.2 FLUENT software is used in this study to simulate the SLM process where a laser beam is considered as a heat source to melt the metal particles. The model considers the thermo-fluid parameters within the melting and solidification approach.

3. Governing equations

3.1 Continuity equation

The mass governing equation for the powder and solid domains takes the form as depicted in the provided Equation (1) which was given by Versteeg and Malalasekera [31].

$$\frac{\partial \rho}{\partial t} + \frac{\partial (\rho \boldsymbol{u})}{\partial x} + \frac{\partial (\rho \boldsymbol{v})}{\partial y} + \frac{\partial (\rho \boldsymbol{w})}{\partial z} \quad (1)$$

where ρ represents fluid density, t is time, and u denotes the velocity vectors for components u, v, and w in the x, y, and z directions, respectively. It is important to note that, in this particular case, the solution is based on a pressure-based solver with incompressible fluid, resulting in the density being equal to zero.

3.2 Navier–Stokes equation

This equation is crucial in the Computational Fluid Dynamics (CFD) code as it embodies the term of viscous stress in the balanced form of momentum. The following equation pertains to momentum in the x-direction, and similar formulations can be derived for the y- and z-directions [31]. It is evident from the equation below that there exists a connection between viscous stress and pressure within the fluid

$$\frac{\partial \rho u}{\partial t} + div\ (\rho u u) = -\frac{\partial p}{\partial x} + div\ (\mu\ grad\ u\ ) + S_{Mx} \quad (2)$$

Equation (2) expresses the momentum in the x-direction, with p denoting pressure, μ representing fluid viscosity, and S stands for the source term. Typically, this equation is reformulated in a more general form, as indicated below [31]:

$$\rho u . \nabla u = -\nabla p + \nabla . \tau \quad (3)$$

here τ is the shear stress tensor and ∇ denotes $\frac{\partial}{\partial x} + \frac{\partial}{\partial y} + \frac{\partial}{\partial z}$

3.3 Energy equation

The energy equation is given by Versteeg and Malalasekera [31] as:

$$u\frac{\partial T}{\partial x} + v\frac{\partial T}{\partial y} = \alpha_{eff}\left(\frac{\partial^2 T}{\partial x^2} + \frac{\partial^2 T}{\partial y^2}\right) \quad (4)$$

The coefficient of average heat transfer (α) can be considered based on the total surface area.

3.4 Heat generation and distribution formulation

A volumetric heat source is suggested to play a role in facilitating the penetration of the laser beam into the powders [32]. The absorptivity profile group is employed in the model, presenting a volumetric Gaussian distribution that accounts for the penetration of the laser beam into the powder [33].

$$q = \frac{9PA}{R^2\pi H\left(1-\frac{1}{e^3}\right)} exp\left(\frac{-9\left(x^2+y^2\right)}{R^2 log\left(\frac{H}{z}\right)}\right) \quad (5)$$

Here P represents the laser power (W), R denotes the laser beam diameter (m), H indicates the heat source penetration depth (m), and A is the materials effective laser energy absorption, it is set as 0.8. ANSYS FLUENT software has limitations in certain cases that necessitate customization of functions or equations essential during simulation processes. Additionally, there are instances where calculations need to be performed based on specific equations at each time step or iterations over cell faces. FLUENT has limitations in this regard; therefore, a User Define Function (UDF) was employed. It is written in C-language, compiled, and interpreted during the simulation. Once interpreted, the function specified for defining the boundary condition, applying material properties, or setting the heat flux becomes available in the graphical interface of FLUENT [34]. In this study, the parameters of the laser have been incorporated into the User Define Function (UDF) and executed over the cell face center at each time step. The widely employed computational approach for comprehending the significance and impact of fluid turbulence behavior is through the use of turbulence models. Numerous turbulence models are integrated into CFD codes for solutions. It is established in the literature that the *k-ε* model delineates the interplay between two fundamental factors in fluid flow issues—kinetic energy and dissipation rate. This model is recognized for its efficacy in connecting the mechanistic effects of kinetic energy (k) and the dissipation rate (ε) of this energy [35].

4. Geometry formation and mesh creation

The model's geometric structure is formulated using WORKBENCH R19.1 and its design modeler software. This software facilitates the preparation of the model for subsequent stages, including meshing and solving. A two-dimensional CFD model is employed to simulate the interaction between the metal powder and the laser beam. The model, is configured with a transient option for a time-dependent solution, and it assumes an average diameter of 48 µm for the metal powder particles. The dimensions of the model are 450 µm in length, 200 µm in width, and 100 µm in thickness, as given in Fig. 2 below. Within the model, the particles are assumed to have a uniform spherical shape and have a uniform arrangement.

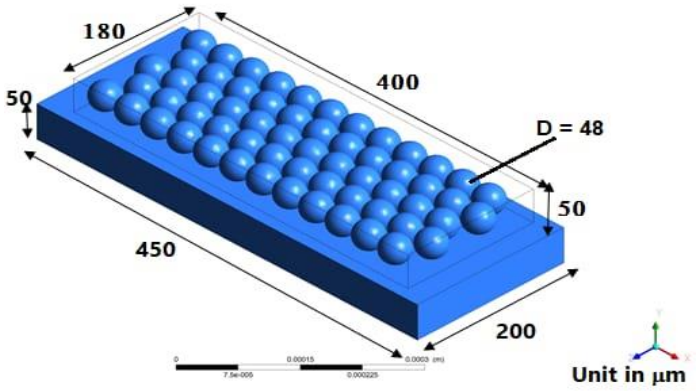

Fig. 2. The geometry of the model is utilized for the validation procedure and mesh analysis.

After establishing the model geometry, it is transferred to the meshing software, where four grids of mesh are created and then investigated in a comprehensive mesh study. The relevance auto mesh factor is configured with four values: 25, 50, 75, and 100. Fig.3 illustrates the mesh graph, where the average cell size is taken as 0.003 mm.

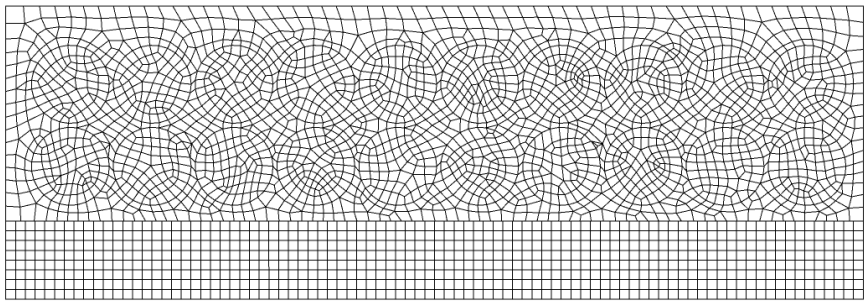

Fig.3. The configuration of the used mesh.

4.1 Mesh Independence Study

During the investigation of mesh independence, the generated grid cases were executed until the simulation data exhibited no divergence attributable to mesh-related issues. The maximum aspect ratio for the considered four mesh factors is less than 4. This value is deemed highly satisfactory and closely approximates the ideal value outlined in the ANSYS manual [36]. Tabel. 1 shows the mesh independence study data, revealing a notable distinction in mass fraction of 0.28 between grid No.1 and No.2, whereas the difference is only 0.01 for grid No.3 and No.4. Hence, grid No.3 was selected for all the cases in this study. It has approximately half the number of cells in comparison to grid No.4, leading to a substantial reduction in computational time.

Tabel. 1: The mesh independence study.

Grid No.	Total number of cells	Mass fraction
1	2300	0.93
2	3052	0.65
3	4624	0.36
4	10836	0.35

4.2 Solver setting

The solver settings comprise important factors including boundary conditions, solution methods, and convergence criteria. Initially, the solution needs to be determined whether the solution is in a steady or transient state. Following that, the gravity factor is selected, and an incompressible fluid flow option is chosen due to the constant density of the fluid. NiBSil material properties are specified, and the turbulence model employed is the K-ε model. Figure .4 illustrates the flowchart that is followed for preparing the computational model.

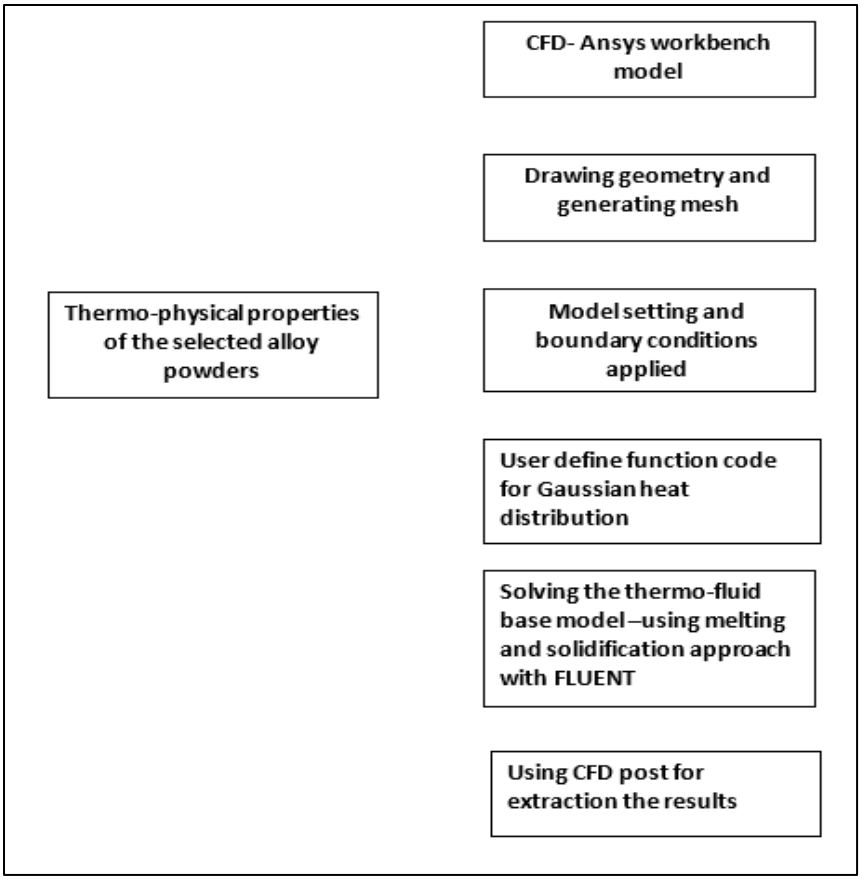

Fig. 4. Flowchart for ANSYS® simulation.

Boundary conditions play a crucial role as they define the physical model by specifying the characteristics of flow at the inlet and outlet, as well as determining whether parts are stationary or moving. In this simulation, all walls within the domain were designated as fixed with slip conditions. This implies that the fluid near the first cell that is adjacent to the wall possesses a velocity value equivalent to the main flow velocity. Regarding the solution method, the study opted for the Semi-Implicit Method for Pressure-Linked Equations (SIMPLE), employing pressure-velocity coupling algorithms. These algorithms are employed to calculate pressure based on the momentum and continuity equations sequentially. For each investigated case, the simulation is conducted using a time step size of 5e-06, encompassing a total of 30 time steps. Additionally, there are 20 iterations per time step, employing the assumed turbulent standard k-epsilon model. Monitoring the convergence is highly significant as it serves as a common practice to determine whether the solution aligns with the convergence criteria or not. Typically, the initial setting involves monitoring the residual values for momentum, continuity, and turbulence factors. Nonetheless, this method alone may not offer an accurate decision on solution convergence, as illustrated by the residual monitoring plot presented in
Fig. .

In
Fig. the moment curve is employed for convergence monitoring, specifying the mass fraction as the convergence criteria in the designated region of interest, particularly within the initial layer of the NiBSi particles. A crucial step in any simulation involves assessing the convergence status for both transient and

steady-state solutions. Hence, in this study, solution convergence was evaluated in the region of interest. A point was established at a location of x=-0.955 and y= 0.055 mm, and the liquid fraction was continually monitored at this point until the variation in the liquid fraction was less than 1% per iteration. Figure 5 illustrates that after 250 iterations, no further changes occurred, providing a clear indication of solution convergence.

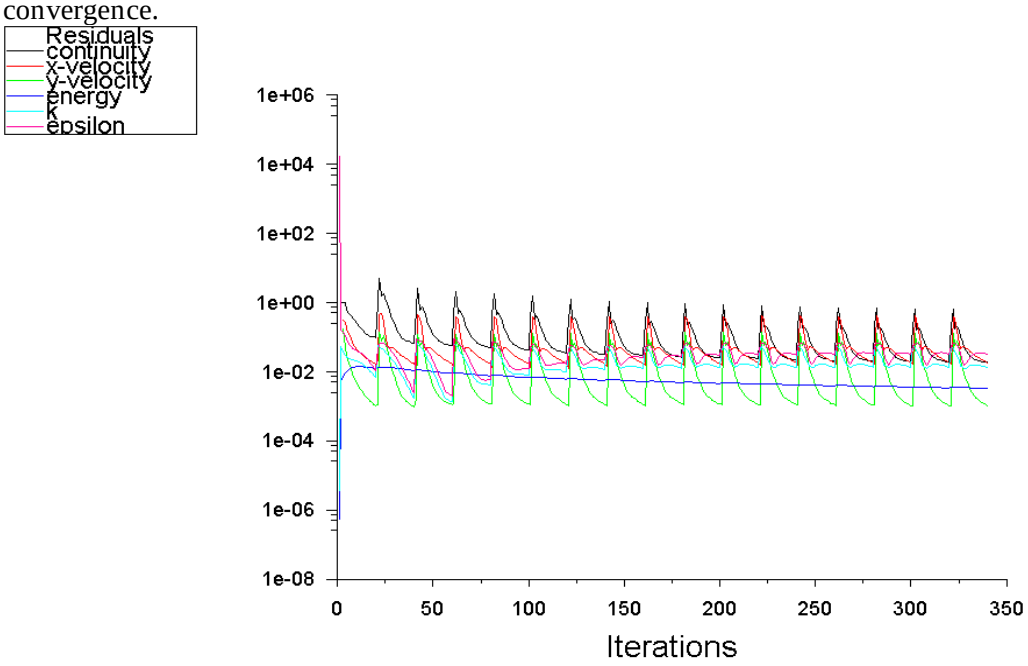

Fig. 5. Numerical solution residuals.

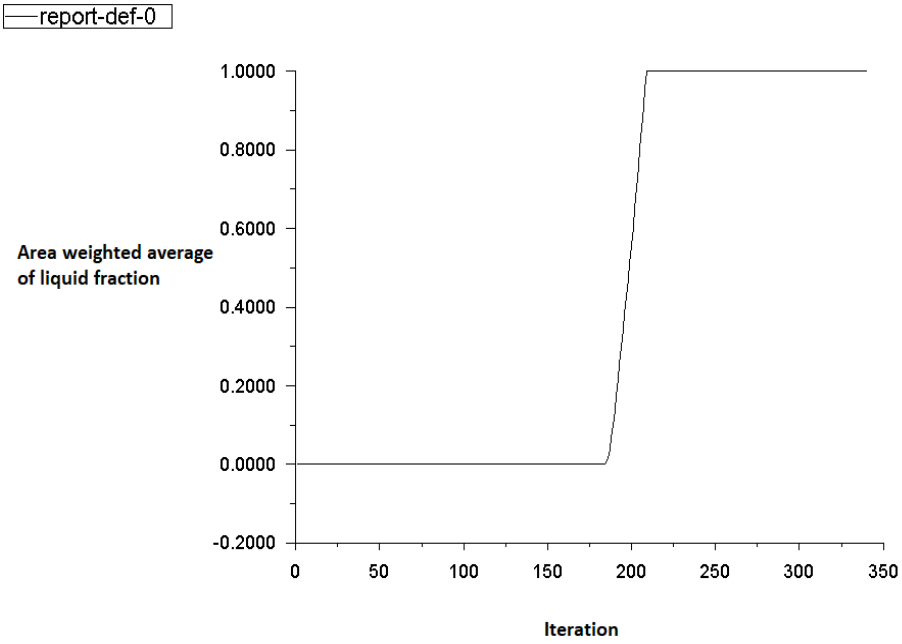

Fig. 5. Convergence graph for the liquid fraction value against iterations, specified at the point (x= -0.955 and y= 0.055 mm) within the domain.

4.3 Model validation

The validation process is a crucial task for any model to confirm and ensure the reliability of the results. In this study, the validation of the model is done by replicating the investigation results of a study conducted by Xia, Gu [37] where Inconel 718 Ni, a nickel-based superalloy, is utilized. Tabel. 2 provides detailed physical properties of the used powder in addition to some of the implemented SLM process parameters.

Tabel. 2: The material properties and parameters utilized in the SLM process [37].

Properties	Value
Density, ρ *(Kg/m³)*	8200
Absorption of superalloy powder, *A*	0.8
Ambient temperature, T_o *(K)*	293
Powder layer thickness, *d (µm)*	50
Radius of the laser beam, *D (µm)*	35
Hatch spacing, *s (µm)*	50
Laser power, *P (W)*	77.5, 88.6, 99.8, 110
Scanning speed, *v (mm/s)*	400

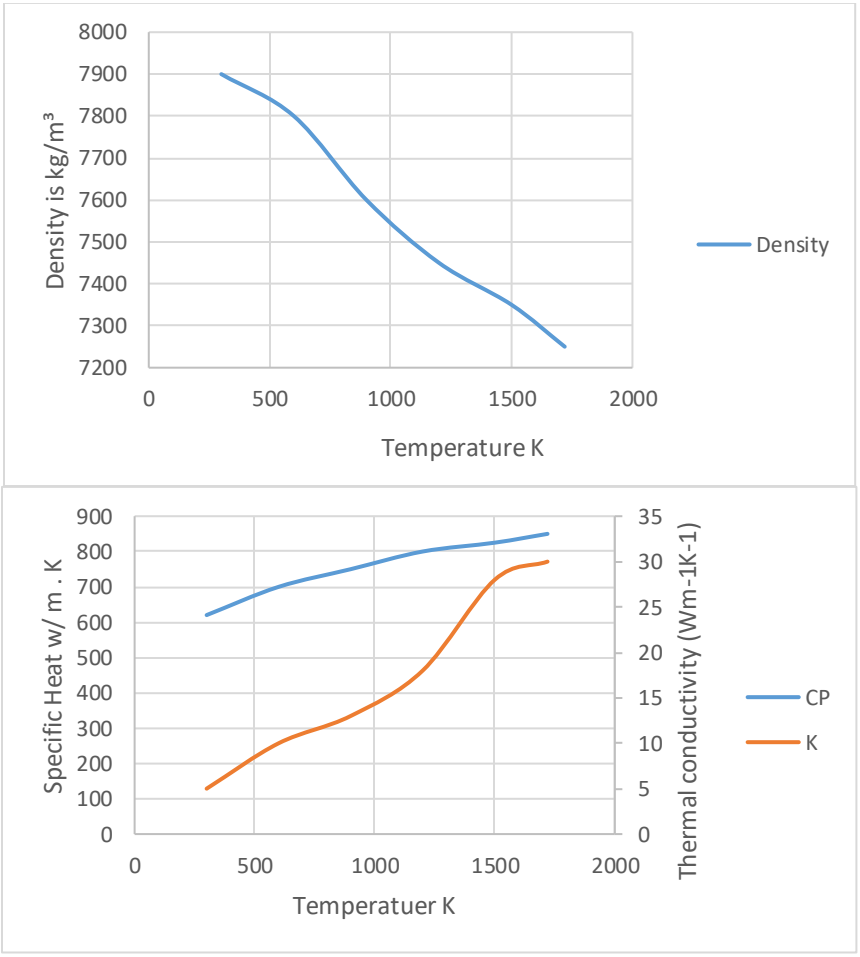

Fig.7. The properties of stainless steel 316L as a function of temperature.

In order to validate the current model a comparison was conducted with the work of Xia, Gu [37] and using the material's properties and process parameters listed in Tabel. 1. The iso-surface method was employed to predict the depth of the molten pool for temperature and mass fraction variables. The average value of three positions was assessed using a CFD probe. The iso-surface threshold for mass fraction was established at 0.9, indicating that regions below this value represent solids, while those above signify liquids. A similar approach was employed for the iso-surface temperature, utilizing a threshold of 1600K, as depicted in

Fig.

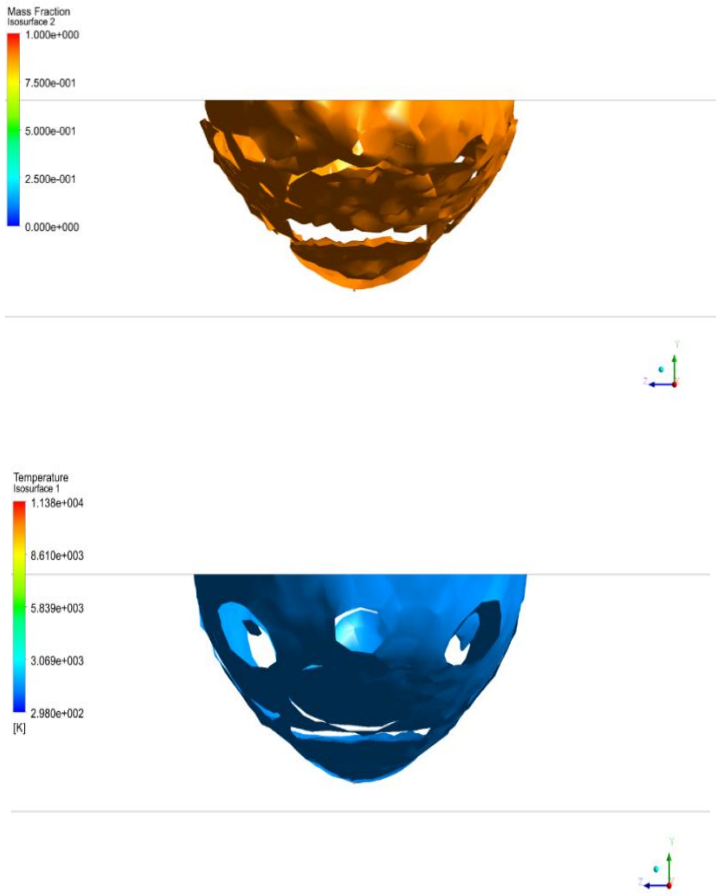

Fig. 8. Iso surface plot; (a) mass fraction assuming 0.9 is liquids phase, (b) iso temperature surface at below solidus temperature.

Tabel.3 A comparison between the model-predicated results and data given in Xia, Gu [37].

Laser power (watt)	Temperature (K)			Weld pool depth (μm)		
	Model prediction	Xia, Gu [37]	Differences (%)	Model prediction	Xia, Gu [37]	Differences (%)
77.5	2080	1905	9.19	25.9	28.3	8.48
88.6	2136	2178	1.93	27.09	26.5	2.23
99.8	2180	2308	5.55	29	25.8	12.40
110	2207	2539	13.08	26.6	23.6	12.71

3. Predicted results

In order to determine the mass faction of the liquid phase in the molten pool a virtual line (a-a) is created at the center of the domain in the middle section. The length of the line is 200 micrometers, and it is located just below the interface between NiBSi powder and stainless steel layer at a 6 micrometer in the negative y direction, as shown in the

Fig.. At this line, the validated mass fraction in the molten pool is computed. Additionally, its position serves as a reference for establishing all parameters in the following sections.

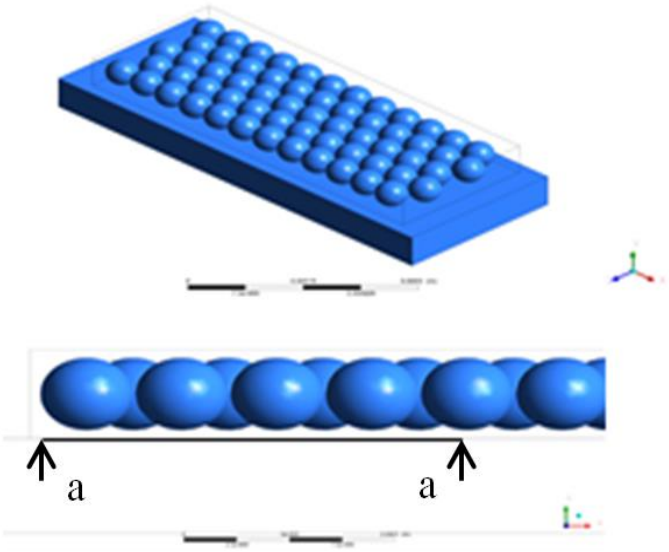

Fig.9: The 3D model shows the orientation of the proposed line a-a where the predicted mass fraction profile and other process parameters are calculated.

Tabel. **4** outlines the design of the undertaken parametric investigation, involving variations in laser power (40, 45, 50, and 55 Watts), and adjustments in scanning speed (60, 65, 70, and 74 mm/s), while maintaining a constant laser spot diameter of 15 µm. The table also illustrates the impact of varying scanning speeds, corresponding to each of the power intensities, on both the liquid fraction area and the average pool thickness. The results affirm a minimal impact of the examined parameters on the liquid fraction area, with the scanning speed demonstrating negligible effects on the average pool thickness. However, the laser power exhibits a notable influence on the average pool thickness. Results in Fig. demonstrate the correlations between temperature and both laser power and scanning speed. It is observed that these relationships are directly proportional and inversely proportional, respectively.

Fig. 4 illustrates the distribution of mass fractions along lines a-a exemplified in

Fig.. Fig. 4 (a to d) shows the mass fraction profile corresponding to various operation parameters, including laser power and scanning speed, as outlined in Tabel. 4. In all the figures (a to c), the attainment of a mass fraction value of one is evident, affirming the successful achievement of complete melting. However, the location along line a-a where complete melting occurs is observed to be contingent on both laser power and scanning speed. In general, the full melting onset point along line a-a appears to be influenced by the scanning speed for a particular laser power value. As the speed increases, the onset point shifts in the positive x-direction, and vice versa. On the other hand, the impact of laser power appears different; an increase in power serves to broaden the region where full melting occurs for all considered scanning speeds.

Tabel. 4: cases considered for the simulation with different input power and laser scan speed with a constant laser spot size.

No.	Power (Watt)	Scan speed (mm/s)	Liquid fraction area on Isosurface 1 ([mm²])	Average pool thickness (μm)
1	40	60	0.0235	65.01
2	40	65	0.0234	65.1
3	40	70	0.029	65
4	40	75	0.0238	65
5	45	60	0.0259	69.2
6	45	65	0.02506	69.45
7	45	70	0.0249	69.5
8	45	75	0.0254	69.6
9	50	60	0.0284	69.6
10	50	65	0.027	71
11	50	70	0.0269	70.1
12	50	75	0.0251	69
13	55	60	0.0308	74.4
14	55	65	0.0302	74.7
15	55	70	0.0299	74.5
16	55	75	0.02978	74.5

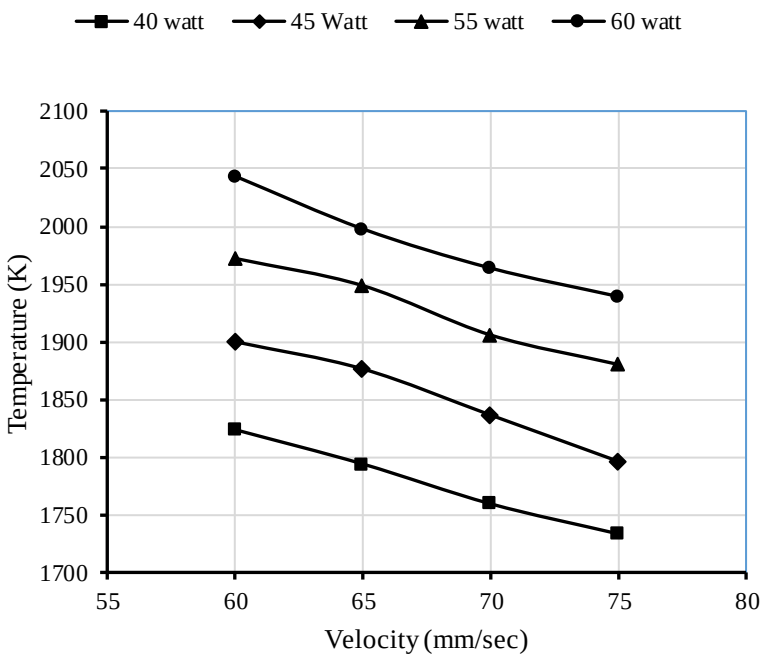

Fig.10: The relationship between the temperature and scanning speed at different laser powers.

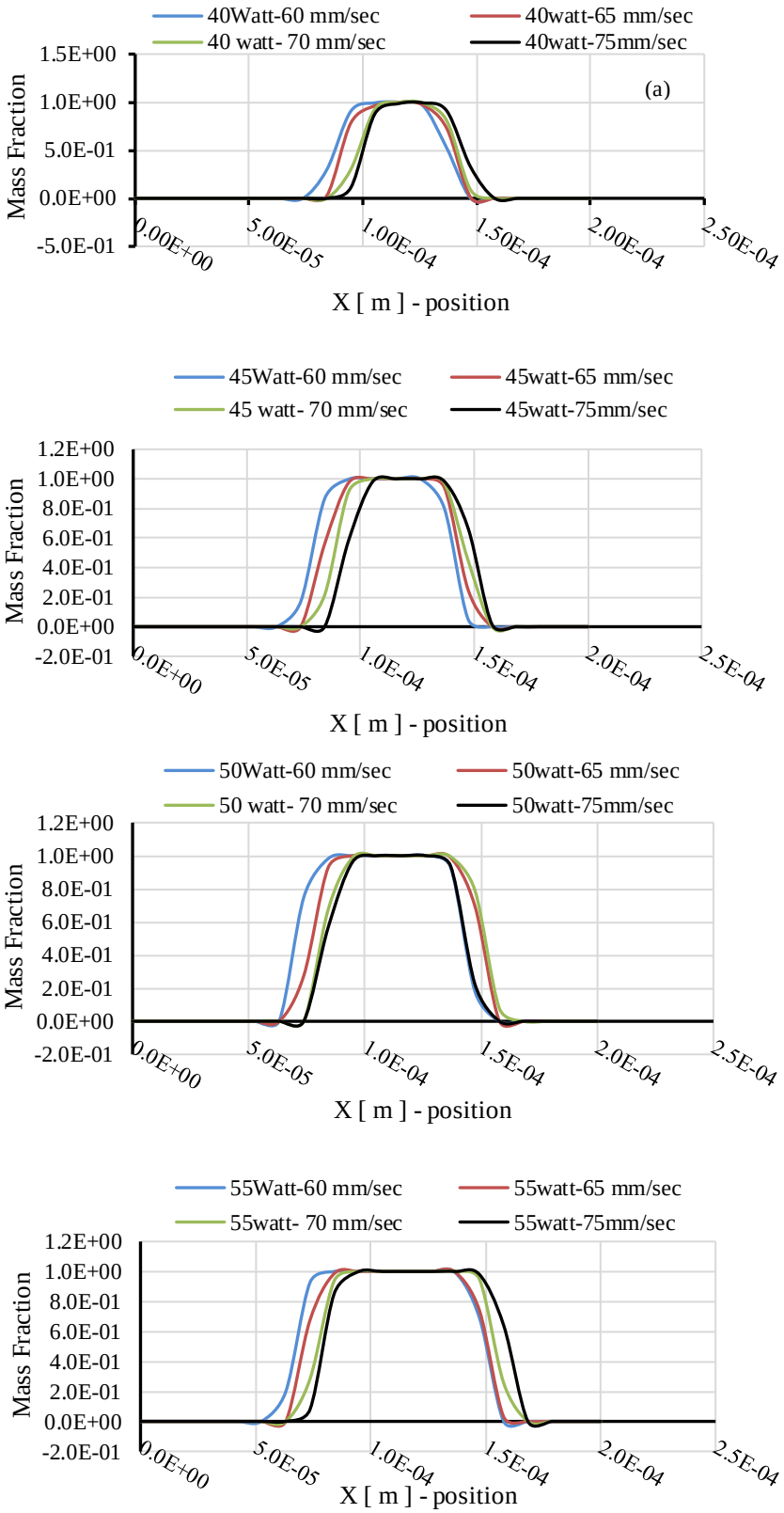

Fig. 4: Mass fraction profile along lines a-a.

In Fig.5, mass fraction contours and iso-surfaces are displayed in a 3D layout, with a value of 0.9 indicating a fully liquid state. Subfigures a, b, c, and d depict instances where the scanning speed is maintained at 65 mm/s, while the laser power is varied at 40, 45, 50, and 55 Watts, respectively. An observable proportional relationship exists between laser power and the size of the fully melted interface region that occurs between the NiBSi particle and the stainless steel substrate.

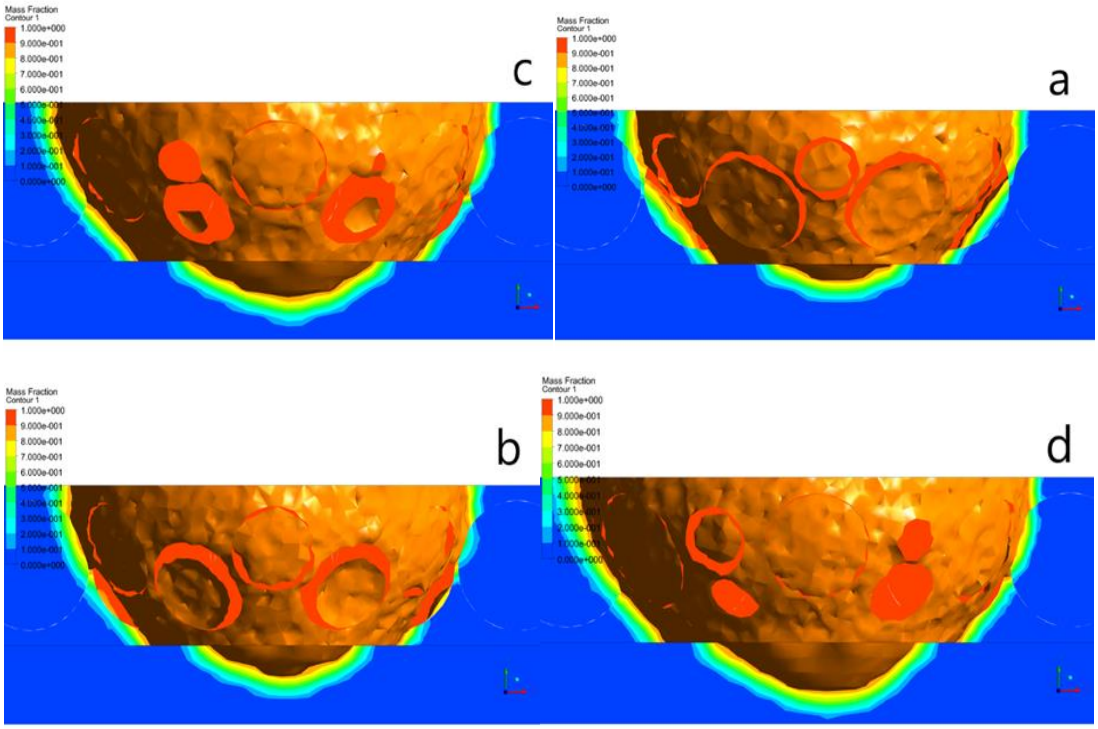

Fig.5: Liquid phase mass fraction contour and iso surface obtained using 65 mm/sec scanning speed, and laser power of (a) 40 Watt, (b) 45 Watt, (c) 50 Watt, and (d) 55 Watt.

5. Conclusions

A CFD model is presented in this study to simulate and analyze two-metal SLM processes typically associated with specific applications like coating. Such applications demand a tailored integration of two metals, necessitating control over the melting and solidification processes at the interface of different metals. The model utilized fundamental principles of classical physics to establish the governing equations, which are then resolved through the application of ANSYS FLUENT software. Moreover, a UDF function was written in C-language to define the heat source. Our study novelty can be explained in the coming points.

1- The model validation was demonstrated by considering the melting of NiBSi powder on a stainless steel substrate, utilizing experimental data available online.
2- The study was carried out to examine process parameters such as liquid mass fraction, laser power, and scanning speed. Four power values and four scanning speeds were used in the study.
3- This consideration will give a real distribution of temperature during coating process.
4- The model predictions exhibited significant concordance with the experimental results (87-98%), validating the model's reliability. Moreover, the parametric study showed a strong correlation between laser power and the size of the fully melted zone. It also affirmed the existence of an optimal interface region between the two metals.

References

[1] Robinson, J., et al., Determination of the effect of scan strategy on residual stress in laser powder bed fusion additive manufacturing. Additive manufacturing, 2018. 23: p. 13-24.
[2] Al-Aloosi, R.A., et al., Influence of scanning velocity on a CoCrMoW alloy built via selective laser melting: microstructure, mechanical, and tribological properties. Journal of Materials Engineering and Performance, 2023. 32(15): p. 6717-6724.
[3] Al-Aloosi,R.A., et al., Efect of scan speed on corrosion and tribocorrosion prperties of coblet-chroium alloy in situe produced by selective laser melting. Rapid prototyping Journal, 2023.
[4] AKM, Yousef., et al., Building a simulation model for the prediction of temperature distribution in pulsed laser spot welding of dissimilar low carbon steel 1020 to aluminum alloy 6061. AIP Conference Proceedings, 2011. 1315(1): p.1425-1430.
[5] MS, Hassan., et al., Synthesis and modeling of temperature distribution for nanoscales produced using Nd:YAG laser. Journal of Nanotechnology, 2016.
[6] Fina, F., S. Gaisford, and A.W. Basit, Powder bed fusion: The working process, current applications and opportunities. 3D printing of pharmaceuticals, 2018: p. 81-105.
[7] Hadi, R.M. and Z.A. Taha, Effect of SiC Addition on Microhardness and Relative Density during Selective Laser Melting of 316L Stainless Steel. Journal of Engineering, 2022. 2022.
[8] Hadi, R. and Z.A. Taha, Mechanical Properties of AISI 316L Stainless Steel Produced Via Selective Laser Melting. Iraqi Journal of Laser, 2022. 21(1): p. 51-60.
[9] Hadi, R.M. and Z.A. Taha, Selective laser melting of Inconel 601 alloy using nanosecond fibre laser. Periodicals of Engineering and Natural Sciences, 2022. 10(3): p. 161-171.
[10] Li, C., et al., On the simulation scalability of predicting residual stress and distortion in selective laser melting. Journal of Manufacturing Science and Engineering, 2018. 140(4): p. 041013.
[11] ZA, Taha., et al., M athematical modeling of laser-assisted transmission lap welding of polymers. Scripta Materialia, 2009. 60(8): p. 663-666.
[12] MM,Hanon., et al., Experimental and theoretical investigation of the drilling of alumina ceramic using Nd:YAG pulsed laser. Optics and Lser Technology, 2012. 44(4): p. 913-922.
[13] HA, Jasim., et al., Process development and monitoring in stripping of a highly transparent polymeric paint with ns- pulsed fiber laser. Optics and Laser Technology, 2017. 39: p. 60-66.
[14] He, K. and X. Zhao, 3D Thermal Finite Element Analysis of the SLM 316L Parts with Microstructural Correlations. Complexity, 2018.
[15] Xiong, W., et al., Effect of selective laser melting parameters on morphology, microstructure, densification and mechanical properties of supersaturated silver alloy. Materials & Design, 2019. 170: p. 107697.
[16] Lo, Y.-L., B.-Y. Liu, and H.-C. Tran, Optimized hatch space selection in double-scanning track selective laser melting process. The International Journal of Advanced Manufacturing Technology, 2019. 105: p. 2989-3006.
[17] Zhang, X., et al., Microstructure evolution during selective laser melting of metallic materials: A review. Journal of Laser Applications, 2019. 31(3).
[18] Mugwagwa, L., et al., Evaluation of the impact of scanning strategies on residual stresses in selective laser melting. The International Journal of Advanced Manufacturing Technology, 2019. 102: p. 2441-2450.
[19] Kong, D., et al., Mechanical properties and corrosion behavior of selective laser melted 316L stainless steel after different heat treatment processes. Journal of Materials Science & Technology, 2019. 35(7): p. 1499-1507.
[20] Wang, Z., et al., Superhydrophobic nickel coatings fabricated by scanning electrodeposition on stainless steel formed by selective laser melting. Surface and Coatings Technology, 2019. 377: p. 124886.
[21] Konovalov, S., et al., Surface modification of Ti-based alloy by selective laser melting of Ni-based superalloy powder. Journal of Materials Research and Technology, 2020. 9(4): p. 8796-8807.
[22] Shojaei, P., et al., Enhancing hypervelocity impact resistance of titanium substrate using Ti/SiC Metal Matrix Nanocomposite coating. Composites Part B: Engineering, 2020. 194: p. 108068.
[23] Freitas, B.J.M., et al., Microstructural characterization and wear resistance of boride-reinforced steel coatings produced by Selective Laser Melting (SLM). Surface and Coatings Technology, 2021. 426: p. 127779.
[24] Cheng, H., et al., High-performance nickel coating on SLM 316L stainless steel processed by jet electrochemical machining and jet electrodeposition. Proceedings of the Institution of Mechanical Engineers, Part B: Journal of Engineering Manufacture, 2022. 236(4): p. 462-472.

[25] Younsi, T., C. Boher, and A. Soveja, Influence of interlayer time on the microstructural state of CoCrMo coatings applied by selective laser melting on an iron-based substrate for different numbers of layers. Materials Today Communications, 2022. 32: p. 103776.
[26] Zhou, R., H. Liu, and H. Wang, Modeling and simulation of metal selective laser melting process: a critical review. The International Journal of Advanced Manufacturing Technology, 2022. 121(9-10): p. 5693-5706.
[27] Liu, B., et al., Predicting the porosity defects in selective laser melting (SLM) by molten pool geometry. International Journal of Mechanical Sciences, 2022. 228: p. 107478.
[28] Yu, T. and J. Zhao, Quantitative simulation of selective laser melting of metals enabled by new high-fidelity multiphase, multiphysics computational tool. Computer Methods in Applied Mechanics and Engineering, 2022. 399: p. 115422.
[29] Xu, G.-G., et al., Particle-scale computational fluid dynamics simulation on selective parallel dual-laser melting of nickel-based superalloy. Journal of Manufacturing Processes, 2022. 73: p. 197-206.
[30] Anand, N., et al., Development of a Comprehensive Model for Predicting Melt Pool Characteristics with Dissimilar Materials in Selective Laser Melting Processes. Journal of Materials Processing Technology, 2023: p. 118069.
[31] Versteeg, H.K. and W. Malalasekera, An introduction to computational fluid dynamics: the finite volume method. 2007: Pearson education.
[32] Kik, T., Heat source models in numerical simulations of laser welding. Materials, 2020. 13(11): p. 2653.
[33] Zhang, Z., et al., 3-Dimensional heat transfer modeling for laser powder-bed fusion additive manufacturing with volumetric heat sources based on varied thermal conductivity and absorptivity. Optics & Laser Technology, 2019. 109: p. 297-312.
[34] Hasan, A., CFD modelling of friction stir welding (FSW) process of AZ31 magnesium alloy using volume of fluid method. Journal of Materials Research and Technology, 2019. 8(2): p. 1819-1827.
[35] Dellinger, G., et al., Computational fluid dynamics modeling for the design of Archimedes Screw Generator. Renewable energy, 2018. 118: p. 847-857.
[36] Ansys, I., ANSYS meshing user's guide. vol, 2013. 15317: p. 724-746.
[37] Xia, M., et al., Selective laser melting 3D printing of Ni-based superalloy: understanding thermodynamic mechanisms. Science Bulletin, 2016. 61(13): p. 1013-1022.

العناصر المحددة لطلاء من النيكل -بورون -سيليكون المنتج بواسطة الصهر بالليزر الانتقائي

ولاء عصام رسول ، زياد اياد طه

معهد الليزر للدراسات العليا، جامعة بغداد، بغداد، العراق

*البريد الالكتروني للباحث: walaa.isam1101a@ilps.uobaghdad.edu.iq

الخلاصة: يتم استخدام نموذج ديناميكية الموائع المحوسبة في هذه الدراسة لمحاكاة وتحليل عمليات الصهر بالليزر الانتقائي ثنائية المعدن المرتبطة عادةً بتطبيقات محددة مثل الطلاء. تتطلب مثل هذه التطبيقات تكاملًا مخصصًا لمعدنين، مما يستلزم التحكم في عمليات الذوبان والتصلب عند السطح البيني للمعادن المختلفة. تم استخدام المبادئ للفيزياء الكلاسيكية لإنشاء المعادلات الحاكمة، والتي يتم حلها بعد ذلك من خلال تطبيق برنامج ANSYS FLUENT. علاوة على ذلك، تمت كتابة وظيفة محدده من قبل المستخدم UDF بلغة Cسي لتحديد مصدر الحرارة. تم إثبات التحقق من صحة النموذج من خلال النظر في ذوبان مسحوق NiBSi على ركيزة من الفولاذ المقاوم للصدأ، وذلك باستخدام البيانات التجريبية المتاحة عبر الإنترنت. بعد ذلك، تم إجراء دراسة لفحص معلمات العملية مثل جزء الكتلة السائلة، وقوة الليزر، وسرعة المسح. تم استخدام أربع قيم طاقة وأربع سرعات مسح في الدراسة. أظهرت تنبؤات النموذج توافقًا كبيرًا مع النتائج التجريبية (87-98%)، مما يؤكد موثوقية النموذج. علاوة على ذلك، أظهرت الدراسة البارامترية وجود علاقة قوية بين قوة الليزر وحجم المنطقة المنصهرة بالكامل. كما أكدت وجود منطقة واجهة مثالية بين المعدنين.

IJL, Issue 2, Vol. 23, 2024 **Research Article**
https://doi.org/10.31900/ijl.v23i2.454

Efficacy of Carbamide Peroxide Assisted by Er,Cr:YGSS Laser Induced Photoacoustic Streaming Technique for Enhancing the Color of Internally Stained Teeth

Aya Saad Wajeh*, Hussein A. Jawad

Institute of Laser for Postgraduate Studies, University of Baghdad, Baghdad, Iraq
** Email address of the Corresponding Author:ayah.saad2102m@ilps.uobaghdad.edu.iq*

Article history: Received 5 Feb. 2024; Revised 21 May 2024; Accepted 27 May 2024; Published online 15 Dec 2024.

Abstract

Objective: To evaluate the impact of photon-induced photoacoustic streaming (PIPS) technique for enhancing tooth color changes using Er,Cr:YSGG (2780 nm) laser with carbamide peroxide.
Materials and methods: A total of 42 sound premolars were included in this study. All teeth were endodontically treated then stained artificially utilizing sheep blood followed by placement of a 3mm layer of resin-reinforced GIC 2 mm apical to the CEJ on the buccal aspect. Such stained teeth were bleached conventionally with 37% carbamide peroxide or treated by PIPS using Er,Cr:YSGG laser (25 Hz frequency, 0.1 W power, 60 µs pulse duration) with 37% carbamide peroxide. The results were evaluated after 1, 2, and 3 weeks, resulted color changes were measured by using a spectrophotometer.
Results: Both techniques resulted in a significant color change at the endpoint of the study. However, intergroup comparison demonstrated that PIPS with 37% carbamide peroxide was significantly ($p < 0.05$) more effective than walking bleaching using 37% carbamide peroxide in bleaching outcomes over all time intervals of the study.
Conclusion: The current study showed that the PIPS technique used to activate bleaching agents containing 37% carbamide peroxide was more efficient in achieving desirable bleaching outcomes than the conventional walking-bleaching techniques.

Keywords: tooth discoloration, tooth bleaching, Er,Cr:YGSS laser, carbamide peroxide, endodontics.

1. Introduction

These days, aesthetics is a field that is becoming more and more important, particularly when it comes to getting a beautiful smile, this is due to the fact that it molds a person's opinion of their own appearance and has a profound psychosocial effect when teeth with pigmentation see a notable color shift, it stands out more because of the stark contrast it creates with the surrounding teeth. [1-3]. When using restorative materials, one should take into account that the crown, which is the visible portion of the tooth in the oral cavity, gets its color from the biomechanical combination of two primary tissues: dentin and enamel. [4].

Numerous reasons, including trauma to the pulp or pulp removal, can result in internal discolorations by allowing blood products and their byproducts to infiltrate into the dentinal tubules. As a result, as hemolysis continues, iron compounds are created that can eventually transform into black ferric sulphide. which represents the most common cause of intrinsic discoloration as stated by Grossman and associates [5], however, discoloration can also be caused by protein degradation, as was the case with pulp necrosis [6,7]. Significantly, dental restoration materials in particular, those used for root fillings also play a significant role in internal discoloration [8]. Remnants of root filling materials and some root canal medications could infiltrate the surrounding dentinal tubules and discolor them if they are left in the pulp chamber. Additionally, the presence of residual tissues in the root canal system not only diminish dentinal permeability but also act as a barrier, preventing the effective penetration of intracanal medications and various bleaching agents into the dentin [9].

Generally, there are three main methods for lightening tooth color; over-the-counter solutions, in-office treatments, and at-home bleaching [10]. The walking-bleaching approach is the most often used technique in dental clinics for teeth that have undergone root canal therapy[11]. The bleaching chemicals sodium perborate, carbamide peroxide, and hydrogen peroxide are the most commonly mentioned in the literature. The mechanism of these agents relies mainly on oxidative processes which mediate reversal of the chromatic shift[12,13]. Such mechanism of whitening depends mainly on breaking down the stain chromatin molecules into smaller chain molecules by the action of the free oxygen radicles that are liberated as byproducts from the hydrogen peroxide agent, where such free radicles will attack the doble bonds of the large chromatine molecules to give the colorless short chromatin chains [12]. Using lasers, especially Er,Cr:YSGG, has become increasingly popular in the last ten years in many dental applications, including root canal therapy, cavity preparation and cleaning, and minor oral procedures, with promising results and safety[14–16]. Moreover, the Er,Cr:YGSS laser demonstrated the ability to both strengthen the resin's attachment to the tooth surface and lessen tooth sensitivity[17]. The efficiency of cement bonding increased when dental zirconia was treated with the Er,Cr:YSGG laser [18]. Photon-induced photoacoustic streaming (PIPS) is a new type of laser technique that was just introduced to enhance the activation process of the bleaching mechanism[11]. When agitating a 5.25% NaOCl solution in PIPS, the Er,Cr:YSGG laser produced better results than the traditional approach in eliminating mature bacterial biofilm from intricate root canal networks[19]. Using a sub ablative power level erbium:yttrium-aluminum-garnet(ER:YAG) laser with a radial or conical tip, this thermophotocatalytic method works. The unique characteristic of PIPS that sets it apart from other techniques is that the tip is positioned above the orifice within the coronal chamber without coming into touch with the dentinal walls [12]. It is noteworthy that (Er,Cr:YSGG) PIPS is frequently used to activate intracanal irrigation materials [20, 21], to de-bond extra coronal lithium disilicate [22,23], and improve the bonding of extra coronal repair of all sorts [21].

The effects of lasers on dental hard tissues depend on a number of variables, such as the kind of tissue being treated, exposure time, irradiation mode, power density, and wavelength [9]. This study aimed to evaluate the PIPS technique impact enhancing tooth color changes using Er, Cr:YSGG laser with 37% carbamide peroxide

2. Theory

This in vitro study included a total of 42 sound premolars that were extracted for orthodontic reasons which were selected according to the following criteria:

1. Maxillary premolar with neither decay, abrasion, nor previous fillings.
2. Teeth that were extracted for orthodontic reasons.
3. Patients aged between 15-30 years old (approximately similar pattern of dentinal tubules).
4. No signs of internal resorption as examined by periapical x-ray.

This was followed by performing root canal treatment for these teeth that we did an access opening by handpiece using carbide round bur size 8.Stenderization of the buccal wall thickness of 2.5±0.3mm which was verified using a manual caliper(Figure 1).

Fig.1: Calibration of the thickness of the buccal wall.

By visual inspection of the root tip, we estimated the working length of the teeth before achieving instrumentation to size of X3 BY ProTaper technique. Root canals were then irrigated with 2.5% NaOCl and 17% EDTA, then distilled water before obturating by single cone technique (Figure 2).

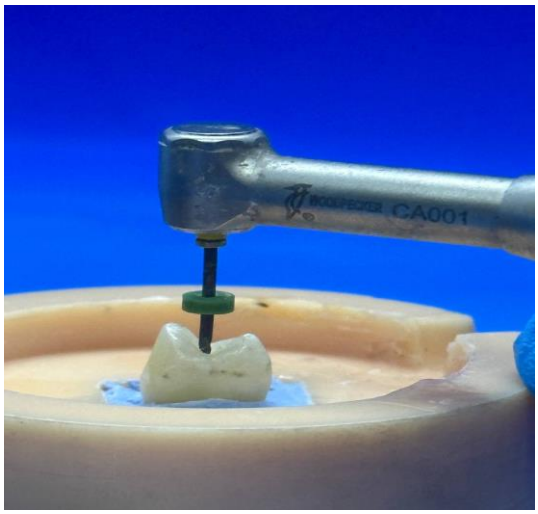

Fig.2: Using rotary instrumentation for the teeth.

2.1 Artificial staining

The method was originally introduced by Freccia and Peters (1982)[24], to artificially mimic internal staining of teeth and it was later modified by substituting human blood by sheep blood [10]. Briefly, each sample was put in an Eppendorf tube that contain 4 mL of sheep's blood. These tubes were centrifuged (PLC-03, Gemmy industrial corp., Taiwan) for 20 minutes at a speed of 3400 RPM and 37°C temperature. This process was repeated twice a day for three successive days, the teeth were rinsed under running tab water after each centrifugation, then returned to the tubes, and kept in 100% humidity at 37°C. Then we

put the blood and distilled water inside new tubes were centrifuged them to begin hemolysis, so, the supernatant layer was then removed away (Figure 3) after such teeth were removed from their original tubes to these new tubes on day 4 so after removing the supernatant layer, such teeth were put inside Eppendorf tubes before centrifuging them for 20 min o the 3 days. after six days, we repeated the same procedure as the first six days to create deep artificial staining of the teeth to get a total of 12 days of staining.

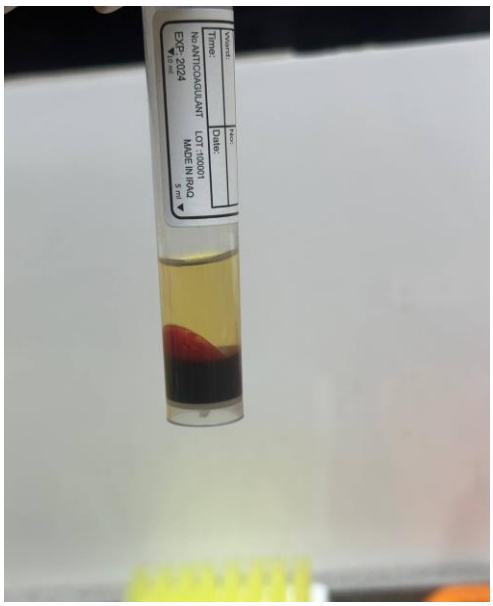

Fig. 3: Isolation supernatant layer from centrifuged stained teeth.

2.2 Color measurement

After finishing staining process, the teeth were rinsed under running water and air dried. This followed by placement of a 3 mm layer of GIC (Equia Forte, GC, Japan) that was placed 2 mm apical to the CEJ in order to prevent diffusion of the bleaching agent through the dentinal tubules, and to infiltrate through the root canal to the periapical region beside that it also prevent cervical root resorption [25]. The measurement of the photo properties of buccal area of the crown was done using a (Vita Easyshade Advance Spectrophotometer) (Vita Zahnfabrik, Germany) (figure 4). Where we repeat each measurement three times to take the average reading of them using the Commission International de l'Eclairage(CIELAB).These measurements were conducted by using the device was first was calibrated as follows: the probe tip was placed on the calibration port aperture as stated in the manufacturer's instructions. Following every measurement, the recorded values included ΔL* (representing brightness), Δa* (indicating redness), and Δb* (representing yellowness/blueness) of the specimen. After bleaching, repeated measurements were performed on specimen which were evenly distributed into two groups. Total color change (ΔE*) was determined by using the following formula:

$$\Delta E_{*2} = \sqrt{(\Delta L^*)^2 + (\Delta a^*)^2 + (\Delta b^*)^2} \qquad (1)$$

A. Group 1: PIPS with 37% carbamide peroxide

The pulp chamber was directly filled with 0.5 mL of 37% carbamide peroxide (Whiteness Super Endo, FGM, Brazil) using the tip of the delivery bleaching tube. Following the bleaching gel application, it was activated with PIPS using Er,Cr:YSGG laser 2780 nm (Biolase, WaterLase ®iPlus, USA)(Fig5).

According to the pilot study, the parameters of laser application were as follows: 1 minute exposure time, 60 µs pulse duration, 0.1W output power at a frequency of 25 Hz, dose of 500 J/cm^2 and o.333 J/cm^2 energy density using a 6mm tip diameter (Biolase, USA). The water and air systems remained closed during this process, avoiding any contact of the fiber optic tip with the pulp chamber walls. The fiber optic tip was placed within the endodontic access cavity and directly in the bleaching gel.

Following the aforementioned PIPS activation, the bleaching gel was replaced, and the PIPS device was left for 10 minutes to cool down. Once the PIPS tip had cooled down, the activation procedure was redone, resulting in a total of three 1-minute PIPS activations, amounting to 3 minutes in total. After 30 minutes had elapsed, tap water was used to thoroughly rinse away the bleaching gel. Next, a cotton pellet was inserted in the pulp chamber, and a provisional seal of the access cavity was done with the GIC. This bleaching process was repeated at 7-day intervals, lasting for 21 days total. Following every 7-day bleaching session, the teeth were stored in distilled water at 100% humidity and a temperature of 37°C, color measurements were taken on days 7, 14, and 21 as described above.

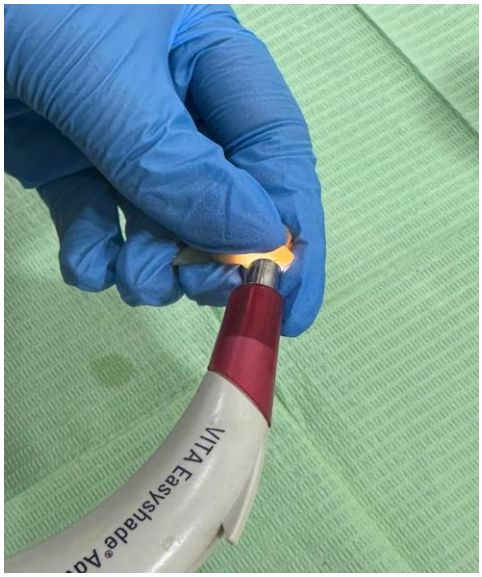

Fig. 4: Color Measurement by using VITA Easyshade.

B. Group 2: Walking bleaching using 37% carbamide peroxide:

Around 0.5 mL of the 37% carbamide peroxide walking-bleaching gel (Whiteness Super Endo, FGM, Brazil) was directly placed into the pulp chamber by the delivery tip of the bleaching tube. Following the bleaching gel application and packing, a cotton pellet was positioned over the gel. Resin-reinforced GIC was used as a filling to temporarily seal the access cavity. Then the gel was washed away, after each 7-day treatment session, followed by thorough cleaning of the teeth before conducting the color measurements. This sequence was repeated over three 7-day intervals over 21 days of treatment. At the end of each 7-day session, the teeth were stored in distilled water in 100% humidity and at 37°C. Color measurements were taken on days 7, 14, and 21, as previously outlined.

Fig. 4: Activation of carbamide peroxide.

2.3 Statistical analysis

The distribution of data was first checked by Shapiro-Wilk's test. Descriptive statistics were expressed as mean and standard deviation (SD) which showed normal distribution of data. Intragroup comparisons for color changes over the time intervals of the study were conducted by using two-ANOVA. If the results were significant, *post hoc* analysis was performed to highlight changes within the same group. Intergroup comparison for the mean of ΔE was performed by unpaired t-test. A p-value < 0.05 was considered significant. All analyses were conducted by using SPSS software (version 26, IBM, USA).

3. Results

The data were normally distributed, therefore, parameter statistical assays were used for analyses. Results of the two-way ANOVA revealed that the whitening of the discolored teeth was significant (p-value 0.05) when treated with PIPS with 37% carbamide peroxide (Group 1). These changes followed a time-dependent manner as shown by further analysis using LSD post hoc which demonstrated that the mean value of ΔE was significantly increasing considering the following up of the progress in the color variation until the end of the third week. Table 1 shows the mean value of (ΔE) of this group at the three-week intervals.

In Group 2, it is observed that there is a highly statistically significant difference between the baseline color measurements (ANOVA p-value 0.001). Similar to Group 1, there was an observable change over time interval as the impact of bleaching on color variations was noticed from the LSD test. Table 2 shows the mean value of (ΔE) of Group 2 at the three-week intervals. The results indicated that there was a highly significant difference between the two bleaching methods as shown in Figure 4. At the end of the first, second, and third weeks we compared the change of ΔE of the two groups, where there was Statistical differences in ΔE were observed between Groups 1 and 2 after the collection of the results for the 21 days of bleaching procedure. The mean bleaching values of Group 1 (PIPS +37% carbamide peroxide) were statistically different from those of Group 2 (walking bleaching 37% carbamide peroxide) with reported p values of 0.01, 0.001, and p 0.01 respectively in Table 3 and Figure 6.

Table 1. Mean Color Differences (ΔE) in pips with 37% carbamide peroxide group at 7, 14, and 21 Days.

	1st w/Δ E	2nd w/Δ E	3rd w/Δ E	
Mean	**C** 13.55	**B** 18.93	**A** 24.64	
Median	14.43	17.60	25.01	
SD	2.24	3.46	1.38	0.05
MIN	11.01	16.33	23.11	
MAX	15.22	22.85	25.79	

*LSD test was used to calculate the significant differences between tested mean, the letters (A, B, and C) LSD represented the levels of significant, highly significant start from the letter (A) and decreasing with the last one. Similar letters mean there are no significant differences between the tested mean. p≤0.05 were considered significantly different

Table 2. Mean Color Differences (ΔE) in walking bleaching 37% carbamide peroxide group at 7, 14, and 21 Days.

Statistics	1st w/Δ E	2nd w/Δ E	3rd w/Δ E	*P-VALUE
Mean	C 7.81	B 11.90	A 17.43	
Median	7.38	11.83	16.69	
SD	3.24	4.35	4.44	0.001
MIN	2.89	6.59	11.21	
MAX	13.14	19.60	23.52	

*LSD test was used to calculate the significant differences between tested mean, the letters (A, B, and C) LSD represented the levels of significant, highly significant start from the letter (A) and decreasing with the last one. Similar letters mean there are no significant differences between the tested mean. p≤0.05 were considered significantly different.

Table 3. Intergroup comparison of means of Δ E at 7, 14, and 21 Days.

	First week		Second week		Third week	
Statistics	G1/Δ E	G2/Δ E	G1/Δ E	G2/Δ E	G1/Δ E	G2/Δ E
Mean	13.55	7.81	18.93	11.90	24.64	17.43
Median	14.43	7.38	17.60	11.83	25.01	16.69
SD	2.24	3.24	3.46	4.35	1.38	4.44
MIN	11.01	2.89	16.33	6.59	23.11	11.21
MAX	15.22	13.14	22.85	19.60	25.79	23.52
P value	0.01 H.Sig		0.001 H. sig		0.01 H. sig	

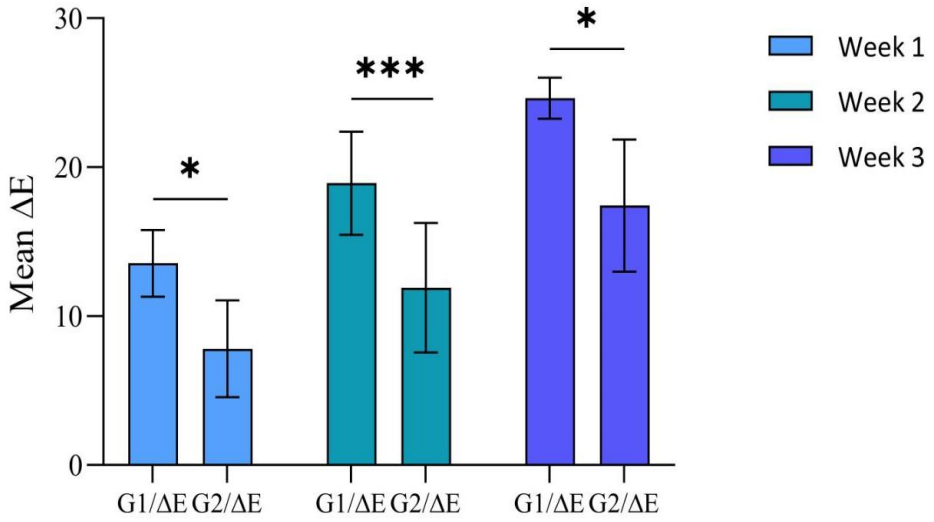

Fig. 6: Mean Color Differences (ΔE) between Group 1 (PIPS +37% carbamide peroxide) and Group 2 (walking bleaching Sodium perborate- 20% H_2O_2) at 7, 14, and 21 Days. Group 1 exhibited significantly higher color change throughout the study period as compared to Group 2. G: Group. P value * <0.05, *** <0.001 by using unpaired t-test.

4. Discussion

Teeth discolored due to endodontic treatment can vary in its density due to many factors like the age of the patient, type of tooth, type of root canal medicaments, age of filling, patient habits, etc. so for that our statistical results of the teeth pigmentation were varied accordingly which was in a good agreement with the study of Nandita et al. [26].The pigmented teeth could be lightened via various methods and materials, carbamide peroxide is one of most common bleaching agents used. In our experiment we have used such agent either with or without PIPS. It is known that PIPS produced shock wave that virtually able to facilitate the penetration of the bleaching agent by reducing the surface tension and heating of this material also enhanced the effectiveness of the peroxide agent[27]. The amount of H_2O_2 liberated as a result of the bleaching agent's byproduct is positively correlated with the effectiveness of any bleaching process [26]. The oxidative impact of free radicals produced from H_2O_2 breakdown which is the basic factor for the bleaching process, where such mechanism of bleaching depend on breaking down the lengthy chromatin molecules that of the stain which have unsaturated double bonds that make them susceptible to be distracted, this results in the creation of shorter molecules [11]. In our experiment we have chosen carbamide peroxide which achieved significant whitening for intrinsic pigmented teeth in a manner of results that were in a good agreement with studies of Cooper etal and Mokhlis [28, 29]. Since the amount of H_2O_2 produced is directly related to the bleaching agent's efficacy, as was previously noted, this quantity is crucial to understanding the study's findings, which demonstrated that using PIPS boosted the effectiveness of carbamide peroxide by stimulating more than H_2O_2 conventional carbamide peroxide alone , while Senem in 2021 found different results due to use of different laser [11]. According to research by Warren et al.[30], carbamide peroxide at15% releases 5.4% H_2O_2, 20% releases 7% H_2O_2, and at 35%, 10% H_2O_2. Nevertheless, Rokaya found that only an estimated 12.3% H_2O_2 was produced after 37% carbamide peroxide underwent a chemical reaction in Groups 1 and 2, bleaching gels which gave accepted agreement with such study [31]. Water has a strong absorption of the Er,Cr:YSGG wavelength of light, therefore an increased water ratio in the bleaching gel would increase the agent's activity. The laser is a crucial part of the bleaching process because it ionizes the H_2O_2 in the bleaching substance, which decreases pigmentation and results in the desired color shift [32]. This work used the PIPS technique at sub ablative power settings with an Er,Cr:YGSS laser. The bleaching agent is easily heated when exposed to the laser beam because

the Er,Cr:YGSS laser is substantially absorbed by water [33]. Sheep's blood was used by Arslan et al. to artificially stained teeth, which were subsequently bleached using various liquid and gel forms of H_2O_2 with or without the application of PIPS, they found that employing the liquid form of H_2O_2 allowed for greater color shift when the PIPS approach was applied. They proposed that the use of PIPS raised the pulp chamber's temperature and allowed H_2O_2 to permeate deeper, improving internal bleaching which was somehow agreed to the study of Arsalan et al.[34], in order to consider the whitening procedure's effectiveness, we should have a change of a minimum of 5 units of the ΔE [35]. Despite the fact that DiVito demonstrated that the PIPS approach only raised temperatures by 1.2–1.4°C during the course of 20–40 seconds of activation, there was no thermal side effect on the dentin walls [36].

5. Conclusions

The current study showed promising results when PIPS technique was used to activate bleaching agents containing 37% carbamide peroxide in achieving desirable bleaching outcomes. Although the walking-bleaching method was also capable of altering tooth color change, but combination of PIPS technique with 37% carbamide peroxide emerged as a more efficient technique for reversing severely discolored teeth.

References

[1] Joiner, A.; Luo, W. Tooth colour and whiteness: A review. Journal of Dentistry 2017, 67, S3-S10. https://doi.org/10.1016/j.jdent.2017.09.006.
[2] Montero, J.; Gómez-Polo, C.; Santos, J.A.; Portillo, M.; Lorenzo, M.C.; Albaladejo, A. Contributions of dental colour to the physical attractiveness stereotype. J Oral Rehabil 2014, 41, 768-782. 10.1111/joor.12194.
[3] Al-Zarea, B.K. Satisfaction with appearance and the desired treatment to improve aesthetics. Int J Dent 2013, 2013, 912368. 10.1155/2013/912368.
[4] Jawad, H.A. Investigation on picosecond laser ablation of dental material using FIB/SEM techniques. Indian Journal of Science and Technology 2010, 3.
[5] Grossman, L.; Oliet, S.; Del Rio, C. Replantation, transplantation, and endodontic implants. Endodontic Practice. 11th ed. Philadelphia, PA: Lea & Febiger 1988, 329-348.
[6] Howell, R.A. Bleaching discoloured root-filled teeth. Br Dent J 1980, 148, 159-162. 10.1038/sj.bdj.4804406.
[7] Attin, T.; Paqué, F.; Ajam, F.; Lennon, A.M. Review of the current status of tooth whitening with the walking bleach technique. Int Endod J 2003, 36, 313-329. 10.1046/j.1365-2591.2003.00667.x.
[8] Abbott, P.V. Aesthetic considerations in endodontics: internal bleaching. Pract Periodontics Aesthet Dent 1997, 9, 833-840; quiz 842.
[9] Al-Karadaghi, T.S.; Gutknecht, N.; Jawad, H.A.; Vanweersch, L.; Franzen, R. Evaluation of Temperature Elevation During Root Canal Treatment with Dual Wavelength Laser: 2780 nm Er,Cr:YSGG and 940 nm Diode. Photomed Laser Surg 2015, 33, 460-466. 10.1089/pho.2015.3907.
[10] Ahrari, F.; Akbari, M.; Mohammadpour, S.; Forghani, M. The efficacy of laser-assisted in-office bleaching and home bleaching on sound and demineralized enamel. Laser Ther 2015, 24, 257-264. 10.5978/islsm.15-OR-15.
[11] Senem Y.Ö.;Ertuğrul K. Comparison of Walking-Bleaching and Photon-Initiated Photoacoustic Streaming Techniques in Tooth Color Change of Artificially Colored Teeth. PHOTOBIOMODULATION, PHOTOMEDICINE, AND LASER SURGERYVolume 39, Number 5, 2021
[12] Kwon, S.R.; Wertz, P.W. Review of the Mechanism of Tooth Whitening. J Esthet Restor Dent 2015, 27, 240-257. 10.1111/jerd.12152.
[13] Lo Giudice, R.; Pantaleo, G.; Lizio, A.; Romeo, U.; Castiello, G.; Spagnuolo, G.; Giudice, G.L. Clinical and Spectrophotometric Evaluation of LED and Laser Activated Teeth Bleaching. Open Dent J 2016, 10, 242-250. 10.2174/1874210601610010242.
[14] Al-Karadaghi, T.S.; Franzen, R.; Jawad, H.A.; Gutknecht, N. Investigations of radicular dentin permeability and ultrastructural changes after irradiation with Er,Cr:YSGG laser and dual wavelength (2780 and 940 nm) laser. Lasers Med Sci 2015, 30, 2115-2121. 10.1007/s10103-015-1757-y.
[15] Ali Jawad, J.H. Cavity Disinfection Using Er, Cr: YSGG Laser Induced Photoacoustic Streaming Technique. Iraqi Journal of Laser 2022, 21.

[16] Almiran, D.A.; Alkurtas, S.A. A comparison between Er, Cr: YSGG 2780 nm laser and carbide fissure bur in root-end resection. Iraqi Journal of Laser 2020, 19, 1-11.
[17] Mubaraq, R.M.; Basima Mohammed Ali, H. PDF Influence of Er:Cr;YSGG laser Desensitization on SBS of resin cement to dentin. Iraqi Journal of Laser 2022, 21, 18-27. 10.31900/ijl.v21i1.304.
[18] Muhammed, F.S.; Jawad, H.A. Pulsed Er,Cr:YSGG Laser For Surface Modification of Dental Zerconia Ceramic. Iraqi Journal of Laser 2021, 20, 21-29. 10.31900/ijl.v20i1.230.
[19] Ibrahim, G.I.; Jawad, H.A. Investigating the effect of Er,Cr:YSGG laser agitation of sodium hypochlorite on the removal of mature biofilm in the complex root canal systems using atomic force microscopy. J Dent Res Dent Clin Dent Prospects 2023, 17, 154-161. 10.34172/joddd.2023.40463.
[20] Fasanaro, T.S. Bleaching teeth: history, chemicals, and methods used for common tooth discolorations. J Esthet Dent 1992, 4, 71-78. 10.1111/j.1708-8240.1992.tb00666.x.
[21] Rasheed, S.S.; Jawad, H.A. Permeability of Radicular Dentine after Using Different Irrigant Activation Techniques Including Photo Induce Photoacoustic Streaming Technique. Iraqi Journal of Laser 2021, 20, 43-50. 10.31900/ijl.v20i1.269.
[22] Fateima Sameir, M.; Hussein Ali, J. The Influence of Short Pulse Er:Cr: YSGG Laser on the Shear Bond Strength of Cad-Cam Zerconia Material to Resin Cement. Indian Journal of Forensic Medicine & Toxicology 2021, 15, 3018-3024. 10.37506/ijfmt.v15i3.15762.
[23] Al-Karadaghi, S.S.; Jawad, H.; Al-Karadaghi, T. The influence of pulse duration and exposure time of Er,Cr:YSGG laser on lithium disilicate laminate debonding, an in vitro study. Heliyon 2023, 9, e14600. 10.1016/j.heliyon.2023.e14600.
[24] Freccia, W.F.; Peters, D.D. A technique for staining extracted teeth: a research and teaching aid for bleaching. Journal of Endodontics 1982, 8, 67-69. https://doi.org/10.1016/S0099-2399(82)80260-4.
[25] Akcay, M.; Arslan, H.; Yasa, B.; Kavrık, F.; Yasa, E. Spectrophotometric analysis of crown discoloration induced by various antibiotic pastes used in revascularization. J Endod 2014, 40, 845-848. 10.1016/j.joen.2013.09.019.
[26] Nandita B. ; Kishore K. ; Rohit P. ; Ruchika G. and Divya G. An in-vitro Comparison of the Bleaching Efficacy of 35% Carbamide Peroxide with Established Intracoronal Bleaching Agents . Journal of Dentistry and Oral Sciences.2020,p.1-10.
[27] Sabreen S.; Hussein A. Smear Layer Removal from the Apical Third Using the Er,Cr:YSGG Photon-induced Photoacoustic Streaming .Iranian Endodontic Journal.10.22037/ieg.v16i4.34544.
[28] Cooper, J.S.; Bokmeyer, T.J.; Bowles, W.H. Penetration of the pulp chamber by carbamide peroxide bleaching agents. J Endod 1992, 18, 315-317. 10.1016/s0099-2399(06)80479-6.
[29] Mokhlis GR, Matis BA, Cochran MA, Eckert GJ. A clinical evaluation of carbamide peroxide and hydrogen peroxide whitening agents during daytime use. J Am Dent Assoc 2000;131:1269–1277. Crossref, Medline, Google Scholar
[30] Warren MA, Wong M, Ingram TA 3rd. In vitro comparison of bleaching agents on the crowns and roots of discolored teeth. J Endod 1990;16:463–467. Crossref, Medline, Google Scholar
[31] Rokaya ME, Beshr K, Hashem Mahram A, Samir Pedir S, Baroudi K. Evaluation of extraradicular diffusion of hydrogen peroxide during intracoronal bleaching using different bleaching agents. Int J Dent 2015;2015:493795. Crossref, Medline, Google Scholar
[32] Wetter, N.U.; Barroso, M.C.; Pelino, J.E. Dental bleaching efficacy with diode laser and LED irradiation: an in vitro study. Lasers Surg Med 2004, 35, 254-258. 10.1002/lsm.20103
[33] Armengol, V.; Jean, A.; Rohanizadeh, R.; Hamel, H. Scanning electron microscopic analysis of diseased and healthy dental hard tissues after Er:YAG laser irradiation: in vitro study. J Endod 1999, 25, 543-546. 10.1016/s0099-2399(99)80376-8
[34] Arslan, H.; Akcay, M.; Yasa, B.; Hatirli, H.; Saygili, G. Bleaching effect of activation of hydrogen peroxide using photon-initiated photoacoustic streaming technique. Clin Oral Investig 2015, 19, 253-259. 10.1007/s00784-014-1255-9.
[35] Bersezio, C.; Martin, J.; Pena, F.; Rubio, M.; Estay, J.; Vernal, R.; Junior, O.O.; Fernandez, E. Effectiveness and Impact of the Walking Bleach Technique on Esthetic Self-perception and Psychosocial Factors: A Randomized Double-blind Clinical Trial. Oper. Dent. 2017, 42, 596–605.
[36] DiVito, E.E.; Colonna, M.P.; Olivi, G. The photoacoustic efficacy of an Er: YAG laser with radial and stripped tips on root canal dentin walls: an SEM evaluation. J Laser Dent 2011, 19, 156-161

.

كفاءة مادة البيروكسايد كاربمايد في ازالة التصبغات اللونية الداخلية للاسنان بمساعدة تقنية ليزر Er,Cr:YSSG المحتث بالأمواج الضوئية الصوتية

اية سعد وجيه ، حسين علي جواد

معهد الليزر للدراسات العليا، جامعة بغداد، بغداد، العراق

*البريد الالكتروني للباحث: ayah.saad2102m@ilps.uobaghdad.edu.iq

الخلاصة

هدف البحث: تقييم تأثير تقنية الليزر المحتث بالامواج الضوئية الصوتية (PIPS) في تعزيز تغييرات لون الأسنان باستخدام الليزرEr ، Cr:YSGGمع بيروكسيد الكارباميد.

مواد وطرائق البحث: مجموعة من 42 سنًا سليمًا تم تضمينها في هذه الدراسة. تمت معالجة جميع الأسنان لبياً ثم تم تلوينها بشكل صناعي باستخدام دم الخروف ثم وضعت طبقة بسمك 3 مم من إسمنت الأيونومر الزجاجي (GIC) المعزز بالراتنج على مسافة 2 مم تحت المَوصِلُ المِلاَطِيُّ المينائِيّ (CEJ) من جانب السن الخارجي. بعد ذلك، تم تبييض الأسنان بواسطة تقنية PIPS باستخدام بيروكسيد الكارباميد بتركيز 37% أو باستخدام التبييض المشي التقليدي بواسطة بيروكسيد الكارباميد بتركيز 37%. تم تقييم النتائج بعد 1 و 2 و 3 أسابيع. تم قياس التغييرات في لون النتائج باستخدام جهاز الطيف اللوني.

النتائج: أدت كلتا التقنيتين إلى تغيير لون كبير في نهاية الدراسة. ومع ذلك، أظهرت المقارنة بين المجموعات أن تقنية PIPS باستخدام بيروكسيد الكارباميد بتركيز 37% كانت أكثر فعالية بشكل ملحوظ ($p < 0.05$) من التبييض المشي التقليدي باستخدام بيروكسيد الكارباميد بتركيز 37% فقط في نتائج التبييض على مدى جميع فترات الدراسة.

الاستنتاج: أظهرت الدراسة الحالية أن تقنية PIPS المستخدمة لتنشيط عوامل التبييض التي تحتوي على بيروكسيد الكارباميد بتركيز 37% كانت أكثر فعالية في تحقيق نتائج التبييض المرغوبة من تقنيات التبييض التقليدية.

IJL, Issue 2, Vol. 23, 2024
https://doi.org/10.31900/ijl.v23i2.466

Research Article

Evaluation of Erbium Family Lasers' Effects on Retention of Dental Fiber Post to Resin Cement: Primary Review

Rawaa Abdul Hadi Ahmed*, Basima Mohammed Ali Hussein

Institute of Laser for Postgraduate Studies, University of Baghdad, Baghdad, Iraq
** Email address of the Corresponding Author:* rawaa.abd2102m@ilps.uobaghdad.edu.iq

Article history: Received 15 Mar. 2024; Revised 8 May 2024; Accepted 28 May 2024; Published online 15 Dec. 2024

Abstract

Objective: The most common causes of fiber post-failure are inadequate restorations and dislodgement. The fiber post surface's composition and topography can be altered with laser irradiation which could enhance its retention. This review discusses the effect of the Er:YAG and Er,Cr:YSGG lasers on the surface of fiber posts (FPs) and their strength of adhesion to resin cement in teeth with endodontic therapy.
Materials and Methods: A thorough search considering Google Scholar and PubMed, Medline, Scopus, and Web of Science published data from 2013 to 2023 which concentrate on the Erbium family lasers in the fiber post modification to optimize retention and longevity of the coronal restoration in endodontically treated teeth.
Results: Twelve studies were recognized and included as reliable sources and reviewed in the study. Data indicated that Surface modification was more effectively achieved with the Er,Cr:YSGG laser than with the Er:YAG laser. In addition to several other evaluation methods, this was primarily accomplished by measuring the pull-out and bush-out shear bonding strength of the fiber post.
Conclusion: Er:YAG laser, and Er,Cr:YSGG Laser pre-treatment of FP surfaces were effective in providing high shear bonding strength as a result of surface modification. Bond strength may be reduced and fiber post surfaces may be damaged by high-laser power irradiation.

Keywords: fiber post, shear bonding strength, push-out, pull-out, Erbium family lasers.

1. Introduction

Endodontically treated teeth are less strong and more susceptible to breaking compared to vital and healthy teeth. This may be due to changes in dental tissue composition and physical characteristics after root canal treatment. In the case of severely damaged teeth, an endodontic post is required to restore and reinforce the tooth [1]. Different types of posts are used to restore the teeth after root canal treatment, including cast ceramic and metal posts and prefabricated metal and fiber posts (FPs) [2]. Aesthetic restorations are becoming more important, and fiber-reinforced posts are a good choice because their modulus of elasticity is similar to dentin's, so stresses can be distributed evenly across the remaining root structure instead of

concentrated in one area to modify failure mode to least damage to the remaining tooth structure [3]. The polymeric epoxy resin used to make FPs has a high conversion rate. It has cross-linked structures that could be strengthened by fibers made of silica, carbon, quartz, or zirconia. These fibers could make up to 30- 50% of the fiber matrix [4]. Luting a post inside the root canal is a technically challenging procedure and adhesive techniques are recommended with appropriate bonding protocols for post-placement; this is to preserve the optimum amount of dentin, enhancing post-retention, resistance to root fracture, and reduce microleakage [5]. The smooth surface of unmodified fiber posts and their unreacted resin component weaken their mechanical interlocking with resin cement despite silane application [6]. The length, design, diameter of the post, and surface treatments made to the post surface are ranked as factors affecting post retention in many in vitro studies[7] . Uncovering monomers in the polymer matrix of the glass post can only be possible with surface treatments applied to the surface of the glass fiber post therefore; multiple surface treatments like hydrofluoric acid etching, sandblasting, silicoating, and hydrogen peroxide application were suggested to enhance the micro-mechanical interlocking due to their ability for resin coating removal and exposure of the impeded fibers [8]. However, none of the pretreatment methods are effective enough to recommend their use in daily practice [9].

Recently, one of the most recent innovations that could influence surface modification of the material to enhance bond strength and roughness is laser technology [10]. Various dental applications have been suggested for lasers, which are generally safe such as roughening zirconia restoration surface [11] or zirconia implant surface roughness [12] reducing tooth sensitivity [13], and improving caries resistances [14]. The Erbium lasers (2780nm and 2940nm) are among the famous types of lasers used in dentistry. They are in the medium-infrared spectrum, their beam is absorbed by soft tissue at 100-300μ and dentinal walls at up to 400μ [15]. Because water is the chromophore target, their usage in dentistry goes beyond soft tissues such as mucosa and gingiva, to the hard ones, including enamel, dentine, and carious tissue. The thermal effects of erbium lasers on the target tissues can be detected through vaporization. A photomechanical effect is created when water molecules explode, which aids in the ablative and cleaning processes [16]. However, the actual effect of laser application and its correct parameters is still controversial and needs more research.

So, this study aims to review the articles published around 2013-2023. These papers mainly discussed the effects of the erbium laser family on post-surface treatment and how altered their intra-radicular dentin bond strength.

2. Methodology

2.1 Data Source and Search Strategy

This review was performed through an electronic search on the following websites: MEDLINE (PubMed), Embase (Elsevier), Web of Science (Clarivate), and Google Scholar. Studies concentrating on the use of the Er, Cr:YSGG, and Er:YAG lasers for surface modification of the fiber posts were included and reviewed. All are in a full-text format and have the laser as a main study group or sub-groups with if included, a comparison with other modification techniques. Preparing for this review started first with the selection of sequenced articles which was performed by reading the abstract first and then data collection then arranging from the full-text arrangement and tabulating to summarize essential data and facilitate analysis. Only manuscripts published in the English language within the previous ten years were included in this search, till November 2023 by utilizing the following keywords: “fiber post”, “Er,Cr:YSGG”, “shear bond strength”, “SBS” ,: Er:YAG laser “pull out” or “push out” tests. An additional manual search was conducted through the relevant papers' references list.

Articles of the following categories were not included: Unpublished articles in trusted journals, irrelevant studies, individual viewpoints, and publications lacking an abstract or publications of case reports with a short follow-up period; all review studies and social media sources were also excluded.

3. Result

Following the initial search, 88 articles were found in total; 40 articles were still there after the duplicate and excluded items were removed. To comprehend the Erbium family laser effect on surface modification of fiber posts, Google Scholar and PubMed searches yielded 12 papers that were included in this review. Table 1 provides a summary of the findings of the listed studies. With Er,Cr:YSGG and Er:YAG laser, several surface treatment methods such, as sandblasting, hydrofluoric acid, Nd:YAG laser, and air ablation were included in this study. Topics included are modification of fiber post-surface roughness, and testing bond strength specifically shear bond strength. In addition to that, a variety of types of fiber posts such as quartz and glass were considered in this review. Every study included and reviewed used dual-cured resin cement as a luting material. The universal testing machine's cross-head speed was set to 0.5,1 and 2mm/min for evaluating either pull or push-out shear bonding strength.

3.1 Fiber post surface treated with Er:YAG laser

Er:YAG laser was used to treat the post surface. It can be absorbed by hydroxyl groups in the post, causing ablation of the organic matrix, exposure of the fibers, and increasing the surface roughness [17]. However, the actual effect of laser application and its suitable parameters still needs more research to exclude some differences in the effect and results of laser application in this field. Numerous research has recently investigated the impact of varying Er:YAG laser powers on fiber posts. Akin et al [18] showed that 150 mJ and 10 Hz increased glass fiber post-bonding. But Tuncdemir et al [19] found that utilizing the aforementioned parameters with an Er:YAG laser did not result in a statistically significant change to the push-out bond strength of quartz fiber posts. On the other hand, Arslan et al [20] examined the effects of a 4.5W, 10Hz using Er:YAG laser on glass fiber posts and found that 450 mJ of irradiation strengthened the pull-out bond between the fiber posts and the resin core. Furthermore; Gomes et al [21] revealed that the bond strength between the posts that were exposed to the Er:YAG laser irradiation and the root dentin was comparable to that of the posts that received only silane treatment. Moreover; Gorus et al [22] assessed the glass fiber post's micro-push-out bond strength; they found that the laser-treated group had reduced fiber post-bonding strength to resin cement due to Er:YAG irradiation. Recently, Raafat et al [23] applied Er:YAG laser and revealed that laser treatment for the cylindrical post surface using 10Hz, 1.5W, and pulse duration 100µs for 60sec can enhance its bond strength to intra-radicular dentin. Two possible reasons for studies that yield inconsistent results are differences in the type of fiber post and the laser settings.

3.2.Fiber post surface treated with Er,Cr:YSGG laser

As a result of Er,Cr:YSGG laser applied on fiber post surface, surface modification, wettability, and interface adhesion and stability have all may be enhanced [24]. Kurtulmus-Yilmaz et al. [25] found that the post/resin core micro-push-out bond strength was dramatically enhanced when glass fiber posts were irradiated with (1-1.5) W of Er,Cr:YSGG laser instead of without surface treatment. This was in contrast to a previous study made by Cengiz et al [26], Er,Cr:YSGG laser with 3.5W and 4.5W power for 60s did not improve the push-out bond strength of glass fiber and decreased in un quartz fiber or zirconia root posts. Another study by Gomes et al. [21] reported that all areas of the root showed an increase in the push-out bond strength of the fiber posts after being irradiated with an Er,Cr:YSGG laser set at 150mJ, 10 Hz, 1.5W, and140µs pulse duration. While, Ghavami et al. [27] concluded that the adhesion of the fiber post was not improved by irradiating an Er,Cr:YSGG laser with an MZ8 tip, at 20Hz, 140µs, and a mixture of 80% water and 60% air in the noncontact mode for 10 sec. Moreover; using a power of 1.5W made the bond strength of the post worse. After exposure to 1W laser power, there was no appreciable difference between the experimental and control groups. Hashemikamangar et al. [28] proved that the micro-push-out strength of fiber posts was improved by irradiating them with Er,Cr:YSGG laser at 1W and 1.5W, 20 Hz, and 140 µs.

Table 1: General Information of Reviewed Article**.**

Author; date	Types of fiber post/cement	Surface treatment	Laser parameters	Shear bond strength	Result /conclusion
Raafat et al.; 2023	Glass fiber post /dual-cured self-adhesive resin cement	-control/silane - Er:YAG laser	Er:YAG laser cylindrical fiber tip 10 Hz , 1.5W, 100µs. for 60 sec.	push-out test/ at 1 mm/min	Significant increase in bonding by laser
Amr Mekky et al.; 2022	Glass fiber post / self-adhesive resin cement	-no treatment -air-borne particle abrasion -diode laser -Er,Cr:YSGG laser	Er,Cr:YSGG, 1.5W, 10Hz, 140µs, for 60 seconds. Sapphire MGG6: 60% water, 40% air	pull-out test / at 1mm/min	Er,Cr:YSGG Significant increased bonding
Gorus et al.; 2020	Glass fiber post /Clearfil SA cement	-control -sandblasted - Er:YAG laser.	Er:YAG 2940nm 1.5W,10H for 60 sec.	push-out test, 0.5 mm/min.	Significant reduction of bonding
Rezaei-Soufi et al.; 2019	Quartz fiber /posts dual-cure resin cement.	-control -Er,Cr:YSGG laser	Er,Cr:YSGG laser (0.5, 1.0, 1.5)W, 20Hz, 150µs, with MZ6 tip, 10% water, 15% air for 30 sec.	Pull out test, 1 mm/min	Er,Cr:YSGG laser Significant increased bonding to dentin
Hashemika-mangar et al.; 2018	Glass fiber posts/ resin cement.	-control -Sandblasting -Er,Cr:YSGG laser irradiation at (1, 1.5, 2)W.	Er,Cr:YSGG laser. For every laser power, 20 Hz, 60% water, 40% air, 60µs. Two cycle with 40sec for each.	push-out/ 1mm/min	The fiber post's bonding strength improved by 1 W.
Ghavami-Lahiji et al.; 2018	- Conical Exacto Glass fiber -Double-tapered White Post DC Glass fiber posts	-no treatment -Er,Cr:YSGG laser irradiation at (1, 1.5)W, MZ8 tip	Er,Cr:YSGG laser settings: 1W or 1.5W at 20 Hz, 140 µs, 80% water, 60% air, 10 sec.	push-out test/ 1mm/min	1.5W decreased Bonding strength or no effect.
Gomes et al.; 2018	-Glass fiber posts – -Conventional -dual polymerizing resin cement	-Control-silane -Er:YAG laser -Er,Cr:YSGG -diode laser	Er:YAG 1.5 W/10Hz 100 µs, 60sec/Water spray (25 mL/min) Er,Cr:YSGG 1.5W, 10Hz, 140 µs, 60s/60% water 40% air, MG6 Sapphire tip	Push out test/ 0.5 mm/min speed	Er,Cr:YSGG laser radiation only enhanced the bonding.
Cengiz et al.; 2016	-Snowpost fibre post, - Quartz post Zirconia post/ Luting resin composite	-control -Er,Cr:YSGG laser at 3.5W and 45W	-Er,Cr:YSGG used at 3.5W and 4.5W power for 60 s, 60 µs, 20 Hz. 85% air-cooling, 75% water.	push out test/ 1mm/min	Er,Cr:YSGG laser did not enhance pushout bond strength.
Kurtulmus-Yilmaz et al.; 2014	- Quartz post Translucent fiber post -Glass fiber post, - Dual Resin core material.	-control -sandblast -hydrofluoric acid -24% H_2O_2 -CH_2Cl_2 - Er,Cr:YSGG .	-MG6 sapphire tip - noncontact mode, (1, 1.5, 2)W / 20Hz, 140 µs with 80% water and 60% air for 30 sec.	Micro-push out /1min/mm	Post/core interface better with 1W and 1.5W Er,Cr:YSGG.

Akin et al.; 2014	- quartz, Translucent, light post -Dual-cured composite luting cement	-control-no treatment -sandblasted - silica coated -hydrofluoric - acid-etched -Nd:YAG laser - Er:YAG laser	- 4mm titanium articulated arm pulsed at 10Hz, 150mJ, 1.5W, 700µs, and 20sec, with water irrigation.	Push out test/ 1 mm/min	Er:YAG laser enhanced bonding of fiber posts without considering Surface roughness.
Tuncdemir et al.; 2013	-Quartz fiber posts -self-curing adhesive cement	-control - alumina airborne abrasion -Er:YAG laser	Er:YAG laser 150mJ for 60sec, 100µs, 10Hz, with a R14 handpiece, non-contact with no air or water	push-out test/ 1 mm/min	Er:YAG laser did not influence push-out bond strength.
Arslan et al.; 2013	-FRC posts - Rebilda DC cement	- Control -air abrasion with 50-µm alumina - Er:YAG laser	Er:YAG laser, (1.5, 3, 4.5)W, 10Hz, for 60sec, 100µs, optical tip 400µm diameter.	pull-out tests/ 2 mm/min	Improved Pull-out bonding at 4.5W Er:YAG laser.

Rezaei-Soufi, et al [29] tested fiber posts without surface treatment. Results showed lower bonding strength to dentin compared to those treated with (0.5, 1, and 1.5) W Er,Cr:YSGG laser by Z6 tip. Recently, Amr Mekkyet al. [30] showed that the pull-out bonding strength of the glass fiber post to root dentin was improved by irradiation with Er,Cr:YSGG laser, and Sapphire MGG6 fiber tip.

4. Discussion

The target material's chemical and physical properties, as well as the many laser radiation parameters, determine the extent to which an irradiated substrate's surface is altered. Surface cleaning and chemical modification of surface qualities improvement or deterioration of bonding properties are both achievable depending on material properties and laser radiation parameters [4]. Despite having comparable wavelengths, Er:YAG and Er,Cr:YSGG lasers exhibit distinct water absorption differences. Er:YAG laser absorbs more water than Er,Cr:YSGG laser. Additionally, Er:YAG laser uses a water irrigation system to apply water to the surface directly, generating a water layer. Er,Cr:YSGG lasers use pressured air and water to create a water mist. The water pellicle generated on the glass fiber post during Er;YAG laser irradiation may have consumed energy since water absorbs erbium laser energy. The irrigation volume in this system was 5 times that of the Er,Cr:YSGG laser, which may affect the energy that reached the irradiated surface[31]. Because of the smaller water flow that allows more energy to contact with the target surface, glass fiber posts exposed to the Er,Cr:YSGG laser irradiation showed increased ablation of the polymeric matrix which led to enhance both surface roughness and bonding strength[6] . Glass fibers and the resin matrix will likely melt when exposed to high power laser irradiation. A solidification procedure that incorporates both layers into one another comes after this one. Low bond strength was obtained because of this altered surface topography which could prevent resin cement from entering the post surface [31]. High-power density Er,Cr:YSGG laser irradiation reduces dental post-flexural strength and modulus. When surface roughening fiber posts and resin cement improve contact, structural changes that affect durability must be considered [8].

This review assessed the pull-out or push-out bond strength of the fiber post to the dentinal wall or resin cement used for luting. The pull-out test measures the complete detachment force of a post from the entire length of the canal, enabling the evaluation of both shear and tensile stresses. However, one limitation of this test is the challenge of precisely controlling the applied load along the longitudinal axis of the samples [32].On the other hand, compared to the usual shear test, the push-out test more accurately and reliably measures bond strength. Uneven stress distribution in thick samples limits push-out strength testing; slicing the samples to make smaller pieces could help resolve this issue [33].

5. Conclusions

1-The improvement of fiber post retention was achieved more effectively by the Er,Cr:YSGG laser than by the Er:YAG laser.
2- Fiber post-structural damage can occur when the power of the Er,Cr:YSGG laser is more than 2W.

References

[1] Bhuva B, Giovarruscio M, Rahim N, Bitter K, and Mannocci F. "The restoration of root filled teeth: a review of the clinical literature," Int. Endod. J.2021; 54 (4): 509–535. doi: 10.1111/iej.13438.
[2] Lazari PC, de Carvalho MA, Del Bel Cury AA, and Magne P. "Survival of extensively damaged endodontically treated incisors restored with different types of posts-and-core foundation restoration material." J. Prosthet. Dent.2018 May; 119 (5): 769–776. doi: 10.1016/j.prosdent.2017.05.012.
[3] Wang X, Shu X, Zhang Y, Yang B, Jian Y, and Zhao K, "Evaluation of fiber posts vs metal posts for restoring severely damaged endodontically treated teeth: a systematic review and meta-analysis.," Quintessence Int.2019; 50(1): 8–20. doi: 10.3290/j.qi.a41499.
[4] Davoudi A et al., "Laser Treatment of Fiber Post and Final Push-Out Bond Strength: A Systematic Review and Meta-Analysis". Photobiomodulation Photomed. Laser Surg. 2020January; doi: 10.1089/photob.2020.4809.
[5] Ali, A.J.K R, J, "The Effect of the Type of Post Space Irrigation on the Push-Out Bond Strength of Glass Fiber Post (An in vitro Study)." Res. Med. Dent. Sci., 2021; 9(5) : 118–123.
[6] Mishra L et al., "Effects of surface treatments of glass fiber-reinforced post on bond strength to root dentine: A systematic review." Materials (Basel). 2020;13(8). doi: 10.3390/MA13081967.
[7] Dentistry R. "A systematic review of factors associated with the retention of glass fiber posts."2015; 29(1): 1–8. doi: 10.1590/1807-3107BOR-2015.vol29.0074.
[8] Hasham M, Hashem A, and Hamza F."Effect of Different Surface Treatments of Glass Fiber Posts on their Surface Roughness and Flexure Properties. Maced. J. Med. Sci. 2021; 9. (D): 229–234.
[9] Kürkçüoğlu I, Kucukesmen C, Özkır S, and Yilmaz B, "Effect of surface treatment on roughness and bond strength of CAD-CAM multidirectional glass fiber-reinforced composite resin used for implant-supported prostheses." Polym. Int.2021 Jan; 70(10). doi: 10.1002/pi.6173.
[10] Salman, S.Q and Hussein B, M, A. "Topographical Analysis of Human Enamel after Phosphoric Acid Etching and Er,Cr:YSGG Laser Irradiation." Shahid Beheshti Univ. Med. Sci.2023; 14(e68). doi: 10.34172/jlms.2023.68.
[11] Dawood,R.M, and Ibraheem AF. "Evaluation of Shear Bond Strength of Zirconia to Tooth Structure after Different Zirconia Surface Treatment Techniques," J. Baghdad Coll. Dent.2015; 27(1): 77–85. doi: 10.12816/0015268.
[12] Muhy.S,R and Hussein,B.M.A. "analysis-of-ND-YAG-laser-1064-and-532-nm-interaction-with-zirconia-dental-implant-after-different-exposure-time." J. Res. Med. Dent. Sci.2019Nov; 5(7): 40–47.
[13] Mubarak R.M, Hussein B. M .A. "Influence of Er : Cr ; YSGG laser Desensitization on SBS of resin cement to dentin." Iraqi J. Laser2022; 21(1): 18–27.
[14] Hadi.A. A. and Hussein.B. M .A. "Role of Er,Cr :YSGG Laser and Fluoride in Caries Resistance". Journal of Research in Medical and Dental Science. 2022; 100(8): 19-25.
[15] Johar K. & Kirpa J, Fundamentals of laser dentistry. Jaypee Brothers Medical Publishers (P) Ltd. https2011.doi.org/10.5005/jp/books/11324
[16] Convissar RA, "Laser dentistry 101: An introduction to wavelengths and laser-tissue interaction," Seminars in Orthodontics.2020; 26(2): 74–79. doi: 10.1053/j.sodo.2020.06.001.
[17] Oz O,P,Secilmis A, and Aydin C. "Effect of Laser Etching on Glass Fiber Posts Cemented with Different Adhesive Systems," Photomed. Laser Surg.2018; 36 (1): 51–57. doi: 10.1089/pho.2017.4304.
[18] Sipahi C, Piskin B, Akin GE, Bektas OO, and Akin H. "Adhesion between glass fiber posts and resin cement: evaluation of bond strength after various pre-treatments.," Acta Odontol. Scand.2014 Oct; 72(7): 509–515.doi: 10.3109/00016357.2013.875586.
[19] Tuncdemir AR, Yildirim C, Güller F, Ozcan E, and Usumez A."The effect of post surface treatments on the bond strength of fiber posts to root surfaces." Lasers Med. Sci.2013Jan; 28 (1):13–18. doi: 10.1007/s10103-012-1053-z.
[20] Arslan H, Kurklu D, and Benan L, "parameters on the pull-out bond strength of the fiber posts Effects of post surface treatments including Er : YAG laser with different parameters on the pull-out bond strength of the fiber posts," no. November 2013, doi: 10.1007/s10103-013-1485-0.

[21] Gomes KGF, Faria NS, Neto WR, Colucci V, and Gomes EA, "Influence of laser irradiation on the push-out bond strength between a glass fiber post and root dentin." J. Prosthet. Dent.2018; 119(1): 97–102. doi: 10.1016/j.prosdent.2017.01.013.
[22] Gorus Z and Uner DD, "The evaluation of bond strength of glass fiber posts subjected to different surface treatments." 2020; 26(12):29–32. doi: 10.5455/annalsmedres.2019.07.408.
[23] Raafat W, Kheiralla L, and Nabil O, "Effect of laser surface treatment of glass fiber posts on their bond strength to intra-radicular dentin at different root levels: An in-vitro study." Int. J. Appl. Dent. Sci.2023; 9(1):149–155.doi: 10.22271/oral.2023.v9.i1c.1672.
[24] Kırmalı Ö, Akçakuş Battal T, Turker N, and Dündar A, "Mechanical properties of glass-fibre-reinforced composite posts after laser irradiation with different energy densities." Aust. Endod. J.2021; 47(1): 34–42. doi: 10.1111/aej.12443.
[25] Kurtulmus-Yilmaz S, Cengiz E, Ozan O, Ramoglu S, and Yilmaz HG, "The effect of Er,Cr:YSGG laser application on the micropush-out bond strength of fiber posts to resin core material," Photomed. Laser Surg.2014; 32 (10). doi: 10.1089/pho.2014.3780.
[26] Cengiz S, Koçak S, Koçak M, Velioğlu N, Sadettinoğlu K, and Özcan M, "Effect of Er,Cr:YSGG laser surface conditioning on the adhesion of fiber-reinforced composite and zirconia intraradicular posts to the root dentin." J. Adhes. Sci. Technol.2016; 30(18): 1957–1967. doi: 10.1080/01694243.2016.1170587.
[27] Ghavami-Lahiji S, Benedicenti M, Karimian S, Shahabi R, "Influence of Er , Cr : YSGG Laser Surface Treatments on Micro Push-Out Bond Strength of Fiber Posts to Composite Resin Core Materials." J. Dent. Biomater.2018; 5(1):533–542.
[28] Hashemikamangar SS, Hasanitabatabaee M, Kalantari S, Gholampourdehaky M, Ranjbaromrani L, and Ebrahimi H, "Bond strength of fiber posts to composite core: Effect of surface treatment with Er,Cr:YSGG laser and thermocycling." J. Lasers Med. Sci.2018; 9(1): 36–42.doi: 10.15171/jlms.2018.09.
[29] Rezaei-Soufi L, Tapak L, Forouzande M, and Fekrazad R, "Effects of motion direction and power of Er,Cr:YSGG laser on pull-out bond strength of fiber post to root dentin in endodontically-treated single-canal premolar teeth." Biomater. Res.2019 ;23(1): 1–8. doi: 10.1186/s40824-019-0165-y.
[30] Amr. Mekky , El-Hakim.M, Shokry.T," "Effect of Posts Surface Treatments on the Pull-out Bond Strength of Glass Fiber Post to Root Dentin 'A Comparative In - Vitro Study'.2022 ;2(1):1–13.
[31] Siqueira CB, De Faria NS, Raucci-Neto W, Colucci V, and Gomes EA, "Evaluation of Mechanical Properties of Glass Fiber Posts Subjected to Laser Surface Treatments." Photomed. Laser Surg.2016; 34(10): 460–466. doi: 10.1089/pho.2016.4144.
[32] Souza JCM et al., "Surface modification of glass fiber reinforced composite posts to enhance their bond strength to resin - matrix cements : an integrative review".2021; no. 0123456789.
[33] Al-Azzawi AKJ, "The Effect of Waterlase Laser and Herbal Alternative , Green Tea and Salvadora Persica (Siwak) Extract on Push - Out Bond Strength." J. Baghdad Coll. Dent.2014; 26 (2)1–6. doi: 10.12816/0015187.

تقييم تأثير ليزر عائلة الاربيوم على قوة ارتباط الوتد الليفي مع الاسمنت الراتنجي:دراسه أستطلاعية

رواء عبد الهادي احمد، باسمه محمدعلي حسين

معهد الليزر للدراسات العليا، جامعة بغداد، بغداد، العراق

*البريد الالكتروني للباحث: rawaa.abd2102m@ilps.uobaghdad.edu.iq

الخلاصة

الهدف: الأسباب الأكثر شيوعا في فشل ارتباط الوتد الليفي هو الترميم الغيركافي والازاحه. التركيب السطحي للوتد الليفي يتأثر بواسطة إشعاع الليزر وقد يعزز من قوة التصاقه. في هذه الدراسة الاستطلاعية نناقش تأثيرليزر Er,YAGو ليزرEr,CR:YSGGعلى سطح الوتد الليفي وقوة التصاقه بالاسمنت الراتنجي في الأسنان المعالجة لبيا.

الطرق: تم بحث شامل في مقالات محرك كوكل وPubMedوMedlineوWeb of Scienceنشرت من 2013 إلى 2023وتركز على تأثير ليزر عائلة الاربيوم على تغير سطح الوتد الليفي وتحسين قوة الصاقه لكي تطيل عمر الحشوة التاجيه في الاسنان المعالجه لبيا.

النتائج: تم مراجعة اثني عشر دراسة، وتضمينها على أنها موثوقة بُحثت في الدراسة. وتشير البيانات إلى أن تعديل السطح تم تحقيقه بشكل أكثر فعالية باستخدام ليزر Er,Cr:YSGG من ليزر Er,YAG. وبالإضافة إلى العديد من أساليب التقييم الأخرى، تم إنجاز ذلك أساسا بقياس قدرة السحب والضغط مقياسالقوة الالصاق.

الاستنتاجات: المعالجة المسبقة لسطح الوتد الليفي بواسطه ليزر Er,YAG وليزر Er,Cr:YSGG كانت فعالة في توفير قوة ترابط عالية نتيجة لتعديل السطح. قد يتم تقليل قوة الالصاق وتتضرر أسطح الوتد الليفي بسبب الإشعاع العالي لطاقة الليزر.

IJL, Issue 2, Vol. 23, 2024
https://doi.org/10.31900/ijl.v23i2.475

Research Article

Investigation of Polarization Preservation in Water Channel by Using Mueller Matrix Based on Single Photon Detection

Ghada Qusai Ramzi*, Ahmed Ismael Khaleel

Institute of Laser for Postgraduate Studies, University of Baghdad, Baghdad, Iraq
** Email address of the Corresponding Author:ghada.ramzi2201m@ilps.uobaghdad.edu.iq*

Article history: Received 21 Apr. 2024; Revised 27 May 2024; Accepted 29 May 2024; Published online 15 Dec. 2024

Abstract: Polarization encoding in quantum key distribution systems is widely used for distributing secret keys between a sender and a receiver. As the polarization-encoded photons pass through the quantum channel, their polarization states might be changed. A prior verification of the channel characteristic is required in order to investigate the effect of the channel on the polarization of the photons passing through it. In this work, an experimental investigation of polarization preservation of a pure water channel is presented. The investigation relies on the verification of the Mueller matrix in order to check the polarization preservation of the channel. The measurements were carried out using a single photon detection module. The results showed that the polarization of the optical pulses is preserved when passing through the pure water channel and it can be used as a quantum channel in the quantum key distribution systems.

Keywords: quantum key distribution, Mueller matrix, polarization encoded pulses, single photon detection.

1. Introduction

The implementation of quantum cryptography is based on quantum mechanics laws to send data with high security between the sender and receiver by quantum key distribution (QKD) [1]. Quantum cryptography depends on optical sources to generate photons as a carrier of information [2]. Single photons can be approximately by highly attenuated coherent source instead of single photon source because single photons are troublesome to be experimentally observed [3]. The security requirement of quantum cryptography is a highly polarization-maintaining channel called the quantum channel known as a medium to transmit and isolate single photons from interactivity with the environment [4]. Quantum cryptography has been experimentally proved over different channels including free space [5,6], and optical fiber [7,8], besides them the water channels such as seawater or oceanic water[9,10]. The fulfillment of underwater QKD dealing with photon polarization depends on the polarization preservation of the water channel. Pure water is an ideal optical medium, while seawater and oceanic water are complicated and have different optical characteristics [9]. In this work, pure water was studied at first by measuring the Mueller matrix to consider how the polarization preserves or changes in the water channel. The experiment was performed to measure

the Mueller matrix of the water channel as a primary step before QKD with low power levels by a highly attenuated laser source to generate approximately single photons according to the necessity of quantum cryptography. The laser source must be used within the blue-green optical window of seawater (430 to 570 nm) because it has less attenuation in water in contrast to other wavelengths [10].

2. Theory

Polarization properties of electromagnetic radiation passing through a linear medium can be described by either Stokes vector for partially polarized light or, by Jones vector for completely polarized light [11, 12]. A Stokes vector S gives a description of the polarization state of the light beam, it consists of six various measurements of the polarization state in front of the detector [12, 13].

$$s = \begin{bmatrix} s_0 \\ s_1 \\ s_2 \\ s_3 \end{bmatrix} = \begin{bmatrix} I_H + I_V \\ I_H - I_V \\ I_P - I_M \\ I_R - I_L \end{bmatrix} \quad (1)$$

where S_0, S_1, S_2 and S_3 are the entire components of Stokes vector, I_X is the intensity of light measured with a polarizer oriented at different angles in front of the detector, x: H, V, P, M, R and L.so, (I_H) is for horizontal linear polarization, (I_V) for vertical linear polarization, (I_P) for +45° linear polarization, (I_M) for −45° linear polarization, (I_R) for right circular polarization, and (I_L) for left circular polarization [12]. The medium has an impact on the polarization of light passing through it, which modifies the Stokes or Jones vector so that the medium can be represented by a transfer matrix usually known as the Mueller matrix[11]. The Mueller matrix (M) is 4 × 4 matrix widened in 1943 by Swiss–American physicist Hans Mueller[14]. It describes an optical system as shown in Figure 1, which acts as an operator that connects the incoming light with received light.

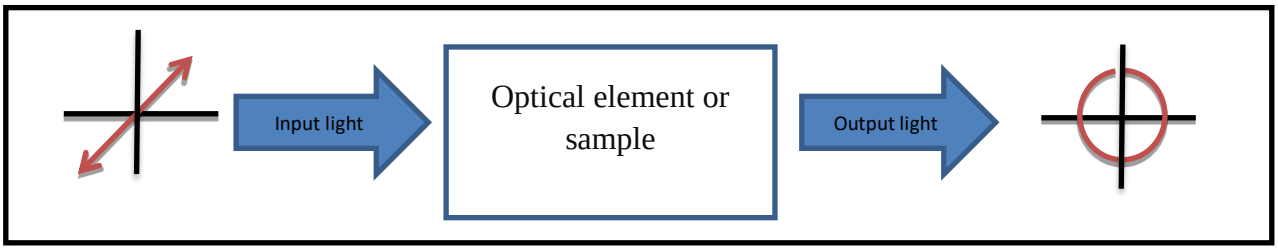

Fig. 1. The transformation of polarization of light by a medium described by the Mueller matrix.

The Mueller–Stokes formalism is given by:

$$s_{out} = M.s_{in} \quad (2)$$

$$\begin{bmatrix} S'_0 \\ S'_1 \\ S'_2 \\ S'_3 \end{bmatrix}_{out} = \begin{bmatrix} M_{11} & M_{12} & M_{13} & M_{14} \\ M_{21} & M_{22} & M_{23} & M_{24} \\ M_{31} & M_{32} & M_{33} & M_{34} \\ M_{41} & M_{42} & M_{43} & M_{44} \end{bmatrix} . \begin{bmatrix} S_0 \\ S_1 \\ S_2 \\ S_3 \end{bmatrix}_{in} \quad (3)$$

where S_{in} and S_{out} are the Stokes vectors of the input and output light, respectively and M is the is 4 × 4 Mueller matrix for the system including the optical elements and samples [14,15]. M_{11} describes the

transmitted intensity of light [14]. The first row of elements of the Mueller matrix characterizes the diattenuation of materials which describes the difference in transmitted intensity between two incident orthogonal polarizations [14,16]. The first column of elements characterizes the capability of materials to modify the polarization of the light. The enduring elements of the matrix characterize the retardance of the materials [16].

The theoretical normalization of Mueller matrix elements can be achieved by dividing each of the 16 elements by M_{11}. The normalized values are specified[13,14].

$$\begin{bmatrix} 1 & m_{12} & m_{13} & m_{14} \\ m_{21} & m_{22} & m_{23} & m_{24} \\ m_{31} & m_{32} & m_{33} & m_{34} \\ m_{41} & m_{42} & m_{43} & m_{44} \end{bmatrix} where\ m_{ij} = \frac{M_{ij}}{M_{11}} \quad (4)$$

The normalized elements (m_{ij}) are constrained between ±1[14].Mueller matrix is normalized to possess polarization-dependent information regardless of the intensity of the light source[14]. Some optical elements can preserve the polarization of incoming light, these polarization preservation properties of that element can be recognized from diagonal elements(m_{22},m_{33},m_{44}) of the Mueller matrix which must be equal to 1 for transmitted light, in this case, these elements refer to the material do not have an impact on the polarization state of incoming light. This means the optical element will not change the polarization state [14]. For example, if m_{33} =1 means that incoming linear 45^0 or -45^0 polarized light will remain with the same polarization state. The normalized elements of the Mueller matrix of an optical sample that will not alter the polarization of light will be expressed as,

$$\begin{bmatrix} 1 & 0 & 0 & 0 \\ 0 & 1 & 0 & 0 \\ 0 & 0 & 1 & 0 \\ 0 & 0 & 0 & 1 \end{bmatrix} \quad (5)$$

This shape of the normalized Mueller matrix for transmitted light is known as a unit matrix[9]. When the light beam passes through a medium with polarization preservation property, the polarization state of the input beam is equal to the polarization state of the output beam as the diagonal elements are equal to 1 and non-diagonal elements are equal to zero[9,14]. Many optical elements can preserve the polarization state of the light such as a neutral density filter [10], transmissive liquid crystals [13], and oceanic water[17] and in this work, the interested sample is (a water channel) while each individual other linear optical element has its own matrix [18].

3. Experimental Work

The experimental setup is shown in Figure 2.

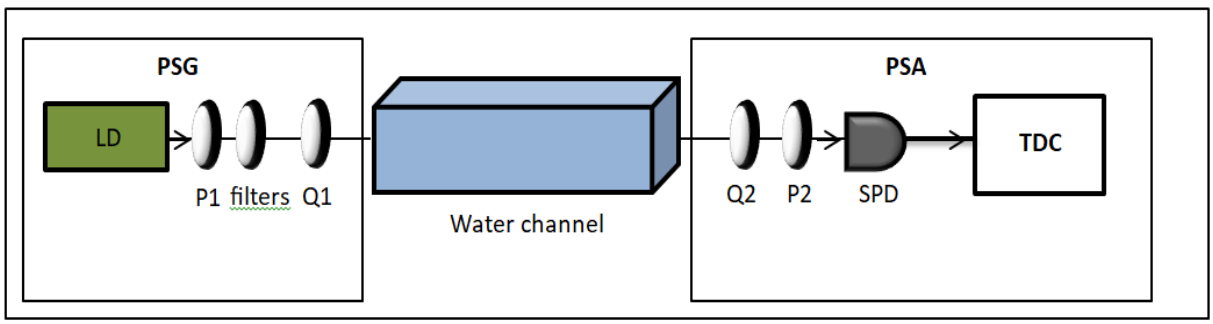

Fig. 2. Experimental setup.

The setup consists of a polarization state generator (PSG) which contains a laser diode **(LD)** (THORLABS, LP520-SF15). The center wavelength of the LD is 520 nm, and the average output optical power is 12 mW with a repetition rate of 1 MHz and a pulse width of 5 ns. Followed by a polarizer (P1), a combination of filters (THORLABS, NE510B-A T=0.1%, NE520B-A T=0.01%, NE13B-A T=0.05% where T is the filter's transmittance) for reaching the desired mean photon number per pulse (μ), and quarter wave plate (Q1) to obtain circular polarization state), followed by water channel; (a glass tank of (120cm × 80cm ×15cm) filled with 90L of pure water. After the water channel, the polarization state analyzer (PSA) is arranged. PSA consists of a quarter wave plate (Q2) and, a polarizer (P2) acting as an analyzer. In addition, the single photon detector module (SPDM) (ID100 single photon detector from id-quantique with a detection efficiency of 35% at 500 nm). The output signal of SPDM was monitored using (ID800) an 8-channel time-to-digital converter (TDC).

To conclude the set of 16 linear equations, the following states were generated as six different polarization states: horizontal (H), vertical(V), 45° linear polarization(D), -45° linear polarization(A), right circular polarization (R) and left circular polarization (L), by changing both of polarizer and analyzer angles and set the quarter wave plates (Q1) at 45^0 , and (Q2) at -45^0 in order to acquire linear polarization state. For circular polarization state, both (Q1) and (Q2) are set at either 45^0 or -45^0. Table 1 lists the elements of Mueller matrix ,when each element represents a combination of P_1 and P_2 .

Table 1. The elements of Mueller Matrix

M_{11}	**M_{12}**	**M_{13}**	**M_{14}**
(HH+HV+VH+VV)	(HH+HV+VH-VV)	(DH+DV-AH-AV)	(RH+RV-LH-LV)
M_{21}	**M_{22}**	**M_{23}**	**M_{24}**
(HH-HV+VH-VV)	(HH-HV-VH+VV)	(DH-DV-AH+AV)	(RH-RV-LH+LV)
M_{31}	**M_{32}**	**M_{33}**	**M_{34}**
(HD-HA+VD-VA)	(HD-HA-VD+VA)	(DD-DA-AD+AA)	(RD-RA-LD+LA)
M_{41}	**M_{42}**	**M_{43}**	**M_{44}**
(HR-HL+VR-VL)	(HR-HL-VR+VL)	(DR-DL-AR+AL)	(LL-RL-LR+RR)

4. Steps of measurements

1- At the beginning, the appropriate power of the LD must be set, by the aid of using optical filters (attenuators) the desired power that produces (μ) equal to 0.1 can be reached , this value of μ is the suitable value used in QKD systems.

2-The power of LD was measured before and after the water channel using a power meter [PM100D] in order to calculate the transmittance.

3-To calculate the elements of mueller matrix, for example ($M_{21)}$, four measurements are necessary: (HH), (VV), (HV) and (VH). These measurements can be achieved as follows: the measurement (HH) is obtained by setting P1 at 90^0, P2 is set at 90^0, (Q1) and (Q2) were adjusted at $+45^0$, -45^0 respectively to preserve linear polarization state, after setting the polarizers and quarter wave plates at the appropriate orientations, the output signal from the SPDM is recorded as counts by using TDC. This step was repeated for (VV), (HV) and (VH) by changing the polarization angles of P1 and P2 once at 0^0 to get vertical polarization state and 90^0 to get horizontal polarization state.

4- In order to conclude element M23, the required measurements are (DH, DV, AH, and AV), which can be achieved by changing the angle of P1 at D= 450 and A= -450 linear polarization state, P2 is set at 90 for

horizontal polarization state and 0 for vertical polarization state, and taking into consideration both of Q1 and Q2 were adjusted at 45,-45 to keep linear polarization state.
5-If the measurement requires a circular polarization state, such as M14 (RH,RV,LH,LV). The measurement was achieved by setting P1 at 45 0 and P2 was changed between 00 and 900, Q1 was rotated at 450 to obtain right circular polarization R and 1350 to obtain left circular polarization L, and Q2 was adjusted at 0 0 to keep the linear polarization at PSA.
6- In order to calculate the entire set of Mueller matrix elements, the previous procedure was repeated considering different polarization states for each element.

5. Results and discussion

The experimental results can be summarized as follows:
The measured average optical power (Pavg) of LD before and after the water channel is 8.75µW and 6.94 µW respectively, and the transmittance of the water channel was 0.793%.
The counts measured by TDC resulting from the procedure of finding Mueller matrix elements are recorded for all the desired polarization states, as listed in Table 2.
Using the results from step 2, (Pavg) is calculated using the following equation (Table 2):

$$p_{avg} = N * P_{single} \quad (6)$$

Where:
N: the number of counts
Psingle: the average power of a single photon and it is calculated as:

$$P_{single} = hvf = \frac{hc}{\lambda} \quad (7)$$

Where:
h: planks constant 6.63*10-34 j.s.
v: the frequency in Hz.
c: speed of light in free space 3*108 m/s.
λ: the wavelength of laser beam.
f: repetition rate in MHz.
$P_{single} = \frac{6.63*10^{-34}*3*10^{8}}{520*10^{-9}} 10^{6} = 3.825 * 10^{-13}\, w.$

The normalized value for each calculated value of the power is found by dividing all 16 elements by M11 as listed in Table 2.

The resulting Mueller matrix for the water channel used (pure water) is shown below:

$$M_{pure\ water} = \begin{vmatrix} 1.000 & -0.908 & 0.128 & 0.014 \\ -0.953 & 0.972 & 0.007 & -0.008 \\ -0.152 & -0.257 & 0.989 & 0.161 \\ -0.058 & 0.035 & 0.080 & 0.992 \end{vmatrix}$$

Table. 2. Calculated Mueller matrix elements

M_{ij}	Calculation of Mueller matrix elements based on TDC counts	P_{avg} (nw)	m_{ij}
M11	HH+HV+VH+VV 64+39+221+25383= 25707	9.8329275	1.000
M12	HH+HV+VH-VV 52+32+558-24829= -24187	-9.2515275	-0.908
M13	PH+PV-MH-MV 8585+6206-5177-6300=3314	1.267605	0.128
M14	RH+RV-LH-LV 14378+10826-13802-11038= 364	0.13923	0.014
M21	HH-HV+VH-VV 157-31+393-24736= -24499	-9.3708675	-0.953
M22	HH-HV-VH+VV 98-24-160+25144= 25058	9.564685	0.972
M23	PH-PV-MH+MV 8780-7967-5052+6289= 2050	0.784125	0.007
M24	RH-RV-LH+LV 10729-14465-11694+13302= -2128	-0.81396	-0.008
M31	HP-HM+VP-VM 78-107+9977-13868= -3920	-1.4994	-0.152
M32	HP-HM-VP+VM 52-37-15393+8747= -6631	-2.5363575	-0.257
M33	PP-PM-MP+MM 14393-294-87+11415= 25427	9.7258275	0.989
M34	RP-RM-LP+LM 12464-12318-10278+14287= 4155	1.5892875	0.161
M41	HR-HL+VR-VL 58-35+9989-11581= -1506	-0.576045	-0.058
M42	HR-HL-VR+VL 44-34-10905+11796= 901	0.3446325	0.035
M43	PR-PL-MR+ML 9056-7455-3923+4373=2057	0.7868025	0.080
M44	LL-RL-LR+RR 12088-248-222+13898= 25516	9.75987	0.992

In this work, the water channel was prepared in order to simulate seawater, and its characteristics were studied by the 4 × 4 Mueller matrix to investigate its polarization preservation properties, the 16 elements of the Mueller matrix were experimentally measured using an attenuated coherent optical source [LD and a combination of filters] to get an approximate mean photon number equals to 0.1. Polarizers and quarter-wave plates at PSG and PSA are changed, and the low-level optical pulses are detected by SPD and recorded in terms of counts by TDC. At each step, the orientation of the optical elements was changed so as to obtain new readings for each element of the matrix. The resultant calculated 16 elements were normalized to total transmitted intensity and the achieved Mueller matrix is nearly to the unit matrix which shows the ability of the water channel to preserve the polarization of the input beam.

6. Conclusions

According to the resulted normalized Mueller matrix of the water channel, and in comparison with an ideal normalized matrix it was found that the Mueller matrix of transmitted light passing through the water channel is nearly a unit matrix. The minimum value of the diagonal element is equal to 0.972, and the maximum value of the non-diagonal element is equal to 0.161, which means that the water channel used did not alter the polarization state of the light passing through it. In consequence, the Mueller matrix can be used as a method to study the effect of a medium on the polarization of the light passing through it.

References

[1] M. E. Sabani, I. K. Savvas, D.Poulakis, And G. C. Makris," Quantum Key Distribution: Basic Protocols And Threats", In 26th Panhellenic Conference On Informatics (PCI 2022),(November 25–27, 2022).
[2] Ch.Portmann, R. Renner," Security in quantum cryptography", Arxiv:2102.00021v2 [Quant-Ph] 30 Aug 2021.
[3] A. I. Khaleel And S. Kh. Tawfeeq, Real Time Quantum Bit Error Rate Performance Test For A Quantum Cryptography System Based On BB84 Protocol, Iraqij. Laser, Part A, Vol. 8, Pp. 29-35(2009)
[4] R.J. Hughes D. M. Alde, P. Dyer, G. G. Luther, G. L. Morgan and M. Schauer," Quantum Cryptography" [Quant-Ph], LA-UR-95-806, Tue, 4 Apr 1995.
[5] A. C.Casado, V. Fernández, N. Denisenko," Free-space quantum key distribution" Chapter from the book "Optical Wireless Communications", pp. 589-607 doi: 10.1007/978-3-319-30201-0_27 Springer.(2016)
[6] A. F. Mushatet, S.Kh. Tawfeeq , "Modeling and Simulation for Performance Evaluation of Optical Quantum Channels in Quantum key Distribution Systems", Al-Khwarizmi Engineering Journal, Vol. 17, No. 2, June, (2021) Journal P. P. 31-44.
[7] P. D. Townsend," Quantum Cryptography on Optical Fiber Networks" Elsevier, Volume 4, Issue 4, October 1998, Pages 345-370.
[8] A. I. Khaleel," Coherent One-Way Protocol: Design and Simulation", International Conference on Future Communication Networks, 2012 .
[9] S.ZHAO,W. LI, Y. SHEN, Y. YU, X.HAN, H. ZENG," Experimental Investigation Of Quantum Key Distribution Over A Water Channel", Applied Optics, Vol. 58, No. 14 , 10 May 2019.
[10] P. Shi, S.Zhao, W. Li And Y.Gu, "Feasibility Of Underwater Free Space Quantum Key Distribution", , Arxiv:1402.4666 [Quant-Ph],4 april 2014.
[11] A. A. Kokhanovsky ," Light Scattering Reviews 4: Jones and Mueller matrices: structure, symmetry relations and information content, Springer Berlin Heidelberg, July 25, 2009.
[12] S. JIAO," Polarization-Sensitive Mueller-Matrix Optical Coherence Tomography", ProQuest, December 2003.
[13] K. Dev, A. Asundi," Mueller–Stokes polarimetric characterization of transmissive liquid crystal spatial light modulator", Elsevier, Vol. 50, Issue 4, April 2012, PP.599-607
[14] James N. Hilfiker, Nina Hong And Stefan Schoeche, Mueller Matrix Spectroscopic Ellipsometry, Adv. Opt. Techn. 2022; 11(3–4): 59–91
[15] ARTUR CARNICER, 1,* SALVADOR BOSCH, 1,3 AND BAHRAM JAVIDI, Mueller matrix polarimetry with 3D integral imaging, Vol. 27, No. 8 | 15 Apr 2019 | OPTICS EXPRESS 11525
[16] C. Welsha , S. Roccaseccab , K. Nguyenc , R. Martind , C. Keysera," Diagonal Mueller matrix measurements based on a single pulse LiDAR polarimeter", SPIE Vol. 11412 114120I-1, 2020.

[17] A. A. Kokhanovsky, Parameterization Of The Mueller Matrix Of Oceanic Waters, Institute Of Environmental Physics, University Of Bremen, Bremen, Germany, JOURNAL OF GEOPHYSICAL RESEARCH, VOL. 108, NO. C6, 3175, Doi:10.1029/2001JC001222, 2003.
[18] E. Hecht," optics", Pearson Education,5th edition ,england , October 5, 2016.

التحقق من المحافظة على الاستقطاب في قناة الماء باستخدام مصفوفة مولر بالاعتماد على كشف الفوتون المنفرد

غادة قصي رمزي* ، احمد اسماعيل خليل

معهد الليزر للدراسات العليا، جامعة بغداد، بغداد، العراق

*البريد الالكتروني للباحث: ghada.ramzi2201m@ilps.uobaghdad.edu.iq

الخلاصة: ان بروتوكول توزيع المفتاح الكمي المعتمد على ترميز الاستقطاب هو بروتوكول يتم استخدامه بشكل واسع من اجل مشاركة مفتاح سري ما بين المرسل والمستقبل. بينما تنتقل النبضات البصرية التي يتم ترميز استقطابها من خلال القناة الكمية, فان حالات الاستقطاب لتلك النبضات من الممكن ان تتغير. لذلك من المطلوب التحقق المسبق من صفات القناة من اجل التحقق من تأثير القناة على استقطاب النبضات التي تمر من خلالها. في هذا العمل, التحقق عمليا من المحافظة على الاستقطاب للماء النقي يتم تقديمه. التحقق يستند على تحقيق مصفوفة مولرمن اجل التأكد من محافظة القناة على الاستقطاب. تم اجراء القياسات باستخدام كواشف الفوتون المنفرد. اظهرت النتائج انه يتم المحافظة على استقطاب النبضات البصرية عند مرورها من خلال قناة الماء النقي ويمكن استخدامها كقناة كمية في توزيع انظمة المفتاح الكمي.

IJL, Issue 2, Vol. 23, 2024
https://doi.org/10.31900/ijl.v23i2.463

Research Article

Clinical Applications of a 940 nm Diode Laser for Laser Troughing Versus Conventional Method: A Preliminary Study

Humam Barrak[1,*], Shaimaa S. Mahdi[2], Salah A. Alkurtas[3]

[1]*Institute of Laser for Postgraduate Studies, University of Baghdad, Baghdad, Iraq*
[2]*College of Science for Women,Baghdad University,Baghdad, Iraq*
[3]*Al-Turath University, Maxillofacial Consultant, Department of Dentistry, Baghdad, Iraq*
** Email address of the Corresponding Author:drhumam08@gmail.com*

Article history: Received 11 Mar. 2024; Revised 7 May 2024; Accepted 2 Jun. 2024; Published online 15 Dec. 2024

Abstract

Background/purpose: Gingival troughing is the procedure of deflecting the marginal gingiva away from a tooth in order to provide a better visualization of the finish line. In this case report study, monitoring and assessment of the clinical outcomes of two gingival troughing techniques was conducted, also the patient satisfaction during application. Two techniques were applied: the traditional method (retraction cord) and the diode laser (940 nm) method which was compared in terms of bleeding, discomfort, and operating time.

Materials and methods: Three individuals who required two crowns on natural teeth on the same side were indicated. Before the treatment, the patient's gingival and periodontal health were healthy, and they showed no symptoms of gingival recession or inflammation. One tooth was selected randomly for conventional therapy utilizing a double retraction cord, while the other was treated with a 940nm diode laser. The teeth were prepared with a 0.5 mm sub-gingival finish line, and temporary crowns were made. Patients were followed at 48-72 hours and after 5 days. Operation time and hemorrhage scores were measured at the operation time while VAS score was measured after the complete cessation of the anesthetic effect at day zero and during the follow-ups. These measurements and patients' feedback provided valuable data for evaluating the effectiveness of both techniques in promoting healing and reducing post-operative complications.

Results: The tooth that received the laser treatment showed approximately no bleeding at the operation time, minimal time to complete the procedure and no pain. In all cases, results showed that laser treatment saved troughing time, it also revealed that laser treatment resulted in a reduced risk of infection due to its sterilizing effect.

Keywords: Diode laser, Gingival troughing, Laser therapy, Retraction cords, Soft tissues.

1. Introduction

The use of diode lasers in soft tissue surgery has gained much interest in literature [1, 2]. In recent years, there have been some alterations in the conventional approaches in dental practice due to the availability of new treatment equipment[3, 4]. The laser's action mechanism on tissue is determined by the laser settings

and the properties of the tissue[5]-[6, 7]. Different types of lasers have been used in soft tissue management like Nd:YAG laser, diode, CO_2, and Erbium laser family [8]. Laser application served as an adjunctive or alternative treatment option after considering conventional therapy, as a result of its variable peculiarities, including hemostasis [9], sterilization [10, 11], and ablation [12] or vaporization[13]. For that reason, the laser's coagulating effect is used because it can provide a gingival trough to aid in impression registration [14]. Gingival trough is the narrow space between the epithelium-free gingival margin and the adjacent tooth while gingival troughing is the procedure of deflecting the marginal gingiva away from a tooth,[15].

The process of preparing for a full crown frequently needs a subgingival placement of the finishing line may be due to the presence of caries, previous restoration, the need for additional retention or esthetic demand [16]. A detailed impression is required to seal the edge of the preparation accurately. Lateral and/or vertical gingival displacement, together with moisture control, is frequently required for registering the finish line after the preparation of the final impression [17]. The gap must be sufficiently large to accept adequate thickness of elastomeric impression material, which provides its strength to avoid tearing of the impression during removal and allows it to withstand deformation during the pouring of the impression [18]. Formerly, there were several ways for gingival troughing [19], including; mechanical methods with retraction cords or paste, chemo-mechanical methods with retraction cords soaked with a hemostatic solution, surgical techniques such as gingivectomy and laser surgery using different laser wavelengths.
In this preliminary study, a comparison of two methods of gingival troughing was made using laser and retraction cords in terms of pain, bleeding, and operation time.

2. Materials and methods

This preliminary study compared the effect of laser surgery in gingival troughing to the traditional method of using retraction cords. The patients signed an informed consent form after receiving thorough information about the potential dangers and advantages. Three healthy volunteer patients were in good health and received the same treatment process, they needed crown restorations on two natural teeth on the same side. The selected teeth should not have any periodontal pocket surpassing 3 mm, and the treatment requires optimal gingival health. The patient was informed and agreed to the treatment plan. Then Informed Consent Form (ICF) was signed, and the treatment protocol was established to complete the treatment.
The teeth were prepared in a chamfer finish line around 0.5 millimeters positioned apically to the gingival margin during the first visit. The double-cord technique was used on one tooth and the laser treatment was used on the other.
For the trough prepared by the retraction cord method, the procedure started with the insertion of a number 000 cord (Ultrapak™ E Knitted Epinephrine Displacement Cord, Ultradent Products Inc, USA) at the base of the gingival sulcus using a blunt instrument. Next, a number 1 cord (Ultrapak™ E Knitted Epinephrine Displacement Cord, Ultradent Products Inc, USA) was placed to ensure the finishing line was visible. The first cord inserted remained in place for the entire recorded time, while the second cord was inserted for only 1-3 minutes to achieve the desired tissue displacement which was removed prior to taking the impression. For the laser troughing procedure, the gingiva was troughed using a 940nm diode laser (Epic, BIOLASE Technology, USA). Before beginning the operation, the optical fiber tip was initiated by burning pigment from the articulating paper on it. Then the laser was set at low power settings ranging from 1 to 1.3 W. In this case report, a 1W power in a pulsed mode was sufficient to achieve troughing in all the cases included, depending on the tissue type to reduce the risk of tissue charring. Since charring, is an adverse side effect that can occur during laser usage due to either moving the tip too slowly or using too much power.

To achieve troughing, the sulcular epithelium was removed by passing the tip along the gingival sulcus while facing away from the prepared tooth and toward the soft tissue. A full all-around trough was obtained by a constant and steady short brushing strokes which were used to remove the sulcus lining carefully [20]. To remove debris and avoid bacterial contamination, the tip was continually cleansed with gauze. The amount of excised epithelium was sufficient to allow for the impression material placement and to visualize the finish line. Figure 1 depicts teeth preparations and gingival troughing in all participants.

After the gingival troughing procedure, impression registration using a polyether impression material was done. Later on, it was poured with die stone to prepare the cast. Finally, Zirconia crowns were fabricated. The patient was followed at 48-72 hours and after 5 days.

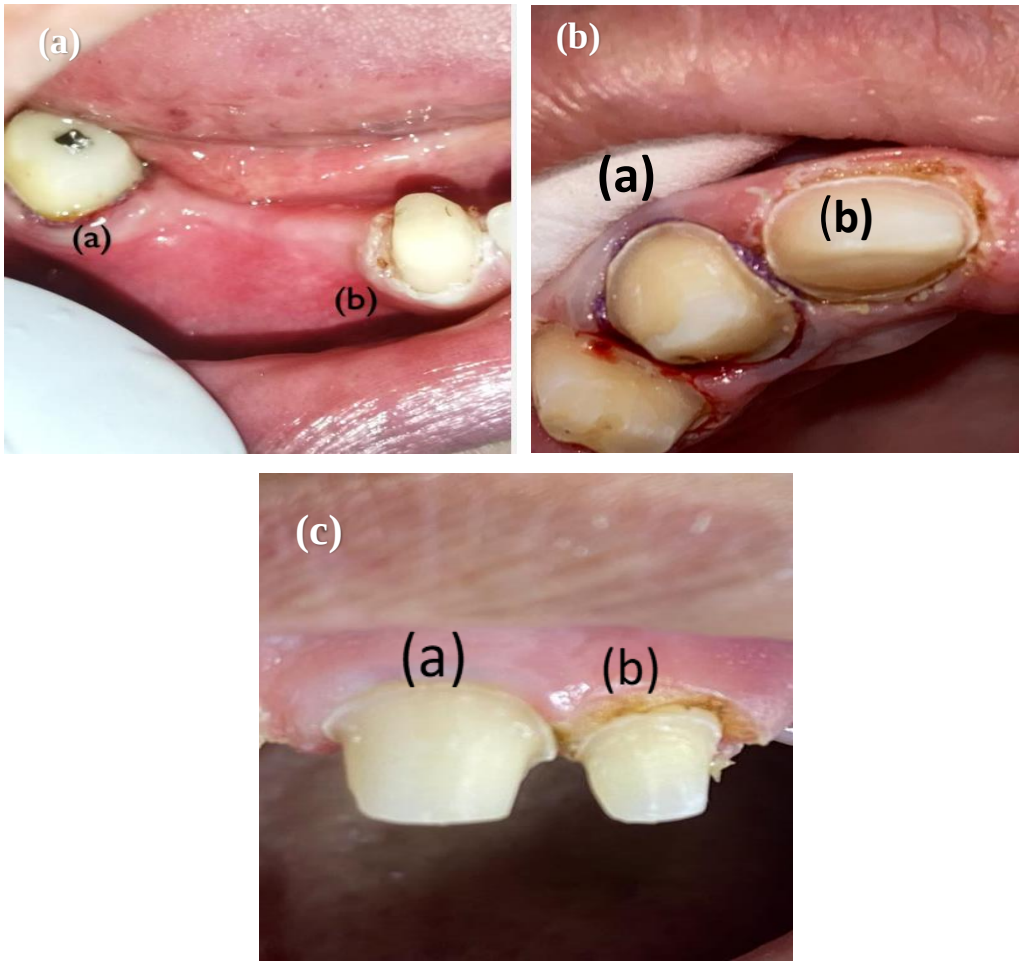

Fig. 1: Teeth preparations and gingival troughing for all the cases using (a) double-cord and (b) laser.

The time required to place and remove the retraction cord is recorded from the start of the procedure until the cord is removed while the laser troughing time is recorded from the start of the procedure until the impression is registered. Pain levels were assessed at the operation time using a visual analog scale (VAS), a pain scale assessment chart that can be printed and used so that adults and children can indicate the current intensity of pain they are experiencing [21]. Furthermore, the amount of hemorrhaging immediately following the removal of each retraction system was scored from 0 to 2 [22], as shown in table 2.

Table 1. Hemorrhage scores.

Score	
0	No bleeding
1	Controlled bleeding within 1 min
2	Uncontrolled bleeding within 1 min

3. Results and Discussion

The time taken for the retraction cord placement and for the laser troughing procedure was recorded as well as the time for the completed procedure which included both insertion and removal of the retraction cord together with impression registration for the traditional method group while for the laser group it includes only laser troughing with impression registration. The operation time for the laser troughing was considerably lower, with minimal patient discomfort. Table 2 shows the time needed for the gingival troughing process in seconds and for the completed procedure in minutes in both methods. The pain experienced during the process was recorded during treatment, and the VAS score was performed at the same session of finish line preparation after the complete cessation of anesthetic effect at day zero and during the follow-ups at 48-72 hours and after 5 days as shown in Table 3. It showed almost no pain in the laser-treated tooth compared to the conventional method in which the patient experienced discomfort. The bleeding tendency during the process was measured using a hemorrhage score that showed no bleeding during laser troughing when compared to the retraction cord process, which caused a slight hemorrhage, as shown in Table 4.

Table 2. Operation time.

Methods	Gingival troughing in seconds			The completed procedure in minutes		
	Case #1	Case #2	Case #3	Case #1	Case #2	Case #3
Retraction cord	182	185	186	11 min	12 min	13 min
Laser	17	16	16	8 min	7 min	7 min

Table 3. VAS score.

Follow-ups	Laser			Retraction cord		
	Case #1	Case #2	Case #3	Case #1	Case #2	Case #3
Day 0	1	1	1	4	6	3
Day 2-3	0	1	0	2	2	0
Day 5	0	0	0	0	0	0

Table 4. Hemorrhage score.

Methods	Hemorrhage score		
	Case #1	Case #2	Case #3
Retraction cord	1	2	0
Laser	0	0	0

4. Discussion

Retraction cords are the most widely used and popular method for gingival displacement. Although the retraction cord provides the intended retraction, it is a difficult approach that requires physical manipulation of the tissue, which might result in gingival bleeding [23]. Thus, using a retraction cord carries the risk of epithelial attachment injury and pain during cord installation, which may necessitate local anesthetic. Furthermore, additional time is necessary, and it may cause gingival bleeding and oozing [14]. Currently, laser applications are gaining much interest. One of the recent uses is for gingival troughing. Lasers remove the epithelial lining from the sulcus without damaging the tissue [20]. In the current preliminary study, we are exploring the use of soft tissue diode laser to counteract the disadvantages of the traditional method to achieve gingival displacement by comparing the two methods regarding operation time, pain, and hemorrhage. Table 2 shows that laser troughing reduced the total operation time by almost 50%, which is very beneficial for both the operator and the patient. This result came in agreement with Melilli et. Al., [24] who reported that diode lasers saved time compared to traditional retraction cords. The pain experienced by the patient in this study was recorded using VAS; the patient complained of discomfort during the insertion of the cord at the operation time and also complained of irritation at the follow-up visit after 48 hours; this result is similar to Einarsdottir et al., [25] who reported higher VAS levels in a randomized clinical trial of 67 individuals. However, VAS levels for the laser treatment showed almost no pain and discomfort due to the laser's ability to seal nerve endings [26]. The hemorrhage score demonstrated in Table 4 showed immediate hemorrhage for the retraction cord compared to the laser treatment that showed more control to hemorrhage as reported by Gururaj et. al. [27]. More clinical trials with larger samples are required to compare gingival displacement methods and produce more definitive results. Diode lasers are becoming more widely used as alternatives to electro-surgery systems and retraction cords, and this trend is set to continue in the future.

5. Conclusion

This study indicates that laser troughing saved time in minimizing operation time and ease of operation and did not cause bleeding. Additionally, the patient reported minimal discomfort, no pain and was more relaxed during troughing compared to the retraction cord placement.

Ethical approval

All procedures performed in the study involving human participants were in accordance with the ethical standards of the institutional and/or national research committee and with the 1964 Helsinki declaration and its later amendments or other comparable ethical standards.

References

[1] R. Gounder and S. Gounder, "Laser science and its applications in prosthetic rehabilitation," Journal of lasers in medical sciences, vol. 7, p. 209, 2016.
[2] A. I. Al-Khassaki, J. N. Ahmed, and A. S. Al-Allawi, "Histological Assessment of Anti-inflammatory Effectiveness of 940 Nanometer LLLT on Carrageenan Induced Arthritis in Temporomandibular Joint in Wistar Albino Rats," Indian Journal of Public Health Research & Development, vol. 10, 2019.
[3] D. A. Almiran and S. A. Alkurtas, "A comparison between Er, Cr: YSGG 2780 nm laser and carbide fissure bur in root-end resection," Iraqi Journal of Laser, vol. 19, pp. 1-11, 2020.
[4] R. A. Faris and A. Al-janabi, "Ultrafast lithium disilicate veneer debonding time assisted by a CO 2 laser with temperature control," Optics Continuum, vol. 2, pp. 825-837, 2023.
[5] S. S. Mahdi, K. A. Aadim, and M. A. Khalaf, "New Spectral Range Generations from Laser-plasma Interaction," Baghdad Science Journal, vol. 18, pp. 1328-1328, 2021.

[6] N. A. Dween, M. K. Dhahir, and T. N. Aldelaimi, "Evaluation of 940 nm Diode Laser in Esthetic Crown Lengthening," Iraqi Journal of Laser, vol. 22, 2023.
[7] R. Hashim, M. Dhahir, and S. A. AlKurtas, "PDF Effectiveness of 980nm diode Laser in reduction the diameters of exposed dentinal tubules for hypersensitive tooth," Iraqi Journal of Laser, vol. 22, pp. 33-42, 2023.
[8] F. E. Musaa, L. G. Awazli, and F. Alhamdani, "Gingival enlargement management using diode laser 940 nm and conventional scalpel technique (A comparative study)," Iraqi Journal of Laser, vol. 16, pp. 1-9, 2017.
[9] N. A. Owaid, H. A. Jawad, and A. A. Maazil, "Evaluation of Low Level Laser Therapy using 785 nm Diode Laser on the Enhancement of Chronic Wound Healing," Iraqi Journal of Laser, vol. 15, pp. 41-46, 2016.
[10] A. A. Shaheed, H. A. Jawad, B. Hussain, and A. M. Said, "Healing of Apical Periodontitis after Minimally Invasive Endodontics therapy using Er, Cr: YSGG laser: A Prospective Clinical Study," Systematic Reviews in Pharmacy, vol. 11, 2020.
[11] N. M. Abdulmalek and M. K. Dhahir, "Laser Densification of Prepared SiO2 Sol-Gel Thin Films," Baghdad Science Journal, vol. 15, pp. 0234-0234, 2018.
[12] Z. J. Naeem, A. M. Salman, R. A. Faris, and A. Al-Janabi, "Highly efficient optical fiber sensor for instantaneous measurement of elevated temperature in dental hard tissues irradiated with an Nd: YaG laser," Applied Optics, vol. 60, pp. 6189-6198, 2021.
[13] A. A. K. Aldelaimi, T. N. Aldelaimi, and S. M. Al-Gburi, "Using of diode laser (940 nm) in orofacial region," Journal of Research in Medical and Dental Science, vol. 5, p. 34, 2017.
[14] V. Bennani, D. Schwass, and N. Chandler, "Gingival retraction techniques for implants versus teeth: current status," The Journal of the American Dental Association, vol. 139, pp. 1354-1363, 2008.
[15] X. Tao, J.-W. Yao, H.-L. Wang, and C. Huang, "Comparison of Gingival Troughing by Laser and Retraction Cord," International Journal of Periodontics & Restorative Dentistry, vol. 38, 2018.
[16] P. Łabno and K. Drobnik, "Comparison of horizontal and vertical methods of tooth preparation for a prosthetic crown," Journal of Pre-Clinical and Clinical Research, vol. 14, 2020.
[17] B. Benson, T. Bomberg, R. Hatch, and W. Hoffman Jr, "Tissue displacement methods in fixed prosthodontics," The Journal of prosthetic dentistry, vol. 55, pp. 175-181, 1986.
[18] S. A. Bernauer, J. Müller, N. U. Zitzmann, and T. Joda, "Influence of preparation design, marginal gingiva location, and tooth morphology on the accuracy of digital impressions for full-crown restorations: an in vitro investigation," Journal of Clinical Medicine, vol. 9, p. 3984, 2020.
[19] K. D. Prasad, C. Hegde, G. Agrawal, and M. Shetty, "Gingival displacement in prosthodontics: A critical review of existing methods," Journal of interdisciplinary dentistry, vol. 1, pp. 80-86, 2011.
[20] V. K. Ch, N. Gupta, K. M. Reddy, N. C. Sekhar, V. Aditya, and G. M. Reddy, "Laser gingival retraction: a quantitative assessment," Journal of Clinical and Diagnostic Research: JCDR, vol. 7, p. 1787, 2013.
[21] O. Karcioglu, H. Topacoglu, O. Dikme, and O. Dikme, "A systematic review of the pain scales in adults: which to use?," The American journal of emergency medicine, vol. 36, pp. 707-714, 2018.
[22] A. Gupta, D. Prithviraj, D. Gupta, and D. Shruti, "Clinical evaluation of three new gingival retraction systems: A research report," The Journal of Indian Prosthodontic Society, vol. 13, pp. 36-42, 2013.
[23] M. Thimmappa, M. Bhatia, P. Somani, and D. Kumar, "Comparative evaluation of three noninvasive gingival displacement systems: An in vivo study," The Journal of the Indian Prosthodontic Society, vol. 18, p. 122, 2018.
[24] D. Melilli, R. Mauceri, A. Albanese, D. Matranga, and G. Pizzo, "Gingival displacement using diode laser or retraction cords: A comparative clinical study," American Journal of Dentistry, vol. 31, pp. 131-134, 2018.
[25] E. R. Einarsdottir, N. P. Lang, T. Aspelund, and B. E. Pjetursson, "A multicenter randomized, controlled clinical trial comparing the use of displacement cords, an aluminum chloride paste, and a combination of paste and cords for tissue displacement," The Journal of prosthetic dentistry, vol. 119, pp. 82-88, 2018.
[26] L. Walsh, P. L'Estrange, and G. Seymour, "High magnification in situ viewing of wound healing in oral mucosa," Australian dental journal, vol. 41, pp. 75-79, 1996.
[27] R. Gururaj, S. Jayesh, and S. Nayar, "Comparative Evaluation of Four Factors in Gingival Retraction Using Three Different Gingival Retraction Techniques: In Vivo Study," Indian Journal of Public Health Research & Development, vol. 10, 2019.

التطبيقات السريرية لليزر الدايود 940 نانومتر لحفر اللثة باستخدام الليزر مقابل الطريقة التقليدية: دراسة أولية

همام ثامر براك*[1]، شيماء صالح مهدي[2]، صلاح عبد المهدي القرطاس[3]

[1]معهد الليزر للدراسات العليا، جامعة بغداد. بغداد، العراق
[2]كلية العلوم للبنات، جامعة بغداد. بغداد، العراق
[3]جامعة التراث، استشاري جراحة الوجه والفكين، قسم طب الاسنان، بغداد، العراق

*البريد الالكتروني للباحث: drhumam08@gmail.com

الخلاصة

الخلفية\الغرض: حفر اللثة هو ابعاد اللثة المحيطة بعنق السن بعيدا عن السن, من أجل توفير رؤية أفضل لتحضير السن من الجهه الثوية. في هذه الدراسة ، تمت مراقبة وتقييم للنتائج السريرية لتقنيتين لحفر اللثة ، بلاضافة الى تسجيل تجربة المريض أثناء العملية. تم تطبيق تقنيتين: الطريقة التقليدية (سلك الازاحة) وطريقة ليزر الدايود (940 نانومتر) و تمت مقارنتها من حيث النزيف ، وانزعاج المريض ووقت العملية.

المواد والطرق: حيث تمت الدراسة على ثلاثة أفراد بحاجة إلى تيجان على أسنان طبيعية على نفس الجانب. وتم اختيار افراد ذو لثة صحية، بدون أي أعراض لتراجع اللثة أو التهابها. تم اختيار التقنية بشكل عشوائي حيث عرض احد الاسنان للعلاج التقليدي، بينما تم علاج الآخر باستخدام ليزر الدايود. تم تحضير الاسنان لاستقبال التيجان باستخدام قطر 0.5 ملم من جهة اللثة، وتم عمل تيجان مؤقتة. وكانت متابعة المرضى خلال 48-72 ساعة ومن ثم بعد 5 أيام. الوقت المستغرق لاتمام العملية ومقياس النزيف تم قياسه اثناء العملية في حين مقياس الالم تم قياسه اثناء العملية وخلال فترة المتابعة. تم اخذ النتائج والبيانات من اجل تقييم فعالية كلا التقنيتين في تسريع الشفاء والحد من مضاعفات ما بعد الجراحة .

النتائج: اظهرت النتائج ان الاسنان التي تلقت العلاج بالليزر لم يحدث فيها أي نزيف في وقت العملية، وقد استغرقت ايضا وقت اقل لإكمال العلمية ولم يشكو المريض من الم. وفي جميع الحالات المعالجة، أظهرت النتائج أن العلاج بالليزر أدى إلى تقليل الوقت المستغرق لاكمال العملية، كما أن العلاج بالليزر يقلل من خطر الإصابة بالعدوى بسبب تأثيره التعقيمي المعروف. علاوة على ذلك، أظهرت الأسنان التي تلقت العلاج بالليزر وقت شفاء أسرع من الطريقة التقليدية.

IJL, Issue 2, Vol. 23, 2024 **Research Article**
https://doi.org/10.31900/ijl.v23i2.474

Exposure of Maxillary Impacted Canine (Buccal vs Palatal) by Diode Laser (810+980)nm

Alaa faiz Abdullah[1,*], Soudad Salman Ahmed[2], Balsam Saadi Abdul Hameed[3]

[1] *Health Ministry of Iraq, Baghdad, Iraq*
[2] *Department of Physics, College of Science, University of Baghdad, Baghdad, Iraq*
[3] *Consultant maxillofacial surgeon, Imam Al-Kazemin Medical City, Baghdad, Iraq*
** Email address of the Corresponding Author: aalaa.faez2102m@ilps.uobaghdad.edu.iq*

Article history: Received 6 Apr. 2024; Revised 26 Jun. 2024; Accepted 10 Jul. 2024; Published online 15 Dec. 2024

Abstract

Background: Diode lasers(810+980) provide deep soft tissue penetration and have minimal interaction with tooth-hard tissues and excellent coagulation/haemostasis.
Objective: The aim of the current research was the exposure of maxillary buccally impacted canines by diode laser(810+980)nm in comparing palatally impacted canines depending on these parameters (pain, oedema, healing time).
Materials and methods: All patients with an impaction of the maxillary canines, such as buccal or palatal impaction, were required to be exposed. They were separated into two groups: one with seven patients in the buccal position and another with seven patients in the palatal position. Systemically healthy patients in two groups had treatment with diode lasers (980+810)mn. This study did not allow the inclusion of patients who were pregnant or in any other medically compromised patients. Pain, edema, and healing were recorded using follow-up scores on the first, second, and fifth days as well as the first and second week following surgery and statistically examined.
Results: The age mean in this study five male and nine female was 26.2. $P \leq 0.05$ was designated as the significant level..patients with buccally impacted canines exposure experience less pain, less swelling, and healing more quickly than patients with palatally impacted canines.
Conclusion: Patients with buccally impacted canines had less pain and swelling and faster wound healing than patients with palatally impacted canines when exposed.

Keywords: buccally impacted canine, diode laser, palatally impacted canine.

1. Introduction

A tooth that does not erupt after the regular development pattern is finished is known as an impacted tooth. After the third molar teeth. Maxillary canines are the teeth that are impacted the most often. Maxillary

canine impaction is a common clinical problem. Canine impaction could arise from a regional, systemic, or hereditary reason or factors. The diagnosis and localization of the impacted canine is the most important step in the care of impacted canines, based on clinical and radiographic assessments. [1]. Early detection of possible impaction and intervention is the ideal strategy for treating impacted maxillary canines. In the event that prevention is not possible, doctors may want to think about orthodontic treatment combined with the canine is surgically exposed in order to draw with occlusion. Open communication between the oral surgeon and orthodontist is crucial in this situation because it will enable the implementation of the proper surgical and orthodontic procedures [2]. Depending on where it is in relation to the dental arch, the maxillary canine impaction may be palatal or labial. Two-thirds of maxillary canines that are impacted are located palatally, and around one-third are labially impacted [3.4]. There are numerous methods for exposing impacted canines. First, the most popular approach nowadays is conventional canine exposure, which uses a scalpel and has the advantages of being inexpensive and having a long-lasting tool; however, achieving hemostasis may be challenging[5,6,7,8,9]. Second, excellent hemostasis can be achieved with electrocautery, which seals blood vessels; while cutting at the same time. However, compared to scalpel surgery, thermal damage from increased heat generation might cause healing to be delayed. [9, 10]. Third, the arsenal of an orthodontist has recently expanded to include lasers. In places with limited access, the contact cutting mode is crucial because it offers an improved vision of the bloodless site and the ability to execute delicate soft tissue treatments, but the disadvantage is the high cost of the laser device. These complementary applications include laser exposure of teeth that are superficially impacted, laser gingivectomy to enhance bracket placement or dental hygiene, and aesthetic laser gingival recontouring [11].

2. Materials and Method

fourteen cases, who were chosen for this study and their ages ranged from 19 to 31. Each case was systemically healthy. Patients were excluded from this study if they were medically comprised patients as well as pregnant women. Cases (2 groups) went to the teaching hospital, Imam Al-Kazemin Medical City had case sheets (clinical investigation, extraoral investigation, intraoral examination, medical history, & dental history), and were treated by diode laser(810+980)nm(Quicklase, UK). Prior to the surgery, all patients had CBCT(Cone beam computed tomography) to determine the position of the tooth and see if there was bone covering the impacted tooth or not. The pain, oedema, and healing time score were evaluated after surgery follow-up visits.

3. Surgical procedure

A. Buccally impacted canine exposure

1. first topical anesthesia was used (20% Benzocaine topical anesthesia gel), if the patient complains of pain or discomfort then infiltrative local anesthesia(lignospan special. Lidocanie2% with adrenaline(epinephrine) 1:80,000,2.2ml of solution per cartridge,septodent, France).
2. The patient, the assistant, and the operator were all wearing safety glasses. Avoiding instruments with highly reflective or mirrored surfaces was advised due to the possibility of laser beam reflection.
3. After determining the location of the canine impaction and if covered by bone or not by CBCT(Cone beam computed tomography).
4. The operation started. Once the tooth's location has been established, create a window using a dual diode laser ((810+980 nm), Power 2.5W with 400µm optical fiber diameter at 60 mJ of output energy and continuous mode) for showing the canine impaction crown. Figure1.
5. If was covered by bone that was very thin bone removed by curette. Normal saline was used to irrigate the surgery site.
6. Then the orthodontist comes and places a bracket on the crown of the impacted canine.

7. Provide the patient with instructions, medicine, and a follow-up appointment.

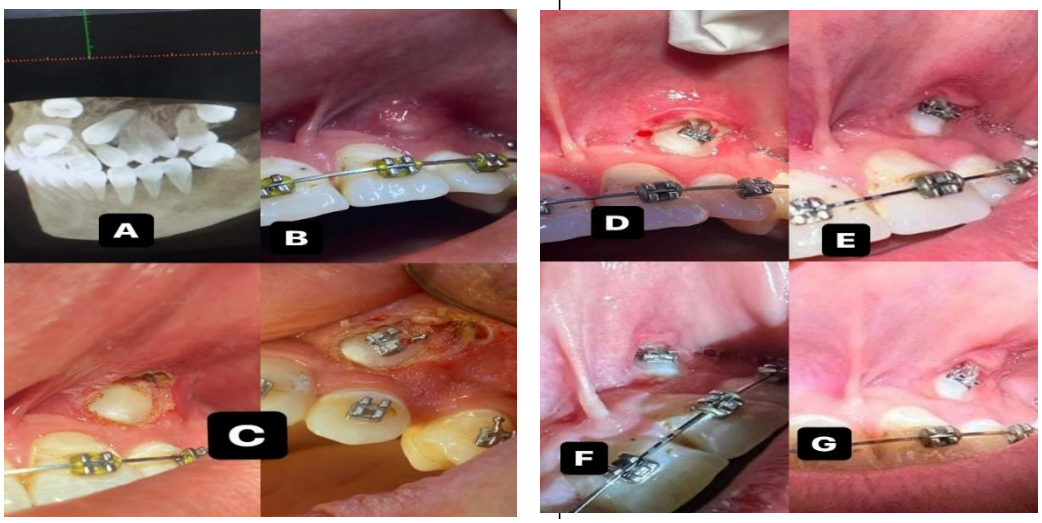

Fig. 1: exposure of buccally impacted canine by laser .A: Cone beam computed tomography.B: before treatment. C: exposure of impacted canine and bracket placement D: two days following surgery,E: five days following surgery F: one week following surgery, G: two weeks following surgery.

B. Palatally impacted canine exposure

1. first topical anesthesia was used (20% Benzocaine topical anesthesia gel) if the patient complained of pain or discomfort then infiltrative local anesthesia(lignospan special. Lidocanie2% with adrenaline(epinephrine) 1:80,000,2.2ml of solution per cartridge,septodent, France).
2. The patient, the assistant, and the operator were all wearing safety glasses. Avoiding instruments with highly reflective or mirrored surfaces was advised due to the possibility of laser beam reflection.

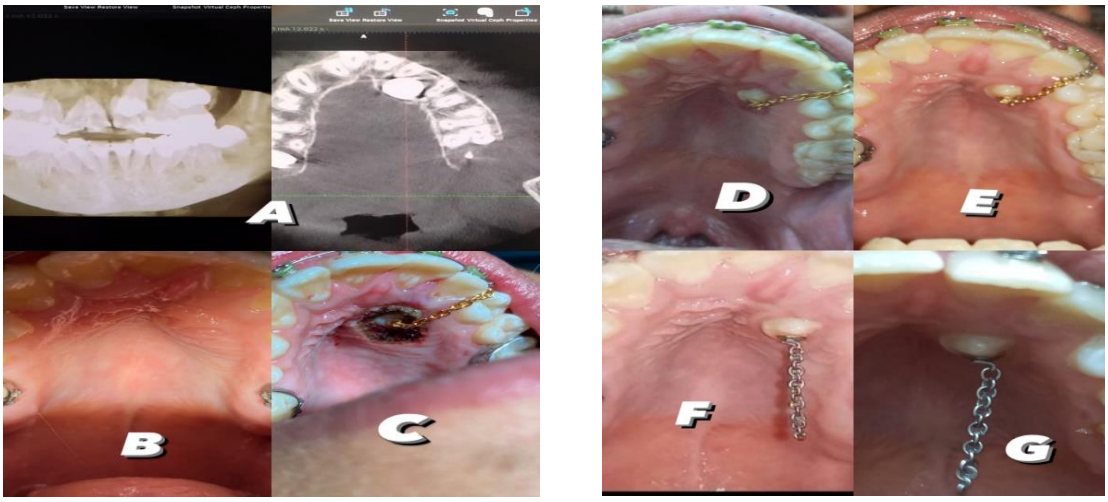

Fig.2: exposure of palatally impacted canine by laser .A:Cone beam computed tomography.B:before treatment.c: exposure of impacted canine. D: two days following the procedure, E:five days following the procedure, F: one week following surgery:, G:2 weeks following surgery.

3. After determining the location of the canines impaction and if coveresd by bone or not by CBCT(Cone beam computed tomography).
4. The operation started. Once the tooth's location has been established, create a window using a dual diode laser ((810+980 nm), Power 2.5W with 400µm optical fiber diameter at 60 mJ of output energy and continuous mode) for showing the canine impaction crown. Figure2.
5. If it is covered by bone, we remove it using a handpiece with a round bur and irrigation by normal saline to avoid getting heat on the bone.
6. . insertion of bracket by orthodontist
7. Provide the patient with instructions, medicine, and a follow-up appointment.

4. Clinical Assessments

The following parameters were assessed for both groups: pain score (Visual Analog Scale (VAS)) (Sung YT, 2018) [12],oedema score(swelling)(Marini L,2018) [13], and healing (Healing index of landry,turnbull, and howley)(Gangwani KD,2018) [14]. Pain was evaluated two hours , two and three days after surgery according to the following scores:0.no pain,1-3.mild,4-6.moderate,7-10.severe.Oedema was evaluated one, five days after surgery according to the following scores: 1. very slight oedema (hardly visible), 2. slight oedemata, 3 moderate oedema (about 1 mm raised skin), 4. severe oedemata (extend swelling even beyond the application area). Healing was evaluated one,two weeks after surgery according to the following scores: 0. very poor: Tissue color: more than 50% of gingivae red Response to palpation:bleeding Granulation tissue: present Incision margin: not epithelialised, with loss of epithelium beyond margins Suppuration: presen,1. poor: Tissue color: more than 50% of gingivae red Response to palpation: bleeding Granulation tissue: present Incision margin: not epitheliased with connective tissue exposed.,2.good: Tissue color: less than 50% of gingivae red Response to palpation: no bleeding Granulation tissue: noneIncision margin: no connective tissue exposed,3.very good: Tissue color: less than 25% of gingivae red response to palpation: no bleeding granulation tissue: noneIncision margin: no connective tissue exposed,4.excellent: Tissue color: all gingivae pinkResponse to palpation: no bleeding granulation tissue: noneIncision margin: no connective tissue exposed.

5. Statistical Analysis

The data was compiled and analyzed using statistical methods. The data analysis was conducted using JMP 16 software, developed by Gary in the United States. This investigation involved conducting descriptive and association tests to compare the two laser procedures. The student's t-test and the Oneway test were employed for quantitative variables. The significance level was established at $P < 0.05$.

6. Result

6.1. Pain score

In the buccal group, Two hours *after exposure* less pain than in the palatal group, but in two, or three days, The pain disappeared between the two groups.
in two groups
A.Pain score (2 hours) vs. the position of tooth impaction as shown in fig. (3)
(F(1,14)= 1.0833, p. value = 0.3169*)
B. Pain score (2 days) vs. the position of tooth impaction as shown in fig (4)
(F(1,14)= 0.0336, p. value = 0.857)
C. Pain score (3 days) vs. the position of tooth impaction as shown in fig(5)
(F(1,14)= 0.1171, p. value = 0.7377)

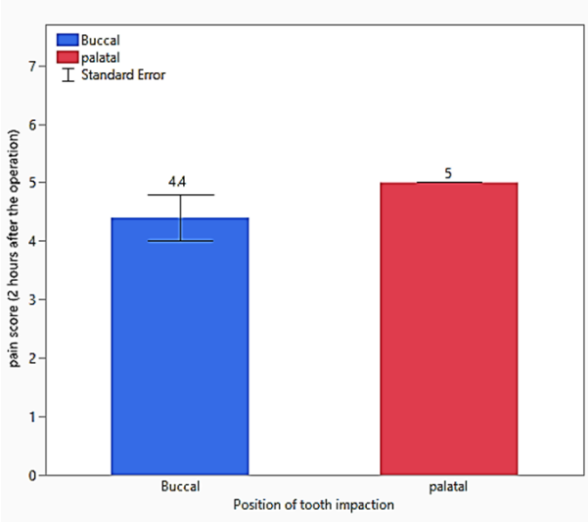

Fig.3: pain score(2 hours after operation) vs. the position of tooth impaction.

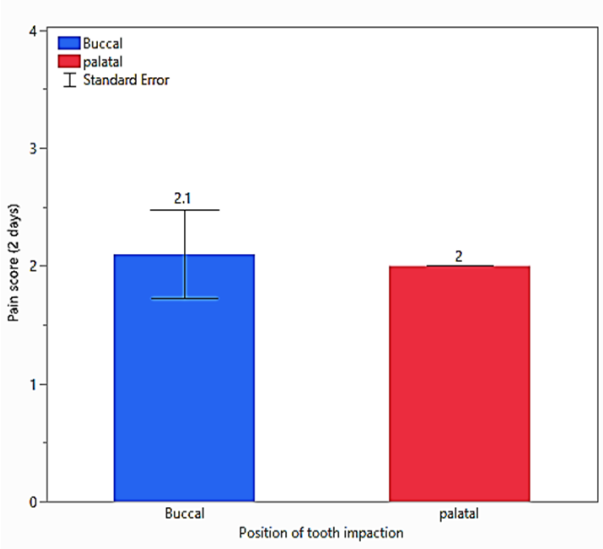

Fig. 4: pain score (2 days after exposure) vs. the position of tooth impaction.

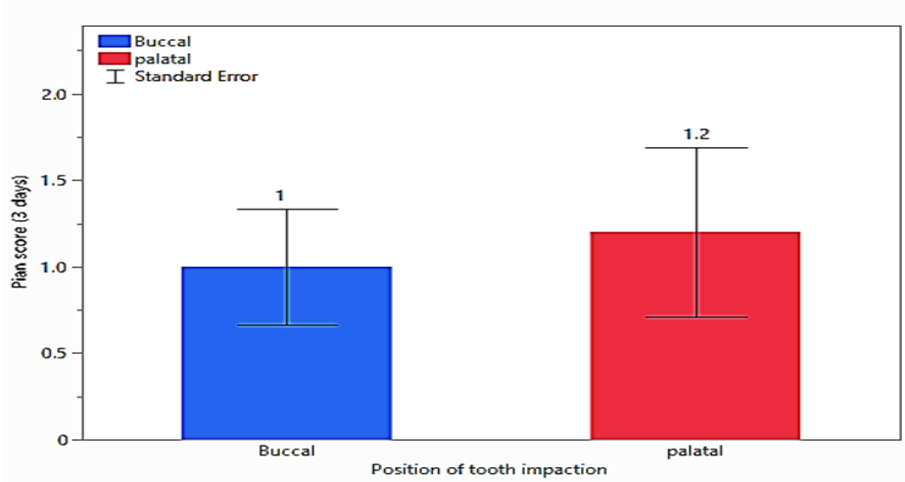

Fig.5: pain score (3days after operation) vs. the position of tooth impaction

6.2 Oedema

In the buccal group, one, and five days after exposure less oedema than the palatal group.
A. Oedema score (1 day) vs. the position of tooth impaction as shown in Figure 6.
(F(1,14)= 0.6190, p. value =0.4455)
B. Oedema score (5 days) vs. the position of tooth impaction as shown in Figure 7.
(F(1,14)= o.5700, p. value =0.2323)

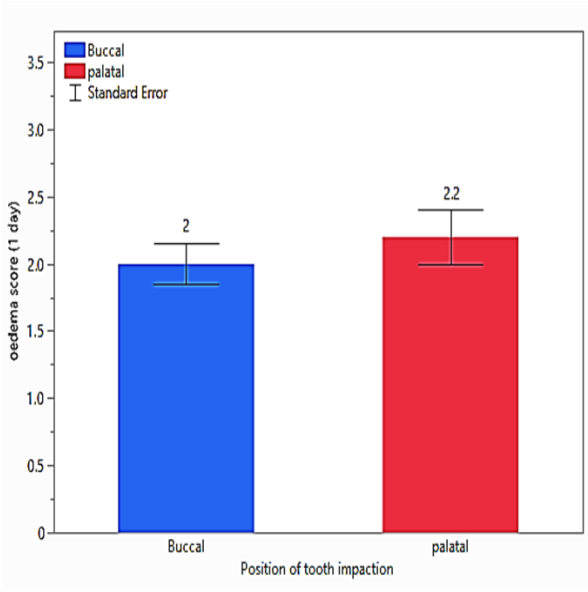

Fig. 6: Oedema score (1 day after operation) vs. the position of tooth impaction

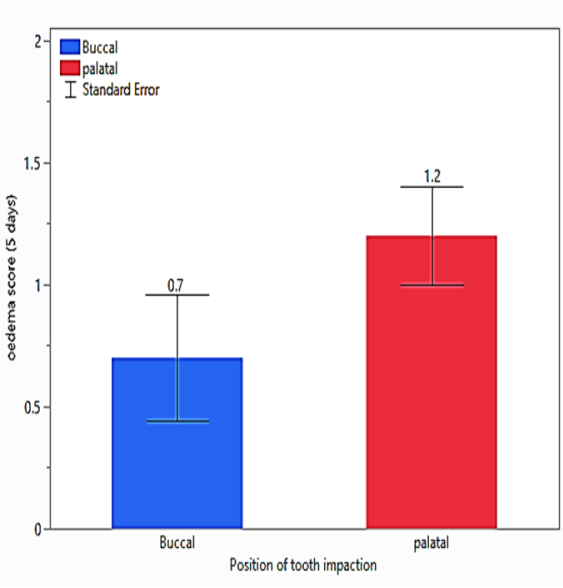

Fig.7: Oedema score(5 days after exposure) vs. the position of tooth impaction

6.3. Healing

In the buccal group, one, or two weeks after exposure faster healing than palatal group.
A. Healing score after one week vs. the position of tooth impaction as shown in Figure 8.
(F(1,14)= 6.5000, p. value = 0.0242*)
B. Healing score after 2 weeks vs. the position of tooth impaction AS shown in Figure 9.
(F(1,29)= 6.5000, p. value = 0.0242*)

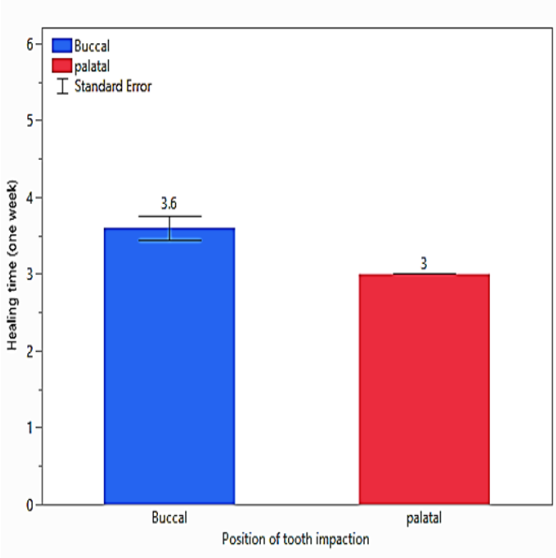

Fig. 8: Healing time score (1 week after exposure) vs. the position of tooth impaction

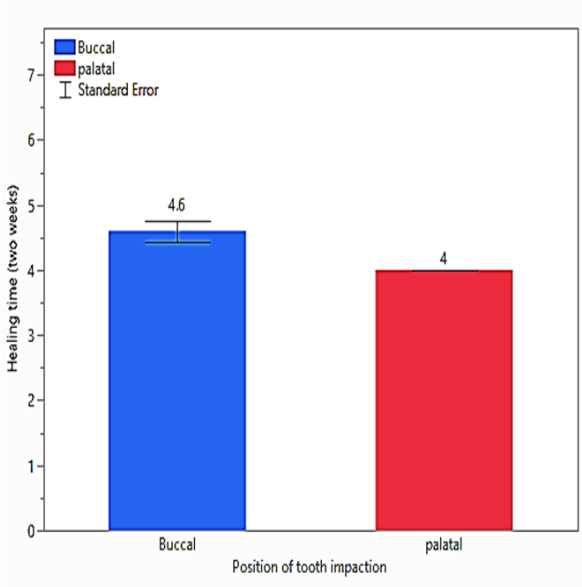

Fig. 9: Healing time score(2 weeks after exposure) vs. the position of tooth impaction

7. Discussion

Diode lasers have been used in oral soft tissue surgery due to their intraoperative and postoperative advantages.

This study aimed to investigate If there was a difference in the location of the impacted canine tooth (bucaal .vs palatal), exposed with a diode laser(810+980nm)depending on these parameters (pain,oedema,healing time).patient with buccally impacted canines usually experiences less pain, oedema, and faster healing process than patients with palatally impacted canines.

Diode lasers (810+980 nm) have minimal interaction with dental hard tissue and produce deep soft tissue penetration and good coagulation/haemostasis [14]. The use of lasers to assist in surgical procedures offers numerous benefits, including the closure of blood vessels and lymphatic vessels, less edema and bleeding during the recovery phase, no sutural requirement, increased patient satisfaction, and the majority of the time, topical anesthesia is sufficient before laser intervention [15]. Many papers in the literature describe the use of laser technology in the surgical exposure of impacted canines. Examples include a comparison between a diode laser and a conventional scalpel or the use of a diode laser only for palatal or buccal exposure. To our knowledge, however, no articles have yet been published in the literature that describe the use of a diode laser (810 + 980 nm) for surgical exposure of the impacted canines in the buccal and palatal regions and comparison of those results. In a previous study, the use of a 980 nm diode laser was shown to minimize bleeding, lessen pain, and allow the attachment of orthodontic brackets during surgical exposure of the maxillary palatal impacted canine[16]. In previous research, Patients performing laser exposure required less intra-operative local anaesthetic than those performing conventional exposure with a scalpel and had less discomfort following surgery (requiring fewer analgesics). The initiated fiber-optic tip of the diode laser device readily cuts, ablates, and reshapes the oral soft tissues with little or less discomfort, bleeding, or suturing required This is compared to using a scalpel [17].In this research, We discovered that when the impacted canine tooth was exposed using a diode laser (810-980)nm and compared in terms of palatal and buccal location, there was a very slight difference in terms of pain, swelling, and healing. However, we concluded that there was less pain and swelling and faster healing in buccally impacted canines than in palatally impacted canines because of thin buccal tissue and may be not covered by bone or covered by shell bone can be removed by curette [18]. Because of the location of impaction in the palate, the thick palatal tissue, and the increased thickness of the cortical bone on the palate[19], also the palate was located on the roof of the mouth, the patient may touch it with his tongue, causing the area to become moist with saliva When compared to canines in buccal position.

8. Conclusion

Diode laser (810+980)nm can be used to expose teeth during orthodontic treatment without producing discomfort or swelling after the procedure, and it helps to keep the area dry so that orthodontic brackets can be applied. A buccally impacted tooth has less pain and less oedema, and the healing time is faster compared to a palatally impacted tooth.

References

[1] Moro H. A better diagnose for canine pathology patients by other associated dental anomalies. Journal of Clinical Review & Case Reports. 2022 Feb 10;7(2):4-8.

[2] Bedoya MM, Park JH. A review of the diagnosis and management of impacted maxillary canines. The Journal of the American Dental Association. 2009 Dec 1;140(12):1485-93.

[3] Littlewood SJ, Mitchell L. An introduction to orthodontics. Oxford university press; 2019 Mar 16.

[4] Kohli SS, Singh Kohli V. Management of Bilaterally Impacted Labial and Palatal Maxillary Canines With One-Year Follow-Up: A Case Report. Journal of Indian Orthodontic Society. 2021 Jan;55(1):73-84.

[5] Fornaini C, Rocca JP, Bertrand MF, Merigo E, Nammour S, Vescovi P. Nd: YAG and diode laser in the surgical management of soft tissues related to orthodontic treatment. Photomedicine and laser surgery. 2007 Oct 1;25(5):381-92.
[6] Sobouti F, Rakhshan V, Chiniforush N, Khatami M. Effects of laser-assisted cosmetic smile lift gingivectomy on postoperative bleeding and pain in fixed orthodontic patients: a controlled clinical trial. Progress in orthodontics. 2014 Dec;15:1-5.
[7] Matthews DC. Seeing the Light-The Truth about Soft Tissue Lasers and Nonsurgical Periodontal Therapy. Journal of the Canadian Dental Association. 2010 Apr 1;76(2).
[8] Ize-Iyamu IN, Saheeb BD, Edetanlen BE. Comparing the 810nm diode laser with conventional surgery in orthodontic soft tissue procedures. Ghana Medical Journal. 2013;47(3):107-11.
[9] Amaral MB, De Ávila JM, Abreu MH, Mesquita RA. Diode laser surgery versus scalpel surgery in the treatment of fibrous hyperplasia: a randomized clinical trial. International journal of oral and maxillofacial surgery. 2015 Nov 1;44(11):1383-9.
[10] Kumar P, Rattan V, Rai S. Comparative evaluation of healing after gingivectomy with electrocautery and laser. Journal of oral biology and craniofacial research. 2015 May 1;5(2):69-74.
[11] Azma E, Safavi N. Diode laser application in soft tissue oral surgery. Journal of lasers in medical sciences. 2013;4(4):206.
[12] Sung YT, Wu JS. The visual analogue scale for rating, ranking and paired-comparison (VAS-RRP): a new technique for psychological measurement. Behavior research methods. 2018 Aug;50:1694-715.
[13] Marini L, Rojas MA, Sahrmann P, Aghazada R, Pilloni A. Early Wound Healing Score: a system to evaluate the early healing of periodontal soft tissue wounds. Journal of periodontal & implant science. 2018 Oct;48(5):274.
[14] Gangwani KD, Shetty L, Kulkarni D, Seshagiri R, Chopra R. Piezosurgery versus conventional method alveoloplasty. Annals of Maxillofacial Surgery. 2018 Jul 1;8(2):181-7.
[15] Seifi M, Matini NS. Laser surgery of soft tissue in orthodontics: Review of the clinical trials. Journal of Lasers in Medical Sciences. 2017;8(Suppl 1):S1.
[16] Migliario M., Rizzi M., Lucchina A. G., and Renò F., Diode laser clinical efficacy and mini-invasivity in surgical exposure of impacted teeth, Journal of Craniofacial Surgery. (2016) 27, no. 8, e779–e784.
[17] Borzabadi-Farahani, A. The adjunctive soft-tissue diode laser in orthodontics. Compend. Contin. Educ. Dent. 2017, 38, e18–e31.
[18] Kokich VG, Mathews DP. Surgical and orthodontic management of impacted teeth. Dental Clinics of North America. 1993 Apr 1;37(2):181-204.
[19] Bishara SE, Ortho D. Impacted maxillary canines: a review. American journal of orthodontics and dentofacial orthopedics. 1992 Feb 1;101(2):159-71.

كشف الأنياب المنطمرة في الفك العلوي (الشدقي ضد الحنكي) بواسطة ليزر ديود (980+810) نانومتر

الاء فائز عبدالله[1,*] ، سؤدد سلمان احمد[2] ، بلسم سعدي عبدالحميد[3]

[1]وزارة الصحة ,بغداد,العراق
[2]كلية علوم فيزياء ،جامعة بغداد،بغداد،العراق
[3]اختصاص جراحه الوجه والفكين ، مستشفى الامامين الكاظمين التعليمية ،بغداد،العراق

*البريد الالكتروني للباحث: aalaa.faez2102m@ilps.upbaghdad.iq

الخلاصة

الهدف: الهدف من البحث الحالي هو كشف الأنياب المنطمرة في الشدق العلوي باستخدام ليزر الدايود (810 + 980) نانومتر في مقارنة الأنياب المنطمرة حنكياً اعتماداً على هذه العوامل (الألم، الورم، زمن الشفاء). **المقدمة**: يوفر ليزر الصمام الثنائي (810 + 980) اختراقًا عميقًا للأنسجة الرخوة وتخثر الدم وتجلط الدم بشكل ممتاز ولديه الحد الأدنى من التفاعل مع أنسجة الأسنان الصلبة.

المواد والطرق: جميع المرضى الذين يعانون من انطمار الأنياب الفكية، مثل انطمار الشدق أو الحنك، يجب أن يتم كشفهم. تم تقسيمهم إلى مجموعتين: واحدة بها سبعة مرضى في الوضع الشدقي والأخرى بها سبعة مرضى في الوضع الحنكي. كان المرضى الأصحاء في مجموعتين العلاج بالليزر ديود (980 + 810) نانوميتر. لم تسمح هذه الدراسة بإدراج المرضى الحوامل أو أي مرضى آخرين معرضين للخطر طبيًا.. تم تسجيل الألم والورم والشفاء باستخدام نتائج المتابعة في الأيام الأول والثاني والخامس وكذلك الأسبوع الأول والثاني. بعد الجراحة وفحصها إحصائيا.

النتائج: كان متوسط العمر في هذه الدراسة خمسة ذكور وتسعة إناث 26.2. تم تحديد $P \geq 0.05$ كمستوى معنوي. المرضى الذين يعانون من الأنياب المنطمرة في الشدق يشعرون بألم أقل وتورم أقل ويشفون بسرعة أكبر من المرضى الذين يعانون من الأنياب المنطمرة في الحنك .

الاستنتاج: كان المرضى الذين يعانون من الأنياب المطمورة في الشدق يعانون من ألم وتورم أقل وشفاء أسرع من المرضى الذين يعانون من الأنياب المطمورة في الحنك عند الكشف.

IJL, Issue 2, Vol. 23, 2024
https://doi.org/10.31900/ijl.v23i2.473

Research Article

Effectiveness of the Er,Cr:YSGG Laser in the Removal of Oral Plexiform Neurofibroma (Case Report)

Zainab Fadhil Odah[1,] *, Hanan Jafer Taher[1], Ammar Saleh AlAlawi[2]

[1]*Institute of Laser for Postgraduate Studies, University of Baghdad, Baghdad, Iraq*
[2]*Laser Surgery unit/Department of Maxillofacial Surgery/Al-Emamein Al-Kadhemein Medical City, Baghdad, Iraq*
* *Email address of the Corresponding Author:zainab.awda2102m@ilps.uobaghdad.edu.iq*

Article history: Received 2 Apr. 2024; Revised 2 Jul. 2024; Accepted 21 Jul. 2024; Published online 15 Dec. 2024

Abstract

Background: Plexiform neurofibroma [PN] is a non-malignant tumor that affects the peripheral nerve sheath and is associated with neurofibromatosis type 1 [NF1.1]. Because they are infiltrative, plexiform neurofibromas can be difficult to cure. Laser therapy has emerged as a potentially effective approach for the management of oral plexiform neurofibromas, rendering it a valuable diagnostic tool within the field of dentistry.
Case Study Presentation: A male patient, aged 60, diagnosed with NF1, presented with painless swellings of the mandibular left edentulous alveolar ridge, which was causing difficulty in wearing a denture. The tumor was diagnosed as an oral plexiform neurofibroma. The entire lesion was excised surgically using an Er,Cr:YSGG laser system with specific parameters to minimize thermal damage to the surrounding tissues. Histological analysis confirmed the diagnosis of plexiform neurofibroma, with minimal thermal damage and desiccation observed at the excision margin.
Conclusion: The utilization of the Er,Cr:YSGG laser [2780 nm] for excision biopsy of plexiform neurofibroma led to exceptional postoperative healing and minimal thermal damage to the tissue. The laser's ability to precisely ablate the target tissue while minimizing damage to the surrounding structures was crucial in preserving the integrity of the specimen for histopathological analysis.

Keywords: neurofibromatosis type 1; plexiform neurofibroma; Er,Cr:YSGG laser; thermal damage; carbonization; desiccation.

1. Introduction

Neurofibromas can be classified into two main groups by the World Health Organization (WHO): dermal and plexiform. Whereas plexiform neurofibromas are linked to several nerve bundles, dermal neurofibromas originate from a single peripheral nerve. Additional subtypes identified by clinicopathology are plexiform neurofibroma, diffuse neurofibroma, epithelioid neurofibroma, and localized neurofibroma (also known as sporadic neurofibroma).[1]
A plexiform neurofibroma also known as pachydermatocoele (PN/P), is a benign tumor that affects the peripheral nerve sheath and consists of many nerve fascicles. It is a diagnostic criterion for

neurofibromatosis type 1 [NF1] and a histological variant of neurofibroma. The likelihood of plexiform neurofibroma progressing into a malignant peripheral nerve sheath tumor is highly potential [2].
Plexiform neurofibroma is a diffuse, elongated fibroma that runs along the nerves. It primarily affects the upper cervical or trigeminal nerves and is characterized by an early-life overgrowth of subcutaneous and epidermal tissue that gives the appearance of wrinkles and pendulous tissue. [1]
The growth of this benign tumor is gradual, and it is invading the adjacent tissue along the nerves. The growth of Schwann cells on the inner side of the nerve sheath is what makes plexiform neurofibroma unique. These cells cause the lesion to become thicker, twist, and turn in strange ways.[3]
NF1, also known as Von Recklinghausen's illness of the skin, is considered to be a definitive indicator of the presence of PN. Although oral lesions are present in around 72% of NF1 patients, the literature has extensively documented only a limited number of these instances. Some common radiologic signs are an enlargement of the mandibular foramen and/or canal, a rise in bone density, the presence of a deep coronoid notch, a depression on the medial side of the ramus, and more than one radiolucency.[4]

Various surgical techniques, including the traditional scalpel, Cryotherapy, electrosurgical scalpel, or lasers, can be used to remove this type of lesion[5]. The field of dentistry extensively utilizes dental lasers across various domains[6]. Lasers are used as very effective scalpels for the excision of maxillofacial tumors with maximal salvage to the surrounding tissues, and they are regarded as standard tools of therapy and care for both patients and surgeons[7]. The interaction of various irradiation parameters, including the laser source's wavelength, the physical characteristics of the exposed tissue, the energy of the laser pulse, continuous wave (CW) or pulsed irradiation, the size of the laser beam on the tissue, the duration of the laser pulse, and the repetition rate, determines the effects and interactions of the laser on tissue[8].
Dentists favor dental lasers due to their hemostatic, antibacterial, decontaminating, and tissue-ablating characteristics. Erbium, chromium: yttrium-scandium-gallium-garnet [Er,Cr:YSGG] lasers are utilized by dental practitioners for a diverse array of applications [9]. The versatility of this treatment enables the treatment of both soft tissues and hard tissues, such as bone, dentin, and enamel. The Er,Cr:YSGG laser employs water on the surface of the tissue to generate a clear, gentle, and uniform ablation, enabling highly accurate cutting. Reports indicate that the utilization of Er,Cr:YSGG lasers results in minimal or negligible harm to tissue, hence expediting the process of wound healing. Additionally, it achieves exceptional hemostasis, minimizes postoperative swelling and pain, requires minimal suturing, sterilizes the surgical site, and enhances patient acceptance and satisfaction.[10,11]

In this paper, we report a case of oral plexiform neurofibroma associated with NF1.

2. Case presentation

A 60-year-old male patient visited the laser medical research clinics of the Institute of Laser for Postgraduate Studies at the University of Baghdad. He sought dental care to remove painless swelling in the mandibular left edentulous alveolar ridge, which was causing difficulty in placing a denture [Figure 1]. Upon questioning the patient's medical background, he revealed that the onset of swelling had started disrupting the functionality of his denture approximately one year ago, showed a rapid enlargement within a span of less than two months, and persisted. The swelling exhibited a growing pattern, devoid of any concurrent pain or hemorrhage. The patient possessed a medical background of type I neurofibromatosis, characterized by the presence of several small tumors dispersed throughout the body. Furthermore, the history revealed a familial background. The intraoral examination demonstrated the presence of a non-ulcerated, widespread, unilateral swelling in the mandibular left edentulous alveolar ridge, which was found to be sessile. The swelling was devoid of discomfort. It had a diameter of around 10 mm and was solid when touched. Initial diagnosis of oral neurofibroma was established and scheduled the complete removal of the lesion using laser technology. The patient provided informed written consent before the excision procedure. The local ethics committee approved the research and conducted it in accordance with the ethical guidelines outlined in the 1964 Declaration of Helsinki and its subsequent revisions. Following the administration of 2% lidocaine and a 1:80,000 adrenaline dosage, the entire lesion was removed from its base, along with 2mm of healthy tissue, in order to distinguish between the healthy and diseased tissue.

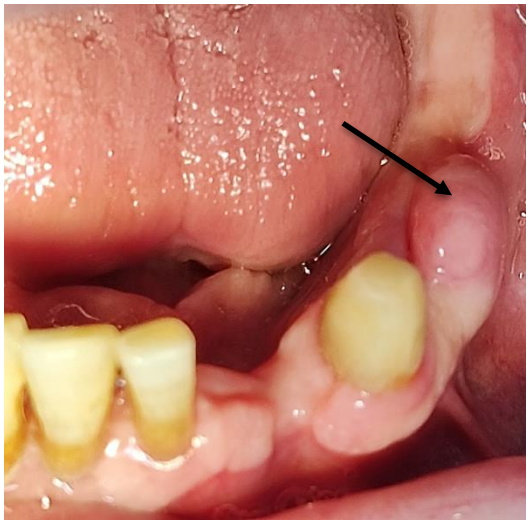

Fig. 1: Oral Plexiform Neurofibroma.

The excision was performed using the Er,Cr:YSGG laser system [Waterlase iplus, Biolase, California, USA] with the following specifications: a wavelength of 2780nm, a power of 2.75 W, a pulse repetition rate of 75 Hz, air at 20%, and water at 40%. The MGG6 tip in H mode was used in contact with the oral lesion. The duration of the treatment is around 10 minutes.
These laser parameters were selected based on the settings offered by the manufacturer, which correspond to other studies dealing with oral benign soft tissue lesions.

Ultimately, coagulation was accomplished by utilizing a laser bandage with a power output of 0.5 W, a frequency of 30 Hz, 1/20% water/air spray, and a non-contact mode for the tip [Figure 2]. The wound following the surgical intervention underwent secondary healing. Following quick fixation in a 10% formalin solution, the excision biopsy was subsequently subjected to histological investigation in order to determine the nature of the lesions. The analysis revealed the presence of an oral plexiform neurofibroma, along with indications of thermal damage and desiccation at the margin of the excision.

Fig. 2. Immediately after removal of the lesion.

Thermal damage was measured in millimeters and found it to be 0.2 mm. Desiccation was observed, but carbonization did not. The patient was recalled on days 1, 3, and 7 to assess the healing progress, and found no problems. By day 7 after the surgery, the lesion had fully healed [Figure 3]. Additionally, the patient received a referral for further prosthetic management.

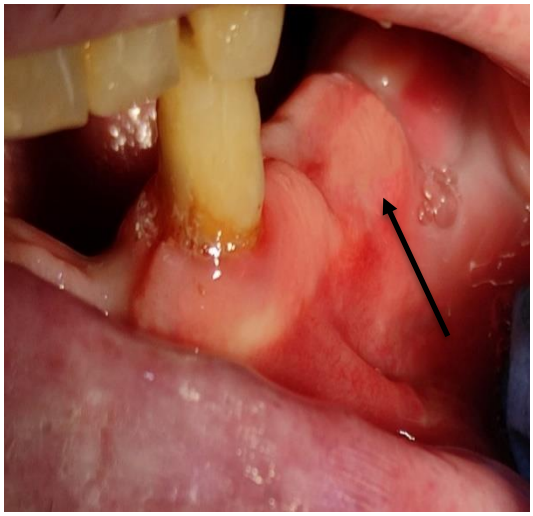

Fig. 3. 7 days post-operatively.

3. Discussion

Neurofibromatosis type 1 is an autosomal dominant condition affecting several organ systems with a diverse array of clinical presentations. It is one of three illnesses grouped together under the general term "neurofibromatoses." The other two, schwannomatosis and neurofibromatosis type 2, differ from neurofibromatosis type 1 both clinically and genetically. The neurofibroma - a nerve sheath tumor that develops in close proximity to spinal, peripheral, or cranial nerves - is the characteristic that distinguishes neurofibromatosis type 1[12].

Pathogenic variations in the NF1 gene lead to the loss of functional neurofibromin, which is the cause of NF1. NF1 is mainly characterized by the presence of pigmented lesions, such as cafe-au-last spots, two or more neurofibromas of any type, or one or more plexiform neurofibromas, Freckling in the axillae or groin, Optic glioma, two or more Lisch nodules, dysplasia of the sphenoid, dysplasia or thinning of the long bone cortex, first-degree relative with NF1[13].

The preferred treatment for plexiform neurofibroma is surgical excision. However, achieving total resection can be challenging due to the tumor's infiltrative features. The tumor may become intertwined with nearby tissues and nerves, making complete removal difficult and potentially resulting in a recurrence[13].

In this current study, the patient had an overgrowth on his mandibular left edentulous alveolar ridge. Possible treatment options for PN encompass the traditional scalpel, electrocautery, and laser therapy.

Lasers can cause thermal damage to tissues. However, by carefully adjusting variables such as power output, type of optic fiber, emission modes, and wavelength, it is possible to reduce or eliminate these effects on the target and surrounding tissues. It is important to consider emission modalities, particularly continuous wave [CW] or pulsed emission. Clinicians should consistently choose pulsed emission, as it permits the residual tissue to cool prior to the subsequent laser energy pulse. This process serves the purpose of controlling tissue overheating. In order to achieve the desired therapeutic effect with the shortest possible irradiation period, it is necessary to minimize the heat impact on tissues[14,15].

Amaral et al. [2018] [15] examine a case of a 44-year-old female patient diagnosed with neurofibromatosis type 1 [NF1]. The patient exhibited the presence of intraoral neurofibromas, specifically localized on the tongue. A surgical laser with a high-power diode and a wavelength of 808 nm was employed to remove a

neurofibroma from the patient's tongue. The technique yielded negligible hemorrhaging, and sutures were unnecessary.

Furthermore, in 2020, a single neurofibroma located in the gingiva was surgically removed utilizing a diode laser operating at a wavelength of 940nm and a power of 3 W. The patient exhibited consistent recovery over a period of six months, without any reoccurrence[16].

In 2024, a case report describes a 73-year-old male patient with a solitary, non-syndromic plexiform neurofibroma at the upper anterior alveolar ridge, the lesion was successfully removed using a 940 nm diode laser, with good precision, little bleeding, and a positive postoperative healing[17].

The Er,Cr;YSGG laser readily absorbs water and does minimal damage to adjacent tissues, especially the underlying muscle layers. A limited amount of tissue stress has a role in facilitating a positive healing process after surgery, which is characterized by the production of minimal scars[18].

Studies have indicated that the utilization of the Er,Cr:YSGG laser in surgical procedures yields superior outcomes in terms of postoperative wound healing compared to alternative laser technologies. Patients who undergo surgery with Er,Cr:YSGG lasers report a significant decrease in their recovery time. In light of these conditions, the question arises as to how improved or equivalent healing outcomes can be achieved following an intervention that involves thermal injury. Previous studies have provided evidence that low-level laser treatments can effectively suppress anti-inflammatory mechanisms, promote cellular stimulation, expedite tissue regeneration, enhance wound healing, and reduce pain and edema. From a certain standpoint, when considering the potential improvement in healing after a thermal injury, it appears that the application of laser surgery can have a beneficial impact on neighboring tissues. This is likely to accelerate the healing process by inhibiting the inflammatory pathway and promoting regeneration through mechanisms such as angiogenesis, collagen deposition, fibroblast proliferation, and tissue re-epithelialization.[19] In comparison with our study, we also found that the healing progression with the Er,Cr,YSGG laser is favorable and more eventful.

Sarkar et al. reported that treatment with Er,Cr:YSGG laser results in little patient discomfort, no need for anesthesia, minimum bleeding, and good wound healing[20].

The Er,Cr:YSGG laser has a sterilizing effect since it eliminates many bacterial and viral colonies that could potentially cause infection. This contributes to faster recovery time[21]. The laser management on the first day of wound development increases the number of polymorphonuclear neutrophils and mast cells, which accelerates healing[19].

Tissues subjected to irradiation consistently exhibit thermal damage as a result of the photothermal effects. When a laser beam is incident, there is a notable rise in temperature over 100°C, leading to the vaporization of tissue. The temperature in this region has risen by more than 50°C. In the field of oral pathology, it is crucial to minimize peripheral damage, particularly in cases with suspicious lesions, in order to preserve the integrity and legibility of the specimen's edges.[22] This work demonstrates the safe utilization of the Er,Cr;YSGG laser in oral biopsy operations, specifically when employing controlled power levels and fluence regulation.

This current case did not exhibit carbonization, either at the macroscopic or microscopic level. This is attributed to the utilization of air/water spray with an Er,Cr;YSGG laser.

A scholarly publication in 2010 entitled " Histologic evaluation of thermal damage produced on soft tissues by CO 2, Er,Cr:YSGG and diode lasers"[23] examined the thermal impacts of various laser types on soft tissues. The samples of Er,Cr:YSGG that were subjected to irradiation using a water/air spray exhibited a carbonization area that was less than 25% of the perimeter of the irradiation margin. Significant differences were seen when comparing individuals exposed to water/air spray irradiation to those who were not, indicating a moderate carbonization area.

Conversely, we observed the presence of desiccation in the form of a highly eosinophilic layer along the excision margin [Figure 4]. Desiccation occurs due to the photothermal impact of a laser[24]. The use of Er,Cr;YSGG laser [2780 nm] with 2.75 W output power in pulsed wave mode, a pulse duration of 60 μs, and a 600 μm fiber tip showed optimal results for excising a plexiform neurofibroma associated with NF1, showing minimal damage to the tissue, and protecting the tissue for an adequate histopathological analysis.

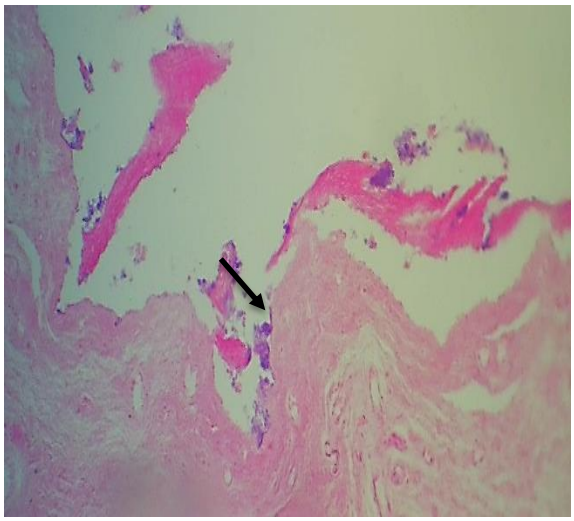

Fig. 4: Cross-sectional histological view of plexiform neurofibroma 10x showing the marginal desiccation.

References

[1] Aldelaimi TN. Massive Pediatric Facial Plexiform Neurofibromatosis in Iraq. J Dent Oral Disord Ther. 2013;1(1):13

[2] Wu YH, Wang YP, Sun A, Chang JYF. Oral plexiform neurofibroma. Vol. 11, Journal of Dental Sciences. Association for Dental Sciences of the Republic of China; 2016. p. 468–9 .

[3] Khetrapal S, Jairajpuri Z, Rana S, Pujani M, Jetley S. Plexiform Neurofibroma: An Unusual Diagnosis of Lip Swellings. IJSS Case Reports Rev [Internet]. 2015;12. Available from: www.ijsscr.com

[4] Zwane NP, Noffke CEE, Raubenheimer EJ. Solitary oral plexiform neurofibroma: Review of literature and report of a case. Oral Oncol [Internet]. 2011;47[6]:449–51. Available from: http://dx.doi.org/10.1016/j.oraloncology.2011.04.005

[5] Gholizadeh N, Taheri JB, Namazi Z, Mashhadiabbas F, Bakhtiari S, Rahimzamani A, et al. Excision of Different Oral Benign Exophytic Lesions With a Diode Laser: A Clinical Case Series. J Lasers Med Sci 2020;11(4):502–8.

[6] Al-Karadaghi TS, Franzen R, Jawad HA, Gutknecht N. Investigations of radicular dentin permeability and ultrastructural changes after irradiation with Er, Cr: YSGG laser and dual wavelength (2780 and 940 nm) laser. Lasers Med Sci. 2015Nov;30:2115-21.

[7] Aldelaimi AA, Enezei HH, Aldelaimi TN, Mohammed KA. Tumors of craniofacial region in Iraq (clinicopathological study). J Res Med Dent Sci. 2021 Feb;9(1):66-71.

[8] Al-Alawi AS. The effectiveness of Diode Laser 810 nm in the removal of oral pyogenic granuloma in repetitive pulsed mode. Iraqi JMS. 2017; Vol. 15(3): 262-267.

[9] Rasheed SS, Jawad HA. Smear Layer Removal from the Apical Third Using the Er, Cr: YSGG Photon-induced Photoacoustic Streaming. Iran Endod J. 2021;16(4):238.

[10] Tunc SK, Yayli NZ, Talmac AC, Feslihan E, Akbal D. Clinical comparison of the use of er, cr: Ysgg and diode lasers in second stage implant surgery. Saudi Med J. 2019;40[5]:490–8 .

[11] Al-Ani AJ, Al-Alawi AS, Taher HJ. Analysis of the Temperature Elevation of the Dual-Wavelength Diode Laser and the Er, Cr: YSGG Laser in Oral Soft Tissue Incisions. J Lasers Med Sci. 2023;14 .

[12] Gutmann DH, Ferner RE, Listernick RH, Korf BR, Wolters PL, Johnson KJ. Neurofibromatosis type 1. Nature Reviews Disease Primers. 2017 Feb 23;3(1):1-7 .

[13] Armstrong AE, Belzberg AJ, Crawford JR, Hirbe AC, Wang ZJ. Treatment decisions and the use of MEK inhibitors for children with neurofibromatosis type 1-related plexiform neurofibromas. Vol. 23, BMC Cancer. BioMed Central Ltd; 2023 .

[14] Cercadillo-Ibarguren I, España-Tost A, Arnabat-Domínguez J, Valmaseda-Castellón E, Berini-Aytés L, Gay-Escoda C. Histologic evaluation of thermal damage produced on soft tissues by CO 2, Er,Cr:YSGG and diode lasers. Med Oral Patol Oral Cir Bucal. 2010 Nov;15 .[6]
[15] Amaral FR, Ferreira MVL, Costa LAP, de Oliveira PAD, Soares BM, Souza PEA, et al. Use of surgical laser for excision of a neurofibroma associated with neurofibromatosis type-1. J Lasers Med Sci. 2018;9[3]:219–22 .
[16]]Ravindran DM, Ravi S, Santhanakrishnan M, SK B. LASER Assisted Excision of Solitary Neurofibroma in the Gingiva. Cureus. 2020 Feb 28 ;
[17] Al-Ali MM, Al-Otaibi LM, Al-Bakr I, AlALi MM, AlOtaibi LM, AlBakr I. Excision of Solitary Non-syndromic Oral Plexiform Neurofibroma Utilizing a Diode Laser: A Case Report. Cureus. 2024 Feb 29;16.(2)
[18] Tandon S, Lamba AK, Faraz F, Chawla K. Treatment of Pyogenic Granuloma using Er,Cr:YSGG Laser. Int J Laser Dent. 2013 Apr;3[1]:29–32 .
[19] Eroglu CN, Tunç SK, Elasan S. Removal of Epulis Fissuratum by Er,Cr:YSGG Laser in Comparison with the Conventional Method. Photomed Laser Surg. 2015;33[11]:533–9 .
[20] Sarkar S, Kailasam S, Hari Iyer V. Effectiveness of Er,Cr:YSGG Laser in the Excision of different Oral Soft Tissue Lesions. J Indian Acad Oral Med Radiol 2013;25:10–2.
[21]]Tuppili M, Babu B, Uppada UK, Naagmega S, Amirisetty R. Erbium,Chromium:Yttrium-Scandium-Gallium-Garnet Laser-assisted Excision of Peripheral Giant Cell Granuloma. Int J Laser Dent 2014;4(2):54–8.
[22] Romeo U, Libotte F, Palaia G, Del Vecchio A, Tenore G, Visca P, et al. Histological in vitro evaluation of the effects of Er:YAG laser on oral soft tissues. Lasers Med Sci. 2012 Jul;27[4]:749–53 .
[23] Cercadillo-Ibarguren I, España-Tost A, Arnabat-Domínguez J, Valmaseda-Castellón E, Berini-Aytés L, Gay-Escoda C. Histologic evaluation of thermal damage produced on soft tissues by CO 2, Er,Cr:YSGG and diode lasers. Med Oral Patol Oral Cir Bucal. 2010;15[6]:912–8 .
[24] Lukač M, Košir J, Žel T, Kažič M, Šavli D, Jezeršek M. Influence of tissue desiccation on critical temperature for thermal damage during Er:YAG laser skin treatments. Lasers Surg Med. 2024;56[1]:107–18.

فعالية ليزر الاربيوم كروميوم في إزالة الورم الليفي العصبي الضفري الفموي

زينب فاضل عودة [1]، حنان جعفر طاهر [1] ، عمار صالح العلوي[2]

[1]معهد الليزر للدراسات العليا، جامعة بغداد، بغداد، العراق
[2]وحدة الجراحة بالليزر/قسم جراحة الوجه والفكين/مدينة الامامين الكاظمين الطبية/جامعة بغداد، بغداد، العراق.

*البريد الالكتروني للباحث: zainab.awda2102m@ilps.uobaghdad.edu.iq

الخلاصة

الخلفية: الورم الليفي العصبي الضفري [PN] هو ورم غير خبيث يؤثر على غمد الأعصاب الطرفية ويرتبط مع الورم الليفي العصبي من النوع 1 .[NF1.1] وقد ظهر العلاج بالليزر كنهج فعال محتمل لإدارة الأورام الليفية العصبية الضليعية الفموية، مما يجعلها أداة تشخيصية قيمة في مجال طب الأسنان.

عرض دراسة حالة: مريض ذكر، يبلغ من العمر 60 عامًا، تم تشخيصه بالإصابة بالورم الليفي العصبي من النوع الاول، أظهر تورمًا غير مؤلم في الحافة السنخية اليسرى للفك السفلي. قمنا بتشخيص الورم على أنه ورم ليفي عصبي ضفيري فموي واستأصلناه جراحياً باستخدام نظام ليزر .Er, Cr:YSGG تسبب هذا الإجراء في أضرار حرارية طفيفة وأدى إلى الشفاء الناجح بعد الجراحة.

الاستنتاج: استخدام ليزر Er,Cr:YSGG [2780 نانومتر] لخزعة استئصال الورم الليفي العصبي الضفيري أدى إلى شفاء استثنائي بعد الجراحة، والحد الأدنى من الضرر الحراري للأنسجة، والتوصيف النسيجي للورم الليفي العصبي الضفيري.

IJL, Issue 2, Vol. 23, 2024
https://doi.org/10.31900/ijl.v23i2.478

Research Article

Evaluation of Anti-Cancer Activity of Silver@Gold Nanoparticles by Hybrid Technique

Zainab Shaheed Kadhim, Haider Y. Hammod*

Department of Physics, College of Science for Women, University of Baghdad, Iraq
** Email address of the Corresponding Author:dr.hayder.y.phy@gmail.com*

Article history: Received 23 May 2024; Revised 20 Jul. 2024; Accepted 1 Aug. 2024; Published online 15 Dec. 2024

Abstract: This research deals with the evaluation of the anti-cancer activity of Ag@Au NPs synthesis by a hybrid system combining laser and plasma jet techniques. The effect of NPs on inhibiting the growth of breast cancer cells and normal cell lines was studied. Firstly, silver nanoparticles were prepared using a Nd:YAG laser with a wavelength of 1064 nm, a frequency of 6 Hz, an energy of 1000 mJ, and a number of pulses of 558. In the second step, we take different ratios between Ag NPs and gold salts as follows: (1:9, 2:8, and 3:7), respectively, and exposed to a plasma jet system for 3 minutes. The NPs were checked using X-ray diffraction, UV-vis spectroscopy, and field emission scanning electron microscopy (FE-SEM). The highest rate of inhibition of breast cancer cells was 66% after 48 hours when the concentration was 100% with a ratio of 3:7. As for its toxicity to normal cells, the highest toxicity was 16% after 24 hours when the concentration was 100% for 3:7. The expected results could provide new light on the effectiveness of these particles in treating cancer and stimulate future research in this field.

Keywords: Hybrid system, laser ablation, plasma jet, anticancer.

1. Introduction

Nanotechnology is the study and application of materials with sizes as small as 100 nanometers (nm). They are employed in a wide range of industries, including agriculture, food processing, material science, cosmetics, medicine, and diagnostics. Nano-sized inorganic compounds have demonstrated remarkable antibacterial activity at extremely low concentrations because of their high surface area-to-volume ratio and distinctive physical and chemical properties [1]. There are three primary methods available for producing nanoparticles: chemical, physical, and biological approaches [2].

Noble metal nanoparticles, such as gold and silver, are highly sought after due to their distinct optical, chemical, physical, and electrical properties. Au and Ag nanoparticles both demonstrate a plasmonic effect due to the scattering and absorption of light. Au nanoparticles (NPs) and Ag nanoparticles (NPs) exhibit insensitivity to physical variables such as light, air, electrical characteristics associated with size, magnetic properties, exceptional conductivity, and chemical stability [3].

The production of metal oxide and metal nanoparticles can be achieved by a straightforward method called Pulsed Laser Ablation in liquid environments (PLAL).The laser ablation process is significantly influenced by the specific properties of the laser beam employed, such as the number of pulses, wavelength, pulse duration, and energy. The ablation rate is directly proportional to the number of laser pulses, which is particularly evident in the case of dielectrics, semiconductors, and single metals [4]. PLAL offers a multitude of desirable advantages. This methodology is a direct and effective method for generating a large number of nanoparticles that are evenly dispersed in a liquid medium [5].

Plasma, often known as the fourth state of matter, is a plasma consisting of charged and neutral particles that interact together. Plasma encompasses gaseous nebulae, the interiors of stars, atmospheres, and interstellar hydrogen. Plasma consists of negatively charged electrons and positively charged ions of atoms, and it constitutes approximately 99% of all matter in the universe [6]. Plasma is often a gas that has been ionized. The process involves the aggregation of charged particles, including electrons, ions, and molecules. The term "ionized" refers to the presence of one or more free electrons [7].

Cancer encompasses a wide range of diseases, including liver, stomach, lung, bladder, colon, and breast cancers, which are the most prevalent. Given its prevalence among women, this study specifically targets breast cancer as opposed to other types of cancer. The expansion of breast cancer involves the activation or inactivation of several gene types that are necessary for promoting malignancy. While breast cancer is mainly a genetic disease affecting somatic cells, there are instances where it is associated with genetic disorders. Breast cancer is categorized as a metastatic neoplasm. It usually manifests in the axillary lymph nodes, but it can also metastasize to any location in the skeletal system or bone marrow [8].

In this study, the aim was to prepare Ag@Au nanoparticles using a hybrid system (laser-plasma jet) and test their inhibition on breast cancer and normal cells.

2. Experimental Procedures

2.1 synthesis of nanoparticles

2.1.1 Prepared Ag NPs using Nd:YAG system as a core

Using the pulsed laser ablation technique, Ag NPs were created in liquid (PLAL) and a pure silver plate (0.5×0.5) cm with a purity of 99.99%. They were then 5 ml of deionized water put in a 10–20 ml glass beaker and 5 cm away from the laser source. The laser source was a Q-switched Nd:YAG laser with a frequency of 6 Hz, wavelength of 1064 nm, and energy of 1000 mJ. As seen in Fig.1 (A).

(A) **(B)**

Fig.1. The prepared Ag@Au NPs by a hybrid system (A) Nd:YAG laser (B) plasma jet.

2.1.2 Prepared Au NPs using plasma jet as a shell

The (AuCl4•3H2O) hydrogen tetrachloroaurate trihydrate, which has a partial weight of 393.83 g/mol, a purity of ≥ 99.9%, and a concentration of 0.5 mM, has been prepared as a shell. The required weight is calculated using the following equation (1) [9]:

$$Concentration\left(\frac{mol}{liter}\right) = \frac{mass(g)}{Molecular\ weight\ \left(\frac{g}{mol}\right) * Volume\ (liter)} \qquad (1)$$

2.1.3 Prepared Ag@Au NPs

A cylindrical metal tube with a diameter of 1 mm is securely fastened in a vertical position by the catcher. With the plasma jet technique, the length of the plasma between the two electrodes was 1 cm, the flow meter was 3 liters/minute, the voltage was 20 kV, and the gas used was argon.
After that, we added Ag NPs prepared by the Nd:YAG method, as shown in Fig.2(a) to gold salts in the following ratios: (1:9, 2:8, and 3:7), respectively. The mixture was then exposed to the plasma system for 3 minutes until the color of the solution turned violet.

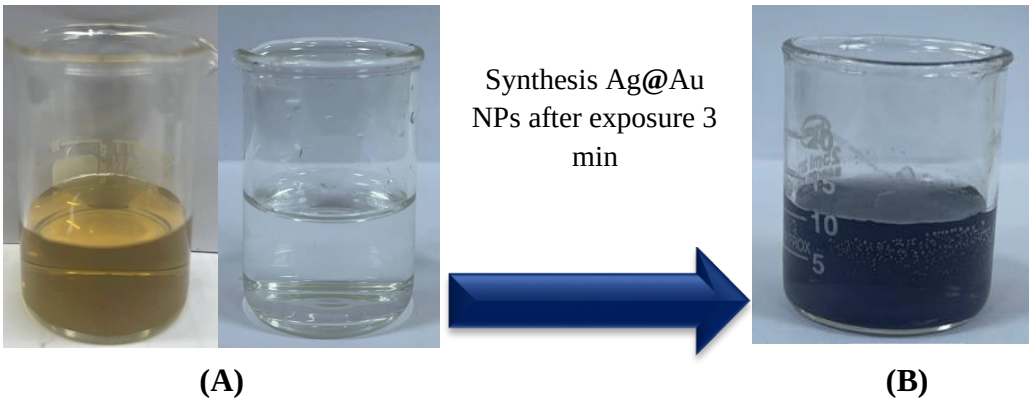

Fig.2. Preparation Ag@Au NPs (A) Ag NPs by Nd:YAG and gold salts (B) Ag@Au NPs by plasma jet.

2.2 The impact of prepared nanoparticles on breast cancer cells

This study utilized cell lines derived from cancer patients. The research utilized 96 (12×8) microtiter plates for tissue culture, with each plate being seeded with 10,000 cells. The cells were subsequently incubated at a temperature of 37 °C for a duration of 24 hours to form a monolayer, as confirmed by the use of an inverted microscope. In addition, a solution containing diluted silver nanoparticles (Ag NPs) and gold nanoparticles (Au NPs) is administered to the cells, whereas no treatment is given to the control wells. The indicated stages have been performed three times, following which they were subjected to re-incubation at a temperature of 37 °C. The growth medium was poured out after 48 hours of incubation. The methods were repeated three times to verify the authenticity, employing a 50µl crystal violet assay, followed by an incubation period of 20 minutes. The cells were observed using an inverted microscope, captured with a digital camera, and recorded individually to obtain the data. The results of the experiment are analyzed using Graph Pad Prism version 8 [9].

3. Results and Discussion

The reaction process causes the solutions' hue to change, which is connected to the creation of metal nanoparticles (NPs) made using the Ar jet technique and the metal salts' prepared solutions. The color shift gives the first hint regarding the formation of NPs during mixing in metal salt solutions. Metal particles take on their non-metal color due to surface plasmon resonance (SPR), which happens when a metal's particle diameter becomes close to a nanometer, as in the case of gold and silver. Thus, the spectrum analysis equipment has been applied at visible light wavelengths to prove the NPs formation. The ultraviolet-visible absorption spectra connected to colloidal Ag@Au NPs at different ratios (1:9, 2:8, and 3:7), and compare results (Ag NPs) only and at visible light wavelengths (590, 598,608) nm, respectively. In the ultraviolet-visible spectrum of Ag NPs when exposed to Nd:YAG laser, the sharp peak is at about 415 nm. As a varied Ag@Au NPs ratio, the UV-visible absorption spectra of colloidal Ag@Au NPs are shown in Figure 3.

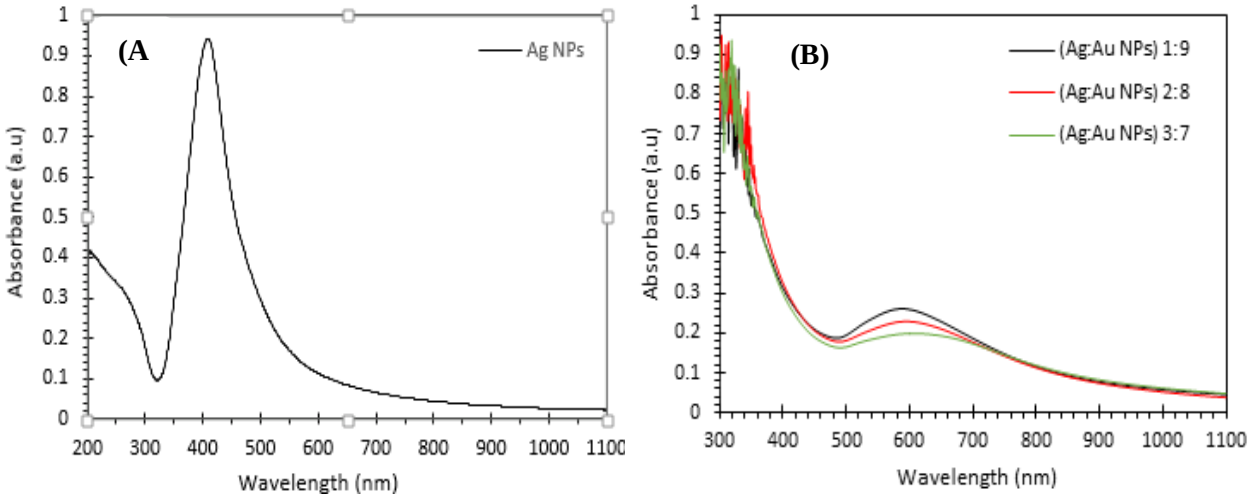

Fig. 3. UV-visible absorption spectrum of NPs prepared using hybrid (laser-plasma) system as a different ratios functions: (A) Ag NPs (B) Ag@Au NPs.

3.1 X-Ray Diffraction (XRD)

The dried Ag NPs produced by the pulse laser system were placed on a hot plate at 30°C. Figure.4 (A) shows the XRD Ag NPs spectrum, the peaks at angles of (38.29, 44.44, 64.56, and 77.64) correspond to (111), (200), (220), and (311) planes of Ag. The XRD analysis of Ag@Au NPs using a plasma jet revealed several Bragg reflection peaks at specific 2-theta values (38.12°, 44.3°, 46.21°, 54.83°, 64.42°, and 77.45°). These peaks correspond to the (111), (200), (231), (142), (220), and (311) planes of pure silver, as determined by the face-centered cubic structure, as shown in the Figure.4 (B). The aforementioned pattern has demonstrated that peaks' diffraction patterns cannot be replicated in other kinds of material, proving the prepared sample's purity and lack of additional impurities [10]. The crystal size of silver nanoparticles is 45 nm, and the crystal sizes of Ag@Au NPs for the following ratios (1:9, 2:8, 3:7) are (45, 48, and 17) nm, respectively, using the Debye-Scherer equation (2) [11].

$$D = \frac{k\lambda}{\beta \cos\theta} \qquad (2)$$

Where D is the crystallite size, k is the Scherer's constant (k = 0.9), λ for X-ray wavelength, and β for full width at half maximum (FWHM) of the peaks at the θ diffracting angle relative to Bragg's angle position.

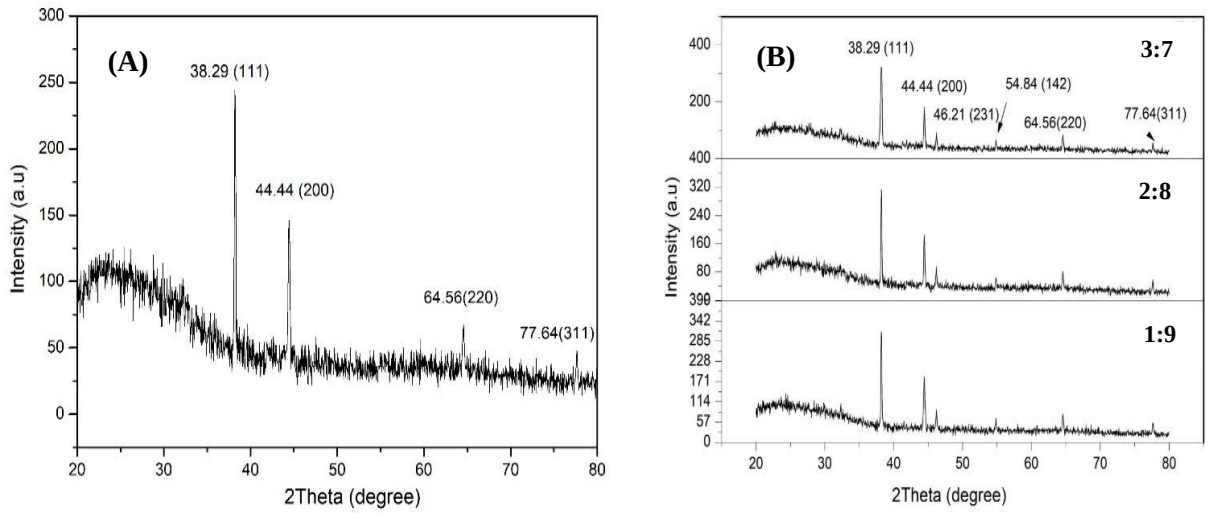

Fig.4. X-ray patterns of NPs prepared using a hybrid (laser-plasma) system as different ratios functions: (A) Ag NPs (B) Ag@Au NPs.

3.2 Field Emission Scanning Electron Microscopy Study (FE-SEM)

FE-SEM images show the morphological properties of Ag NPs and Ag@Au NPs synthesized with a plasma jet (see Figure 5).

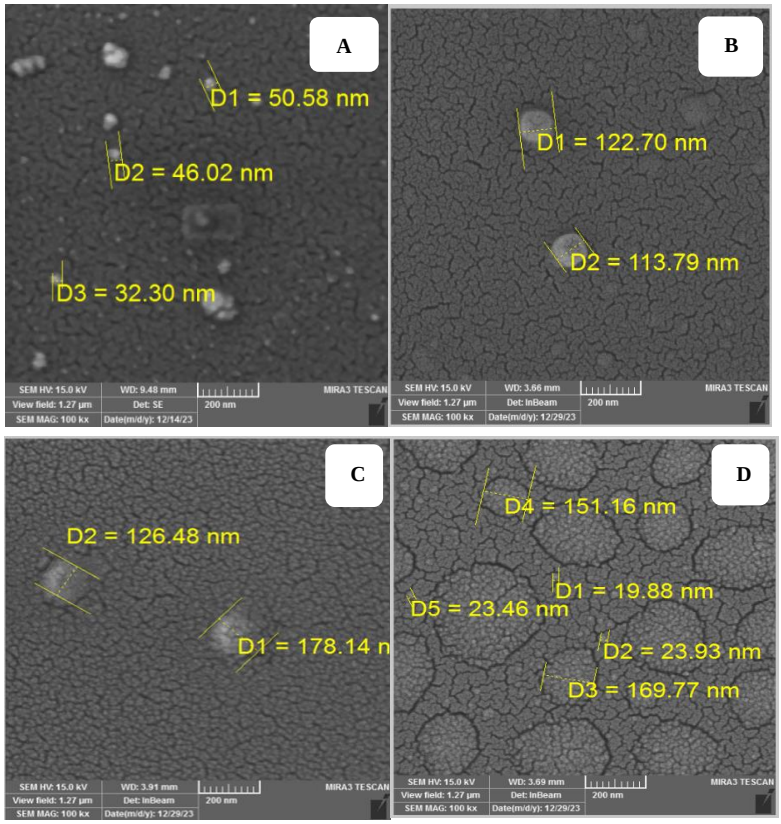

Fig.5. FE-SEM pictures of the colloidal nanoparticles: (A) Ag NPs (B) Ag@Au NPs 1:9 (C) Ag@Au NPs 2:8 (D) Ag@Au NPs 3:7.

Figure 5 (a) displays a well-dispersed picture of Ag NPs with a spherical shape and sizes ranging from 32 to 50 nm. The images revealed highly agglomerated spherical Ag@Au NPs in the sample, as determined by FESEM. It is likely that chemical processes or pre-experimental conditions led the spherical particles to cluster together and form agglomerated formations. This can occur due to forces between particles such as superposition and surface cross-linking. Agglomerated nanoparticles provided a significant benefit in preparation since they could influence the physical and chemical properties of the particles. It may result in an increase in particle interface area, leading to better surface interactions and performance.

3.3Transmission Electron Microscopy (TEM)

The synthesis of core/shell nanoparticles was confirmed using transmission electron microscopy (TEM) analysis utilizing the hybrid method was employed because of its capability to accurately determine the thickness and distance between the core and shells. TEM analysis provided further data regarding the morphology, dimensions, and clustering of the particles. The transmission electron microscopy (TEM) images reveal that the Ag@Au NPs exhibit a configuration of interlocking spheres, forming dense clusters. It is noteworthy that not all ratios demonstrate the synthesis of core/shell structures, particularly the 1:9 ratio. The reason for this is that the proportion of silver particles is significantly smaller than that of gold particles. Additionally, gold ions have the ability to reduce silver on their surface due to the electrical disparity. This prevents the formation of a silver core that is coated with a layer of gold, as depicted in Figure 6.

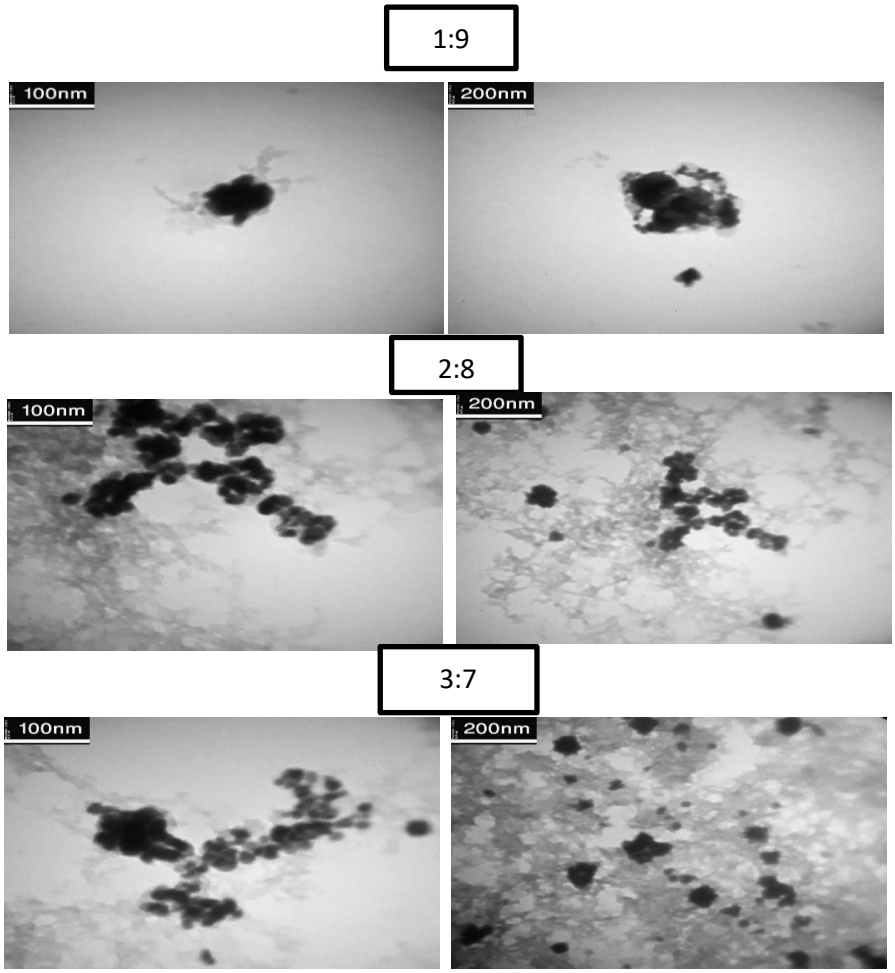

Fig.6. TEM image of Ag@Au NPs by the hybrid system.

Furthermore, TEM examination revealed the presence of two distinct zones. The core is represented by the dark inner area, while the light part around the dark region represents the shell. This confirms the synthesis of core/shell nanoparticles at the ratios of 2:8 and 3:7.

3.4 Cytotoxicity Assay

The cytotoxicity of the various series with Ag@Au NPs at different ratios has been evaluated in vitro using the normal cell line (REF) and the breast cancer cell line (MDA) after exposure for 24 and 48 hours. As shown in Fig.6 (A) and (B), respectively, the greatest rate of destruction for the breast cancer cell line (MDA) was 55% after 24 hours when the concentration of core-shell nanoparticles was 100% for 3:7 , and the greatest rate was 63% after 48 hours for 3:7. According to Fig.7 (A) and (B), for the normal cell line (REF), the highest toxicity was 16% after 24 hours when the concentration of core-shell nanoparticles was 100% for 3:7, and the lowest toxicity was 5.6% when the concentration was 12.5% for 1:9. Similarly, for the 48-hour period, the highest toxicity was 21% when the concentration was 100% for 2:8 and 3:7, and the lowest toxicity was 7% when the concentration was 12.5% for 1:9, which stars means [(*) refer ($p \leq 0.05$), (**) refer ($p \leq 0.01$), (***) refer ($p \leq 0.001$), and (****) refer ($p \leq 0.0001$)].

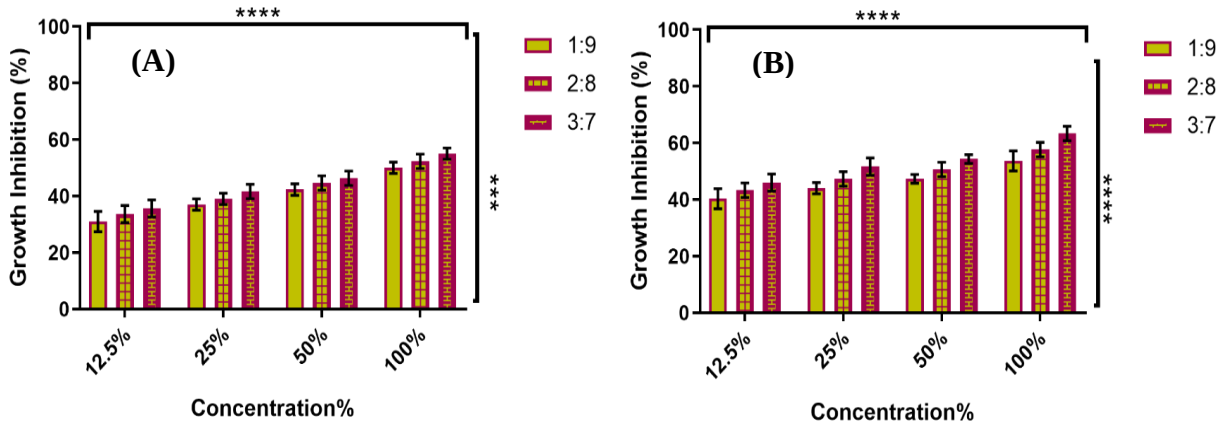

Fig.6. Growth inhibition of the breast cancer cells line (MDA) as different ratios of Ag@Au NPs: (A) After 24 hours (B) After 48 hours.

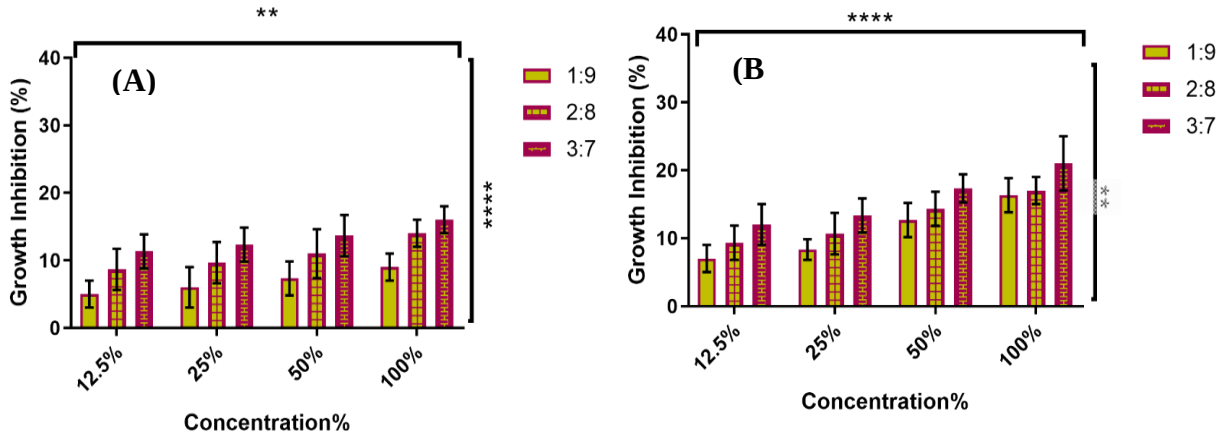

Fig.7. Growth inhibition of the normal cells line (REF) as different ratios of Ag@Au NPs: (A) After 24 hours (B) After 48 hours.

3. Conclusions

In conclusion, this research successfully evaluated the anti-cancer activity of gold-coated silver particles prepared using a hybrid system combining laser and plasma techniques. The study showed the ability of these particles to inhibit the growth of breast cancer cells, with the highest inhibition rate at 66% after 48 hours at a 100% concentration of 3:7. In addition, the toxicity was relatively low to normal cells, with the highest toxicity rate of 16% after 24 hours at 100% concentration for the same ratio. These results highlight the effectiveness of Ag@Au NPs in cancer treatment and pave the way for future research in this promising field.

References

[1] Shanan, Z. J., Abdalameer, N. K., & Ali, H. M. (2022). Zinc Oxide Nanoparticle Properties and Antimicrobial Activity. *International Journal of Nanoscience*, *21*(03), 2250017.
[2] Ijaz, I., Gilani, E., Nazir, A., & Bukhari, A. (2020). Detail review on chemical, physical and green synthesis, classification, characterizations and applications of nanoparticles. *Green Chemistry Letters and Reviews*, *13*(3), 223-245.
[3] Kamil, A. A., Bakr, N. A., Mubarak, T. H., & Al-Zanganawee, J. (2021). Synthesis and study of the optical and structural properties of Au and Ag nanoparticles by pulsed laser ablation (PLAL) technique. *Digest Journal of Nanomaterials & Biostructures (DJNB)*, *16*(4).
[4] Majeed, M. S., Mahmoud, S. M. M., Rasheed, R. M., & Rashad, A. A. (2024). Synthesis AgO Nanoparticles by Nd: Yag Laser with Different Pulse Energies. *Baghdad Science Journal*, *21*(1), 0217-0217.
[5] Nasif, H. K., Ahmed, B. M., & Aadim, K. A. (2021). Synthesis Emission Spectra of (LIPS) Technique for Cu, Ag Nanoparticles and their Antibacterial Activity. *Al-Mustansiriyah Journal of Science*, *32*(3), 49-57.
[6] Adil, B. H., Al-Shammari, A. M., & Murbat, H. H. (2020). Breast cancer treatment using cold atmospheric plasma generated by the FE-DBD scheme. *Clinical Plasma Medicine*, *19*, 100103.
[7] Mazhir, S. N., Abdullah, N. A., al-Ahmed, H. I., Harb, N. H., & Abdalameer, N. K. (2018). The effect of gas flow on plasma parameters induced by microwave. *Baghdad Science Journal*, *15*(2), 0205-0205.
[8] Ingvarsson, S. (2001, October). Breast cancer: introduction. In *seminars in CANCER BIOLOGY* (Vol. 11, No. 5, pp. 323-326). Academic Press.
[9] Mohammed, M. S., Adil, B. H., Obaid, A. S., & Al-Shammari, A. M. (2022, February). Plasma Jet Prepared Gold and Silver Nanoparticles to Induce Caspase-Independent Apoptosis in Digestive System Cancers. In Materials Science Forum (Vol. 1050, pp. 51-63). Trans Tech Publications Ltd.
[10] Abdullah, Q. N., Obaid, A. S., & Bououdina, M. (2018). Influence of gas carrier on morphological and optical properties of nanostructured In2O3 grown by solid-vapour process. Ceramics International, 44(5), 4699-4703.
[11] Kanagaraj, J., Senthilvelan, T., Panda, R. C., Aravindhan, R., & Mandal, A. B. (2014). Biosorption of trivalent chromium from wastewater: an approach towards Green chemistry. *Chemical Engineering & Technology*, *37*(10), 1741-1750.

تقييم النشاط المضاد للسرطان للجسيمات النانوية الفضة/الذهب بواسطة النظام الهجين (الليزر، نفاثة البلازما)

زينب شهيد كاظم ، حيدر يحيى حمود*

قسم الفيزياء، كلية العلوم للبنات، جامعة بغداد، العراق

*البريد الالكتروني للباحث:dr.hayder.y.phy@gmail.com

الخلاصة: يتعامل هذا البحث مع تقييم النشاط المضاد للسرطان لتوليف Ag/Au NPs بواسطة نظام هجين يجمع بين تقنية الليزر والبلازما النفاثة. تمت دراسة تأثير NPs على تثبيط نمو خلايا سرطان الثدي وخط الخلايا الطبيعية. أولاً، تم تحضير الجسيمات النانوية الفضية باستخدام ليزر Nd:YAG بطول موجي 1064 نانومتر، وتردد 6 هرتز، وطاقة 1000 مللي جول، وعدد من النبضات 558. الخطوة الثانية، نأخذ نسبًا مختلفة بين Ag NPs وأملاح الذهب على النحو التالي: (1:9 و 2:8 و 3:7)، على التوالي، وتعرض لنظام نفاث البلازما لمدة 3 دقائق. تم فحص NPs باستخدام حيود الأشعة السينية والتحليل الطيفي للأشعة فوق البنفسجية والمجهر الإلكتروني لمسح الانبعاثات الميدانية (FE-SEM). كان أعلى معدل لتثبيط خلايا سرطان الثدي 66٪ بعد 48 ساعة عندما كان التركيز 100٪ بنسبة 3:7. أما بالنسبة لسمية الخلايا الطبيعية، فإن أعلى سمية كانت 16٪ بعد 24 ساعة عندما كان التركيز 100٪ لمدة 3:7. يمكن أن توفر النتائج المتوقعة ضوءًا جديدًا على فعالية هذه الجسيمات في علاج السرطان وتحفيز الأبحاث المستقبلية في هذا المجال.

IJL, Issue 2, Vol. 23, 2024
https://doi.org/10.31900/ijl.v23i2.482

Research Article

IRAQI JOURNAL OF LASER

Enhancement of The Sensitivity of The Refractive Index Sensor Based on D-shaped Coreless Fiber

Dina N. Abdullah*, Hanan J. Taher

Institute of Laser for Postgraduate Studies, University of Baghdad, Baghdad, Iraq
* *Email address of the Corresponding Author: dina.neamat2201m@ilps.uobaghdad.edu.iq*

Article history: Received 5 Jun. 2024; Revised 25 Jul. 2024; Accepted 7 Aug. 2024; Published online 15 Dec. 2024

Abstract: A refractive index sensor has been developed using a D-shaped coreless fiber (DSCF) sensor technique. This sensor comprises a segment of coreless fiber (CF) spliced between two single-mode fibers (SMFs). The middle of the CF length was polished using a grinding wheel to reduce the diameter on one side, creating a D-shaped cross-sectional profile. The DSCF sensor's performance was tested using different concentrations of sodium chloride (NaCl) solutions, with refractive indices (RI) ranging from 1.33 to 1.38. The optimal polishing depth (PD) of 31 µm was determined experimentally, and this was achieved by extending the polishing duration using a grinding wheel. This led to a sensitivity increase from 70.2nm/RIU to 98nm/RIU, meaning the sensitivity increased by 1.4 times. The DSCF sensor is a high-performance, versatile, and cost-effective device with strong interference ability, suitable for various applications.

Keywords: D-shaped coreless fiber (DSCF), refractive index(RI)sensor, coreless fiber (CF), multimode interference (MMI), Mach– Zehnder Interferometer (MZI).

1. Introduction

In a rapidly changing technical world, fiber optic sensors are essential in a wide range of fields such as mechanical, biochemical, biomedical, and spacecraft applications [1–4] to measure physical, chemical, or biological properties due to their excellent sensing and physical properties by examining the wavelength shift, polarization or change in light intensity [5–7]. The optical fiber sensor often incorporates an optical fiber interferometer to measure the phase difference between light beams. There are various layouts of optical interferometers such as Fabry–Perot interferometer , Sagnac fiber interferometer ,Michelson fiber interferometer, and MZI [8–11]. The MZI is the more traditional interferometer to sense RI, concentrations, temperature, and strain because it has versatile flexible geometry and high sensitivity [12–14]. This type of interferometer can be fabricated using various structures, such as the (SMS) structure, which consists of a segment of multimode fiber (MMF) spliced between two single-mode fibers (SMF), or the (SCS) structure involves splicing a CF to act as the sensing part instead of the typical MMF between two SMFs [11]. There are many techniques were used to enhance the sensitivity via increase the evanescent wave leaks from the sensing part(CF) in SCS structure by etching the CF [15] , utilizing offset optical fiber [16], heating and tapering a CF-SMF[17,18] or by removing a layer from one side of the CF to obtain the DSCF [19,20].

D-shaped optical fibers are manufactured using various methods such as chemical etching, laser ablation, and mechanical polishing [15,19,21] .Sensors based on D-shaped optical fiber were developed in two ways , the first was without the need for splicing and used only one type of fiber, such as MMF which showed relatively high sensitivity [22,23]. Another type of sensor based on the D-shape was designed using a structure consisting of photonic crystal fiber (PCF) or coreless fiber as the sensing part [19,24,25]. In addition, a D-shaped sensor was fabricated using plastic optical fiber core for an expanded RI measurements [26]. The SCS MZI structure was used in this paper utilizing the grinding wheel to side-polish the CF to enhance the structure's sensitivity and then attain DSCF sensor for the RIs measurement .Also, the optimal depth was determined by extending the polishing process duration through three experimental tests.

2. The principles of the DSCF sensor

The SCS-MZI interferometer used in this work comprises of two splicing regions, the first splicing region represents a beam splitter coupler where the light enters and splits into two beams, the reference beam travels into the core of the CF, while the sensing beam is guided by air or another medium, with the condition that RI of the ambient environment is lower than the RI of the CF to ensure that the principle of total internal reflection is achieved and the second splicing region is represented a combiner where the reference beam recombined with the sensing beam at the second splicing region causes interference that is represented in Fig.1which shows the SCS structure .The changing in length and diameter of CF caused changing in the sensitivity and the peak spectral response of CF according to MMI theory that was caused by the self-imaging effect can be calculated by using Eq.1 [27–29].

$$\lambda o = P(n_{CF} D_{2CF}/L_{CF}) \quad (1)$$

nCF and DCF were the RI and the diameter of the CF segment in the SCS proposed sensor, respectively and P acts as the self-imaging number which means constructive interference number.

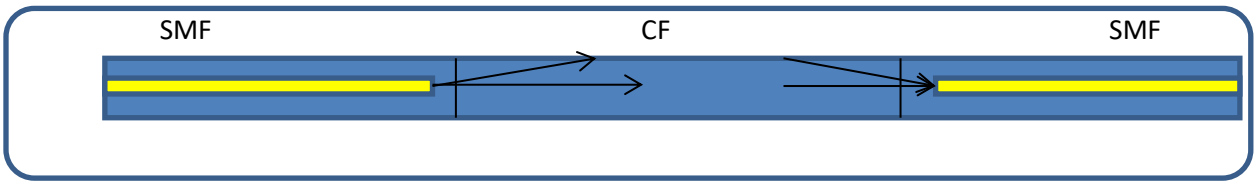

Fig.1: Schematic of in line MZI with inner couplers SCS structure

The principle of the DSCF sensor enhances sensitivity by reducing the distance between the CF and analytes by polishing one side of a coreless fiber. As the polishing deepens, the evanescent wave strength increases, allowing for more precise measurements. The RI of the external environment is determined by changes in transmitted light power or wavelength shifts. Increasing the polishing depth decreases the output intensity. As shown in Fig .2, there are five sections in the DSCF structure: lead in SMF, transitional length (L1), coreless flat section (CFL), transitional length (L2), and lead out SMF. The light inputs from the lead in SMF into the CF divide into two divisions, one of which is transmitted in the air in L1 and the other is coupled to the CFL. The CFL works as a multimode waveguide. The L1 provides an efficient way to excite the high-order modes and strong evanescent waves of the CFL multimode waveguide, which enhances the RI sensitivity. Then the light is recollected from the CFL by the fiber core in the L2 section for output measurement. This technique is based on the interaction between the evanescent wave of the surface of the D-shaped fiber and the external environment resulting in optical transmission attenuation. In other words, The optical transmission structure can be disrupted by reducing the diameter of the optical fiber on one side that disruption allows for the excitation of higher order modes, which in turn brings the fiber core in closer proximity to the measured physical quantity [19,20].

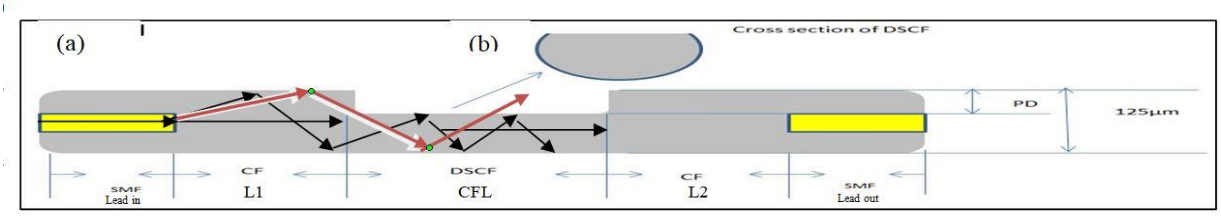

Fig2: Schematic diagrams of (DSCF) (a) vertical section, and (b).cross section of DSCF

This adjustment facilitates more precise and accurate measurements. The RI of the external environment (analyst) is measured by detecting the change in transmitted light power or the shift in wavelength. The RI sensing characteristics of three fabricated DSCFs with different PDs based on the percentage of output intensity of DSCFs were experimentally investigated by extending the duration. It is also clear that as the PD increases, the evanescent field becomes stronger.

3. Materials and method

3.1 The fabrication and characterization of SCS sensing structure

SCS structure was fabricated by splicing a single segment of 6cm long of CF [30,31] with a uniform RI of 1.46 and a diameter of 125 µm (Thorlabs) between two single-mode fibers (SMF-28) with an RI of 1.451 for the core and 1.444 for the cladding by an optical fiber arc fusion splicer (FSM-60S) to create the SCS structure. To prepare the fibers for the splicing process, the outer coating of the CF and 2 cm from the end of the SMFs were stripped using an optical fiber stripper. Then, the fiber terminations of SMFs and CF were cut at a right angle using an optical fiber cleaver (CT-30), this precise cut ensures proper alignment during splicing. After that, SMF was spliced with CF using an optical fiber arc fusion splicer, the splice mode was auto SM/NZ/DS/MM and the heater mode was 60 mm FP-03. Finally, the other end of CF was spliced to the other SMF in a similar manner. Fig.3 illustrates (a) a schematic diagram of the SCS structure and (b) the transmission spectrum (reference) of the SCS structure measured by an optical spectrum analyzer (OSA).

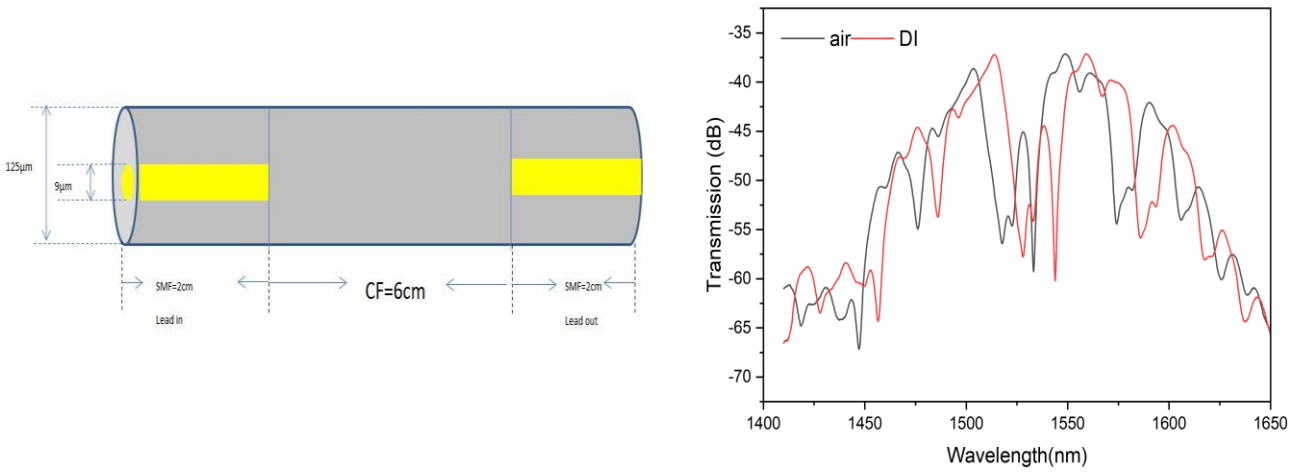

(a) **(b)**

Fig.3: SCS MZI structure (a)schematic diagram of SCS structure(b)transmission spectrum of SCS structure.

3.2 The fabrication and characterization of the DSCF sensing structure

The SCS sensor was initially fixed onto a holder fiber from the SMFs at both ends. One end of the SMF was connected to a 635 nm laser diode (Thorlabs), while the other end of the second SMF was connected to a visible spectrometer (CCS series spectrometer-Thorlabs) with a wavelength range of 350-700 nm as shown below in Fig.4.

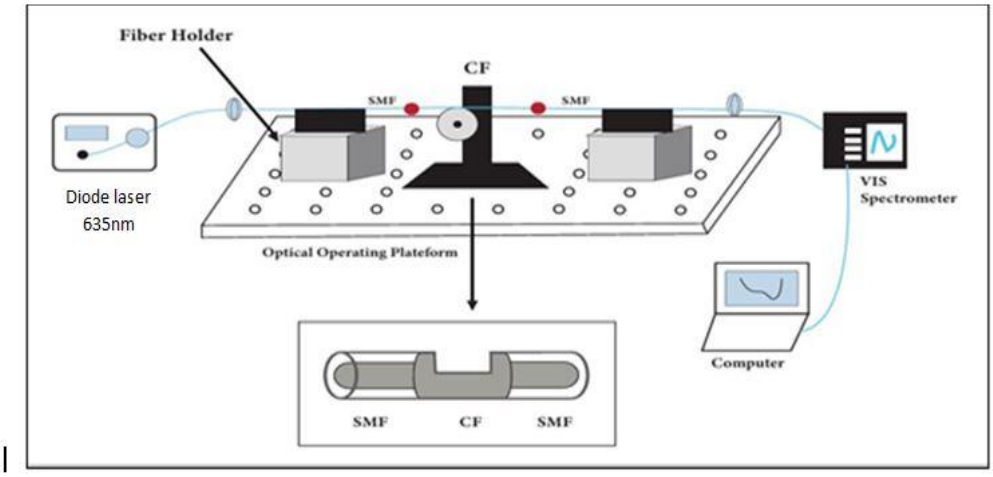

Fig.4: The polishing device to fabricate and characterize the DSCF sensor.

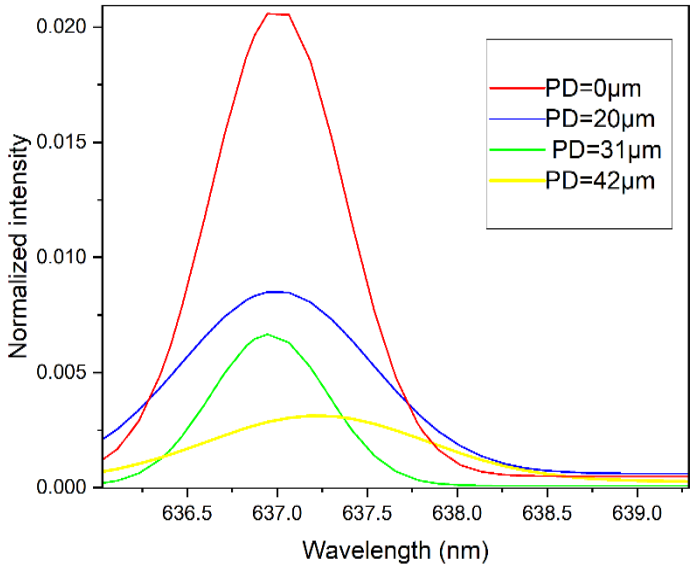

Fig.5: The relation between the intensity and the wavelength with different polishing depths

The middle of CF was placed on a grinding wheel for polishing until the desired depth was achieved, resulting in the fabrication of the DSCF. The peak of the output intensity (I in) was recorded before the DSCF (operating the grinding wheel) at an external RI of air=1. As the grinding wheel operated, the peak of intensity gradually decreased as the polishing duration extended. After turning off the grinding wheel,

the peak of the intensity after DSCF (I out) was recorded, and the remaining intensity was calculated using Eq. 2:

$$\text{The remaining intensity} = (I_{out} / I_{in}) \% \quad (2)$$

To determine the optimal PD experimentally, the first step was repeated three times with three SCS structures. Each time, the polishing period was extended more than the previous period to increase the PD. The output intensity recorded by the spectrometer decreased as the PD increased, as shown in Fig.5. This indicates that there is attenuation in output power because the evanescent wave leaks from the surface of the DSCF structure due to a decrease in the diameter of the CF from one side. This resulted in three different PDs (20 µm, 31 µm, 42 µm) as shown in Fig.6. The remaining intensity was calculated using Equ.3 for each PD of the fabricated DSCF structure.Then, the transmission spectrum was measured by OSA as shown in Fig.7, and the sensitivity was calculated to choose the optimal polishing depth which achieved the highest sensitivity among the three structures, as shown in Fig.8.

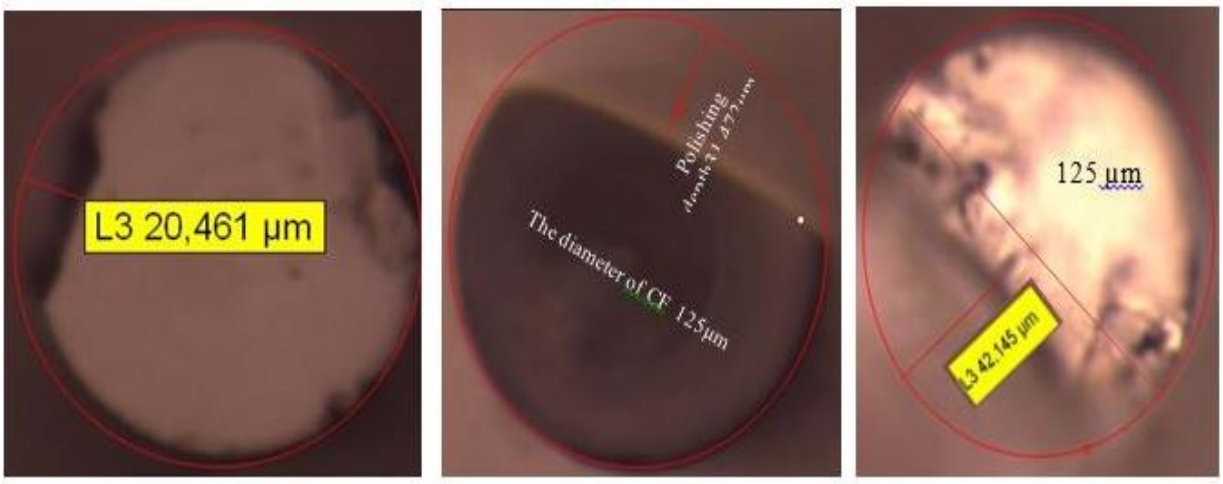

Fig.6: The image under the microscope showed the cross-section of DSCF when PD equal to (a) 20µm, (b) 31µm, and (c) 42µ.

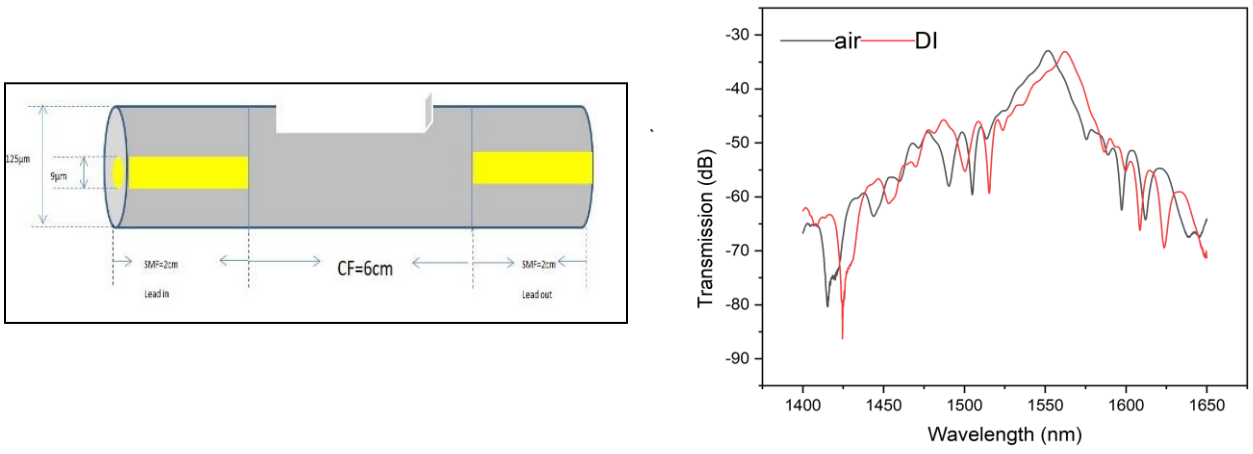

(a) **(b)**

Fig.7: DSCF structure (a)schematic diagram of DSCF structure(b)transmission spectrum of DSCF structure.

3.3 The preparation of Sodium Chloride (NaCl) solution

The NaCl solutions used in this study had concentrations ranging from 5% to 25%. To prepare these solutions, specific amounts of NaCl powder were weighed using an electronic scale and then dissolved in 100 ml of deionized water (DI) at room temperature using a magnetic stirrer. For example, to prepare 5%, 10%, 15%, 20%, and 25% of NaCl solutions, 5g, 10g, 15g, 20g, and 25g of NaCl powder should be added to 100 ml of DI, respectively. The RIs corresponding to these concentrations were demonstrated in Table 1 [32]. The RIs of the prepared solutions were measured by an Abb refractometer to evaluate the sensitivity of this proposed sensor.

Table 1: The refractive indices of the NaCl concentrations.

NaCl Concentrations (%)	DI	5	10	15	20	25
Refractive Index (RIU)	1.33	1.34	1.35	1.36	1.37	1.38

4. The experimental setup

Firstly, one end of the SCS sensor was connected to a broadband source (BBS) with a wavelength range of 1500-1600 nm, and the other end of the sensor was connected to the OSA (YOKOGAWA AQ6370C OSA) to determine the sensitivity of this structure by measuring its transmission spectra before polishing the CF.

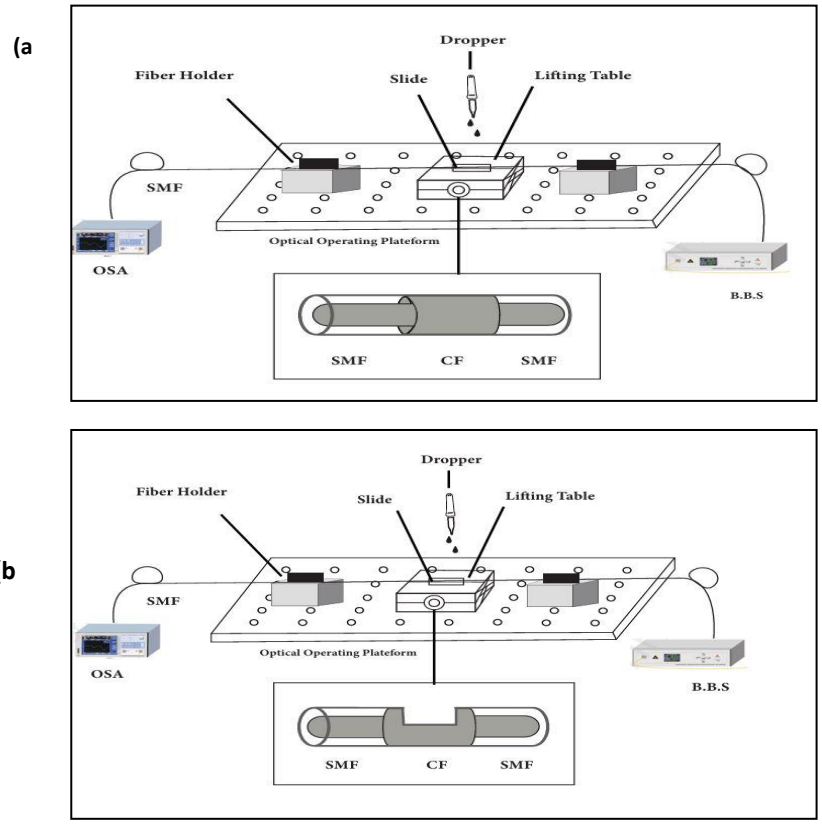

Fig.8: Experimental setup of DSCF RI sensor with different concentrations of NaCl solution by OSA (a) Testing the sensor before DSCF (b) Testing DSCF sensor.

The SCS structure was examined by OSA with different concentrations of NaCl from 5% to 25 % with an increase of 5%. Secondly, after fabrication, the DSCF sensor was connected with OSA from one side and BBS from the other side as present in Fig.8(a) to calculate the sensitivity by OSA for the three different polishing depths with the same previous method and concentrations that were used before the DSCF sensor. This is demonstrated in Fig. 8 (b)

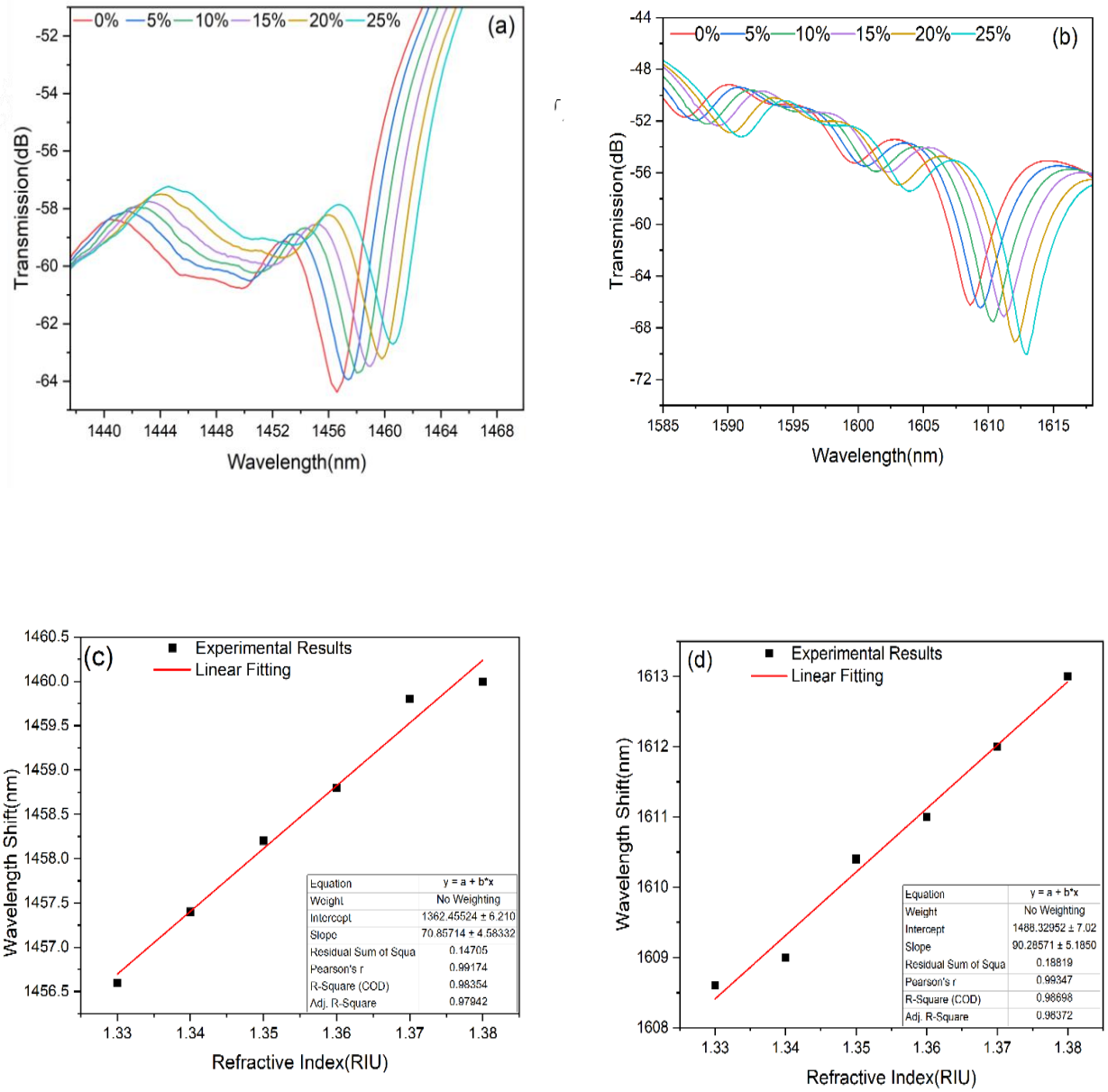

Fig.9: Transmission spectra and sensitivity measured with the different concentrations of NaCl solution respectively ((a), and (c)) before DSCF, ((b), and(d)) after DSCF.

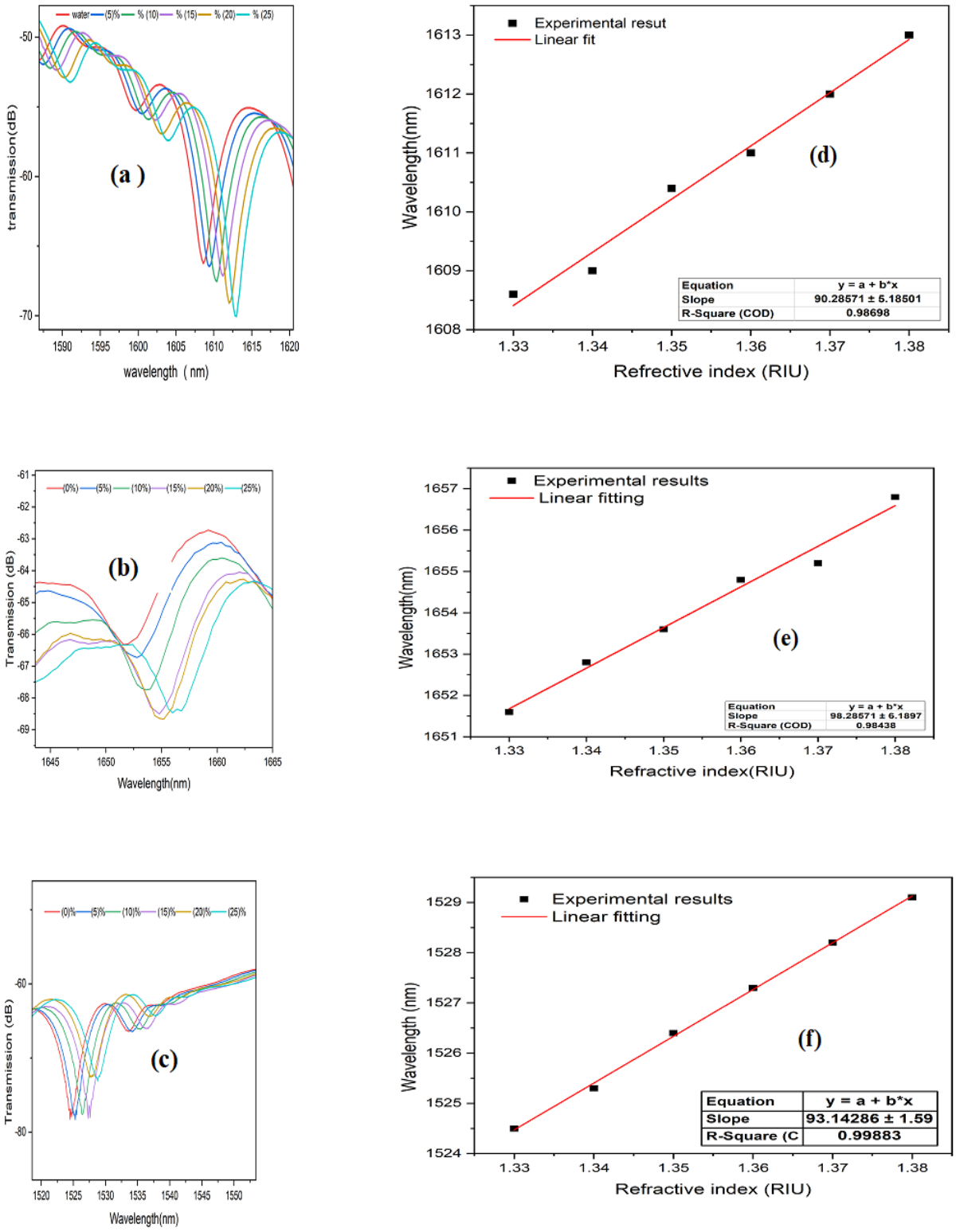

Fig. 10: Transmission spectra recorded by OSA from the measurements of the DSCF sensor with three different PDs (a) for PD=20µm (b) for PD=31µm and (c) for PD= 42 µm. Experimental results of RI when (d) PD=20µm (e) PD=31µm (f) PD= 42

Table 2: The relationship between the remaining intensity and the sensitivity to choose the optimal depth.

Structure Name	Polishing Depth(μm)	(I_{out}/I_{in})%	Sensitivity (nm/RIU)
structure1	20	80	90
structure 2	31	70	98
structure 3	42	42	93.14

was done to prevent any interference from the residual solution on the surface. The SCS sensor was placed on a lifting table and fixed at both ends with fiber holders. The sensing area was placed on the slide, and the NaCl solution was dripped onto the slide until the sensing area was fully immersed. Every step was recorded and fixed, starting with air, so that the spectrum coincided with the previously recorded air spectrum. Each step was recorded and fixed by OSA starting with air to investigate its transmission spectra, and the sensitivity(S) was calculated from the slope between the shift in wavelength and the corresponding RI (n) of each using concentration. This is illustrated in Eq.3 [33]:

$$S = \Delta\lambda_{shift}/\Delta n \quad (3)$$

Where Δλ shift represented the shift in wavelength.

OSA tested the DSCF sensor to measure the transmission spectra shown in Fig. 9 using various RIs of NaCl solutions ranging from 1.33 to 1.38 in increments of 0.01 for each RI measurement. These measurements were taken both before and after the polishing process, with the NaCl solutions replacing air as the cladding. Fig. 9(a) and (b) compare the transmission spectra measured by OSA before and after using the grinding wheel, respectively.

It was observed that several dips will appear in the transmission spectrum due to the MMI in the FCL , Then this dip shifted towards longer wavelengths as the RI of the NaCl solution increased. In Fig. 9 (c), the experimental results show an increase in sensitivity, calculated from the slope of the linear fitting, from 70.8 nm/RIU before the DSCF to 90 nm/RIU after the DSCF as demonstrated in (c) and (d) respectively. In this study, three different PDs were created of 20 μm, 31 μm, and 42 μm. The corresponding sensitivities were 90nm/RIU, 98nm/RIU, and 93.14nm/RIU, respectively, as shown in Fig. 11. When the PD had a depth of 20 μm, the peak of the output intensity decreased, but there was no significant energy loss. Upon increasing the PD depth to 31 μm, the sensitivity increased to 98nm/RIU, indicating the optimal polishing depth. Fig. 10 illustrates the transmission spectra measured by OSA, and the sensitivity calculated from the linear fitting demonstrated that the 31 μm PD achieved the highest sensitivity among the three DSCF sensors, with a good linearity of 9.8. The three polishing depths and their corresponding sensitivities are summarized in Table 2.

It was observed that the linear fitting curve of the experiment after one month is very close to the linear fitting curve of the original experiment, and the sensitivity decreased from 98.2 to 93.7 which confirms that the sensor is with good repeatability which is illustrated in Fig.11. To compare with the proposed structures, Table 3 shows a comparative analysis of the results between the sensors of different structures reported previously.

Table 3: shows a comparative analysis of the results between the sensors of different structures reported previously To compare with the proposed structures.

Structure	RI Range	RI Sensitivity (nm/RIU)	References
Core-offset SMF	1.33-1.374	78.8	[32]
Double tapered SMF	1.348-1.403	68.6	[34]
SCS Structure offset fiber [16]	1.33-1.38	98.768	[16]
Tapered Splicing SMF-PCF-SMF	1.33-1.38	20 pm / RIU	[17]
DSCF SCS Sensor	1.33-1.38	98.2	In this work

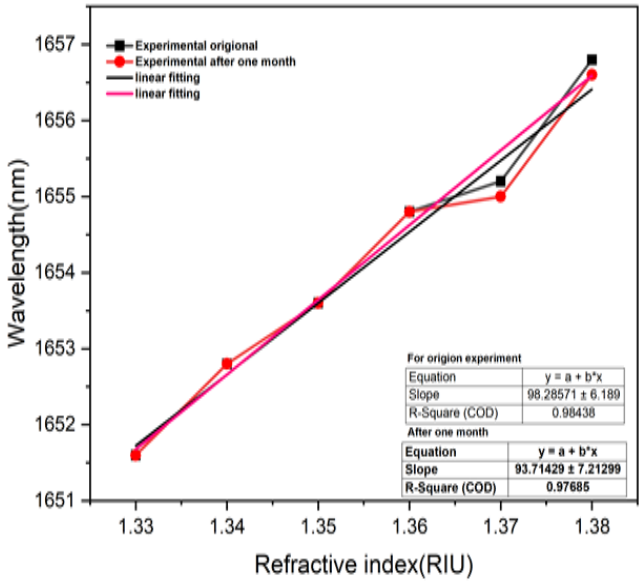

Fig.11: A comparison chart of the original experimental result when the PD was 31µm and the experimental result after one month.

5. Conclusion

A DSCF for RI sensors based on SCS structure has been created using a grinding wheel to improve sensitivity to the surrounding refractive index. Three different DSCF structures with varying polishing depths were fabricated for experimental comparison and their RI sensing characteristics are demonstrate. The optimal polishing depth was 31 µm achieved the highest sensitivity of 70 to 98 nm/RIU for different concentrations of NaCl solution ranging from 1.33-1.38 and the correlation coefficient (R2) was 9.8. Further optimization schemes are under study to enhance the sensitivity. This makes the DSCF sensor suitable for many applications like biosensors and environment pollution, easy to fabricate, good stability, and compact.

References

[1] Keirsse J, Boussard-Pledel C, Loreal O, Sire O, Bureau B, Leroyer P, Turlin B, Lucas J. "IR optical fiber sensor for biomedical applications," (2003). Vib Spectrosc; 32:23–32.

[2] García Esteban-Barcina I, Beloki Perurena J, Zubia Zaballa JA, Aldabaldetreku Etxeberria G, Illarramendi Leturia MA, Jiménez Hernández F. "An Optical Fiber Bundle Sensor for Tip Clearance and Tip Timing Measurements in a Turbine Rig," (2013).
[3] Jha R, Gorai P, Shrivastav A, Pathak A. "Label-Free Biochemical Sensing Using Processed Optical Fiber Interferometry: A Review," (2024). ACS Omega; 9:3037–3069.
[4] Friebele EJ, Askins CG, Bosse AB, Kersey AD, Patrick HJ, Pogue WR, Putnam MA, Simon WR, Tasker FA, Vincent WS. "Optical fiber sensors for spacecraft applications," (1999). Smart Mater Struct; 8:813.
[5] Abbas HK, Mahdi ZF. "D-shape Optical Fiber Development and Enhancement as a Refractive Indices Sensor Using Surface Plasmon Resonance," (2023). Iraqi J Laser; 22:80–90.
[6] Li X, Zhang H, Qian C, Ou Y, Shen R, Xiao H. "A new type of structure of optical fiber pressure sensor based on polarization modulation," (2020). Opt Lasers Eng; 130:106095.
[7] Polygerinos P, Seneviratne LD, Althoefer K. "Modeling of light intensity-modulated fiber-optic displacement sensors," (2010). IEEE Trans Instrum Meas; 60:1408–1415.
[8] Zhang J, Sun Q, Liang R, Wo J, Liu D, Shum P. "Microfiber Fabry–Perot interferometer fabricated by taper-drawing technique and its application as a radio frequency interrogated refractive index sensor," (2012). Opt Lett; 37:2925–2927.
[9] Smetana J, Walters R, Bauchinger S, Ubhi AS, Cooper S, Hoyland D, Abbott R, Baune C, Fritchel P, Gerberding O. "Compact Michelson interferometers with subpicometer sensitivity," (2022). Phys Rev Appl; 18:34040.
[10] Lin W, Shao L, Liu Y, Bandyopadhyay S, Liu Y, Xu W, Liu S, Hu J, Vai MI. "Temperature sensor based on fiber ring laser with cascaded fiber optic Sagnac interferometers," (2021). IEEE Photonics J; 13:1–12.
[11] Mohammed SA, Al-Janabi AH. "All fiber chemical liquids refractive index sensor based on multimode interference," (2018). Iraqi J Laser; 17:33–39.
[12] Liu W, Wu X, Zhang G, Li S, Zuo C, Fang S, Yu B. "Refractive index and temperature sensor based on Mach-Zehnder interferometer with thin fibers," (2020). Opt Fiber Technol; 54:102101.
[13] Wang S, Lv R, Zhao Y, Qian J. "A Mach-Zehnder interferometer-based High Sensitivity Temperature sensor for human body monitoring," (2018). Opt Fiber Technol; 45:93–97.
[14] Wang S, Ma Y, Chen W, Wang S, Yi Y, Li X, Lu C, Zhang S, Geng T, Sun W. "Ultrasensitive strain sensor based on Mach-Zehnder interferometer with bent structures," (2021). J Light Technol; 39:6958–6967.
[15] Hamza N. "Enhanced refractive index sensor based on etched coreless fiber," (2020). Authorea Prepr.
[16] Taher HJ, Mejble AR. "S and U Shape Offset Studying of the Refractive Index Sensor Based on Coreless Fiber," (n.d.).
[17] Salman NA, Taher HJ, Mohammed SA. "Tapered splicing points SMF-PCF-SMF structure based on Mach-Zehnder interferometer for enhanced refractive index sensing," (2017). Iraqi J Laser; 16:19–24.
[18] Bakurov DD, Ivanov OV. "Control of Excitation of Cladding Modes by Tapering an Insertion of Special Fiber," (2021). Sensors; 21:2498.
[19] Dong H, Chen L, Zhou J, Yu J, Guan H, Qiu W, Dong J, Lu H, Tang J, Zhu W, Cai Z, Xiao Y, Zhang J, Chen Z. "Coreless side-polished fiber: a novel fiber structure for multimode interference and highly sensitive refractive index sensors," (2017). Opt Express; 25:5352.
[20] Liu Y, Zhang W, Tong Z, Wang X, Liu D, Wang M, Yu H. "Research on MZI sensor for refractive index and temperature based on D-shaped no core fiber," (2024). Opt Mater (Amst); 148:114933.
[21] Hu C, Wang C, Zhou S, Zhu Z, Wu H, Sun K, Ma X. "Simulation and experimental investigation of the surface morphology formation mechanism of a D-shaped fiber processed using a pulsed CO2 laser," (2022). Opt Laser Technol; 153:108195.
[22] Abbas HK, Mahdi ZF. "D-shape Optical Fiber Development and Enhancement as a Refractive Indices Sensor Using Surface Plasmon Resonance," (2023). Iraqi J Laser; 22:80–90.
[23] Chen M, Lang T, Cao B, Yu Y, Shen C. "D-type optical fiber immunoglobulin G sensor based on surface plasmon resonance," (2020). Opt Laser Technol; 131.
[24] Falah AAS, Wong WR, Mahamd Adikan FR. "Single-mode eccentric-core D-shaped photonic crystal fiber surface plasmon resonance sensor," (2022). Opt Laser Technol; 145.
[25] Liang H, Shen T, Feng Y, Liu H, Han W. "A d-shaped photonic crystal fiber refractive index sensor coated with graphene and zinc oxide," (2021). Sensors (Switzerland); 21:1–16.
[26] De-Jun F, Mao-Sen Z, Liu G, Xi-Lu L, Dong-Fang J. "D-shaped plastic optical fiber sensor for testing refractive index," (2014). IEEE Sens J; 14:1673–1676.
[27] Ballato J, Dragic P. "Glass: the carrier of light-a brief history of optical fiber," (2016). Int J Appl Glas Sci; 7:413–422.

[28] Huang S-C, Lin W-W, Tsai M-T, Chen M-H. "Fiber optic in-line distributed sensor for detection and localization of the pipeline leaks," (2007). Sensors Actuators A Phys; 135:570–579.
[29] Choi S, Eom TJ, Yu JW, Lee BH, Oh K. "Novel all-fiber bandpass filter based on hollow optical fiber," (2002). IEEE Photonics Technol Lett; 14:1701–1703.
[30] Razali NM, Lokman MQ, Zuikafly SNF, Ahmad F, Yahaya H. "Simulation of Self-Image Interference in Single Mode-No-Core-Single Mode Fiber with COMSOL Multiphysics," (2022). J Phys Conf Ser; 2411.
[31] Mejbel AR, Taher HJ. "Coreless fiber length influence for refractive index measurements based on lateral offset structure," (2022). NeuroQuantology; 20:2337.
[32] Zhao Y, Li XG, Cai L. "A highly sensitive Mach-Zehnder interferometric refractive index sensor based on core-offset single mode fiber," (2015). Sensors Actuators A Phys; 223:119–124.
[33] Cennamo N, Massarotti D, Conte L, Zeni L. "Low cost sensors based on SPR in a plastic optical fiber for biosensor implementation," (2011). Sensors; 11:11752–11760.
[34] Yang W, Pan R, Yu X, Fan J, Xiong Y, Wu M. "A high sensitivity asymmetric double tapered fiber interference sensor," (2020). Optik (Stuttg); 210:164495.

تحسين حساسية مستشعر معامل الانكسار بالاعتماد على الالياف عديمة النواة على شكل حرف D

دينا نعمت عبدالله *,حنان جعفر طاهر

معهد الليزر للدراسات العليا، جامعة بغداد، بغداد، العراق

*البريد الالكتروني للباحث: *dina.neamat2201m@ilps.uobaghdad.edu.iq*

الخلاصة

تم تطوير مستشعر لقياس التغير في معامل الانكسار للمحيط باستخدام تقنية مستشعر الألياف غير النواة على شكل حرف(D) . يتكون هذا المستشعر من قطعة من الألياف غير النواة (CF) ملحومة بين ليفين أحادي النمط (SMF). تم تلميع منتصف طول الألياف غير النواة باستخدام عجلة طحن لتقليل القطر من جانب واحد، مما أدى إلى إنشاء مقطع عرضي على شكل حرف D. تم اختبار أداء مستشعر DSCF باستخدام تركيزات مختلفة من محاليل كلوريد الصوديوم (NaCl)، حيث تتراوح معاملات الانكسار (RI) من 1.33 إلى 1.38. تم تحديد عمق التلميع الأمثل (PD) عند 31 ميكرومتر تجريبياً، وتم تحقيق ذلك عن طريق تمديد مدة التلميع باستخدام عجلة الطحن. أدى ذلك إلى زيادة الحساسية من 70.2 نانومتر/وحدة معامل الانكسار إلى 98 نانومتر/وحدة معامل الانكسار، مما يعني أن الحساسية زادت بمقدار 1.4 مرة. يعتبر مستشعر DSCF جهازاً عالي الأداء ومتعدد الاستخدامات وذو تكلفة فعالة مع قدرة قوية على التداخل، وهو مناسب لمجموعة متنوعة من التطبيقات.

IJL, Issue 2, Vol. 23, 2024
https://doi.org/10.31900/ijl.v23i2.477

Research Article

Surface Topography of Primary Teeth Enamel After Sub-ablative Er;Cr:YSGG Laser Irradiation: An In Vitro Study

Saba Amer Abed Mahdi *, Basima Mohammed Ali Hussein

Institute of Laser for Postgraduate Studies, University of Baghdad, Baghdad, Iraq
** Email address of the Corresponding Author:sabaamer804@gmail.com*

Article history: Received 24 Apr. 2024; Revised 25 Aug. 2024; Accepted 27 Aug. 2024; Published online 15 Dec. 2024

Abstract

Objective: To evaluate the effect of different sub-ablative irradiation parameters of Er;Cr:YSGG laser on the surface topography of primary teeth enamel with white spot lesions.
Materials and Methods: A total of 30 primary posterior teeth with sound enamel were immersed in demineralization solution at (pH 4.4) to artificially induce enamel white spot lesions. They were randomly divided into three groups: L1, L2, and L3 groups were irradiated with Er;Cr:YSGG laser irradiation at the power of 0.75W, 0.5W, and 0.25W respectively, 20Hz frequency, and 40% air/ 60% water irrigation. Surface topography was evaluated with a profilometer and scanning electron microscope.
Results: Surface roughness evaluation with scanning electron microscope images revealed a non-significant increase in surface roughness after the demineralization process. Laser irradiation with different powers leads to a non-significant increased surface roughness with altered topography and a more pronounced effect with the laser group L1 and to a lower extent groups L2 and L3.
Conclusion: Increased surface roughness of the primary teeth enamel after sub-ablative power irradiation with Er;Cr:YSGG laser, with a rough and irregular surface devoid of smear layer, the roughness increase was proportional with the increased irradiation power.

Keywords: Er;Cr:YSGG. White spot lesion. Primary teeth. Roughness. SEM.

1. Introduction

The prevention and treatment of dental caries remains a pressing concern within the field of dentistry, given the implications for public health and human well-being. The development of dental caries is marked by changes in the apatite crystals of the enamel, which can result in the formation of white spot lesions, initial enamel caries, dentin involvement, and cavitation. Despite modern advances in dental care, the prevention and treatment of dental caries continue to be an active area of research worldwide. In the early stages of enamel caries, the appearance of chalky irregularities indicates a disruption in biological mineralization activity, resulting from a loss of mineral content on both the enamel surface and subsurface [1].

Contemporary approaches to caries management prioritize non-cavitated carious lesions, with an emphasis on halting or reversing progression and promoting remineralization, rather than resorting immediately to drilling and filling procedures [2].

Fluoride topical treatment is a widely used method for remineralization and stabilization of early carious lesions. Sodium fluoride, acidulated phosphate fluoride, and MI paste plus are commonly employed for this purpose.). When fluoride is topically applied to white spot lesions (WSLs) in vivo, it can be eliminated through various mechanisms such as back diffusion, back exchange, and migration from the mineral to the surrounding tissue fluid, saliva, or plaque fluid [2]. However, the amount of fluoride released from the reservoir over time decreases. This approach of topical application of fluoride has drawbacks including the possibility of dental fluorosis, particularly in children [3]. Furthermore, the remineralization process may lead to external staining. Besides, this method requires the patient's consent and takes more time to complete. If superficial remineralization is performed while the lesion is still porous, it may cause unpredictable and persistent white discoloration [4]. Early preventive methods are insufficient to prevent new caries lesion development in high-risk individuals [2]. In recent years, however, this approach has been challenged by a need for minimally invasive and less traumatic dental caries management and prevention methods for young children. Laser irradiation is one such solution that can increase fluoride uptake [5]. Lasers are increasingly being employed in the prevention of dental cavities due to their notable impact on dental hard tissue[6]. The wavelength of Er;Cr:YSGG laser at 2780nm has many dental applications, including cavity preparation, caries removal, endodontic treatment, and surgical procedures that made the OH groups in hydroxyapatite crystals effectively absorb this wavelength which in turn made the temperature of the tooth surface rises to 800°C at the ablation threshold. This leads to crystallographic changes in the enamel, without causing the carbonated hydroxyapatite to evaporate or melt [7].
The absorbance coefficient of enamel is around 50 mm^{-1}. It was mentioned that the laser beam can pass through the enamel's outer layers at about 21 μm. The oral hard tissues are exposed to Er; Cr:YSGG laser radiation through explosive thermo-mechanical ablation. Under this mechanism, the incident radiation is absorbed by the water molecules within the hydroxyapatite crystals. The water vaporization causes an increase in internal pressure and micro explosions, which in turn cause substrate ejection in the form of inorganic particles and accurate removal of irradiated tissue [8]. This laser should have a lower energy density than ablation to prevent cavities since its absorption by hydroxyapatite hydroxyl groups and water is high at 2780nm. While an energy density of 8.5 J/cm^2 improves enamel acid resistance, lower fluences can be used as fluoride dentifrice substitutes. An enhanced enamel surface temperature would only produce chemical changes. Best-case laser irradiation should increase enamel hardness without affecting surface roughness [3].

Several explanations have been offered for the remineralization potential of lasers. One possibility is that laser irradiation reduces enamel permeability by melting, fusing, and recrystallization of enamel crystals [9]. Another theory proposes that the photochemical effect of laser leads to protein decomposition and reduction of carbonate content at temperatures ranging between 650°C and 1100°C rendering the enamel more acid-resistant. [10]. According to some other research, laser irradiation may encourage the development of microspaces in enamel, which would improve fluoride incorporation or diffusion across its structure and enable the creation of a fluoride reservoir important for preventing dentin erosion [11].

Surface roughness is the term used to describe irregularities or tiny indentations and projections that affect the surface's properties, including brightness, quality of adhesion, and wetting capacity. Devices like roughness meters can measure a surface's imperfections, or tiny saliencies and re-entries [12].

Roughness assessments after remineralization affect aesthetics and indicate bacterial adherence, plaque development, and exogenous staining. Compared to flat surfaces, rough and irregular surfaces create more dental biofilm that matures faster. Studies have shown that demineralized enamel, which is rougher than sound, can hold more biofilm than sound enamel [13]. Qualitative enamel surface roughness study with SEM evaluation is subjective and may favor the initial hypotheses. Since scanning electron microscopy can't provide enough quantitative data, enamel deterioration can't be continuously measured. Profilometers provide more descriptive data to quantify enamel damage severity [14].

Profilometry was used to quantify surface roughness in this study because it can accurately and precisely measure it without further measurements. Many researchers found profilometric quantitative evaluation beneficial. [14, 15, 16]

In the present study, to mimic the situations in the oral cavity adjacent to the teeth, samples with white spot lesions were used. [7]. This study aims to evaluate the surface topography of primary teeth enamel with artificially induced white spot lesions subjected to Er;Cr:YSGG sub ablative irradiation parameters as a remineralization method, evaluated with a profilometer and scanning electron microscopy (SEM).

2. Materials and Methods

2.1 Sample Collection and Preparation

For this study, 30 primary posterior teeth were used that had either been extracted for orthodontic reasons or had been naturally exfoliated. Samples were collected from private dental clinics in Baghdad city over a period of three months, From May to August of 2023. A 40X optical microscope (OLYMPUS/BX51, Korea) was used to examine the crowns and choose teeth that did not have any flaws, cracks, cavities, wear, fluorosis, or spots [15]. First, an ultrasonic scaler was used to get rid of residual tissue and other waste. The teeth were then polished with fluoride-free pumice (Perfection Plus, Hants, UK) and protective rubber caps. A water-cooled cutting disc was used to separate the roots 2 mm below the CEJ. The buccal surface of each sample was polished with Sof-Lex™ discs (3M™ ESPE, USA) on a slow-speed handpiece, disinfected for up to one week in 0.1% chloramine T solution (BDH, England), and then stored in distilled water for weekly refreshment until use [17, 18]. Samples were placed inside cold-cure acrylic cylinder blocks (Duracryl® Plus, Spofa Dental, Kerr business, Czech Republic), and only the smooth surface came out. After putting 3x3 mm adhesive tape on each enamel-polished surface, the samples were painted twice with Flormar's acid-resistant nail polish and then taken off to make a window [19]. Teeth blocks were kept in distilled water at room temperature to protect them from drying out. Teeth were put in a solution for demineralization that had 2.20 mmol/L of calcium chloride, 2.20 mmol/L of monosodium phosphate, 1 mol/L of potassium hydroxide, and 0.05 mol/L of acetic acid to make white spot enamel lesions. The solution has a pH of 4.4 and was kept in a light-resistant container in a 37° water bath (BS-11/LAB COMPANOIN, Korea) for 4 days, or until a change in the enamel surface that could be seen in both wet and dry conditions was seen [20] and confirmed by reading from a DIAGNOdentTM pen 2190 (KaVo, Biberach, Germany). The final fluorescent value for each sample was found by taking the average of three readings in a row for each tooth [21].

2.2 Experimental groups

After the WSLs were created, each sample was washed with 10 ml of deionized water and dried with a stream of compressed air. The samples were then randomly split into four groups of 10 (n=10):

- Group (L1): Samples were treated with an Er.Cr:YSGG laser at 0.75 W/20 Hz and 60% water with 40% air.
- Group (L2): Samples that were cut with an Er.Cr:YSGG laser set to 0.5 W, 20 Hz, and 60% water and 40% air.
- Group (L3): Samples were treated with an Er.Cr:YSGG laser at a power level of 0.25 w/20 Hz and 60% water and 40% air.

2.3 Laser irradiation

Irradiating the sample enamel with an Er;Cr:YSGG laser (2780nm, Waterlase iPlus; Biolase, Irvine, CA, USA) was done. The laser was used for 10 seconds at 0.25 W, 0.5 W, and 0.75 W total power, with 20 Hz repetitions. 40% air and 60% water spray were used for watering. A fiber optic system with a 600µm beam

width MZ6 sapphire gold tip and a distance of 1-2 mm in a non-contact (H) mode was used to send the energy [22]. A computerized numerical control machine (CNC) was used to standardize lasing [23]. The Laser irradiation setup is shown in Figure 2.

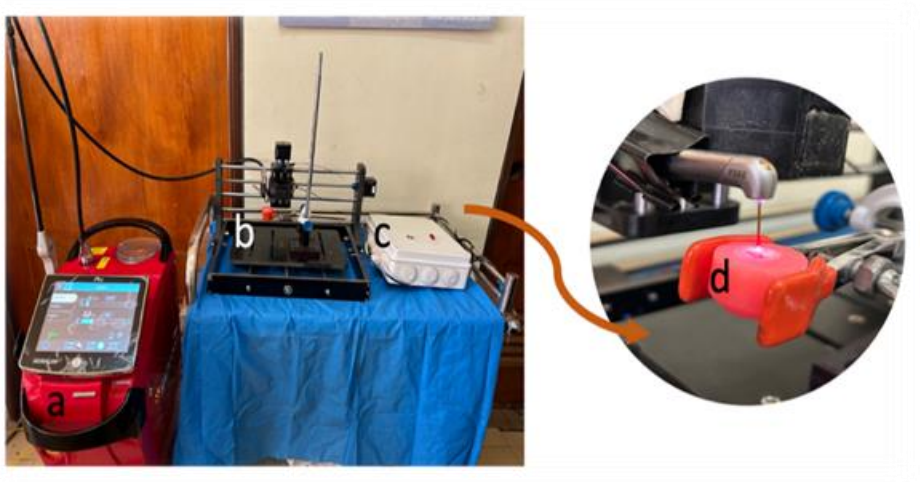

Fig.1. Left: Laser irradiation setup, a. Er;Cr:YSGG Laser, b. CNC machine, c. Power supply. Right: d. sample Irradiation.

2.4 Enamel Surface Roughness Evaluation

Samples Ra "the average distance from the profile to the mean line over the length of assessment" was found with a profilometer (SRT-6210, China). The surface roughness tester has a diamond tool with a 5 µm radius that is straight across from the sample's surface. The speed was set to 0.1 mm/sec and the cut-off distance was set to 0.25 mm. To find the surface roughness value, three measurements were taken of each sample, and the mean of those three measurements was used [24-27]. There were measurements taken before and after WSLs induction, and after laser treatment.

2.5 Scanning Electron Microscopy

A scanning electron microscope (SEM, TESCAN, VEGA II/Republic of Czech) was used to look at the features of one sample from each group. The magnification was set to 2000x. The samples were coated with gold using a sputter coating method (Emitech-K500X, Quorum Technologies, Ashford, UK) before they were analyzed by SEM.

2.6 Statistical Analysis

Different types of statistics were used to look at the data, such as descriptive statistics, a one-way analysis of variance (ANOVA), Tukey's HSD test, and the Paired t-test. The significance level that was picked was set at $p \leq 0.05$. The IBM SPSS 29 program was used to analyze the data.

4. Results

4.1 DIAGNOdent™ pen readings

According to the manufacturer's instructions, specimens with scores ranging from 14 to 20 were classified as having WSLs [28].

4.2 Enamel Surface Roughness Evaluation

The mean and standard deviation of the samples' roughness values of the study groups in addition to a one-way ANOVA test before and after WSL induction and after laser irradiation are shown in Table (1). Pairwise comparisons of roughness between groups using paired t-test after WSL induction in Table (2) and between measurements after WSL induction and after laser irradiation in Table (3).

Table 1. Roughness mean, standard deviation, and one-way ANOVA test of the study groups at baseline, after WSL induction, and after laser irradiation.

Roughness	Mean ± S.D.	Mean ± S.D.	Mean ± S.D.
Group	**Baseline**	**After WSL induction**	**After Laser irradiation**
0.75W (L1)	3.3 ± 0.27	3.40 ± 0.24	3.45 ± 0.25
0.5W (L2)	3.19 ± 0.21	3.31 ± 0.24	3.43 ± 0.27
0.25W (L3)	3.2 ± 0.32	3.45 ± 0.4	3.5 ± 0.25
*F value**	1.169	0.642	0.298
*P-value**	0.33	0.72	0.93

*One-way ANOVA

Table 2. Pairwise comparisons of roughness between groups using paired t-test after WSL induction.

Roughness	Baseline	After WSL induction	Mean difference	t-statistics	P-value
0.75W (L1)	3.3 ± 0.27	3.40 ± 0.24	-0.10	-1.02	0.30
0.5W (L2)	3.19 ± 0.21	3.31 ± 0.24	-0.12	-1.1	0.30
0.25W (L3)	3.2 ± 0.32	3.35 ± 0.4	-0.15	-1.11	0.29

Table 3. Pairwise comparisons of roughness between groups using paired t-test after WSL induction and after laser irradiation.

Roughness	After WSL induction	After laser irradiation	Mean difference	t-statistics	P-value
0.75W (L1)	3.40 ± 0.24	3.45 ± 0.25	-0.16	-1.45	0.19
0.5W (L2)	3.31 ± 0.24	3.43 ± 0.27	-0.14	-1.33	0.29
0.25W (L3)	3.35 ± 0.4	3.5 ± 0.25	-0.11	-0.73	0.48

4.3 SEM Evaluation

Figure 2 displays the morphological properties of the samples following demineralization and after laser irradiation. The SEM photos display structures at a magnification of 2.00 k. The degraded enamel surfaces in the control sample (N) subjected to demineralization solution only, had rough and etched structures accompanied by a smear layer. The L1 sample displayed imperfections characterized by rough and uneven surfaces with sharp edges, deep craters, empty interprismatic areas, pointed enamel projections, and many porosities. Additionally, no smear layer was seen. The enamel rods displayed melting and fusing when subjected to irradiation with a laser power of 0.5W and 0.25W in L2 and L3 respectively.

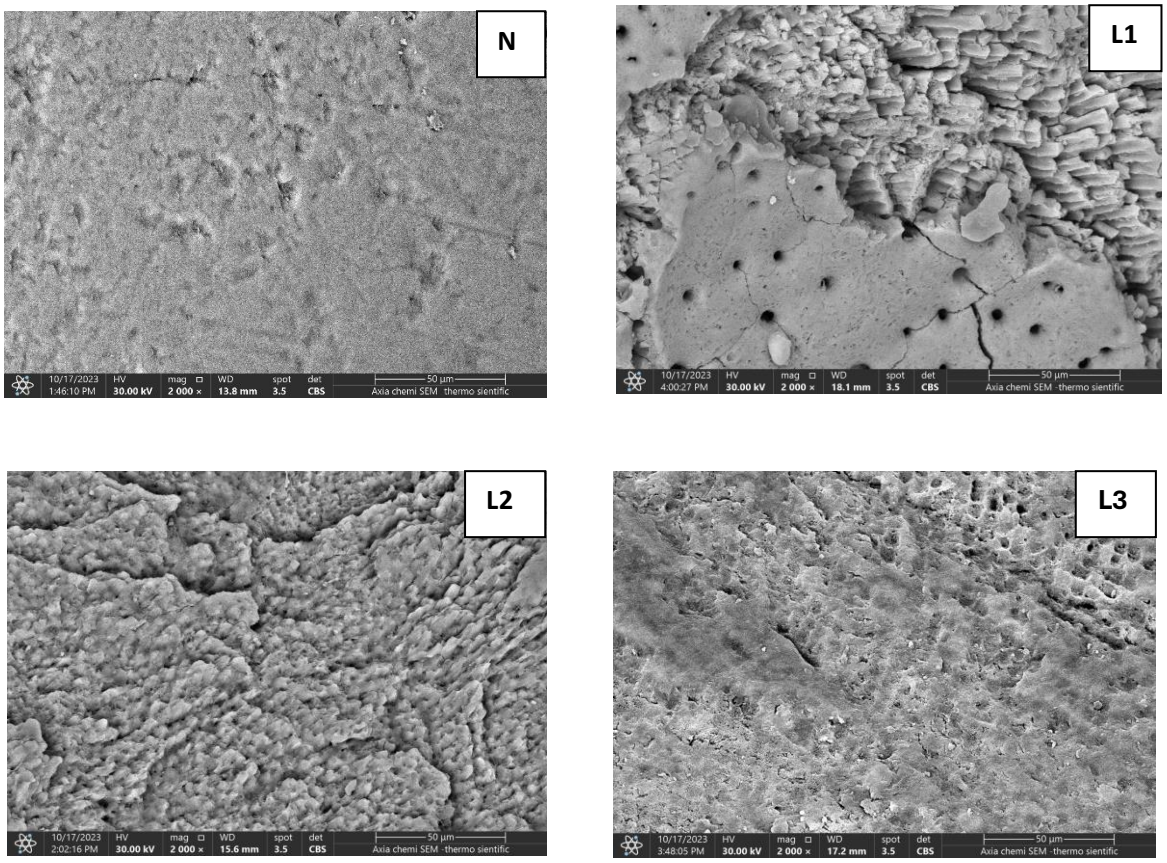

Fig.2. SEM images at 2.00k magnification of the study groups after treatment.

5. Discussion

Treatment of deciduous teeth with laser can have an impressive effect on the three heads of a triangle that involves more comfort for dentists as it decreases working time, and decreases fear feeling while childe under dental work by reducing noise and vibration associated with conventional methods of drilling and more acceptable for parents. This approach enhances the patient's comfort and willingness to cooperate [29].

To simulate the demineralization process occurring in the vicinity of the teeth in vivo, the researchers utilized acetate buffer. This choice was made because acetate buffer can stimulate the development of white spot lesions (WSLs) at a deeper and more rapid rate when compared to lactate buffer to simulate carious lesion development. Concurrently, the addition of calcium and phosphate to the acidic buffer system

resulted in the solution being partially saturated, thereby creating a surface topography similar to that of natural WSLs. The surface topography of this area is characterized by an undamaged outer surface and the removal of minerals from the underlying subsurface [18]. In addition, the pH of the demineralization solution was modified to 4.4 to promote the breakdown of hydroxyapatite and fluorapatite crystals in a cumulative process within a specific time. These crystals normally need a pH of 5.5 and 4.5 respectively to be dissolved creating initial caries, which is also proposed by Gouda et al. [30].

According to the findings of Apel et al., the ablation threshold for the Er,Cr:YSGG laser ranged from 10 to 14 J/cm² [31]. The current investigation involved the application of an Er,Cr:YSGG laser beam to the experimental groups at varying sub-ablative powers of 0.25, 0.50, and 0.75 W, and a frequency of 20Hz, air/ water ratio of 40%/ 60% and H mode. When these parameters were used, in addition to pulp vitality preservation from possible thermal damage. Demineralization of enamel was significantly reduced when these parameters were used, in addition to pulp vitality preservation from possible thermal damage resulting from laser application. MZ6 laser tip with a diameter of 600µm diameter was used to achieve high energy density with low laser power in order to focus the laser irradiation within the focal length according to the manufacturer's instruction; this was also adopted by several other researchers [32-34].

The reason of choosing frequency at 20Hz is to be clinically effective and allow ample cooling between pulses achieving the desired impact and avoiding thermal pulp injury in accordance with earlier studies as Erkmen Almaz et al. and Zezell et al. [32, 34]. In addition to water irrigation to cools oral tissues and avoids the formation of acid-soluble chemical phases. It acts as a cooler during dental laser treatment, protecting the tooth and surrounding tissues In this study, the irrigation was set to a 40% air, and 60% water ratio, which allowed for proper cleaning, and it was proven that such a ratio do not elevate pulpal temperature over the critical value preventing necrosis [7].

The finding of scanning electron microscopy (SEM) image of the control sample (N), the sample surface displayed a pattern of degraded enamel surface that was not clearly distinguishable, with a smear layer covering. The application of Er;Cr:YSGG laser, specifically at irradiation levels of 0.75W (Group L1), results in a modified morphology characterized by heightened surface irregularities, exposure of enamel rods, and non-significant increased roughness measurements with possible signs of ablation. These surface alterations and roughness were reduced as the laser power decreased. The SEM images of group L2 and L3 exhibited a decreased amount of structural alteration and fusion with partial sealing of the enamel prisms more harmonious with the 0.25W laser-irradiated group L3. Statistically, the mean difference of roughness measurements after WSL induction and after laser irradiation (L1, L2, and L3) was non-significant but increased with increased laser power. Roughness may has an impact on the preventive measures because it may enhance plaque accumulation and requires more precise oral hygiene protocols. In a study conducted by Ghabuk and Al-Shamma, treatment options with Opalustre and Sylc were investigated, and both demonstrated the ability to reduce the surface roughness of the artificial WSL. [35] The observed augmentation of surface roughness, although it was non-significant, after laser irradiation is consistent with the conclusions made by Gouda et al., Malik et al., and Sun et al. [30, 36, 37]. Gouda et al. set that the utilization of laser irradiation on an enamel surface resulted in an increased level of roughness that subsequently creates a retentive niche for fluoride, which demonstrated improved resistance to dissolution [30]. Additionally, in a study conducted by Adel et al., they concluded that Er,Cr,YSGG laser using sub-ablative parameters in histological examination, a significantly less lesion depth compared with the control group.[38]. The Er;Cr:YSGG laser penetration depth of up to 5µm, and the WSL have a minimum depth of 300-500 µm [39, 40].

The increased roughness observed after irradiation on the enamel surface is due to the sub-ablation process. The induced structural modifications by the sub-ablation process are promoted by phase transformation or melting of inorganic compounds, in addition to the expansion of the organic matrix, as reported by Ersahan and Sabuncouglu. [12]. Among the different effects of absorbed laser energy results in thermal energy conversion, which leads to the boiling of the water inside the tooth. This will lead to steam creation at high pressure, and later on will be rapidly vaporized, eventually, the previously smooth surface tooth will change to a rough surface with sharp edges. The altered surface is usually devoid of carbonization and smear layer [41]. In addition, the inclusion of water during the process of irradiation

greatly amplifies the ablation effect, as Erbium lasers exhibit a pronounced affinity for water. Colucci et al. (2015) found that there is an inverse relationship between the quantity of water and the laser's intensity on the enamel surface [42].

The parameters used in this study could be recommended as they did not significantly increase the surface roughness of the primary teeth enamel. The determination of appropriate laser parameters is of significant relevance, as the presence of damage and alterations in the enamel surface can lead to the development of biofilms and the invasion of germs [32].

6. Conclusions

Within the limitation of this study, a non-significant increase in surface roughness of the primary teeth enamel with WSL after sub-ablative power irradiation with Er;Cr:YSGG laser, with a rough and irregular surface devoid of smear layer, the roughness increase was proportional with the increased irradiation power.

References

[1] Abdel-Hakim SM, Metwalli N, El-Askary F, Wassel M. Microhardness, sem and color change analysis of artificial enamel lesions in primary teeth treated with resin infiltration, CPP-ACP or fluoride gel: An in vitro study. Egypt Dent J. 2016;62:3735–44. [Google Scholar]
[2] Assarzadeh H, Karrabi M, Fekrazad R, Tabarraei Y. Effect of Er:YAG Laser Irradiation and Acidulated Phosphate Fluoride Therapy on Re-Mineralization of White Spot Lesions. J Dent (Shiraz). 2021 Sep;22(3):153-161. doi: 10.30476/DENTJODS.2020.86300.1187. PMID: 34514061; PMCID: PMC8417547.
[3] Ahmed Adnan Hadi, Basima Mohammed Ali, Role of Er.Cr: YSGG Laser and Fluoride in Caries Resistance, J Res Med Dent Sci, 2022, 10 (8): 019-025.
[4] Mandava J, Reddy YS, Kantheti S, Chalasani U, Ravi RC, Borugadda R, et al. Microhardness and penetration of artificial white spot lesions treated with resin or colloidal silica infiltration. J Clin Diagn Res. 2017;11:C142–6. [PMC free article] [PubMed] [Google Scholar]
[5] Jahanimoghadam F, Poureslami H, Shamsaddin H, Horri A, Khazaeli P, Mahvi AH. Effect of Er:YAG laser on sodium fluoride varnish uptake by primary tooth enamel: an in-vitro study. Res Report Fluoride 2016 Oct-Nov;49: 538-48.
[6] Rezaei Y, Bagheri H, Esmaeilzadeh M. Effects of laser irradiation on caries prevention. J Lasers Med Sci 2011; 2(4):159-64.
[7] Molaasadollah F, Asnaashari M, Mashhadi Abbas F, Jafary M. In Vitro Comparison Of Fluoride Gel Alone and in Combination With Er,Cr:YSGG Laser on Reducing White Spot Lesions in Primary Teeth. J Lasers Med Sci. 2017 Fall;8(4):160-165. doi: 10.15171/jlms.2017.29. Epub 2017 Sep 27. PMID: 29071020; PMCID: PMC5642162.
[8] Ramos TM, Ramos-Oliveira TM, de Freitas PM, Azambuja N Jr, Esteves-Oliveira M, Gutknecht N, de Paula Eduardo C. Effects of Er:YAG and Er,Cr:YSGG laser irradiation on the adhesion to eroded dentin. Lasers Med Sci. 2015 Jan;30(1):17-26. doi: 10.1007/s10103-013-1321-6. Epub 2013 May 7. PMID: 23649611.
[9] Ramalho KM, Hsu CY, de Freitas PM, Aranha AC, Esteves-Oliveira M, Rocha RG, de Paula Eduardo C. Erbium Lasers for the Prevention of Enamel and Dentin Demineralization: A Literature Review. Photomed Laser Surg. 2015 Jun;33(6):301-19. doi: 10.1089/pho.2014.3874. PMID: 26067939.
[10] Subramaniam P, Pandey A. Effect of erbium, chromium: yttrium, scandium, gallium, garnet laser and casein phosphopeptide-amorphous calcium phosphate on surface micro-hardness of primary tooth enamel. Eur J Dent. 2014 Jul;8(3):402-6.
[11] Zamataro CB, Ana PA, Benetti C, Zezell DM. Influence of Er,Cr:YSGG laser on CaF_2 -like products formation because of professional acidulated fluoride or to domestic dentifrice application. Microsc Res Tech. 2013 Jul;76(7):704-13. doi: 10.1002/jemt.22221. Epub 2013 Apr 30. PMID: 23630046.
[12] Ersahan S, Alakus Sabuncuoglu F. Effect of surface treatment on enamel surface roughness. J Istanb Univ Fac Dent.2016; 50(1):1-8.
[13] Nogueira RD, Silva CB, Lepri CP, Palma-Dibb RG, Geraldo-Martins VR. Evaluation of Surface Roughness and Bacterial Adhesion on Tooth Enamel Irradiated With High Intensity Lasers. Braz Dent J. 2017 Jan-Feb;28(1):24-29. doi: 10.1590/0103-6440201701190. PMID: 28301014.

[14] Nickolaos Z. Kallis. Evaluation of Enamel Surface Roughness After Laser Removal of Clear Aligner Attachments. Master's thesis. Nova Southeastern University. Retrieved from NSUWorks, College of Dental Medicine. 2017. (116)
https://nsuworks.nova.edu/hpd_cdm_stuetd/116.
[15] Salman SQ, Hussein BMA. Topographical Analysis of Human Enamel after Phosphoric Acid Etching and Er,Cr:YSGG Laser Irradiation. J Lasers Med Sci. 2023 Dec 28;14:e68. doi: 10.34172/jlms.2023.68. PMID: 38318223; PMCID: PMC10843234.
[16] Alyaa J. Abdulwahed, and Saher Sami Gasgoos. (2021). Effect of Er, Cr:YSGG and Diode lasers on surface roughness of enamel around composite restoration: an in vitro study. International Journal Dental and Medical Sciences Research Volume 3, Issue 5, Sep-Oct 2021 pp 1237-1243 www.ijdmsrjournal.com ISSN: 2582-6018
[17] Rahee SS, Jehad RH. Comparing the effectiveness of using three different re-mineralizing pastes on remineralisation of artificially induced white spot lesion. J Bagh Coll Dent [Internet]. 2023 Dec. 15; 35(4):35-4. Available from: https://jbcd.uobaghdad.edu.iq/index.php/jbcd/article/view/3512
[18] Mubarak RM, Hussein BM. Effect of post preparation dentinal hypersensitivity treatment by fractional CO2 (10600 nm) laser on shear bond strength of resin cement to dentin: in vitro study. J Res Med Dent Sci. 2023;11(1):65–72. [Google Scholar]
[19] Soltanimehr E, Bahrampour E, Yousefvand Z. Efficacy of diode and CO2 lasers along with calcium and fluoride-containing compounds for the remineralization of primary teeth. BMC Oral Health. 2019 Jun 19;19(1):121. doi: 10.1186/s12903-019-0813-6. PMID: 31217005; PMCID: PMC6585004.
[20] Mashhour, A., Allam, G. & Wassel, M. Comparative evaluation of prevention of demineralization of artificial enamel caries treated with two fluoride varnishes and 38% SDF in primary teeth: an in vitro study. BMC Oral Health 23, 110 (2023). https://doi.org/10.1186/s12903-023-02799-1
[21] Abdulkareem, Abeer & Hussain, & Rafeeq, Reem & Al-Ani, Reem. (2022). Efficacy of Three Commercially Available Fluoride Releasing Varnishes in Remineralization of Artificial White Spot Lesions Evaluated by Laser Fluorescence: An In Vitro Study. Dental Hypotheses. 13. 117-120.
[22] Yilmaz N, Baltaci E, Baygin O, Tüzüner T, Ozkaya S, Canakci A. Effect of the usage of Er,Cr:YSGG laser with and without different remineralization agents on the enamel erosion of primary teeth. Lasers Med Sci. 2020 Sep;35(7):1607-1620. doi: 10.1007/s10103-020-03015-0. Epub 2020 May 29. PMID: 32472426.
[23] Noor Bader Hassan, Basima Mohammed Ali Hussein, Ahmed Ali Mohammed, "Role of CO2 Laser on SBS between Dental Porcelain and Composite Resin Repair Process", International Journal of Dentistry, vol. 2023, Article ID 1427183, 12 pages, 2023. https://doi.org/10.1155/2023/1427183
[24] Noor Azad Mohammed, Zainab F. Al-Bawi, Balsam saadi Abdulhameed. Evaluation of Lithium Disilicate Surface Morphology Treated with Er,Cr:YSGG and Fractional CO2 Laser . Iraqi Journal of Laser, 2023, 22(2), pp. 71–79. doi:10.31900/ijl.v22i2.408.
[25] Alzaidy AA, Abd-alla MH. The effect of different curing distances on the microhardness of flowable bulk-fill composite materials. J Bagh Coll Dent [Internet]. 2023 Dec. 15; 35(4):20-7. Available from: https://jbcd.uobaghdad.edu.iq/index.php/jbcd/article/view/3507
[26] Hassan, Noor & Hussein, Basima. Intraoral Repair of Dental Ceramics Using Er,Cr:YSGG Laser: Review. Iraqi Journal of Laser. (2023). 22. 27-34. 10.31900/ijl.v22i2.382.
[27] Mubaraq RM, Hussein BM. PDF Influence of Er: Cr; YSGG laser Desensitization on SBS of resin cement to dentin. Iraqi Journal of Laser. 2022 Jun 30;21(1):18-27.
[28] González-Soteloa A, Rodríguez-Vilchisb LE, ContrerasBulnesb R. Effect of Er:YAG and Fluoride Varnishes for Preventing Primary Enamel Demineralisation. Oral Health Prev Dent. 2019; 17: 317–321
[29] Jacboson B, Berger J, Kravitz R, Patel P. Laser pediatric crowns performed without anesthesia: A contemporary technique. J Clin Pediatr Dent 2003;28:11-2
[30] Gouda, Samah & Khairy, Mohamed & el Wakeel, Aliaa. Remineralization of Enamel White Spot Lesion Using Erbium Chromium LASER, Fluoride Varnish or the Combination of Both Versus Sound Enamel: In Vitro Study. Egyptian Dental Journal. (2024). 70. 889-897. 10.21608/edj.2023.249483.2786.
[31] Apel C, Meister J, Ioana RS, Franzen R, Hering P, Gutknecht N. The ablation threshold of Er:YAG and Er:YSGG laser radiation in dental enamel. Lasers Med Sci. 2002;17(4):246-52. doi: 10.1007/s101030200036. PMID: 12417978.
[32] Erkmen Almaz M, Ulusoy NB, Akbay Oba A, Erdem Ü, Dogan M. Thermal, morphological, and spectral changes after Er, Cr:YSGG laser irradiation at low fluences on primary teeth for caries prevention. Microsc Res Tech. 2020;1–10. https://doi.org/10.1002/jemt.23637 23637
[33] Fekrazad R, Ebrahimpour L. Evaluation of acquired acid resistance of enamel surrounding orthodontic brackets irradiated by laser and fluoride application. Lasers Med Sci. 2014 Nov; 29 (6):1793-8.

[34] Zezell DM, Boari HG, Ana PA, Eduardo Cde P, Powell GL. Nd:YAG laser in caries prevention: a clinical trial. Lasers Surg Med. 2009 Jan;41(1):31- 5.
[35] Chabuk MM, Al-Shamma AM. Surface roughness and microhardness of enamel white spot lesions treated with different treatment methods. Heliyon. 2023 Jul 18;9(7):e18283. doi: 10.1016/j.heliyon.2023.e18283. PMID: 37539286; PMCID: PMC10395522.
[36] Malik A, Parmar G, Bansal P, Bhattacharya A, Joshi N. Effect of laser and fluoride application for prevention of dental caries: A polarized microscope analysis. J Dent Lasers. 2015;9(1):11- 5.
[37] Sun X, Ban J, Sha X, Wang W, Jiao Y, Wang W. Effect of Er,Cr:YSGG Laser at Different Output Powers on the Micromorphology and the Bond Property of Non-Carious Sclerotic Dentin to Resin Composites. PLoS ONE ,2015;10(11): e0142311.
[38] Adel SM, Marzouk ES, El-Harouni N. Combined effect of Er,Cr:YSGG laser and casein phosphopeptide amorphous calcium phosphate on the prevention of enamel demineralization. Angle Orthod. 2020 May 1;90(3):369-375. doi: 10.2319/032819-238. PMID: 33378425; PMCID: PMC8032298.
[39] GAHLOT, N. & HIREMATH, V. R. 2021. Lasers in Dentistry. Oral Rehabilitation, 12, 34.
[40] Sadikoglu, Ismail Serhat. (2020). White Spot Lesions: Recent Detection and Treatment Methods. Cyprus Journal of Medical Sciences. 5. 10.5152/cjms.2020.1902.
[41] Sawan MN, Hussain N, Alkurdi MM. Etching of enamel by laser energy for direct bonding of orthodontic appliance and evaluation of shear bond strength. Energy Procedia.2015; 74:1452–1458.
[42] Colucci V, de Souza Gabriel AE, Scatolin RS, Serra MC, Corona SA. Effect of Er:YAG laser on enamel demineralization around restorations. Lasers Med Sci. 2015 May;30(4):1175-81. doi: 10.1007/s10103-014-1534-3. Epub 2014 Feb 13. PMID: 24522657.

تضاريس سطح الاسنان اللبنية بعد التشعيع بالليزر : دراسة مختبرية

صبا عامر عبد مهدي ، باسمه محمدعلي حسين

معهد الليزر للدراسات العليا، جامعة بغداد، بغداد، العراق

*البريد الالكتروني للباحث: sabaamer804@gmail.com

الخلاصة

الهدف: لتقييم تأثير معلمات التشعيع تحت الاستئصالي لليزر Er;Cr:YSGG على التضاريس السطحية لمينا الاسنان اللبنية مع آفات البقع البيضاء.

الطرق: تم إخضاع ما مجموعه 40 سناً خلفياً لبنياً بمينا سليمة في البداية إلى محلول نزع المعادن عند (PH 4.4) لتحفيز آفات البقع البيضاء بشكل مصطنع. ثم تم تقسيمها عشوائياً إلى أربع مجموعات (العدد= 10): مجموعة التحكم(N) ، المجموعة L1 المشعة بليزر 0.75 واط، المجموعة L2 المشعة بليزر 0.5 واط، والمجموعة L3 المشعة بليزر 0.25 واط. تم تقييم التضاريس السطحية باستخدام مقياس خشونة السطح والمجهر الإلكتروني الماسح.

النتائج: كشف تقييم خشونة السطح مع صور المجهر الإلكتروني الماسح عن زيادة غير ملحوظة في خشونة السطح بعد عملية إزالة المعادن. يؤدي تشعيع الليزر بقوى مختلفة إلى زيادة غير ملحوظة في خشونة السطح مع تغير التضاريس وتأثير أكثر وضوحًا مع مجموعة الليزر L1 وبدرجة أقل المجموعتين L2 و L3.

الاستنتاجات: زيادة خشونة سطح مينا الأسنان اللبنية بعد تشعيع الطاقة شبه الاستئصالية باستخدام ليزر Er;Cr:YSGG ، مع سطح خشن وغير منتظم خالٍ من طبقة اللطاخة، وكانت زيادة الخشونة متناسبة مع زيادة قوة التشعيع.

IJL, Issue 2, Vol. 23, 2024
https://doi.org/10.31900/ijl.v23i2.488

Research Article

IRAQI JOURNAL OF LASER

Impact of Low Level Laser Therapy on Mandibular Range Motion in Temporomandibular Joint Disorder in Iraqi Patients

Haidar Flayyih Hasan[1,*], Layla M. H. Al-ameri[1], Ammar Saleh Alalawi[2]

[1]*Institute of Laser for Postgraduate Studies, University of Baghdad, Baghdad, Iraq*
[2]*Department of Maxillofacial Surgery, Al-Imamain Al-Kadhimain Medical City, Baghdad, Iraq*
* *Email address of the Corresponding Author:Haidar.hasan2102m@ilps.uobaghdad.edu.iq*

Article history: Received 13 Jul. 2024; Revised 21 Aug. 2024; Accepted 27 Aug. 2024; Published online15 Dec. 2024

Abstract

Background: Temporomandibular disorder (TMD) is a painful condition that specifically affects the muscles, bones, and temporomandibular joint (TMJ). Pain can vary in intensity, ranging from mild to moderate or severe. It is often accompanied by limited movement of the jaw, resulting in a restriction of mouth opening.
Aim of the study: The purpose of this study was to determine the effect of low-level laser therapy on mandibular range of motion in patients with temporomandibular joint disorders.
Patients and methods: fifteen patients were randomly selected. The mandibular range of motion was evaluated for each patient before treatment and after 3 months, a dual-wavelength (810-980nm) diode laser was used in this study. Three main criteria were utilized in the statistical calculation, they are relaxed mouth opening, full mouth opening, and lateral mandibular movement. Paired t-test and one-way analysis of variance (ANOVA) tests were used for statistical analysis.
Results: The study revealed a significant enhancement in mandibular range of motion in TMD patients during a short period of laser sessions.
Conclusion: Low-level laser therapy is an efficient way to improve the mandibular range of motion in patients with temporomandibular joint disorder.

Keywords: Dual wavelength (810-980nm) diode laser, Low-level laser therapy, Mandibular range of motion, Temporomandibular joint disorder.

1. Introduction

Temporomandibular disorders (TMD) encompass a wide range of conditions that impact the temporomandibular joint (TMJ) and the associated musculoskeletal systems. Temporomandibular disorder (TMD) impairs the regular operation of the temporomandibular joint (TMJ) and results in pain, limited jaw movements, and impaired chewing[1]. An audible clicking or popping noise occurs while the mouth is being opened or closed[2, 3].

The main goals of treatment for individuals with temporomandibular disorders (TMD) are to alleviate discomfort, restore normal chewing ability, increase the range of motion of the jaw, and improve the overall quality of life for patients[4, 5]. The available treatments vary from non-invasive procedures to invasive procedures. While surgical techniques can provide assistance in certain instances[6], it is advisable to prioritize conservative therapy as the initial therapeutic choice. Conservative treatments encompass behavioral therapy, pharmaceutical interventions, and low-level laser therapy (LLLT)[7].

Behavioral therapy is a treatment approach that is rooted in psychology and is recommended for patients who experience chronic temporomandibular disorder pain. This therapy is safe and does not require any invasive procedures. It includes various techniques such as cognitive behavioral therapy, biofeedback, re-education, and relaxation techniques. The goal of this therapy is to reduce pain-related disabilities and improve coping skills by enhancing cognitive and adaptive behaviors[8].

Low-level laser therapy (LLLT) has lately been employed as a conservative treatment modality for persons suffering from temporomandibular disorder (TMD) and myofascial pain[9, 10]. Low-level laser treatment (LLLT) is a type of phototherapy that stimulates biological processes and relieves pain without inducing changes in temperature[11, 12]. The therapy technique is regarded as successful, straightforward, and short-term[13]. It has become popular as an alternative treatment for TMD because of its pain-relieving, anti-inflammatory, and regenerative capabilities[14, 15].

2. Hypothesis

H0: LLLT is not-significantly effective in improving relaxed mouth opening, full mouth opening, and lateral mandibular movement in patients with temporomandibular disorder. H1: LLLT is significantly effective in improving relaxed mouth opening, full mouth opening, and lateral mandibular movement in patients with temporomandibular disorder.

3. Patients and methods

3.1 Study design

This study employed a randomized clinical trial design, with a total of 15 participants. The sample consisted of 11 female and 4 male individuals, with an average age of 31.4 years. The participants in this study were selected from the Department of Oral and Maxillofacial Surgery at Al-Hussein Teaching Hospital in Al-Samawa City. The study received ethical approval from the Research Scientific Committee of Laser Institute, with reference number 1377 on 17/10/2023. Prior to their inclusion in the study, all patients signed a consent agreement before laser sessions.

3.2 Laser system

The apparatus utilized was a Quicklase laser device as in Figure 1. The laser emits light with a dual wavelength of 810-980nm in a continuous mode. A specific handpiece or prism is utilized to deliver the laser radiation in a contact manner, applying the low-power laser to the affected site for 30 seconds for each trigger point. The output power was set to 400 milliwatts. According to the diameter of the prism tip, the spot size was 4 cm. Laser therapy was delivered at many sites on the affected muscle during each session.

3.3 Laser components

The following are the laser device accessories as shown in Figure 1.

a) Laser device
b) Electrical cable
c) Prism
d) Pain therapy

e) Foot switch
f) Fiber optic
g) Goggles

Fig.1. laser apparatus and components.

3.4 Patient selection

3.4.1 Criteria for inclusion and exclusion:

In order to be eligible for participation in the study, patients are required to have a diagnosis based on the Research Diagnostic Criteria for Temporomandibular Disorders (RDC of TMD) as shown in Figure 2 briefly.The study did not include patients who had previously performed TMJ surgical intervention, had a history of radiation therapy or chemotherapy, had an inflammatory or pathological joint disease, had facial trauma, or had congenital dyscrasia such as hyperplasia or hypoplastic changes of the joint.

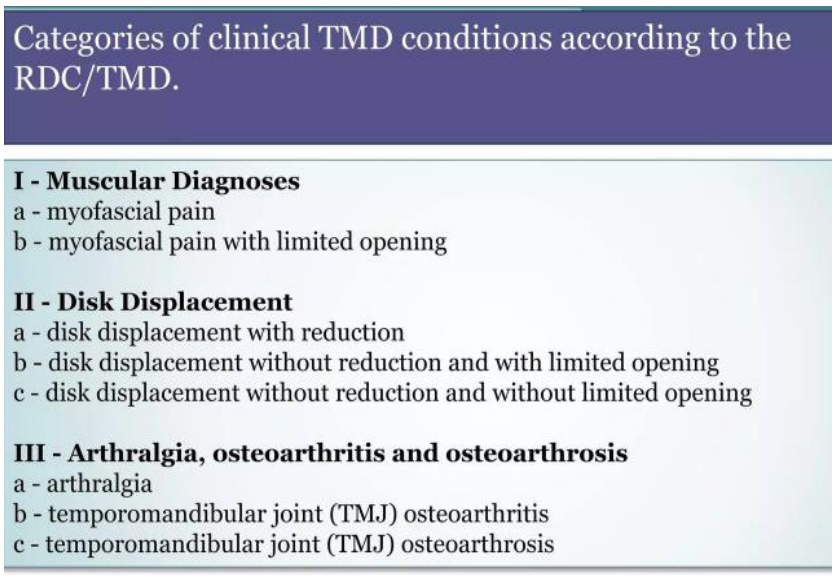

Fig. 2. RDC/TMD (The research diagnostic criteria for temporomandibular disorders is an informative tool used by Schiffman in 1992 to facilitate the diagnosis of the disorder).

3.5 Laser application

The patients underwent low-level laser therapy (LLLT) treatment following a specific protocol. The laser was administered to the tender muscle area twice a week for a total of two weeks, resulting in a total of four treatment sessions as in Figure 3.

Fig. 3: Laser administration.

4. Statistical analysis

Continuous variables were expressed as means and standard deviations or medians with range, depending on whether the distribution was normal or skewed. The categorical variables were represented using frequency and percentages. The One-way repeated measure ANOVA was employed to examine the variations in mean values during the follow-up periods for parametric variables, while the Friedman Rank sum test was utilized for non-parametric variables to assess differences in medians. Furthermore, Cochran's Q test was employed to analyze dichotomous variables. A P-value below 0.05 was deemed to be statistically significant. The data processing, visualization, and statistical analysis were performed using R software packages, specifically dplyr, gt_summary, and ggplot.

5. Results

The study had a cohort of 15 participants, with a mean age of 31.4 years and a standard deviation of 8.3 years. The participants were distributed depending on sex, with 73.3% (n=11) being female and 26.7% (n=4) being male. The sex ratio was calculated to be 0.36, which is known as the female-to-male ratio as shown in Table 1.

Table 1. Description of patient's demographics.

Characteristic	value
Sample size	15
Age	31 ± 8
Gender	11 (73.3%) Female 4 (26.7%) Male
Sex ratio	0.36

[1]Mean ± SD; n (%)

5.1 Statistical criteria

a) Relaxed mouth opening.
Refer to the interincisal distance between the upper and lower central incisor tips in an unassessed vertical mouth open without any force.
b) Full mouth opening.
Refer to the interincisal distance between the upper and lower central incisor tips in a maximum and stressful vertical mouth open.
c) Lateral mandibular movement.
Refer to the horizontal distance between the midlines of upper and lower central incisors.
All these findings were measured by digital vernier.
Functional outcomes were assessed by measuring the first relaxed mouth opening (30.1 ± 8.4 mm), full mouth opening (39.6 ± 9.4 mm), and lateral mandibular movement (7.7 ± 2.8 mm). Further assessments conducted at different time intervals showed that there were insignificant changes in full mouth opening ($p = 0.23$) and relaxed mouth opening ($p = 0.5$). However, there were significant differences observed in lateral mandibular movement ($p < 0.001$) as the following Table 2.

Table 2. Description of clinical parameters stratified by the follow-up time (N=15).

	Baseline[1]	1-week[1]	2-weeks[1]	1-month[1]	3-months[1]	P-value[2]
Relaxed mouth opening (mm)	30.1 ± 8.4	31.0 ± 9.1	30.9 ± 6.5	32.1 ± 6.2	32.0 ± 6.7	0.5
Full mouth opening (mm)	39.6 ± 9.4	40.0 ± 8.5	40.6 ± 7.7	40.1 ± 6.4	42.7 ± 6.3	0.23
Lateral mandibular movement (mm)	7.7 ± 2.8	9.3 ± 3.2	8.6 ± 3.0	10.1 ± 2.4	10.7 ± 2.7	**<0.001**

[1]Mean ± SD; n (%); Median (Range)
[2]One-Way Repeated Measure ANOVA; Friedman Rank Sum Test; Cochran's Q test.

6. Discussion

Individuals diagnosed with temporomandibular disorder (TMD) frequently encounter limited jaw motions and discomfort in the temporomandibular joint (TMJ) region, as well as the muscles involved in chewing and other maxillofacial musculature[15, 16].
The primary aim of this study was to treat the disorder of mandibular motion through a few sessions of laser, hence improving the mandibular range of motion by utilizing a dual-wavelength diode laser(810-980nm), resulting in fewer visits and more significant outcomes.
In this study, a significant p-value <0.001 has been achieved in lateral mandibular movement, with a baseline of 7.7 mm and 10.7 mm after three months of follow-up, since the affected muscle was lateral pterygoid, the lateral movement was enhanced by the accused muscle. this contradicts the findings of Venancio et al. with 0.1762 (right lateral movement) and 0.4143 (left lateral movement) p-values, where the baseline readings 7.69 mm (right lateral movement) and 6.66 mm (left lateral movement) become 8.78 mm and 7.54 mm, respectively[17]. However, it is similar to the findings of Máximo et al.[18]

While vertical mouth opening revealed p-values for both relaxed mouth opening 0.5, and full mouth opening 0.23, with a baseline of 30.1 mm and 39.6 mm, respectively, to become 32.0 mm and 42.7 mm, respectively, after three months of follow-up, also this enhancement in the vertical mouth opening is related to the laser effect on the responsible muscles which were the temporalis and masseter.
This resembles De Godoy et al. with p-values 0.1816 and 0.1727 for maximum active opening and maximum passive opening respectively[19].
It also mimics Catao et al., who got a mouth opening average of 46.34 mm, and after that, the mouth opening increased to 50.05 mm[20].

Low-level laser therapy may not generate thermotherapy[21]. Instead, it may initiate photochemical reactions that may stimulate mitochondrial metabolism[22], boost ATP production, enhance tissue oxygenation through the induction of vascularization, and elevate serotonin and endorphin levels[23, 24]. The laser light used in this field is mostly limited to the range of the red or near-infrared region of the electromagnetic spectrum, specifically between 600 and 1000 nm[25] so in this research, the "Quicklase" 810-980 nm diode laser device was used. The primary chromophore for this wavelength is cytochrome c oxidase [26], which are substances that selectively absorb laser energy. However, in comparison to shorter wavelengths (below 600nm), this chromophore (cytochrome c oxidase) demonstrates the minimum absorption rate for the shorter wavelengths and maximum absorption for the higher (810-980 for example). This is advantageous because laser light in these wavelengths has more penetration inside the tissues so that stimulation of the underlying muscles would occur [25, 27].
Multiple researchers have discovered that mitochondria, particularly the enzyme known as cytochrome c oxidase of the respiratory chain, selectively absorb laser light at these wavelengths [28, 29]. Cytochrome c oxidase plays a role in the production of ATP and also regulates reactive oxygen species[30]. This leads to increased production of growth factors, cell proliferation, and higher amounts of inflammatory mediators and oxygen in the tissue[31].

Our investigation revealed a noteworthy enhancement in mandibular movement among 12 out of 15 individuals, along with improved lateral mandibular movement.
Based on the clinical parameters, the p-values for relaxed mouth opening and full mouth opening were found to be insignificant (0.5 and 0.23, respectively). This means that we cannot rely on these measurements as clinical criteria or diagnostic features in the treatment of temporomandibular joint disorder.

7. Conclusions

It is concluded that low-level laser therapy of diode dual wavelength (810-980 nm) is an important therapeutic modality in case of restricted mandibular movement that is accompanied by temporomandibular joint disorder.

References

[1] Al-Kufi, H.M. and A.M. Al-Bayati, Efficacy of photobiomodulation therapy (PBMT) in management of temporomandibular disorder (TMD). Lasers in Dental Science, 2023. **7**(2): p. 77-83.
[2] Emam, A.-N.M., et al., Efficacy of occlusal splints and low-level laser therapy on the mandibular range of motion in subjects with temporomandibular joint disc displacement with reduction. Journal of International Society of Preventive and Community Dentistry, 2023. **13**(3): p. 229-236.
[3] Ismael, W.K., T. AbdulLateef, and M.K. Shumran, An analysis of the efficacy of platelet-rich plasma injections on the treatment of internal derangement of a temporomandibular joint. Journal of Baghdad College of Dentistry, 2017. **29**(3): p. 39-44.
[4] Gil-Martínez, A., A. Paris-Alemany, I. López-de-Uralde-Villanueva, and R. La Touche, Management of pain in patients with temporomandibular disorder (TMD): challenges and solutions. Journal of pain research, 2018: p. 571-587.
[5] Al-Nakib, L.H., A.O. Abdullah, S.A. Abd Al-Kareem, and S.H. Ali, An Assessment of Sagittal Condylar Position of TMJ Dysfunction in Centric Occlusion by Using Cone Beam Computed Tomography. Journal of Baghdad College of Dentistry, 2016. **28**(2): p. 58-62.

[6] Alshamaa, A. and T. Aldelaimi, Treatment of myogenic temporomandibular joint disorders with diode laser and pharmacotherapy (comparative study). Int Med J, 2020. **25**: p. 461.
[7] Ali, O.A., Z.F. Mahdi, and B.S. Abdulhameed, Efficacy of low-level laser therapy on postoperative sequelae following extraction of impacted mandibular third molars. Iraqi Journal of Laser, 2024. **23**(1): p. 1-11.
[8] Liu, H., et al., The effectiveness of cognitive-behavioural therapy for temporomandibular disorders: a systematic review. Journal of oral rehabilitation, 2012. **39**(1): p. 55-62.
[9] Al-Khassaki, A.I., et al., Evaluation of Anti-nociceptive Activity of 940 Nanometer Low Level Laser Therapy on Temporomandibular Joint in Rats. Prof. RK Sharma, 2019. **13**(1): p. 259.
[10] Al-saadi, M.A., Chronic Orofacial Pain Management: A Narrative Review of Pharmacological and Promising Therapy. Medical Journal of Babylon, 2023. **20**(1): p. 24-27.
[11] Al-ameri, L.M. and R.A. Faris, Biochemical immune effects of low power laser irradiation on leukemia and breast cancer: A review. EurAsian Journal of Biosciences, 2020. **14**(2).
[12] Al-Ameri, L.M., et al., Cell Cycle Response to Low Power Laser Irradiation in Jurkat E6. 1 T-lymphocyte Cell Line. Cell Cycle, 2014. **4**(11).
[13] Abbas, Q.K. and L.M. Al-ameri, Photodynamic effect of Rose Bengal activated by low-level laser light on S. aureus. Iraqi Journal of Laser, 2022. **21**(2): p. 48-57.
[14] Madani, A., F. Ahrari, A. Fallahrastegar, and N. Daghestani, A randomized clinical trial comparing the efficacy of low-level laser therapy (LLLT) and laser acupuncture therapy (LAT) in patients with temporomandibular disorders. Lasers in medical science, 2020. **35**: p. 181-192.
[15] Ahmad, S.A., et al., Low-level laser therapy in temporomandibular joint disorders: a systematic review. Journal of Medicine and Life, 2021. **14**(2): p. 148.
[16] Medhat, A.H. and A.H. Al Haidar, Maximum bite force in relation to maximum mouth opening among primary school children. Journal of Baghdad College of Dentistry, 2019. **31**(4).
[17] De Abreu Venancio, R., C.M. Camparis, and R. De Fátima Zanirato Lizarelli, Low intensity laser therapy in the treatment of temporomandibular disorders: a double-blind study. Journal of oral rehabilitation, 2005. **32**(11): p. 800-807.
[18] Máximo, C.F.G.P., J.F. Coêlho, S.D. Benevides, and G.Â.d.S. Alves. Effects of low-level laser photobiomodulation on the masticatory function and mandibular movements in adults with temporomandibular disorder: a systematic review with meta-analysis. in CoDAS. 2022. SciELO Brasil.
[19] de Godoy, C.H.L., et al., Effect of low-level laser therapy on adolescents with temporomandibular disorder: a blind randomized controlled pilot study. Journal of oral and maxillofacial surgery, 2015. **73**(4): p. 622-629.
[20] Catão, M.H.C.d.V., P.S.d. Oliveira, R.d.O. Costa, and V.S.M. Carneiro, Evaluation of the efficacy of low-level laser therapy (LLLT) in the treatment of temporomandibular disorders: a randomized clinical trial. Revista CEFAC, 2013. **15**: p. 1601-1608.
[21] Ren, H., et al., Comparative effectiveness of low-level laser therapy with different wavelengths and transcutaneous electric nerve stimulation in the treatment of pain caused by temporomandibular disorders: A systematic review and network meta-analysis. Journal of oral rehabilitation, 2022. **49**(2): p. 138-149.
[22] Pruitt, T., et al., Photobiomodulation at different wavelengths boosts mitochondrial redox metabolism and hemoglobin oxygenation: lasers vs. light-emitting diodes in vivo. Metabolites, 2022. **12**(2): p. 103.
[23] Ergün, G., E. Atalar, and G. Aydın, Assessment of the efficiency of low level laser therapy in women with primary fibromyalgia syndrome: a randomized, placebo-controlled, double-blind study. Acta Oncologica Turcica. **53**(2): p. 288-293.
[24] Tam, G., Low power laser therapy and analgesic action. Journal of clinical laser medicine & surgery, 1999. **17**(1): p. 29-33.
[25] Freitas, P.M. and A. Simoes, Lasers in dentistry: guide for clinical practice. 2015: John Wiley & Sons.
[26] Tseng, S.-H., P. Bargo, A. Durkin, and N. Kollias, Chromophore concentrations, absorption and scattering properties of human skin in-vivo. Optics express, 2009. **17**(17): p. 14599-14617.
[27] Al-Tamemi, E.I., Analysis of inflammatory cells in osseointegration of CpTi implant radiated by low level laser therapy. J Baghdad Coll Dent, 2015. **27**(1): p. 105-110.
[28]2022, Mary Ann Liebert, Inc., publishers 140 Huguenot Street, 3rd Floor New …. p. 75-77.
[29] Al-ameri, L.M., Laser Biostimulation Effect on Human Sperm Motility. Iraqi Journal of Laser, 2021. **20**(1): p. 39-42.
[30] Watson, S.A. and G.P. McStay, Functions of cytochrome c oxidase assembly factors. International Journal of Molecular Sciences, 2020. **21**(19): p. 7254.
[31] Assi, A.A., R.A. Faris, B.S. Abdulhameed, and S.S. Almalki, The Effect of Dual Diode Laser:(810,980) nm in Acceleration of Orthodontic Tooth Movement: A Case Report. Iraqi Journal of Laser, 2023. **22**(2): p. 19-26.

تأثير الليزر منخفض المستوى على مدى حركات الفك السفلي في اضطراب المفصل الفكي الصدغي لدى المرضى العراقيين.

حيدر فليح حسن[1] , ليلى محمد حسن[1] , عمار صالح العلوي[2]

[1]معهد الليزر للدراسات العليا، جامعة بغداد، بغداد، العراق
[2]فرع جراحة الوجه والفكين, مدينة الامامين الكاظمين الطبية, بغداد, العراق.

*البريد الالكتروني للباحث: Haidar.hasan2102m@ilps.uobaghdad.edu.iq

الخلاصة

مقدمة: اضطراب المفصل الفكي الصدغي هو حالة من الألم تصيب العضلات, عظام الوجه و المفصل الفكي الصدغي. يتراوح الألم في الشدة من خفيف الى متوسط ثم شديد, الاضطراب عادةً يكون مصاحب لقلة حركة الفك مما ينتج عن تقييد حركة فتحة الفم.

الهدف من الدراسة: الهدف هو تحديد الى أي مدى يكون تأثير الليزر منخفض الشدة على مدى حركات الفك السفلي لدى مرضى اضطراب المفصل الفكي الصدغي.

المواد والطرق: تم اختيار خمسة عشر مريض عشوائياً, وتم قياس مدى الحركات للفك السفلي قبل وبعد العلاج بثلاثة اشهر. تم استخدام ليزر دايود ثنائي الطول الموجي (٨١٠-٩٨٠ نانومتر). اهم المعايير المستخدمة في الحسابات الإحصائية هي: فتحة الفم في حالة استرخاء, فتحة الفم في حالة الشدة و حركة الفك الجانبية. اختبار تي المزدوج, التحليل احادي الاتجاه و انوفا هي البرامج المستخدمة للإحصاء.

النتيجة: أظهرت الدراسة نتائج ملحوظة في تحسن مدى حركات الفك لدى مرضى اضطراب المفصل الفكي الصدغي خلال فترة قصيرة من استخدام الليزر منخفض الشدة.

IJL, Issue 2, Vol. 23, 2024
https://doi.org/10.31900/ijl.v23i2.493

Research Article

Simulation design of Photonic Crystal Fiber Temperature sensor based on Surface Plasmon Resonance

Namaa Salem Rahim*, Soudad S. Ahmed

Department of physics, college of science, university of Baghdad, Baghdad, Iraq
** Email address of the Corresponding Author:namaasalem652@gmail.com*

Article history: Received 22 Jul. 2024; Revised 14 Aug. 2024; Accepted 27 Aug. 2024; Published online 15 Dec. 2024

Abstract: Photonic crystal fiber (PCF) sensors based on surface Plasmon resonance with a gold layer coating are prepared and studied in this paper for detecting environmental temperature. A finite element method is utilized to increase the critical geometry parameter. An air hole on the right side of the PCF core is covered utilizing a gold metal that has a thickness of 50nm. PCF cores with circular air holes coated in gold and filled with water samples had considerable confinement losses in the y-polarization direction. When the temperature rises from 48 °C to 75 °C the RI of water will reduce. Numerical analysis of the suggested sensor was conducted utilizing FEM. Simulation using the COMSOL software was used to estimate performance parameters such as amplitude sensitivity, wavelength sensitivity, and resolution. Results indicate that the air hole covered with (Au) acts as a (SPR) sensing feed to sense the RI of water. In the sensing range (1.32-1.3266), amplitude sensitivity S_A was 422.154 RIU^{-1} and maximum resolution was $2.75 * 10^{-5}$ RIU.

Keywords: Optical Fiber Sensor, Surface Plasmon Resonance(SPR), Photonic Crystal Fiber(PCF), Temperature Sensor, Fabry–Perot interferometer.

1. Introduction

As a consequence of their heightened sensitivity in noticing different biological and chemical elements, SPR fiber sensors have evolved into a desirable study subject in modern years. These fiber sensors have tremendous potential in biomedical and life safety applications [1]. Besides being small, it is also electrically passive, stronger, and has a fast optical reaction, which reduces electromagnetic interference. [2]. in the last 20 years, fiber manufacturing technology has improved significantly. The remarkable characteristics of PCFs that cannot be achieved by conventional optical fibers have attracted a lot of attention in recent years. They are small, which decreases electromagnetic interference, and increases sensitiveness, electrical passiveness, and strength [3]. PCFs differ from traditional optical fibers by having low dispersion, and high reflectivity. The PCF's amazing technique substantially enhances single-mode detention by putting considerable air-filled holes along its length [4] Unlike optical fiber, PCF throughout the cladding part a finite number of holes are distributed along the fiber axis [5-7]. The effect of (PCFs)

contain revealed the possible integrity of optical fibers in biological and chemical detection [8, 9]. The optical fiber-based SPR notices multiple topics of good; for instance, enhanced and elastic optical design, promotion of remote sensing, and continued study [10- 12]. SPR can easily be observed in PCFs, and the sensor can be measured by varying the fiber's factors (pitch size, air hole radius, etc.). Whether the metal covering is deposited within the PCF air holes or on the PCF's outer surface, an SPR effect is generated. There have been extensive studies of SPR sensors using numerous plasmonic materials, excluding copper, gold, and silver [13, 14]. The utilization of optical fiber (SPR) was first obtainable in 1993[15]. In SPR, free electrons inside the metallic film interact with light. During resonance, the energy of light reflected off a metal film drops ominously if electron oscillation frequency matches incident light frequency. The metal layer transmits photon energy to form a Plasmon wave on the surface [16,17].to excite the SPR optical instruments like a diffraction grating, optical fiber, and refractive index prism are operated [18]. At the interface, plasma oscillations are localized. A Plasmon is a representation of plasma frequency established on a quasi-particle [19]. Plasma oscillation signifies that free electrons of the metal oscillate from their equilibrium position [20, 21]. The resonance form depends on the dielectric constant of individually the metal and the dielectric [22]. The SPR result is sensitive to differences in the RI on the metal cover [23, 24]. Various investigations have benefited from the PCF-SPR detector [25-27]. (SPR) established temperature sensors are important because of their increased sensitivity, suitable process, and label-free dimension abilities [28]. The main materials utilized in SPR are aluminum, silver, copper, and gold [29]. Silver and gold are widely utilized as a plasmonic material [30]. Numerous of the PCF-established SPR sensors utilize Au as the Plasmonic quantifiable. Gold is chemically fixed [31]. In this investigation, nevertheless, the sensor implementation was greatly enhanced by utilizing an inner sensing technique. Accordingly, performing sufficient pairing between the SPP mode and the core-guiding mode can enhance the sensor's implementation. Numerous registers of this sensor have been mathematically analyzed, and the prevalence of documented PCF is complex to manufacture due to difficult design and small fiber diameter. The FEM was utilized to analyze PCF established on SPR in this investigation. The simulated PCF's cross-section shows a solid core enclosed by six regular arrays of air holes. The right side of the solid core is covered by gold, and occupied by water. The suggested design performs maximum sensitivity, containing sensor resolution and amplitude sensitivity. The configuration that was presented was very sensitive, constructing it an excellent component for measuring and sensing the temperature of the surrounding environment.

2. Theoretical investigation and design of sensors

A. Sellmeier Equation

The silica is used in the building of the proposed sensor. The arrangement's holes are empty, or filled with air. To calculate the RI of silica, the Sellmeier equation is applied [2]:

$$N_{silica} = 1 + \frac{a_1 \lambda^2}{\lambda^2 - b_1} + \frac{a_2 \lambda^2}{\lambda^2 - b_2} + \frac{a_3 \lambda^2}{\lambda^2 - b_3} \quad (1)$$

Where: N is the refractive index of silica, which changes depending on the wavelength, λ is the wavelength, and Sellmeier coefficients are (a_1 , a_2, a_3) and (b_1, b_2, b_3), where a_1 =0.6961663, a_2 =0.4079426, a_3 = 0.8974794, b_1=0.0684043μm^2, b_2= 0.1162414 μm^{2}and b_2=9.896161μm^2.

B. Drude–Lorentz Model

For determining the real and imaginary components of the dielectric constant (ε) at a higher frequency, the Drude model is not appropriate. A totality of Lorentzian functions can nullify the interband effect (IB). Accordingly, a dielectric function can be expressed as $\varepsilon(\omega) = \varepsilon Drude(\omega) + \varepsilon IB(\omega)$ [2]. The Drude-Lorentz model estimates Au's material distribution as

$$\varepsilon_{Au} = \varepsilon_{\alpha} - \frac{\omega_D^2}{\omega(\omega + j\gamma_{D)}} - \frac{\Delta\varepsilon.\Omega_L^2}{(\omega^2 - \Omega_L^2) + j\Gamma_L\omega} \quad (2)$$

Where: $\varepsilon Drude\ (\omega)$ is the relative Permittivity described by means of the Drude model, ε is the dielectric constant, (IB) is the interband effect, , ε_{Au} is the relative permittivity of gold, ε_{α} is the permittivity of the metals, ω is the Frequency, ω_D is the plasma frequency; $\Delta\varepsilon$ is the weighting factor, and Ω_L and Γ_L respectively, Stand for the oscillator strength and the spectral width of the Lorentz oscillators.

Table 1. Drude-valued Lorentz parameters.

Symbol	ε_∞	$\omega_D/2\pi$	$\gamma_D/2\pi$	$\Omega_L/2\,\pi$	$\Gamma_L/2\,\pi$	$\Delta\varepsilon$	Φ
Unit		(THz)					
Meaning		the plasma frequency	the damping frequency	oscillator strength	The spectral width	The permittivity at high frequency	
Drude-Lorentz	5.9673	2113.6	15.92	650.07	104.86	1.09	14.521

3. Endlessly Single Photonic Crystal Fiber (ESM-PCF)

The PCF indicates slight loss during the largest wavelength series (200 nm to above 2000 nm) while holding a near continuous mode field diameter. This kind is consistent with wholly famous fiber instruments and contains a typical 125 µm outside diameter. A SEM image of PCF is shown in Figure 1.

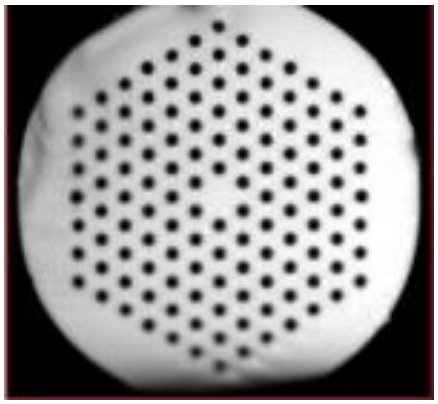

Fig.1: SEM image OF PCF.

4. Structural Technique and Analysis

NKT Inc.'s PCFs typically have an ESM fiber with an external diameter of 125µm. Figure 2 displays an illustration of the suggested sensor, produced by utilizing the COMSOL MULTPHYSICS software. Water is displaced into the air hole (d1). A plasmonic material like gold with a thickness of 50nm covers the air hole (d1). A Perfectly Matched Layer as an edge form has been utilized to absorb the scattering lights to the fiber surface; PML is a circular cover with a thickness of 12µm in the suggested design. Convergence tests also were concluded, and improved with mesh size and the PML thickness for additional precise effects.

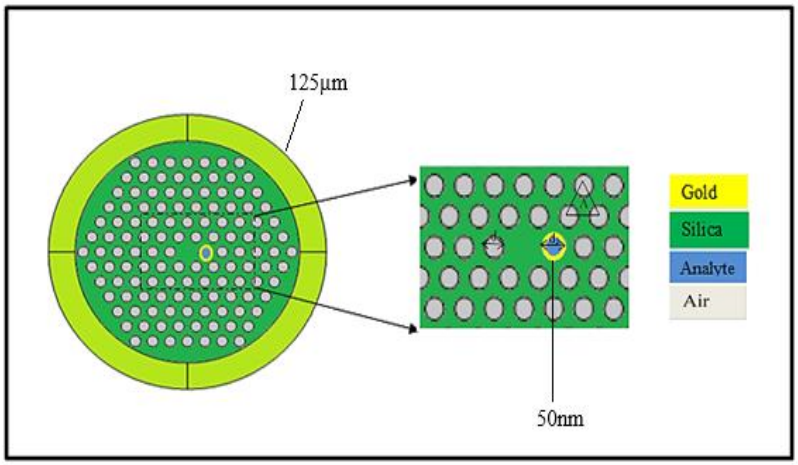

Fig. 2: 2D Cross-sectional observation of the suggested sensor.

5. Results and Discussion

For a specific wavelength, at a given temperature resonance is produced during the phase corresponding to core guiding mode and the Surface Plasmon Polariton mode. Figure (3) shows the electrical-filed distribution for (a) core-guided mode phase-matching condition and (b) SPP mode (y-polarized), respectively, at n_a =1.3266 and t_{Au} =50nm. In addition, Fig (4) illustrates the dispersion relation for y-polarizations around the resonant wavelength among the fundamental core mode and the second SPP mod. The confinement loss of the propagation mode is likewise displayed by this form (red line). There is a significant loss peak at the λ_{res} of 740 nm, where the 2ndSPP mode cross and essential mode were shown by the core. Consequently, the SPP mode obtains the most energy from the fundamental core mode.

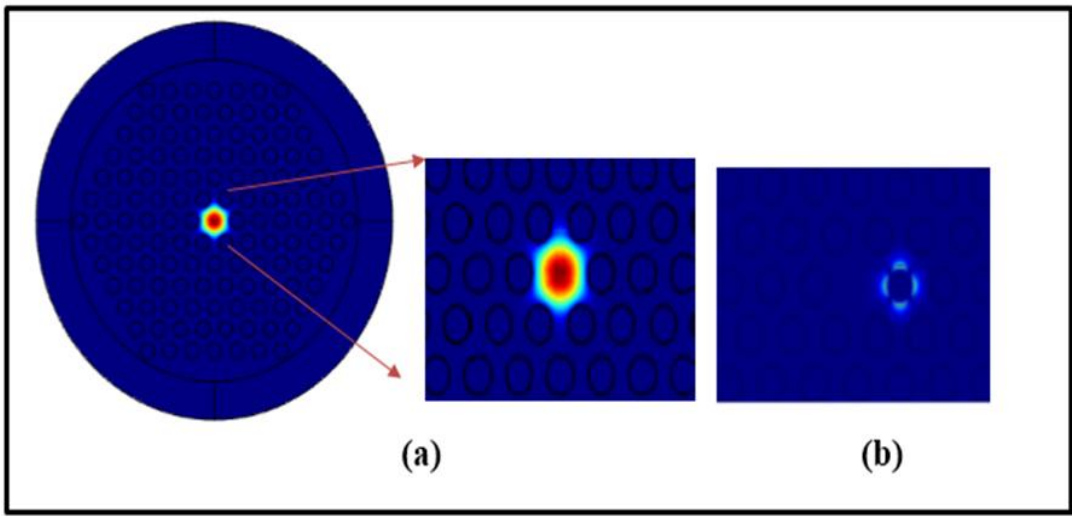

Fig. 3: Electric field distribution at the (a) core-guided mode phase-matching condition, and (b) SPP mode (y-polarized), respectively, at n_a=1.3266 and t_{Au}=50nm.

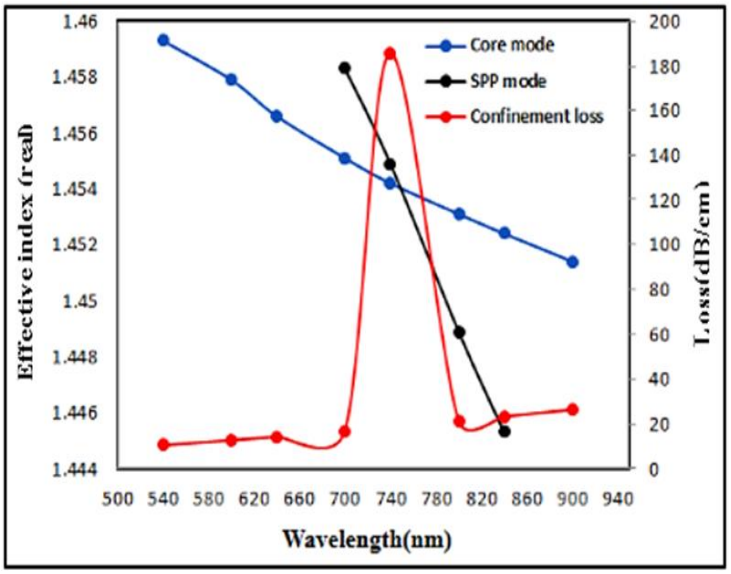

Fig. 4: Dispersion relation of the core-guided mode (blue), SPP mode (black), and loss spectrum (red) at na =1.3266 and t_{Au}=50nm.

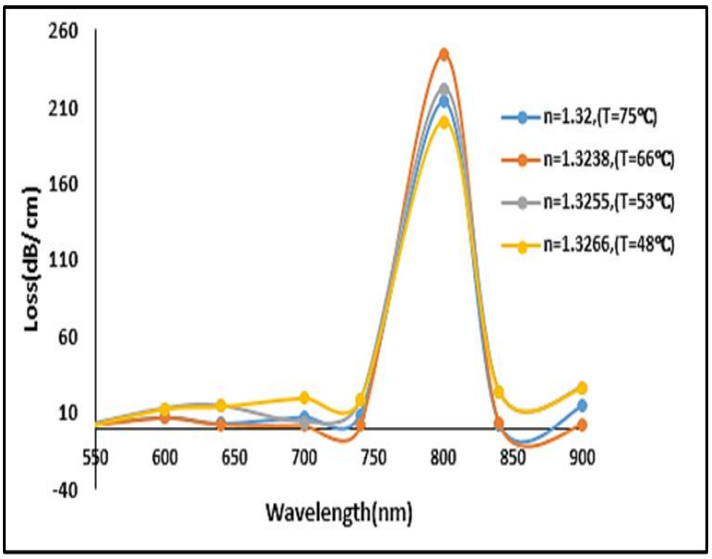

Fig. 5: The confinement loss spectrum of the suggested PCF SPR sensor difference with rise water RI from 1.32 to 1.3266 when temperature ranges from 48 °C to 75 °C.

The Refractive Index (RI) of water at different temperatures can be calculated by [32]:

$$n=n_o+ dn/dT \quad (T-T_o) \qquad (3)$$

Where n_o is the RI of the water at room temperature T_o and (dn/dT) is the thermo-optic coefficient, (dn/dT) of water is (−1.12 * 10^ (-4)/◦C) and (T) is the temperature increasing with water boiling [33]. We provide loss spectra for the core modes throughout the λspectrum of (540–900 nm) for the various RI of the water in order to investigate the RI sensitivity of the sensor. When the temperature rises from 48 °C to 75 °C, as displayed in Figure 5 the peak loss reduces unhurriedly. This is due to a poorer coupling efficiency caused by a larger variance between the Plasmon mode and core guided and a decreased n_{eff} of the Plasmon mode that varies the phase corresponding point.

As shown in Figure 5, the RI of water will reduce as temperature rises. To study the effect of varying refractive indices on the investigated sensor performance, the air hole on the right side of the photonic crystal fiber core was infiltrated with water. The refractive indices (na) of water vary from 1.32 to 1.3266 at a temperature field from 75 °C to 48 °C, Figure (5) shows confinement loss for the water refractive index extending from 1.32 to 1.3266. It was noted that the confinement loss was increased significantly with refractive index and this was because of the decrease in the refractive index difference between the core guided mode and SPP mode. Both wavelength methods amplitude interrogation can be utilized to measure the proposed sensor's implementation. Eq. 4 utilized to calculate the wavelength sensitivity [3]:

$$S_W(\lambda) = \frac{\Delta\lambda_{peak}}{\Delta n_a} \quad (4)$$

Δn_a and $\Delta\lambda_{peak}$ specify the variation in the analyte refractive index and the resonant peaks, correspondingly. Analytes with a refractive index of 1.32, 1.3238, and 1.3255 would be detected by the suggested sensor, and the wavelength sensitivity of an average of 526.3 nm/RIU, 1176.4 nm/RIU and 1818 nm/RIU can be achieved according to Eq. 4. The resolution of the sensor, which determines how well it detects even minute variations in the water RI, is another important consideration. Sensor resolution was determined using Eq. 5 [3]:

$$R = \frac{\Delta na \times \Delta\lambda min}{\Delta\lambda peak}\ [RIU] \quad (5)$$

Where $\Delta\lambda_{peak}$ is the greatest resonant wavelength peak shift, Δn_a is the difference in the refractive index of water, and $\Delta\lambda$min is the lower spectral resolution.2.75*10^(-5) RIU was the maximum resolution, assuming Δna = 0.0011, $\Delta\lambda$min = 0.1, and $\Delta\lambda$peak = 4 nm.

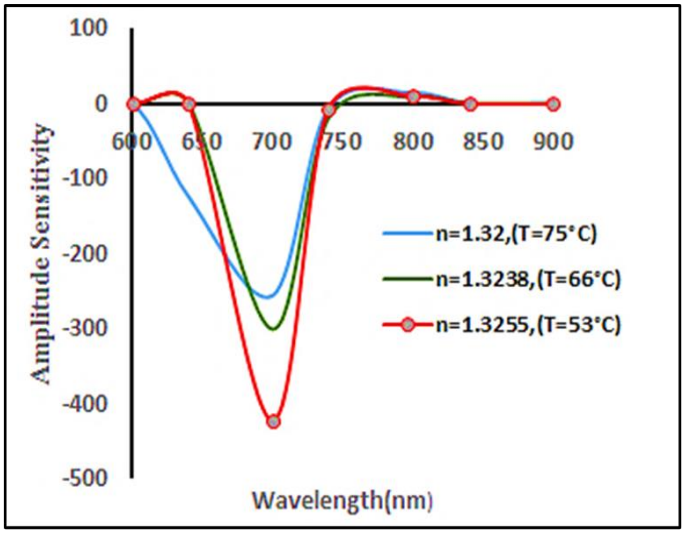

Fig. 6: Amplitude sensitivity relative to wavelength when RI increases from 1.33 to 1.3266.

To get the sensor's amplitude sensitivity, utilize Eq(6) [3]:

$$S_A(\lambda) = -\frac{1}{\alpha(\lambda, n_a)} \frac{\partial\alpha(\lambda, n_a)}{\partial n_a} [RIU^{-1}] \quad (6)$$

The analyte's confinement loss at a given refractive index (RI) is represented by α (λ,na), whereas the difference in confinement loss between two refractive indices is shown by ∂α (λ,na). The amplitude sensitivity of various refractive indices is shown in Figure 6. The greatest amplitude sensitivity for analytes 1.32 to 1.3238, 1.3238 to 1.3255, and 1.3255 to 1.3266 is 255.656RIU^(-1), 300.12RIU^(-1) and 422.154 RIU^(-1) correspondingly.

6. Conclusion

PCF was utilized to present a temperature sensor based on the SPR technique. The PCF core exhibited a notable Y-polarization direction confinement loss after a gold-coated circular air hole on the right side was filled with an analyte (water sample). When the peak of the transmission loss spectrum or the resonant wavelength λres coincides with the SPR sensor's resonant wavelength, the filled analyte may be detected. FEM was employed to examine the basic mode sensor settings. In the sensing range of 1.32 to 1.3266, the maximum resolution of 2.75*10^ (-5) RIU and the amplitude sensitivity of 422.154 RIU^ (-1) were obtained. Due to its great sensitivity, the sensor is useful for biological and chemical sensing applications in the environment, such as detecting heavy metals in water. This sensor measures and detects a number of physical parameters, including chemical composition, strain, temperature, and pressure.

References

[1]E. Khatar and S. S. Bassam, "Surface Plasmon Plastic Optical Fiber Resonance with Multi-Layer as Chemical Sensor", Iraqi J. Phys. 19, 51.(2021)
[2] F. F Abbas, and S. S. Ahmed, "Photonic crystal fiber pollution sensor based on surface plasmon resonance", Iraqi Journal of Science, 658-667.(2023)
[3]G. M.Jassam, and S.S. Ahmed, "D-shaped photonic crystal fiber toxic metal ions (arsenic) sensor based on surface plasmon resonance", Iraqi Journal of Physics, 21(2), 91-98.(2023)
[4] G. M.Jassam and S. S. Ahmed, "Estimating concentration of toxic ions Arsenic in water by using Photonic Crystal Fiber based on Surface Plasmon Resonance (SPR)". Baghdad Science.(2023).
[5] F. F. Abbas and S. S. Ahmed, "Photonic crystal fiber pollution sensor based on the surface plasmon resonance technology", Baghdad Science Journal, 20(2), 0452-0452.(2023)
[6] M. J.Abd Alkareem, and S. S. Ahmed, "Surface Plasmon Resonance (SPR)-Based Multimode Optical Fiber Sensors for Electrical Transformer Oil Aging Detection", Iraqi Journal of Physics, 21(4), 84-91.(2023)
[7]H.Yang ,M. Liu,Y.Chen, L.Guo, G.Xiao, H.Liu, and L.Yuan,"Highly sensitive graphene-Au coated plasmon resonance PCF sensor", Sensors. 21(3), 818.(2021)
[8] P.Singal, and M. Kiroriwal ,"Performance Analysis of Gold-Coated Plasmonic Photonic Crystal Fiber Biosensor", In 2021 International Conference on Circuits, Controls and Communications (CCUBE) (pp. 1-4). IEEE(2021)
[9]M. J.Abd-ALhussain, B. G. Rasheed, and M. A. Fakhri,"Solid-core photonic crystal fiber-based nanolayer glucose sensor",Journal of Optics, 1-13.(2023)
[10] G. M. Jassam, S.S Ahmed, "Acetic acid concentration estimation using plastic optical fiber sensor-based surface plasmon resonance", Iraqi J. Phys. 17, 11.(2019)
[11]L.Liu, S.Deng, J.Zheng, L.Yuan, H.Deng and C. Teng, "An enhanced plastic optical fiber-based surface plasmon resonance sensor with a double-sided polished structure Sensors", 21, 1516.(2021)
[12]C.Odacı, and U.Aydemir, "The surface plasmon resonance-based fiber optic sensors: A theoretical comparative study with 2D TMDC materials",Results in Optics, 3, 100063.(2021)
[13]M.F.Sultan, A.A. Al-Zuky, and S.A.Kadhim, "Surface plasmon resonance based fiber optic sensor: theoretical simulation and experimental realization" ,Al-Nahrain J. Sci. 21, 65.(2018)
[14]G.Opoku, I.Danlard, A.Dede, and E. K.Akowuah, "Design and numerical analysis of a circular SPR based PCF biosensor for aqueous environments", Results in Optics, 12, 100432.(2023)
[15]C.Liu, J.Wang, F.Wang, W.Su, L.Yang, J.Lv, and P. K. Chu, "Surface plasmon resonance (SPR) infrared sensor based on D-shape photonic crystal fibers with ITO coatings" ,Optics Communications, 464, 125496(2020)
[16] X.Yan, Y.Wang, T.Cheng, and S.Li, "Photonic crystal fiber SPR liquid sensor based on elliptical detective channel".Micromachines. 12, 408.(2021)
[17]M. A.Mollah, S. R.Islam, M.Yousufali, L. F.Abdulrazak, , M. B.Hossain, and I. S.Amiri, "Numerical study of circularly slotted highly sensitive plasmonic biosensor: a novel approach",Results in Physics, 16, 102966.(2020)
[18]H. P.Li,J. Ruan, X. Li, G. Y.Wei, and T.He, "High-sensitivity temperature sensor based on surface plasmon resonance photonic crystal fiber" ,Progress In Electromagnetics Research . 116, 11.(2023)
[19] A. K.Paul, M. A.Mollah, M. Z.Hassan, N.Gomez-Cardona, and E.Reyes-Vera, "Graphene-coated highly sensitive photonic crystal fiber surface plasmon resonance sensor for aqueous solution: Design and numerical analysis",In Photonics. 8, 155 MDPI.(2021)

[20] N. S. Rahim, S. S. Bassam, "Estimating sugar concentration in human blood serum using Surface Plasmon Resonance (SPR) –based optical fiber sensor", Iraqi J. Phys. 17, 41.(2019)
[21] M. H.Salman, H. K.Muhammad and H. A.Yasser, "Effects of holes radius on plasmonic photonic crystal fiber sensor with internal gold layer",Periodicals of Engineering and Natural Sciences, 8, 1288 .(2020)
[22] N.Sakib, W.Hassan, Q. M.Kamrunnahar,M. Momtaj, and T.Rahman, "Dual core four open channel circularly slotted gold coated plasmonic biosensor" ,Optical Materials Express, 11, 273 .(2021)
[23] M.lA Mahfuz, M. A.Hossain, E.Haque, N. H.Hai, Y.Namihira, and F.Ahmed, "Dual-core photonic crystal fiber-based plasmonic RI sensor in the visible to near-IR operating band", IEEE Sensors Journal, 20, 7692.(2020)
[24] N. S. Rahim, S. S. Ahmed, and M. F. Sultan, "Optical fiber biomedical sensor based on surface plasmon resonance", Iraqi J. Sci. 61, 1650-1656.(2020)
[25] G. M. Jassam, S. S. Alâ, and M. F. Sultan, "Fabrication of a chemical sensor based on surface plasmon resonance via plastic optical fiber", Iraqi J. Sci. 61, 765.(2020)
[26] W.Yong, S.Yudong, L.Chunlan, L.Lu, Z. Zongda and Z. Yonghui, "Micro-displacement optical fiber sensor based on surface plasmon resonance", Laser Optoelectron. Prog. 55, 040606.(2018)
[27] Y.Yang, Y.Qin, X. Lu, and Y.Zeng, "High-sensitivity three-core photonic crystal fiber sensor based on surface plasmon resonance with gold film coatings",Japanese Journal of Applied Physics, 60, 122002.(2021)
[28]A.S.H.Rabee, M.F.O.Hameed, A.M.Heikal and S.Obayya, "Highly sensitive photonic crystal fiber gas sensor" ,Optik, 188, 78.(2019)
[29] Q.H.Chen, , J.H.Liu, H.F.Luo, Y.X.He, J.Luo and F.Wang, "A liquid refractive index measurement system based on surface plasma resonance" ,Acta Opt. Sin. 35, 166.(2015)
[30] K.M.McPeak, S. V.Jayanti, S. J.Kress, S.Meyer, S.Iotti, A.Rossinelli, and D. J. Norris, ACS photonics, 2, 326.(2015)
[31] R. Otupiri, E. K. Akowuah, S. Haxha, H. Ademgil, F. AbdelMalek, and A. Aggoun, "A novel birefrigent photonic crystal fiber surface plasmon resonance biosensor",IEEE Photon. J., 6, 6801711 (2014)
[32] X. C. Yang, Y.Lu, B. L.Liu and J. Q.Yao, "Temperature sensor based on photonic crystal fiber filled with liquid and silver nanowires", IEEE Photonics Journal, 8, 1.(2016)
[33] P. R. Prasad, S. K.Selvaraja and M.Varma, "Thermo-optic coefficient measurement of liquids using silicon photonic microring resonators" ,arXiv preprint arXiv,1710.03605 .(2017)

مستشعر درجة حرارة بالألياف البلورية الضوئية استنادًا إلى رنين البلازمون السطحي (SPR)

نماء سالم رحيم * ، سؤدد سلمان احمد

قسم الفيزياء، كلية العلوم، جامعة بغداد، العراق، بغداد

*البريد الالكتروني للباحث: : namaasalem652@gmail.com

الخلاصة:تم تحضير ودراسة مستشعرات الألياف البلورية الضوئية (PCF) المستنده على رنين البلازمون السطحي مع طبقة من الذهب في هذا البحث للكشف عن درجة حرارة البيئية. يتم استخدام طريقة العناصر المحدودة لزيادة معلمة الهندسة الحرجة.ثقب الهواء الموجود على الجانب الأيمن من قلب الPCF مغطاة بمادة ذهبية بلازمونية مستقرة كيميائيًا يبلغ سمكها 50 نانومتر. كان للالياف البلورية الضوئية ذات الفتحات الهواء الدائرية المطلية بالذهب والمملوءة بعينات الماء خسائر كبيرة في الحصرفي اتجاه الاستقطاب y. عندما ترتفع درجة الحرارة من 48 درجة مئوية إلى 75 درجة مئوية فإن معامل الانكسارللماء سوف تنخفض.تم إجراء التحليل العددي للمتحسس المقترح باستخدام طريقة العناصر المحدودة.تم استخدام المحاكاة باستخدام برنامج COMSOL لحساب معلمات الأداء مثل حساسية السعة وحساسية الطول الموجي والدقة. تشير النتائج إلى أن فتحة الهواء المغطاة بـ (الذهب) تعمل بمثابة تغذية استشعار (SPR) لاستشعار معامل انكسار الماء.في مدى استشعار (1.32-1.3266), كانت حساسية السعة 422.154(-1) والدقة⟦ 6*10⟧^(-6) RIU.

IJL, Issue 2, Vol. 23, 2024
https://doi.org/10.31900/ijl.v23i2.485

Research Article

IRAQI JOURNAL OF LASER

Photonic crystal fiber drug sensor based on surface plasmon resonance

Sally K. Abbas* and Soudad S. Ahmed

Department of physics, college of science, university of Baghdad, Baghdad, Iraq
** Email address of the Corresponding Author:sallyaljanabi@gmail.com*

Article history: Received 30 Jun. 2024; Revised 14 Aug. 2024; Accepted 3 Sept. 2024; Published online15 Dec. 2024

Abstract: This study introduces a sensor using Photonic Crystal Fiber (PCF) and Surface Plasmon Resonance (SPR) technology. Gold (Au) was applied as a thin coating on a PCF, which had been previously coated with a chemically stable gold compound that exhibits plasmonic properties. The thickness of the gold coating was 40nm. The performance metrics, such as sensitivity (including wavelength sensitivity and amplitude sensitivity) and resolution, were assessed by simulation via the COMSOL program. The suggested sensor was developed utilizing the finite element method and then subjected to numerical analysis. The findings indicate that the surface of Photonic Crystal Fiber when coated with Au, functions as a sensor for detecting the refractive index (IR) of expired pharmaceutical samples. Research is conducted on the effects of the structural parameters on the resonant spectra with the aim of enhancing sensing performance. The highest amplitude sensitivity recorded was 31.2 RIU-1, whereas the maximum resolution reached was 6×10-5 RIU. These measurements were obtained within the detection range of 1.383 to 1.399.

Keywords: COMSOL, PCF, pharmaceutical samples, surface plasmon resonance.

1. Introduction

Many fields rely on optical fiber sensors, including academia, environmental monitoring, and the field of communication technology. Reasons for this include their size, sensitivity, electrical passivity, immunity to electromagnetic interference, bandwidth, and suitability for use in tip-based sensing applications. The majority of these optical sensors detect changes in the refractive index (RI) of a gas or liquid by measuring differences in optical characteristics [1]. The reflectance index (RI) is a crucial metric for characterizing the optical characteristics of fluids. Biotechnology methods [2] also provide important information on drug/DNA interaction and cell growth [3], and this has led to the advancement of RI sensors for use in numerous sectors, including water salinity assessment [4]. Photonic Crystal Fiber (PCF) sensors utilize the propagation of surface plasmons. Due to their high sensitivity, ease of integration, rapid reaction, and immediate findings, they are extensively employed for refractive index monitoring.

When p-polarized light and surface plasmons (SP) reach a phase-matching condition, they stimulate a charge density oscillation at the interface between a metal and a dielectric element, this optical phenomenon

is known as surface plasmon resonance (SPR) [5-9]. PCF-SPR sensors, which integrate the benefits of PCF technology and plasmonic science, have been devised to monitor environmental conditions [10], ascertain solution concentration [11], facilitate water quality control, aid in biomedical treatment [12], identify gases, assist in health diagnostics, and further [13].The evanescent field is the key of PCF-SPR's sensing mechanism. When light of a particular wavelength penetrates the PCF's fiber core and partly passes through its cladding, a transient field is generated. Surface plasmon waves arise from the interaction between electrons in a plasmonic metal surface (such as copper, gold, silver, or aluminum) with evanescent fields. Once the core guiding mode's refractive index (RI) approaches that of the SPPi modes, phase matchings take place, and the two modes are now linked. [14, 15].

PCF-SPR technology addresses the limitations of traditional prism-based SPR sensing, such as large size, the need for precise incidence angle, and many mechanical parts. These limitations restrict distant sensing capabilities and limit the range of applications [16]. Based on sensor assessment, two different sensing modalities are distinguished: interior and outside. The analyte is cast off to charge up the air hole or a metal coating is put around the core in internal sensing or sensing based on nanowires. Positioning plasmonic material outside to act as a sensing medium for exterior applications including D-shape, slit, and microchannel sensors is an additional way to use plasmonic material [17].

A D-shaped PCF sensor based on SPR that was covered by a 40 nm gold layer was suggested by Jassam et al. [18]. Its highest resolution was 4 x 10-5 RIU, and it had an amplitude sensitivity of 99.2 RIU-1 within the detection range of 1.351-1.363. A PCF~SPRr sensor was developed by Mahmood et al. and demonstrated an impressive sensitivity of 164.3 nm/RIU throughout the 1.33–1.3431 analyte refractive index range. The coating that the researchers applied to the air holes was made of plasmonic material, namely gold. They then used analyte samples to fill up these gaps [19]. This effort, however, used an internal sensing approach to substantially improve the sensor's performance. Therefore, by effectively integrating the core-guiding mode with the SPP mode, the performance of the sensor was improved. Due to their small fiber diameter, complicated structure, and tiny air hole diameter, most of the PCF conformations that have been studied were challenging to produce. While the majority of PCF-SPR sensors have undergone mathematical analysis, ESM-12-02 has been subjected to analysis in conjunction with the finite element technique (FEM) for SPR. The manufactured PCF has six air holes organized in a regular pattern around a tiny core. When it comes to sensor resolution and amplitude sensitivity, the suggested framework could provide the greatest sensitivity available.

2. Theoretical investigation and design of sensors

A. Sellmeier Equation

The suggested sensor mostly utilizes silica in its fabrication. All of the openings in the structure are devoid of any substance and are instead occupied by air. The refractive index of silica is defined by equation 1 [20].

$$N_{silica} = 1 + \frac{a_1 \lambda^2}{\lambda^2 - b_1} + \frac{a_2 \lambda^2}{\lambda^2 - b_2} + \frac{a_3 \lambda^2}{\lambda^2 - b_3} \quad (1)$$

Silica's refractive index, denoted as N, is dependent on the wavelength, λ, which is measured in μm. The Sellmeier constants for silica are represented by the sets (a1, a2, a3) and (b1, b2, b3) correspondingly. a1=0.6961663, a2=0.4079426, a3= 0.8974794.

B. Drude–Lorentz Model

At higher frequencies, the real and imaginary components of the dielectric constant cannot be estimated using the Drude model. By expressing the interband effect (IB) as the sum of Lorentzian functions, it may be avoided.

A simple representation of the frequency-dependent dielectric function is $\varepsilon(\omega)=\varepsilon Drude(\omega)+\varepsilon IB(\omega)$. Equation 2 may be used to express the dispersion relation of gold, a noble metal, using the Drude-Lorentz model [21].

$$\varepsilon_{Au} = \varepsilon_{\alpha} - \frac{\omega_D^2}{\omega(\omega+j\gamma_{D)}} - \frac{\Delta\varepsilon.\Omega_L^2}{(\omega^2-\Omega_L^2)+j\Gamma_L\omega} \qquad (2)$$

In this case, εAu stands for the gold substance's permittivity, whereas ε∞ is the gold's permittivity at a high frequency, which is 5.9673. You may express the angular frequency, ω, as ω = 2πc / λ, where c is the speed of light in a vacuum. At 2113.6 THz, the plasma frequency is ωD/2π, while at 15.92 THz, the damping frequency is γD/2π. At 1.09, the weighting factor Δε is set. The Lorentz oscillators have an oscillator power of 650.07 THz and a spectral width of 104.86 THz. While Ω_L and Γ_L are the oscillator strength and spectral width of the Lorentz oscillators

3. Photonic Crystal Fiber designed for Endlessly Single Model

The Single-Mode Solid Core PCF, especially the ESM~12~02 type provided by Thorlabs Assembly, has a stable mode field diameter and shows negligible loss across a wide range of wavelengths from 200 nm to over 2000 nm. An industry standard, the ESM-12-02 has an outside length of 125 µm and is well-matched with most fiber equipment. When it came to sensors, interferometers, and applications that needed short wavelengths like visible light and ultraviolet (UV) radiation, the ESM-12-02 was the way to go. It could produce wideband radiation in a single spatial mode. The physicochemical features of ESM-12-02 are listed in Table 1.

Table 1. Physical properties of PCF.

Photonic crystal fiber Properties	
Core diameter	10.2µm
Holes diameter	2.46µm
Pitch	7.8µm
Outside diameter	125µm

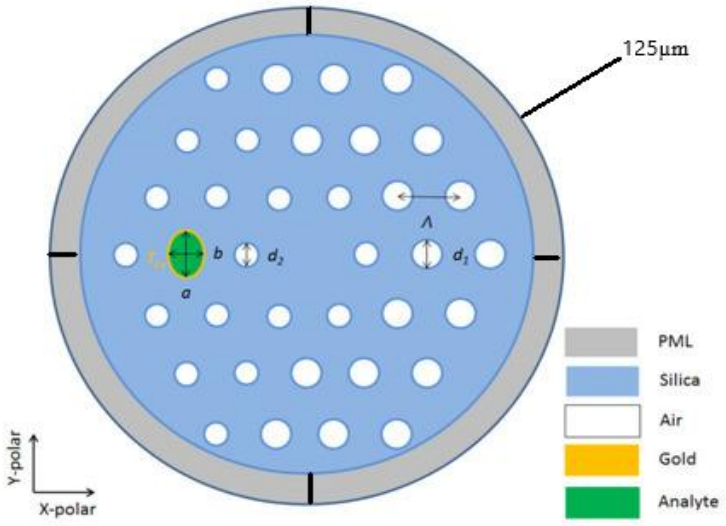

Fig. 1: Cross-sectional observation of the suggested sensor.

The NKT Photonics ESM-12 PCF is specifically engineered to function as a single-mode fiber, maintaining a constant outside length of 125 µm. It works with any fiber tool that is widely used. Figure 1 displays a graphic representation of the PCF~SPR sensor created by the use of the COMSOL MULTPHYSICS tool. After the PCF received a 40 nm covering of plasmonic matter, such as gold, the sample was deposited onto it. As the boundary media, a Perfectly Matched Layer (PML) was used to effectively absorb the scattered light that was directed toward the surface of the fiber. The PML is a round sheet with a thickness of 12 µm in the proposed construction. The convergence experiments were effectively conducted and subsequently adjusted to produce more precise results by adjusting the PML width and mesh sizing.

4. Results and Discussion

When a specified wavelength is produced by the phase of the Surface Plasmon Polariton mode and core controlling in a certain material, resonance results. The connection between the basic mode for y-polarisations and the dispersion of the Second Surface Plasmon Polariton (SSPP) mode is shown in Figure 2. Another thing that this picture shows with the red line is the structure's general propagation mode's confinement loss. An evident decrease in intensity at the specific wavelength of 658 nm was observed, indicating the alignment of the core with the 2nd surface plasmon polariton mode. Consequently, the SPP mode acquires the most amount of energy from the fundamental core mode. In the y-polarization, Figure 2 shows the distribution of the electric field for the phase-matching core mode (b) and the fundamental core-guiding mode (a).

The results were obtained with the analyte having a refractive index of 1.383 and a phase-matching condition used. Even small changes in the analyte's refractive index might have a significant impact on the loss of depth. The suggested PCF sensor's loss spectrum is shown in Figure 3 for different n_a values. Redshift occurred as the peak shifted towards longer wavelengths as the depth of loss increased. This is so because the phase matching point varies with increasing effectual refractive index of the surface plasmon mode. This results in a decreased difference between the core-guided mode and the plasmon mode, hence improving the efficiency of coupling. The maximum attenuation coefficient of 5.79 dB/cm was observed at a wavelength of 658 nm, corresponding to a refractive index of 1.383. The power transmission between the core and SPP phases was more intense as the loss depth increased. The result was caused by an elevation in the refractive index of the substance being analyzed. Therefore, the resonant spectrum was further limited.

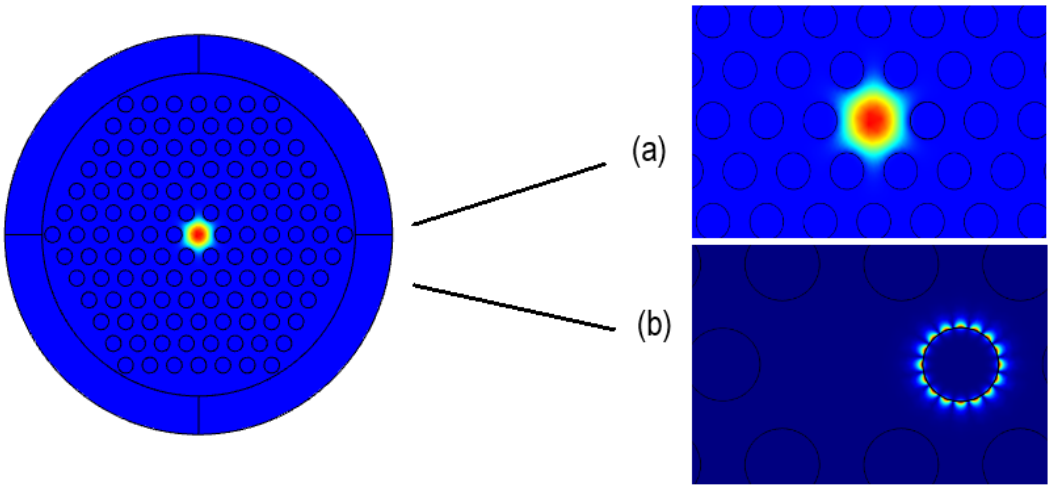

Fig. 2: Electric field distributions at na =1.383 in (a) core-guided mode, (b) SPP mode (y-polarized).

When the refractive index of the analyte increases as shown in Figure 4 the peak loss reduces. This is due to a poorer coupling efficiency caused by a larger variance between the plasmon mode and core guided and a decreased n_{eff} of the plasmon mode that varies the phase corresponding point.

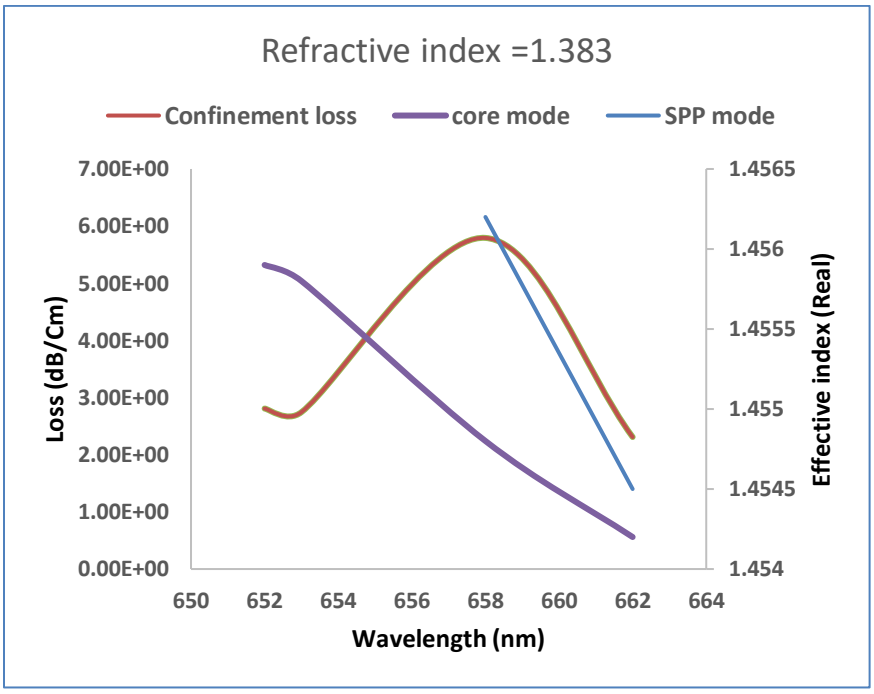

Fig. 3: Dispersion relation between core guiding mode and the second Surface plasmon mode.

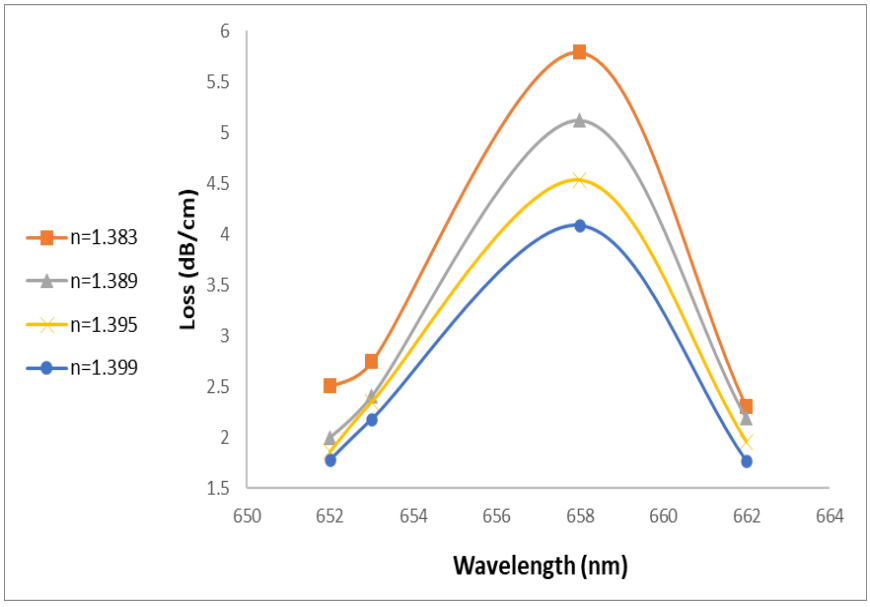

Fig. 4: The confinement loss spectrum of the proposed Photonic Crystal Fiber (PCF) Surface Plasmon Resonance (SPR) sensor varies as the analyte's refractive index (RI) increases from 1.383 to 1.399.

Amplification consideration and wavelength approaches may be employed to evaluate the operation of the planned sensor. Equation (3) is applicable for the calculation of wavelength sensitivity [22]:

$$S_W(\lambda) = \frac{\Delta\lambda_{peak}}{\Delta n_a} \quad (3)$$

The resonant peaks and the fluctuation in the analyte's refractive index are represented by the values of Δλ peak and Δna, respectively.

The proposed sensor is sensitive to wavelengths of 1667 nm/RIU for na = 1.383, 1.389, and 1.395. The resonant wavelength peaks occur at 10 nm for variations in the refractive index of the analyte within the ranges of 1.383-1.389, 1.389-1.395, and 1.395-1.399. These ranges indicate the intervals amongst the points of resonant wavelength. The sensor's resolution is a crucial feature that characterizes its ability to spot even the slightest alteration in the refractive index of the analyte. The resolution (R) of the suggested sensor was denoted by Eq. 4 [22]:

$$R = \frac{\Delta na \times \Delta\lambda min}{\Delta\lambda peak}\ [RIU] \quad (4)$$

The variables in the issue are as follows: The slightest spectral resolution is denoted by $\Delta\lambda_{min}$, while the greatest shift in the resonant wavelength peak is represented by $\Delta\lambda_{peak}$. The change in refractive index (RI) of the analyte or sample is represented by n_a. The greatest resolution achieved was 6×10^{-5} RIU, based on the assumptions that Δn_a (change in refractive index) is 0.006, $\Delta\lambda_{min}$ (minimum change in wavelength) is 0.1, n_a (refractive index) is 1.399, and $\Delta\lambda_{peak}$ (change in peak wavelength) is 10 nm. Finding the sensor's amplitude sensitivity is possible with the help of Equation (5) [22]:

$$S_A(\lambda) = -\frac{1}{\alpha(\lambda, n_a)} \frac{\partial\alpha(\lambda, n_a)}{\partial n_a} [RIU^{-1}] \quad (5)$$

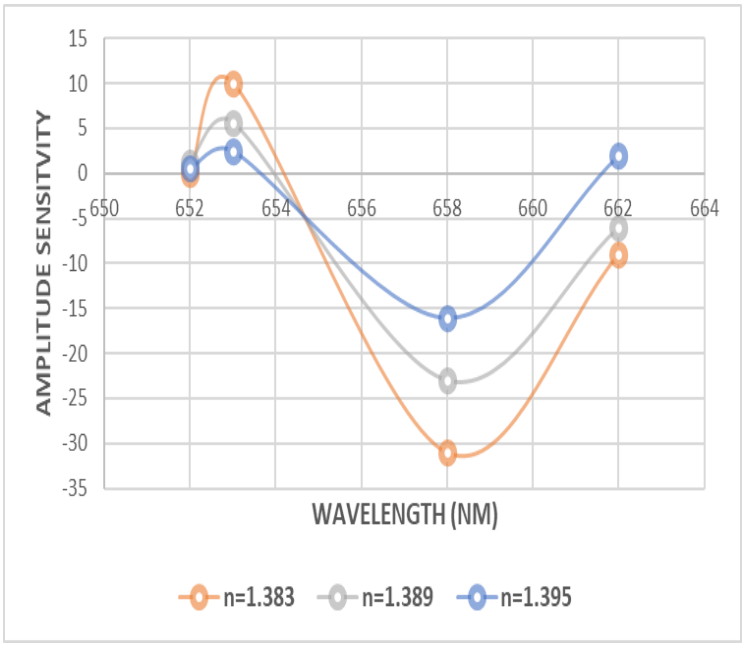

Fig. 5: The amplitude sensitivity changes as the wavelength varies, while the refractive index of the sample increases from 1.383 to 1.399.

In contrast to ∂α (λ, na), which represents the change in confinement loss among two analyte samples with identical refractive indices, α (λ, na) represents the analyte's confinement loss at a certain refractive index. The level of reactivity of different analyte/sample refractive indices is shown in Figure 5. The maximum amplitude sensitivity values were 16 RIU^{-1}, 23.34 RIU^{-1}, and 31.2 RIU^{-1} for refractive index variations of the analyte/sample within the ranges of 1.383-1.389, 1.389-1.395, and 1.395-1.399, respectively.

5. Conclusion

This study utilizes a Photonic Crystal Fiber sensor that operates on the principle of surface Plasmon Resonance (PCF-SPR) to identify expired medication samples. The sensor is designed by applying a gold layer to the air hole located on the right side of the PCF core. Analyzing the resonant wavelength or confinement loss spectrum peak with the actual component of the effective index of the core guiding mode and surface plasmon mode may help identify the unknown material. The Finite Element Method (FEM) was used to examine the basic mode sensor characteristics. The maximum wavelength at which the sensor is sensitive is 1667 nm/RIU, and the maximum amplitude at which it is sensitive is 31.2 RIU^{-1}. These sensitivities were observed within the detecting range of 1.383 to 1.399. The suggested sensor has the potential to function as a biosensor, thanks to its simple design and exceptional sensing capabilities.

References

[1] S.K. Abbas, S.S. Ahmed, "Refractive index sensor based on tapered photonic crystal fiber to determine the performance of different carbonated liquids", J Opt (2023).
[2] D. Pereira, O. Frazão, and J. Santos, "Fiber Bragg grating sensing system for simultaneous measurement of salinity and temperature", Optical Engineering, 43, 299–304 (2004).
[3] F. Jiménez-Márquez, J. Vázquez, J. Úbeda, and J. Sánchez-Rojas, "Low- cost and portable refractive opteoelectronic device for measuring wine fermentation kinetics", Sensors and Actuators B Chemical, 178, 316–323 (2013).
[4] S. Silva, P. Roriz, and O. Frazão, "Refractive index measurement of liquids based on microstructured optical fibers", Photonics, 1, 516-529 (2014).
[5] G. M. Jassam, S. S Ahmed, "Acetic acid concentration estimation using plastic optical fiber sensor-based surface plasmon resonance", Iraqi J. Phys. 17, 11 (2019).
[6] N. S. Rahim, S. S. Ahmed, and M. F. Sultan, "Optical fiber biomedical sensor based on surface plasmon resonance", Iraqi J. Sci. 61, 1650-1656 (2020).
[7] E. Khatar and S. S. Bassam, "Surface Plasmon Plastic Optical Fiber Resonance with Multi-Layer as Chemical Sensor", Iraqi J. Phys. 19, 51 (2021).
[8] N. S. Rahim, S. S. Bassam, "Estimating sugar concentration in human blood serum using Surface Plasmon Resonance (SPR) –based optical fiber sensor", Iraqi J. Phys. 17, 41 (2019).
[9] G. M. Jassam, S. S. Alâ, and M. F. Sultan, "Fabrication of a chemical sensor based on surface plasmon resonance via plastic optical fiber", Iraqi J. Sci. 61, 765 (2020).
[10] N. F. Muhammed, A. I. Mahmood, Sh. A. Kadhim, and I. A. Naseef, "Simulation Design of Hollow Core Photonic Crystal fiber for Sensing Water Quality", J Phys: Conf Ser. 1530 012134 (2020).
[11] S. Maheswaran, P. Kuppusamy, S. Ramesh, T. Sundararajan, and P. Yupapin, "Refractive index sensor using dual core photonic crystal fiber–glucose detection applications", Results Phys., 11, 577– 578 (2018).
[12] M. AF. Gatea, A. H. Jawad, "Thermoplasmonic of single Au@SiO_2 and SiO_2@Au core shell nanoparticles in deionized water and polyvinylpyrrolidone matrix", Baghdad Sci J., 916(2), 0376 (2019).
[13] H. Yuan, W. Ji, S. Chu, Q. Liu, S. Qian, J. Guang, et al. "Mercaptopyridine functionalized gold nanoparticles for fiber-optic surface plasmon resonance Hg2+ sensing", ACS Sens., 4(3), 704–710 (2019)
[14] A. K. Paul, "Graphene-Coated Highly Sensitive Photonic Crystal Fiber Surface Plasmon Resonance Sensor for Aqueous Solution: Design and Numerical Analysis", OSA Contin. 3, 2253 (2020).
[15] M. Li, J. Xu, Q. Zheng, C. Guo, and Y. Chen, "Chemical-based surface plasmon resonance imaging of fingerprints", Analyt. Chem. 94, 7238 (2022).
[16] M. T. Rahman, S. Datto, and M. N. Sakib, "Highly sensitive circular slotted gold-coatedmicro channel photonic crystal fiber basedplasmonic biosensor", OSA Contin. 4, 1808 (2021).

[17] A. A. Rifat, M. R. Hasan, R. Ahmed, and H. Butt, "Spiral Photonic Crystal Fiber Based Dual- Polarized Surface Plasmon Resonance Biosensor", J. Nanophot. 12, 012503 (2018).
[18] G.M. Jassam, S.S. Ahmed, "Tapered PCF Mach–Zehnder interferometer based on surface plasmon resonance (SPR) for estimating concentration toxic metal ions (lead)", J Opt 53, 163–168 (2024).
[19] A. I. Mahmood, R. K. Ibrahim, A. I. Mahmood, and Z. K. Ibrahim, "Design and simulation of surface plasmon resonance sensors for environmental monitoring", J. Phys.: Conf. Ser. (IOP Publishing), p. 012118, (2018).
[20] S. Islam, J. Sultana, A. A. Rifat, R. Ahmed, A. Dinovitser, B. W. H. Ng, H. Ebendorff-Heidepriem, and D. Abbott, "Dual-Polarized Highly Sensitive Plasmonic Sensor in the Visible to Near-IR Spectrum," Opt. Express, vol. 26, no. 23, pp. 30347–30361 (2018).
[21] A. Vial, A. S. Grimault, D. Macías, D. Barchiesi, M. L. De La Chapelle, "Improved analytical fit of gold dispersion: application to the modeling of extinction spectra with a finite-difference time-domain method", Phys Rev B., 71(8): 085416, (2005).
[22] G. M.Jassam, and S. S. Ahmed, "D-shaped photonic crystal fiber toxic metal ions (arsenic) sensor based on surface plasmon resonance", Iraqi Journal of Physics, 21(2), 91-98(2023).

مستشعر الدواء من الألياف البلورية الضوئية يعتمد على رنين البلازمون السطحي

سالي خالد عباس* و سؤدد سلمان احمد

قسم الفيزياء، كلية العلوم، جامعة بغداد، العراق، بغداد

*البريد الالكتروني للباحث: sallyaljanabi@gmail.com

الخلاصة: تقدم هذه الدراسة مستشعرًا يستخدم تقنية الألياف الكريستالية الضوئية (PCF) وتقنية رنين البلازمون السطحي (SPR). تم تطبيق الذهب (Au) كطبقة رقيقة على ألياف كريستالية ضوئية (PCF)، والتي كانت مغلفة سابقًا بمركب ذهبي مستقر كيميائيًا يُظهر خصائص بلازمونية. كان سمك طلاء الذهب 40 نانومتر. تم تقييم مقاييس الأداء، مثل الحساسية (بما في ذلك حساسية الطول الموجي وحساسية السعة) والقرار، عن طريق المحاكاة عبر برنامج COMSOL. تم تطوير المستشعر المقترح باستخدام طريقة العناصر المحدودة ومن ثم إخضاعه للتحليل العددي. تشير النتائج إلى أن سطح الألياف البلورية الضوئية، عند تغليفه بمادة Au، يعمل كجهاز استشعار للكشف عن معامل الانكسار (IR) للعينات الصيدلانية منتهية الصلاحية. يتم إجراء بحث حول تأثيرات المعلمات الهيكلية على أطياف الرنين بهدف تحسين أداء الاستشعار. أعلى حساسية للسعة المسجلة كانت 31.2 RIU-1، في حين أن الحد الأقصى للدقة التي تم الوصول إليها كان 6×10-5 RIU. تم الحصول على هذه القياسات ضمن نطاق الكشف من 1.383 إلى 1.399.

IJL, Issue 2, Vol. 23, 2024
https://doi.org/10.31900/ijl.v23i2.487

Research Article

IRAQI JOURNAL OF LASER

Treatment of Pilonidal Sinus Using 1470nm Diode Laser as Minimally Invasive Technique

Ali Fouad Rashid Al-Khazraji*

Department of surgery, Al-Yarmouk teaching hospital, Baghdad, Iraq
** Email address of the Corresponding Author: aquarius77doc@gmail.com*

Article history: Received 6 Jul. 2024; Revised 22 Aug. 2024; Accepted 9 Sept. 2024; Published online 15 Dec. 2024

Abstract

Background: The term pilonidal sinus refers to a condition that exists in the natal cleft above the coccyx. The incidence rate among males is 2.2-4 times that of females. Sacral abscess characterizes the acute phase, while cyst development or continuous sinus drainage may occur during the chronic phase. In this study, a 1470nm diode laser was used for the treatment of 50 cases of the pilonidal sinus as SiLaT Sinus Laser Therapy.

Aim of the study: to assess the safety and the effectiveness of the use of 1470nm-diode laser for treatment of pilonidal sinus by internal destruction of the granulation tissues and epithelialized sinus using radially emitting probe and assessment of any possible complications and patients' satisfaction.

Patients, Materials & Methods: This is a prospective study with 50 patients; all patients were operated on, in the private clinic under local anesthesia, using a 1470 nm diode laser for SiLaT (Sinus Laser Therapy) between February 2023 and February 2024, all patients surveyed and reported having one or more of complications listed in questionnaire paper (if any).

Results: The surgery was tolerated by all of the patients. According to the sex and Tezel's classification the patients are divided into five types, type I ten cases all are male, type II seven cases (five are male and two are female), type III 21 cases (20 cases are male and one case is female), type IV five cases all are male, type V seven cases all are male. All cases have no major complication in the early postoperative period, closure of sinus pit(s) have occurred between 9-22 days. (74%) of cases have mild pain, (6%) of cases have no pain on analgesic regimen, (20%) of cases have moderate pain No patient experienced significant primary bleeding, 16% of cases experienced a serous discharge that lasts for few days until it ceases on its own. No patient experienced infection. 78% of cases return to work on next day post-operatively, 16% of cases after 1 day of sick leave, 6%of cases after 2 days of sick leave. 2% of cases have been suffered from P.N.S. abscess. All patients were satisfied with the outcome of the operation.

Conclusion: Diode 1470nm laser sinus laser therapy (SiLaT) is a safe and effective procedure associated with a low incidence of postoperative complications, it is an acceptable, and remarkable substitute for traditional surgical treatment techniques and can be regarded as reliable, effective, and easy to use.

Keywords: 1470nm, diode laser, pilonidal sinus, pilonidotomy, pilonidoplasty.

1. Introduction

The term pilonidal sinus refers to a condition that exists in the natal cleft above the coccyx. This may consist of one or more normally uninfected midline holes that connect with a fibrous tract, which is lined by granulation tissue and may contain loosely lying hair within the tract [1]. The Caucasian population has the highest incidence rate; in Europe and the United States, the incidence is 26/100,000, and the majority of patients are between the ages of 15 and 30 [2]. The sinus tract has squamous epithelium lining its smooth interior. The sinus tract eventually ends up in a subcutaneous chamber filled with granulation tissue and hair nests. In actuality, the sinus tract apertures represent the deep cavity's expansion. Because of this, an abscess development might appear lateral to the midline or in the midline itself [3]. The incidence rate among males is 2.2-4 times that of females [4-5]. The PNS can be presented as asymptomatic, but may present as a cyst or a sinus, and can be presented as an abscess. The hair may be projecting from the sinus orifice [6]. The specific etiology of PNS is unclear. It is assumed to be caused by the wrong orientation of developing hair, which leads to a hair follicle rupture [7].

Treatment options:

- In the past decades, several techniques have been offered to treat pilonidal sinus disease, but no gold standard treatment has been established, particularly for complicated patients [8].
- Recurrence differs depending on the primary closure procedure used. A recent meta-analysis showed that regardless of technique, individuals with primary midline closure had a higher recurrence rate (67%) than those with off-midline closure; the least common recurrence rates at any follow-up interval were Bascom cleft-lift and Karydakis flap [9].
- Wilhelm was the first to suggest laser ablation utilizing 1470 nm radial emitting diode laser fiber, which was initially used to treat anal fistulas with an 82% cure rate. The fistula closes as the tissue within gasifies and contracts due to the energy emitted by the circumferential laser at the end of fiber optic [10]. When Dessily et al. employed this method for the first time in 2016 to treat pilonidal sinuses, the results were an 87.5% success rate, a 2.9% recurrence rate, minimal postoperative pain, and small incisions [11].
- A simple operation with little tissue damage and a low chance of recurrence would be ideal. It should also only necessitate a brief hospital stay and a speedy return to normal activities. As a result, there is increasing evidence from small patient series that using a diode laser to treat pilonidal sinuses may be a useful option since it is a minimally invasive operation that does little harm to nearby tissues and has success rates of 80–90% [3,12].
- According to reports, the optimal treatment method should include low rates of wound dehiscence and infection, low rates of recurrence, good cosmetic outcomes, and a brief recovery period [13].

1.1 Study objectives

To assess the safety and the effectiveness of the use of 1470nm-diode laser for treatment of pilonidal sinus by internal destruction using radial optic fiber and assessment of any possible complications and patients' satisfaction.

2. Patients, material & procedure

2.1 Patients

This is a prospective study with 50 patients; three are female and the others (47) are male. They were operated on, in the private clinic as local anesthesia is used for operation and no need for hospitalization, using a 1470 nm diode laser for sinus laser treatment (SiLaT) between February 2023 and February 2024,

due to conditions of pilonidal sinus disease. Patients' ages ranged from 15 to 42 years, with a mean age of 26.5±6.5 years, following a thorough description of the procedure and a discussion of its potential benefits and complications. Preoperative evaluation: A case sheet was designed exclusively for the purpose of reviewing each patient's healthcare details and records. Age, symptoms (history of pus collection, pus discharge, bloody discharge, nodule, itching, pain), any prior surgeries (if any), and past medical history are all considered as part of the patient's history. A verbal agreement was obtained, a clinical evaluation of the patients, and hematological investigations for virological infection. Clinical examination of sinus site and fix its Tezel's classification. Tezel's classification: there are five types according to this classification as shown in Table 1.

Table 1. Tezel's classification types [14]

Type of pilonidal sinus	Presentation
Type I	Asymptomatic pit(s) with no history of drainage or abscess
Type II	Acute pilonidal abscess
Type III	Pit(s) in the navicular area with an abscess or prior drainage history
Type IV	A severe condition in which one or more sinus pit(s) are situated outside the navicular area
Type V	History of recurrent pilonidal sinus

Navicular area: lies between the natal cleft's lateral edges and their posterior extensions, the posterior borders of the anal triangle make the posterior borders of the navicular area as shown in figure 2-1[14].

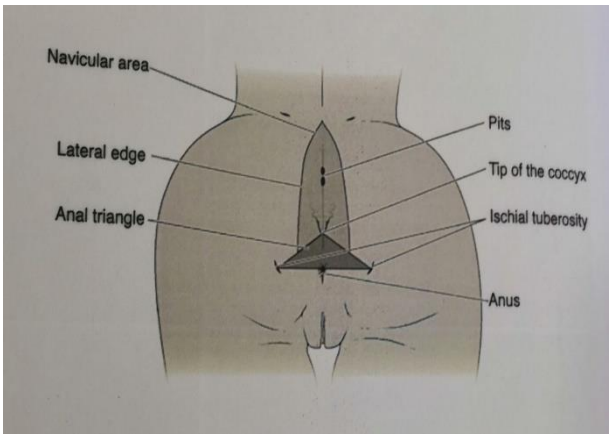

Fig. 1: Navicular area [14].

2.1.1 Inclusion criteria

This study includes all patients who have pilonidal sinus disease regardless the Tezel's classification of the case.

2.1.2 Exclusion criteria

We excluded from our study patients with severe co-morbid illnesses. (None was excluded).

2.2 The Material

The medical laser system and accessories:

2.2.1. Laser system Specification

The laser system employed in this study was a class IV Medical laser system, a 1470nm diode laser, which emits laser at a wavelength in the near-infrared spectrum. The surgeon configured the laser aperture power output to vary between 0.5 and 15 Watts. Wuhan Dimed Laser Technology Co., Ltd. is the Chinese manufacturer of the diode laser (CHEYLAS-45JN) that is utilized. As shown in Figure 2.

Fig.2: laser device used.

2.2.2 Equipment

The following items are arranged on a tray with drapes Figure 3: hypo-allergic surgical tape (4 inches), medical steel kidney dish, two syringes of 10 milliliters, Gauze swabs, Lidocaine solution 1% (50 milliliters), 100 milliliter of 0.9% isotonic normal saline, hydrogen peroxide solution 20%, methylene blue solution (optional), gloves, surgical scalpel size 22, large and small malleable steel probes, curette size 3 and 4mm, brushes, skin biopsy punch tool size 2-4mm, blunt steel cannula, 10 ml sodium bicarbonate solution 10%.

Fig. 3: Equipment.

Also, Doctor Google and completely shielded patient goggles are used during laser irradiation as shown in Figures (4-5).

Fig. 4: Doctor Google.

Fig.5: Completely shielded patient goggles.

2.3 Procedure

With the patient in the prone position and stretching of the natal cleft by using surgical tape (4 inches) on each gluteal area to the side of the surgical couch, an antiseptic 10% povidone-iodine solution was applied, No sedation or IV N.S.A.I.D. was used; instead, one ml of $NaHCO_3$ is added to the 100ml of normal saline (0.9%), a five ml of this solution is used to dilute 5 ml of lidocaine solution 1% without epinephrine (up to total 10 ml) was injected into the skin and subcutaneous tissue around the sinus in the superficial and deep plane around the sinus, using 25-40 ml of diluted lidocaine to anesthetize the area around the sinus. Following the administration of local anesthesia, if the sinus has a pit(s) try to advance the probe in the sinus to identify the sinus space in the subcutaneous area; if not, use the skin biopsy punch tool to create one or two to access to the sinus (at the two ends of the sinus according to its size). Next, using a suitable curette handle curettage the inside of the sinus and get rid of all possible hair, granulation tissue, and debris from inside the sinus, then use the brush the same way as a curette to get rid of all remaining hair and debris, then using one ml of H_2O_2 20% diluted by four ml of normal saline (0.9%), to reach 4% concentration that is needed, and injected inside the sinus using the blunt steel cannula; after that wash the sinus with normal saline (0.9%). Using a radial emitting laser fiber optic of 600μm diameter with a SMA905 connector, the laser energy is delivered at 11W power in continuous wave (CW) mode, entering from one hole to the other and vice versa. The speed of pulling the fiber optic is kept as steady as possible at a rate of 1mm/sec, so each 1mm of the sinus is exposed to 11W for 1sec= 11 joules. The total amount of energy is 11J/mm. Wet gauze with 0.9% normal saline was applied to a sinus site after each full irradiation of the sinus. The skin opening is kept open if it is 2-3 mm in diameter, if larger approximate the edges of the opening using nylon suture 2/0 in mattress pattern to facilitate its closure, and kept for 10-14 days. Then at the end of the operation, use of antiseptic to sterilize the operation site and then dressing. Procedure time is 15-32 minutes with a mean of operation time 23.9±3.9 minutes (mean±S.D.). Figures (6-9) show some cases operated under local anesthesia in the clinic

Fig. 6: left: probing of sinus, right: after completion of the procedure. Tezel's type I.

Fig.7: left: hair exit from the sinus, middle: hair extracted prior to cleansing, right: hair extracted after cleansing the sinus. Tezel's type I.

Fig.8: left: PNS with granulation tissue at the upper pit, right: after laser irradiation, excision of granulation tissue and closure of the wound. Tezel's type III.

Fig.9: left: PNS abscess, left: drainage of pus prior to complete the steps of procedure. Tezel's type II.

2.4 post-operative treatments

For each patient postoperative follow-up date is fixed after 10 days, giving him a prescription of antibiotics and analgesia as follows:

1- Injectable antibiotic for 3-5 days followed by oral one for another 5 days.(ceftriaxone vial 1gm 1*1 / cefixime tab. 400mg 1*1)
2- Single injectable analgesic on the first day (diclofenac sodium amp. 75mg on need), followed by oral analgesia (diclofenac potassium 50mg 1*2 after meal) for 3-5 days.
3- Use of fucidin cream local antibiotic cream (fusidic acid 20mg 2% w/w) for the hole(s) of the sinus and instruction of dressing.

3. Result and discussion

3.1 Results

The results of this study are based on the clinical evaluation of every patient through examination, complaints made by the patient during the procedure, post-operative and clinical follow-up. Under local anesthetic, the surgery was tolerated by all of the patients. Fifty patients, three are female and 47 are male. According to the sex of the patients and their Tezel's classification they were divided into five types: type I ten cases all are male, type II seven case (five are male and two are female), type III 21 cases (20 cases are male and one case is female), type IV five cases all are male, type V seven cases all are male. As shown in Table 2.

Table 2. Patients' sex and Tezel's classification of 50 cases.

Tezel's classification	No. of male Patients	Percentage (%)	No. of female Patients	Percentage (%)	Grand total	Grand percent
Type I	10	20%	0	0	10	20%
Type II	5	10%	2	4%	7	14%
Type III	20	40%	1	2%	21	42%
Type IV	5	10%	0	0	5	10%
Type V	7	14%	0	0	7	14%
Total	47	94%	3	6%	50	100%

First post-operative visit after 7-10 days to check for surgical site infection and removal of suture if used (or maybe post ponded to the next visit), second visit after three weeks to ensure closure of PNS pit(s), all cases tolerate the pain of anesthetic drugs infiltration and the operation itself the pain is simple, all cases have no major complication in early postoperative period (until the closure of PNS pit(s)), closure of sinus pit(s) have occurred between 9-22 days, mean days of closure 15.04±2.8 days. None of the patients experienced any serious intraoperative or postoperative complications; therefore there was no need for hospitalization. All patients have been followed for four months for any recurrence, and only one patient suffered of PNS abscess after primary healing that occurred three months and 17 days, who have been re-operated again as the case of Tezel's classification V, (was primarily type I); yet he was not re-encountered as a new case.

3.2 Post-operative complications / follow-up

Patients were followed on the 7th or 10th day and after 3 weeks post-operatively.

A. Pain was classified as mild, moderate, and severe. As the patient's description, to simplify the pain assessment by patients. As shown by Table (3-2), no patients were suffering from severe pain (0%); 10 patients (20%) (7 with Tezel's type II, 3 with Tezel's type IV) had moderate pain, most patients with Tezel's classification type II (acute PNS abscess) and type IV (PNS outside the navicular area or with granulation tissue that is resected and closure of its defect with suture) were suffering of moderate pain, the first postoperative day's pain necessitated the use of an injectable NSAID analgesic (olfen ampoule) to manage the pain, and then the pain decreased in the following days, the second and third day the pain is mild, later on the pain is mild and occasional (the pain is not always present), or disappeared. The other 37 patients (74%) have mild pain from the start; 29 patients (58%) for two days and 8 patients (16%) for only one day. The last three patients (6%) have no pain on the analgesic regimen mentioned (post-operative treatments), those with Tezel's type I.

B. Bleeding and discharge: As shown by Table (3-2), no patient experienced significant primary bleeding (spontaneous bleeding after surgery) or reactionary bleeding (after six hours). Eight patients 16% experienced a serous discharge; five patients with Tezel's type II (10%), and three patients with Tezel's type IV 6% Postoperative serous discharge is identified by simple dressing soiling that lasts for one to two days until it ceases on its own without medical intervention.

C. Infection: as shown by Table 3, no patient (zero%) developed an infection during the early postoperative period (until the closure of the sinus pit(s)), and the postoperative period passed unnoticeably regarding the infection of the surgical.

D. *Return to work*: 39 patients (78%) return to work on the next day post-operatively, 8 patients (16%) after 1 day of sick leave, the last 3 patients (6%) after 2 days of sick leave (all with Tezel's type II).as shown in table (3-2).

E. *Recurrence*: As seen in Table (3-2), One patient (2%) suffered of P.N.S. abscess after complete primary healing and closure of sinus pits, after three months and 17 days; that is operated on again as a case of SiLaT without re-encountered as a new case, as it is operated no loose hair is found in the pus, so it may be caused by sebaceous cyst infection, sweat gland infection, or even soft tissue cellulitis of the area. After the re-operation, the case is followed up again for new four months. No new recurrence of this specific case.

F. *Satisfaction*: all patients (100%) were satisfied with the procedural results and postoperative conditions, even those who have been suffering from pain and serous secretion as they have lasted for a maximum 2 days, later on, the general condition stabilized as shown in Table 3. Yet they are generally completely satisfied with the result as no active bleeding, no severe pain, and the operation has been finished under local anesthesia with minimal pain, and no major wound or wick drain left.

3.3. Discussion

This prospective study uses a diode laser operating at 1470 nm to treat Pilonidal Sinus Disease (PSD) by minimally invasive laser-induced interstitial thermotherapy by internal destruction of the granulation tissue of the sinus tract using radial emitting laser fiber that irradiates 360° (circumferentially) to enhance sinus healing. The following characteristics were to be prospectively assessed in this study: pain, bleeding, surgical site infection, return to work, overall patient satisfaction, and recurrence. Some cases in this study had post-procedural pain, a few cases had serous discharge, and only one case had recurrence. A 2014 meta-analysis argued that deep excision with secondary healing should be abandoned [15].

Table 3. The results of the patients

Post-operative complications / follow up	No. of Patients	Percentage (%)	Tezel's classification	No. of days
No pain	3	(6%)	I	
Mild	37	(74%)	Different types	
Moderate	10	(20%)	7 of type II 3 of type IV /	
Sever	0	(0%)		/
Bleeding & discharge				
Primary and secondary bleeding	0	(0%)	/	/
Serous discharge	8	(16%)	5 of type II 3 of type IV	Max. 3 days
Infection	0	(0%)	/	/
Return to work				
	39	(78%)	Different types	Next day
	8	(16%)	Different types	After one day sick leave
	3	(6%)	II	After two days sick leave
Satisfaction	50	100%	Different types	/
Recurrence	1	(2%)	Primarily type I	After 3 months and 17 days

Regarding postoperative pain, mild pain had been occurred in (74%) of cases, moderate pain in (20%) of cases, and no pain in (6%) of cases. This is in agreement with three studies that showed significantly lower pain scores after a conservative approach (like sinusectomy or sinusotomy) as compared to en bloc excision.[15] Janjua et al. reported that in the first 24 hours following surgery, the Limberg flap group's mean postoperative pain levels (2.63±0.76) were considerably lower than those of the primary excision group (5.63 ± 0.72) [16]. Likewise, Naeem G. et al. reported that patients in the Limberg group had lower pain on the early postoperative period, higher levels of satisfaction, and starting routine activity compared with primary midline closure [17].

Lim J and Shabbir J found that two methods of limited excision: de-roofing and curettage of the pilonidal sinuses (instead of excision), and that a relatively recent surgery called sinusectomy which entails the removal of the PSD sinuses alone. Researchers found that limited excision causes less pain and allows for an earlier return to work than extensive excision [18]. This is agreed with Girolamo Geraci et al., On the first day, the mean score for postoperative pain was 3.2 ± 1.5; on the third day, it was 2.5 ± 0.8; and on the seventh day, it was 1.2 ± 0.8. Only 30% of patients needed painkillers [19]. So as the procedure is minimally invasive, it is associated with less pain.

Regarding bleeding and discharge in this study, it is classified as:

- Primary bleeding in the early postoperative period (first six hours).
- Secondary bleeding (after six hours).
- Serous discharge post-operatively.

No patient experienced significant primary bleeding (spontaneous bleeding after surgery) or reactionary bleeding (after six hours). Eight patients 16% experienced a serous discharge; five patients with Tezel's type II (10%), and three patients with Tezel's type IV 6% Postoperative serous discharge is identified by simple dressing soiling that lasts for one to two days until it ceases on its own without medical intervention.

In Tavangari et al., we used electrosurgery to unroof the sinus. The only tissue that was removed was nonviable tissue, which included the cavity of the chronic abscess, if any. The base of the sinus was fully cauterized after all granulation tissue, hair, and debris were extracted using a curette. On the seventh postoperative day following surgery, one patient (1.1%) out of 94 was assessed in the emergency room due to wound bleeding, which stopped once a pressure dressing was applied. The patient showed no signs of hemodynamic instability, and a follow-up test revealed normal hemoglobin levels [20].

In Gaurav Wadhawan et al., Fluid collection occurs in 20% of the excision and closure group and 13% of the Limberg flap group; while Hematoma occurs in 20.1% of the excision and closure group and 11.3% of the Limberg flap group [21]. Bugalia RL stated: that hematoma occurred in 4% of cases as follows (Marsupialization 1%, Unroofing 0%, Primary closure 1%, Limberg flap transposition 2%) [22]. In this study, this specific issue is better in SiLaT than in other operations.

Regarding infection and abscess formation, no patient (zero %) developed an infection during the early postoperative period (until the closure of the sinus pit(s)), and the postoperative period passed unnoticeably regarding the infection of the surgical site. Bugalia RL stated: that the most commonly encountered postoperative complication is infection which occurred in 10% of cases as follows (Marsupialization 3%, Unroofing 2%, Primary closure 2%, Limberg flap transposition 3%) [22]. Dessily et al, treated 40 patients with a pilonidal sinus using a radial emitting diode laser probe in order to destroy the sinus epithelium by the delivered energy and achieve obliteration of the tract. The success rate was 87.5%, the recurrence rate 2.9%, and the complication rate 10% (two cases of hematoma and two abscesses "5 %"), all medically treated [7]. The Karydakis flap was associated with a higher wound infection rate than the Limberg flap group in a randomized trial of 100 patients (13/50 vs 4/50 patients) respectively [23].

In Soliman et al., Wound infection was 1 (3.3%) in the Limberg flap group and 6 (20.0%) in the excision and primary closure group [24].

In this study, the primary infection is null, which is better than other surgical procedures, yet we have had 1 case (2%) of recurrence that falls within the accepted ratio.

Return to work: 39 patients (78%) return to work on the next day post-operatively, 8 patients (16%) after 1 day of sick leave, and the last 3 patients (6%) after 2 days of sick leave (all with Tezel's type II).

In Vartanian et al., return to work in excision and midline closure after 10.4–17.5 days, while in excision and off-midline closure return to work after 7–9.3 days and in sinusectomy return to work after 2–16 days [25]. In contrast, in Naeem G. et al., 23 patients (76.6%) start routine activity in the third week in the Limberg flap group, and 18 patients (60%) started routine activity in the same week in the excision and primary midline closure group [17]. As the operation is as minimally invasive as possible, it is faster to return to work.

Recurrence: During the four-month follow-up phase, One patient (2%) suffered of P.N.S. abscess after complete primary healing and closure of sinus pits, after three months and 17 days; that is operated again

as a case of SiLaT without reencountered as a new case, as it is operated no loose hair is found in the pus, so it may be caused by sebaceous cyst infection, sweat gland infection, or even soft tissue cellulitis of the area. After the re-operation, the case is re-followed for new four months. No new recurrence of this specific case. In Soliman et al., Recurrence occurs in 0 cases (0.0%) in the Limberg flap group, while it occurs in 4 cases (13.3%) in the excision and primary closure group, (Follow up period 1 year) [24]. In contrast, in Naeem G. et al., recurrence occurs in 13 cases (43.3%) of the Limberg flap group, primary cases in this group(56.6%); while it occurs in 2 cases (6.6%) of excision and primary midline closure group, primary cases in this group (93.3%), (Follow up period few months in both groups) [17].

Twelve to thirty-six months following our surgical technique, only four recurrences (8.32%) were found; one patient had previously had one operation, two to three surgeries, and lastly one to four surgeries. A second treatment that resulted in permanent healing involved subcutaneous tract excision and pseudocystic cavity unroofing [19].

In Vartanian et al., the lowest rate of recurrence is found in the excision and off-midline closure group (0-6%) in comparison to the sinusectomy group (3-25%) and excision and midline closure group (4-45%) [25].

The operation is as minimally invasive as possible, as it has a better recurrence rate because no need for excessive dissection of normal healthy tissue.

In terms of satisfaction: all patients (100%) were satisfied with the procedural results and postoperative conditions, even those who have been suffering of pain and serous secretion as they have been lasted for a maximum 2 days, later on the general condition stabilized as shown in table (3-2). Yet they are generally completely satisfied with the result as no active bleeding, no severe pain, and the operation has been finished under local anesthesia with minimal pain, and no major wound or wick drain left. In Naeem G. et al., patient satisfaction is assigned that 26 patients (86.6%) were satisfied in the Limberg flap group, while 22 patients (73.3%) were satisfied in primary midline closure [17]. In Girolamo Geraci et al., the questionnaire's results, which assessed patients' satisfaction and pleasure, revealed that 46/48 (96%) of the patients were completely satisfied, and every patient suggested the operation to others (unroofing of pseudocystic cavity)[19].

When the patients were asked if they were satisfied with the outcome of the procedure, 94% of patients in Group I (minimally invasive surgery) said they were, while 5.7% of patients said they were not. In Group II (Karydakis procedure), 31.9% of patients were not satisfied with the surgical procedure's outcome, whereas 68.1% of patients were [26]. From all these studies the satisfaction and recommendation of operation is associated with minimally invasive surgery and primary closure of the wound, in our study the procedure is minimally invasive and no major wound that necessitates primary closure, so associated with high rates of satisfaction.

3.4 Limitations of the study

In this study there are some limitations:

1. The sample size is small.
2. The follow-up period (four months) is short.
3. No specific surgical management group is involved to be compared with.
4. The procedure is the blind control of the tracts that may still contain foreign bodies or untreated epithelium. For this reason, in order to reduce the risk of recurrence, careful cleaning of the cavity is deemed mandatory prior to laser treatment.

4. Conclusions

Diode (1470nm) laser sinus laser therapy (SiLaT) is a safe and effective procedure associated with a low incidence of post-operative complications, despite this study's limitations, which primarily focused on the feasibility, safety, and short-term outcome of the procedure. However, it does require the availability of

instruments (Diode laser system) and a skilled, well-trained surgeon. For the treatment of PNS, these are superior tools to traditional surgical methods.

The benefits of using a laser include its ability to stop bleeding, eradication of the granulation tissue from within the sinus that prevents its healing, the tolerance of laser by patients under local anesthesia, and its decreased risk of complications during or even after the operation, Post-operative pain is minimal, Serous discharge is minimal, Return to work is faster than traditional surgical procedures with very short sick leave (if any), Satisfaction rate is high in SiLaT in comparison to traditional surgical procedures, Recurrence rate is low in this study and Post-operative pain and serous discharge are mostly associated with Tezel's classification II, IV.

References

[1] Hamilton Bailey ML, Norman S. Williams, Christopher J.K. Bulstrode PRO (eds). SHORT PRACTICE OF SURGERY. 27th ed. CRC press Taylor &Francis Group; Vol.2; 2018. Part11; Ch74, p1347-1349.
[2] Manigrasso M, Anoldo P, Cantore G, Chini A, D'Amore A, Gennarelli N, Maione F, Marello A, Schettino P, Sorrentino C, et al. Endoscopic treatment of pilonidal sinus disease: state of art and review of the literature. Front Surg. 2021;8(null):812128.
[3] Spalding M Ch. GJ. Pilonidal Disease Treatment & Management E-medicine [internet]: medscape.com; 2021 [updated Jun 11, 2018. Available from: https://emedicine.medscape.com/article/192668-treatment#d10.
[4] Nixon At, Garza RF. Pilonidal cyst and sinus. StatPearls; 2020.
[5] Duman K, Gırgın M, Harlak A. Prevalence of sacrococcygeal pilonidal disease in Turkey. Asian J Surg. 2017;40(6):434–437. doi: 10.1016/j.asjsur.2016.04.001.
[6] Doll D, Brengelmann I, Schober P, Ommer A, Bosche F, Papalois AE, et al. Rethinking the causes of pilonidal sinus disease: a matched cohort study. Scientific reports. 2021;11(1):6210.
[7] Dessily, M., Charara, F., Ralea, S., Alle, J.L. (2017), Pilonidal sinus destruction with a radial laser probe: technique and first Belgian experience. ActaChirurgicaBelgica, 117: 164- 168. PMID: 28056720 DOI: 10.1080/00015458.2016.1272285.
[8] Isik A, Ramanathan R. Approaches to the treatment of pilonidal sinus disease, clinical practice in 2019. Int Wound J. (2020) 17:508–9. 10.1111/iwj.
[9] Stauffer VK, Luedi MM, Kauf P, et al. Common surgical procedures in pilonidal sinus disease: a meta-analysis, merged data analysis, and comprehensive study on recurrence. Sci Rep. 2018;8:3058.
[11] Dessily M, Dziubeck M, Chahidi E, Simonelli V. The SiLaC procedure for pilonidal sinus disease: long-term outcomes of a single institution prospective study. Tech Coloproctol. 2019;23(12):1133–1140. doi: 10.1007/s10151-019-02119-2.
[12] Giamundo, P., Esercizio, L., Geraci, M., Tibaldi, L., Valente, M (2015) Fistula-tract Laser Closure (FiLaC™): long-term results and new operative strategies. Techniques in Coloproctology. 2015, 19 :449-53. doi: 10.1007/s10151-015-1282-9, PMID: 25724967
[13] Sahsamanis G, Samaras S, Mitsopoulos G, Devrakis T, Dimitrakopoulos G, Pinailidis D. Semi-closed surgical technique for treatment of pilonidal sinus disease. Ann Med Surg (Lond). 2017;3(15):47-51.
[14] Kamal Gupta. Lasers in Proctology. Springer Nature Singapore Pte Ltd.2022; Ch17, 17.10, 17.11, p283-286.
[15] Enriquez-Navascues, J. M.; Emparanza, J. I.; Alkorta, M.; Placer, C. (2014). Meta-analysis of randomized controlled trials comparing different techniques with primary closure for chronic pilonidal sinus. Techniques in Coloproctology, 18(10), 863–872. doi:10.1007/s10151-014-1149-5
[16] Janjua MH, Mohsin J, Fatima J, Siddique MU, Naseem MY, Gill AJ. Comparison of outcome of simple excision and primary closure with Limberg Flap procedure in Pilonidal disease. Isra Med J. 2021; 13(1): 11-14.
[17] Naeem G., Muhammad A. J., Farooq A., Hina K., Muhammad A., Kamaran K., (2022). Limberg Flap Versus Primary Midline Wound Closure in Treatment of Chronic Pilonidal Sinus Disease. P J M H S Vol. 16, No.01, JAN 2022 219. DOI: https://doi.org/10.53350/pjmhs22161219
[18] Lim J and Shabbir J, (2019). Pilonidal Sinus Disease - A Literature Review. World Journal of Surgery and Surgical Research. 2019 | Volume 2 | Article 1117.
[19] Girolamo Geraci, Piero Luigi Almasio, Martina Mongitore, Rosalia Patti, Angelica Abbate, Sara Lo Faso, Bianca Maria Cudia, Gaetano Di Vita., (2020). Recurrent sacrococcygeal pilonidal disease: the efficacy of minimal subcutaneous excision of the sinus and unroofing of pseudocystic cavity. Annali Italiani Di Chirurgia, vol. 91, no. 4, July 2020, pp. 437-41.

[20] Tavangari, Farees Ricky; Lee, Jennifer Amy; Garza, David; Tejirian, Talar . (2017). Outcomes of Unroofing with Limited Excision and Structured Postoperative Care for Pilonidal Disease. The American Surgeon, 83(10), 1045–1049. doi:10.1177/000313481708301006
[21] Gaurav Wadhawan, Dhawal Sharma, KC Vyas., (2020). A comparative study of different treatment outcomes in cases of pilonidal disease. International Journal of Surgery Science 2020; 4(3): 292-297. DOI: https://doi.org/10.33545/surgery.2020.v4.i3e.511
[22] Bugalia RL. Assessment of Surgical Management of Patients Undergo Pilonidal Sinus Disease: A Hospital Based Study. J Adv Med Dent Scie Res 2018;6(4):69-
[23] Mary-Margaret Kober, MD; Usha Alapati, MD; Amor Khachemoune, MD, Treatment Options for Pilonidal Sinus, WWW.MDEDGE.COM/CUTIS, 2018, VOL. 102 NO. 4
[24] Soliman Mohamed, S., O. Alfy, M. LIMBERG FLAP VERSUS EXCISION WITH PRIMARY CLOSURE IN PILONIDAL SINUS. Al-Azhar Medical Journal, 2020; 49(4): 1511-1518. doi: 10.21608/amj.2020.120554.
[25] Vartanian, Emma; Daniel, J. Gould; Lee, Sang W.; Patel, Ketan . (2018). Pilonidal Disease. Annals of Plastic Surgery, 81(6), e12–e19. doi:10.1097/SAP.0000000000001585.
[26] Ozyildiz M, Yazicioglu MB, Coskun M, Turgut HT, Tiryaki C, Civil O, Yuksel A, Yildiz SY. Comparison of results of minimal invasive surgery for pilonidal sinus with Karydakis procedure: less is more. Journal of Turgut Ozal Medical Center. 2017 Jul 1;24(3).

علاج الناسور العصعصي باستخدام ليزر الصمام الثنائي 1470 نانومتر كتقنية طفيفة التوغل مقارنة بالطرق الجراحية

علي فؤاد رشيد الخزرجي

قسم الجراحة, مستشفى اليرموك التعليمي, بغداد, العراق

*البريد الالكتروني للباحث: aquarius77doc@gmail.com

الخلاصة

الخلفية: مصطلح الناسور العصعصي يشير إلى حالة موجودة في منطقة الشق الولادي فوق العصعص. يحتوي الناسور العصعصي (الشعري) عادة على الشعر والأوساخ والأنسجة الحبيبية غير الصحية. يسبب الناسور العصعصي معاناة شديدة ، وفي الغالب تحدث عدوى واخماج فيه، مما يؤدي إلى تسرب القيح ذو رائحة كريهة. معدل الإصابة بين الذكور2.2 - 4 مرات أعلى منها بين الإناث. تتميز المرحلة الحادة بوجود خراج عجزي، في حين خلال المرحلة المزمنة يمكن ملاحظة تكوين الكيس أو إفرازات الناسور العصعصي المستمرة. العملية المثالية يجب ان تكون بسيطًة، مع الحد الأدنى من فقدان الأنسجة ومعدل رجوع للحالة منخفض, علاوة على ذلك، يجب أن تتطلب العملية إقامة قصيرة في المستشفى وعودة سريعة إلى الأنشطة اليومية.

في هذه الدراسة تم استخدام ليزر الصمام الثنائي 1470 نانومتر لعلاج 50 حالة من الناسور العصعصي كعلاج بالليزر SiLaT (بغض النظر عن تصنيف تيزيل للحالات المعالجة) كتقنية طفيفة التوغل ليتم استخدامه ببضع الناسور العصعصي ورأبه دون جرح او استئصال الانسجة السليمة لمنطقة الناسور.

الهدف من الدراسة: مشاركة خبرة فعالية وسلامة استخدام ليزر الصمام الثنائي 1470 نانومتر لعلاج حالات الناسور العصعصي (الشعري) عن طريق تدميرانسجة الناسور داخليا باستخدام الليف البصري ذو الأنبعاث الشعاعي ومقارنة وتقييم أي مضاعفات محتملة ورضا المرضى مع الطرق الجراحية الأخرى.

المرضى والمواد والطريقة: هذه دراسة مستقبلية شملت 50 مريضًا (47 مريضًا ذكرًا و3 مريضات إناث)؛ كان جميع المرضى من العيادة الخاصة وخضعوا لعملية جراحية باستخدام ليزر الصمام الثنائي 1470 نانومتر (علاج الناسور العصعصي بالليزر) SiLaT في الفترة ما بين شباط 2023 وشباط 2024، وقد تم استطلاع رأي جميع المرضى وأفادوا بوجود واحد أو أكثر من المضاعفات المدرجة في ورقة الاستبيان (إن وجدت) . تم استخدام المخدر الموضعي أثناء العملية.

النتائج: تم اجراء العملية لجميع المرضى تحت التخدير الموضعي. حسب الجنس وتصنيف تيزل للناسور العصعصي ينقسم المرضى إلى خمسة أنواع، النوع الأول عشر حالات جميعهم ذكور، النوع الثاني سبع حالات (خمسة ذكور واثنتان إناث)، النوع الثالث 21 حالة (20 حالة ذكور وحالة واحدة أنثى)، النوع الرابع خمس حالات جميعهم ذكور، النوع الخامس سبع حالات جميعهم ذكور. جميع الحالات ليس لها مضاعفات كبيرة في الفترة المبكرة في فترة ما بعد الجراحة (حتى إغلاق الفتحات للناسور العصعصي)، وقد حدث التئام للفتحات بين 9-22 يومًا، متوسط أيام الألتئام 15.04 ± 2.8 يومًا. (74٪) من الحالات عانت من ألم خفيف، (6٪) من الحالات لم تعاني من اي ألم بأستخدام المسكنات، (20٪) من الحالات عانت من ألم متوسط, لم يعاني أي مريض من نزيف أولي (نزيف بعد العملية أو نزيف تفاعلي)، ثمانية مرضى 16٪ عانوا إفرازات مصلية استمرت لمدة يوم أو يومين حتى توقفت دون تدخل طبي. لم يتعرض أي مريض للعدوى. عاد 39 مريضًا (78%) إلى العمل في اليوم التالي بعد العملية الجراحية، و8 مرضى (16%) بعد إجازة مرضية ليوم واحد، وآخر 3 مرضى (6%) بعد إجازة مرضية لمدة يومين, أصيب مريض واحد (2%) من خراج الناسور العصعصي بعد الشفاء الأولي الكامل وإغلاق فتحات الناسور العصعصي بعد ثلاثة أشهر و17 يومًا؛ والتي تم اجراء العملية مرة أخرى كحالة علاج ناسور عصعصي بالليزر دون إعادة احتسابها كحالة جديدة ضمن حساب حالات العمليات. كان جميع المرضى بصورة عامة راضين عن نتائج العملية على الرغم من المضاعفات الطفيفة التي حدثت بعد العملية.

الاستنتاج: العلاج بليزر الصمام الثنائي 1470 نانومتر للناسور العصعصي هو إجراء آمن وفعال وذو معدل منخفض لحدوث المضاعفات ما بعد العملية، وهو بديل مقبول ورائع لتقنيات العلاج الجراحي التقليدية كما ويمكن اعتباره عمليًا وفعالًا. وسهل الاستخدام.